Colloidal Mobility in Contaminated Subsurface Systems: Linking Biological and Chemical Processes

A Dissertation Presented for the

Doctor of Philosophy

Degree

The University of Tennessee, Knoxville

Diliya Utegenovna Murtazina

December 2025

Dedication

To my pápa, Utegén Mikhailovich Murtázin, and máma, Nazilyá Gafúrovna Murtázina:
you are the best parents in the world and my life's blessing

To my wonderful husband, Jean Joseph Merlet

In loving memory of my brother, Timúr Utegénovich Murtázin
(November 16, 1992- September 13, 2015)

Acknowledgments

七転び八起き *"Fall seven times and stand up eight"*

I am eternally grateful for the constant support, guidance, care, and kindness of my advisor, Dr. Terry Hazen, during the 4 years I spent in his lab group. He believed in me even when I didn't. Thank you for taking me under your wing and consistently making time to discuss my progress. I appreciate the time you invested in teaching me how to become a better scientist, challenging me, and encouraging me to strive for excellence. I thank you for your goodwill and optimism, your attentive listening to my concerns, and your occasional check-ins. Being part of Hazen Lab has been an honor and a privilege. I thank my committee members, Dr. Christopher Schadt, Dr. Sindhu Jagadamma, Dr. Qiang He, and Dr. Haochen Li, for their constructive criticism, suggestions, guidance, and support in improving my dissertation. Thank you to Dr. Peter Walian and Lucy Zang at ENIGMA team Lawrence Berkeley National Lab for performing high-resolution electron microscopy imaging (TEM, SEM) of our colloid samples. I learned a great deal from Dr. Walian through our numerous discussions and appreciate his time, tremendous support, and wish for my success. We thank the members of ENIGMA team at Jizhong Zhou's lab at the University of Oklahoma for conducting DNA extraction, 16S PCR, NanoDrop, PicoGreen, data preprocessing, MiSeq sequencing, and extracting metagenomic raw sequencing files. We are grateful to the ENIGMA team at Michael Adams Lab at the University of Georgia for providing data for metal analysis of groundwater.

I am grateful to Dr. Lee Riedinger for providing me with a fellowship opportunity to conduct research at Oak Ridge National Laboratory through the Bredesen Center for Interdisciplinary Research and Graduate Education as a Ph.D. fellow and for becoming a mentor and a dear friend to my family. I thank you, Wanda Davis, the former manager and academic mother of the Bredesen Center, for your encouragement and love. I am grateful for both of your presences in my life even after your retirement.

I thank the members of the Hazen lab group: Andrew Putt, Ye Li, Zabrenna Griffiths, Sa'ad Abd Ar Rafie, Ann-Marie Harik, Isis Fukai, and Katie Walker. Ye and I have many memories from presenting posters at international conferences and from the friendships that have developed between our families. I appreciate my manager, Dominique Joyner, for collecting my samples from the Y-12 National Security Area and for her assistance in facilitating various lab collaborations. Thank you, Dom, for your support, cheerfulness, and friendship. You

significantly accelerated data curation logistics for me. I was so lucky to work with you. I thank the University of Tennessee Gamma Beta Phi Honor Society and the Society of Women Engineers. I thank my undergraduate advisor, Dr. Alexander V. Khoroshev, from Lomonosov Moscow State University, for mentoring and inspiring me. Additionally, I would like to thank my advisors from the University of Illinois at Urbana-Champaign, Dr. Clifford E. Singer and Dr. John R. Abelson, for their guidance and support.

I also thank my awesome friends, Aigerim Kakenova, Sabina Kusainova, Alua Almagambetova, Zhanar Kalizhanova, Elmira Abilova, Azamat Erzhanov, Kairat Tubalykov, Maksim Borovikov, Kristina Medvedeva, Yulia Timokhina, Bakhytnur Gabdullun, Ekeopara Emeka, Rakesh Koti, Itamar Aronson, Oyuna Angatkina, Sara Sultan, Kirtan Davda, Katharina Höland, Artem Maksov, Van-Quan Vuong, Brandon Knorr, Megan Givens, Shelby and Dan Cupp, Nick and Jess Cupp, Matt Lane, Alice and Austin Townsend, for their support. Rebecca Brink, my sweet friend, it has been a great joy, a lot of fun, and a comfort to have you by my side throughout all graduate school. Special kudos to my dearest friend Joni Hall; you are truly a fantastic human. I count my lucky stars for your presence in my life. Igor Gussev, one of my precious friends and fellow Kazakhstan citizen, thank you for encouraging me not to give up and for your tremendous guidance, advice, and moral support, which have been vital in helping me complete my PhD journey.

With all my heart, I thank my máma, Nazilyá Gafúrovna Murtázina, and my pápa, Utegén Mikhailovich Murtázin. I feel incredibly fortunate to be your daughter. Thank you for supporting my passion for science as a child by providing me with encyclopedias and books. Despite the very limited resources and opportunities in my tiny village of just 2,000 people in the steppes of Northern Kazakhstan with a harsh Siberian climate, I am grateful for your role in shaping who I am. Such humble beginnings did not deter me from pursuing a career in science. Thank you for always encouraging me throughout my life and allowing me To chase my dreams, even when they take me to the other side of the world. Pápa, you are one of the brightest people I know. Your wisdom, intelligence, light, humor, and kindness guide me every day. My kind, smart, beautiful, and loving máma, you are my role model. I feel honored and blessed to have you as my parents. I love both of you with all my heart and soul. Everything I am, I owe to you.

To all my dear relatives in Kazakhstan and Russia, especially my grandparents, Gafur (kartaika) and Fanuza (nanaika) Khaziev; my uncle, Marsel, and aunt, Alfiya Khaziev; my uncle,

Fanil, and aunt, Sazhida Muhamedzharov; Lilya and Ruslan Muhamedzharov, and my cousins, Arslan Khaziev, Sultan Khaziev, and Olga Sunyaikina: thank you very much for your love and support. I also wish to express my love and gratitude to my in-laws in France, the Netherlands, and the United States: Cécile, Renaud, Marloes, Benoît, Susan, Geraldine, and Garrett.

I am thankful to Julia and Stas Sinogeikin for inspiring me to work at a national laboratory and pursue my PhD. Thank you for being my second family in the United States, offering your support, care, and love. I also appreciate Laura and Thomas Schrepfer for their love and encouragement. Additionally, I cherish the care and love of Olga Leonidovna, Dobriana, and Karen, who warm my heart.

Finally, I would like to express my gratitude to my brilliant husband, Jean, for his unwavering support, even as he faced his own struggles and challenges throughout his Ph.D. journey alongside mine. I couldn’t wish for a better life partner. I'm incredibly proud of you and grateful for your spirit, intelligence, kindness, optimism, wisdom, wit, and sense of humor, which shine through, especially during difficult times when you always manage to bring a smile to my face. You filled my life with so much light, joy and laughter. I treasure our life with our adorable and amusing cats, Koshka and Aurora, who also helped us survive the COVID-19 lockdown. Your belief in me and encouragement mean the world to me. Thank you for making me a better, happier person. Я люблю тебя.

Abstract

This dissertation investigates how colloids mediate contaminant mobility and microbial community structure in the chemically extreme groundwater of the ENIGMA Field Research Center (eFRC) at the Y-12 National Security Complex. Integrating directional hydrology, conservative tracer tests, ion and metal chemistry, colloid statistics, transmission electron microscopy (TEM), and genome-resolved multi-omics, the work links pore-scale interactions to ecosystem-scale trends and advances colloid transport from idealized theory to field conditions. Electron microscopy revealed ultra-small cells attached to sediment, providing the first direct evidence of such microbial interactions at the eFRC site. A synthesis of colloid transport models (colloid filtration theory, DLVO, and pore-to-continuum-scale approaches) shows why dissolved-phase frameworks fail under nitrate-rich, metal-loaded conditions and motivates empirical tests in this setting. Field analyses demonstrate that hydrologic variability and steep geochemical gradients jointly structure colloid dynamics: shallow intervals exhibit diffuse orientations, whereas deeper zones show stable, aligned transport vectors (Watson-Williams: 26 and 28 vertical and 35 and 36 lateral contrasts significant, $p<0.05$). Bromide behaved conservatively in lab and field, confirming clear picture of advective pathways. Ion data revealed strong nitrate enrichment in upper wells and covariation among sulfate, chloride, and nitrate, consistent with redox stratification and mixed sources. The deep zones paired chemical extremes with intermittently connected flow. Colloid distributions were highly structured (pairwise Kolmogorov-Smirnov $D\approx0.27$-0.46 at L8, all $p<0.001$), with L8 well emerging as a chemically forced, high-mobility, uranium-maximum spot. L7 well was intermediate, and upper and medium wells formed a more stable cluster. Transmission Electron Microscopy images were grouped as abiotic, biotic, and mixed colloids (mineral fragments, EPS-rich aggregates, ultra-small cells, viruses, vesicles) and documented well-specific viral attachment states ($\chi^2=14.26$, df=3, $p=0.0026$). Microbial communities differed strongly among wells (PERMANOVA pseudo-$F=9.74$, $p=0.001$) and tracked geochemistry (Mantel $r=0.628$, $p=0.001$). At the same time, colloids contributed an independent, geochemistry-controlled signal (partial Mantel $r\approx0.143$, $p=0.005$). Genome-resolved results demonstrate abundant mobile genetic elements and *Caudoviricetes*-dominated viromes, recurrent functional groupings (transporter-CRISPR, energy-nucleotide), and a predictive metals panel (W, Zr, B, Cd, Mg, Mn, U). The dominance of *Rhodanobacter denitrificans* spp. under high nitrate, low pH conditions suggest niche-specific

adaptations that reduce microbial diversity. Overall, the findings support a unified framework: geochemical filtering sets community and metabolic structure; hydrologic coupling and colloids redistribute cells, viruses, plasmids, and metals; genomic plasticity consolidates successful adaptations. The work establishes the first metagenomic and viromic baseline for Subsurface Observatory (SSO) wells Saturated Zone 2 (SZ2) and offers a transferable framework for forecasting contaminant mobility and microbial resilience at nuclear legacy sites.

Table of Contents

LIST OF TABLES

LIST OF FIGURES

CHAPTER I Introduction

Background

Nitrate concentrations in drinking water in the United States affect the health of millions of people. Drinking water with a nitrate concentration above 10 mg and L can cause immediate health problems (89 FR 32532, U.S. EPA). One of the highest levels of groundwater contamination stems from nuclear legacy sites. During World War II, the U.S. government established the Manhattan Project, during which three national laboratories were each responsible for separate roles in building an atomic bomb. Oak Ridge National Laboratory was one of these three laboratories, focusing on uranium enrichment. As part of this effort, four unlined impoundments (S-3 ponds) covering approximately 1.44 hectares were constructed on the western side of the Y-12 National Security Complex near Oak Ridge in 1951, with a storage capacity of 9.5 million liters each. From 1951 to 1983, nuclear waste from the Y-12 heavy metals processing plant was deposited in these unlined S-3 ponds. This waste was acidic (pH < 2) and contained uranium and other metals dissolved in nitric acid. In June 1983, the S-3 ponds were neutralized and turned into a parking lot (Moon et al., 2020). Although the site was neutralized more than 40 years ago, the surrounding area still has the world's highest nitrate concentrations in groundwater. Additionally, since the groundwater at the S-3 ponds Area 3 is near the source of contamination, it contains exceptionally high levels of radionuclides, salts, organics, and metals (Cu, Al, Fe, Co, Cd). Other groundwater contaminants include nitrate (up to 11.6 g/L, 190 mM), uranium (140 mg/L), and metals such as nickel (9.4 mg/L), aluminum (560 mg/L), and manganese (170 mg/L) (Thorgersen et al., 2019).

The Oak Ridge Reservation is situated within the Appalachian region, encompassing the western Blue Ridge, Valley and Ridge, and Cumberland Plateau in East Tennessee, USA. The stratigraphic units in this region exhibit diverse lithologies, ranging from Cambrian and Ordovician sections to the younger Devonian and Mississippian units. Due to their compositional and textural properties, each central stratigraphic unit possesses unique mechanical characteristics that respond differently to the deformation events that have impacted these rocks over time. These deformations have resulted in fracture densities and spacings that influence fluid flow through them (Hatcher Jr et al., 1992). Contamination is spread through groundwater and pore water via colloids. Pore water transport describes the movement of water and dissolved substances through the tiny, interconnected spaces (pores) within porous media like soil, rock, and sediment. Hydrological transport is a broader, macro-scale concept that refers to the

movement of water and any associated material throughout the entire water cycle, encompassing surface, atmospheric, and subsurface flows (McCarter et al., 2020).

Colloids are particles with diameters ranging from 1 nm to 1 μm (Fetter et al., 2017) (**Figure 1**). While the terms "nanoparticles" and "colloids" are often used interchangeably, they emphasize different aspects of particle behavior. Nanoparticles are defined explicitly by their size (1-100 nm) (Joudeh and Linke, 2022). In this size range (characterized by exceptionally high surface area, enhanced reactivity, and, in some cases, a quantum-scale effect), their behavior is distinguished from that of larger particles (Hochella et al., 2012; Wiesner et al., 2006). In contrast, colloids are defined by their dispersion rate, which ranges in size from 1 nm to 1 μm, and remain suspended due to electrostatic or steric stabilization (McCarthy and Zachara, 1989; McCarthy and McKay, 2004). Thus, nanoparticles can be considered a subset of colloids. However, colloids can include mineral matter, humic substances, various microorganisms, and insoluble organic fluids (Fetter et al., 2017).

Radionuclides, heavy metals, and organic pollutants can sorb onto colloids suspended in water, acting as carriers for contaminants. The adsorption of several heavy metals and radionuclides onto colloid surfaces has been shown to pose a significant threat to subsurface environments (Buddemeier and Hunt, 1988; Zhang et al., 2024). Even the importance of colloidal transport has been recognized since the 1980s (de Jonge et al., 2004), the underestimation of colloidal movement and colloid-facilitated dissolved pollutants has been observed to impact groundwater quality (Wang, D. et al., 2020). Colloid transport accelerates the relocation of contaminants and can alter soil composition and flow paths. Field studies on the transport of colloids in the subsurface are relatively limited (Zhang et al., 2015). Oudega, for example, is one of the few researchers who conducted both field and laboratory experiments (Oudega et al., 2021). They found that scaling up colloid transport from laboratory columns is difficult due to the complex structures in porous media.

Saprolite (between 2- and 10-meters depth) is typically found in the Y-12 area, located above shale bedrock with limestone interbeds. There are fluctuations in the clay content with depth; the sand fraction (in weight) is approximately 50%, and the silt fraction is about 31%. The clay fraction accounts for 19% of the weight (McKay et al., 2000; Revil, André et al., 2013; Revil, Andre et al., 2013). Understanding the properties and composition of saprolite is important in areas like the Y-12 complex, particularly when considering contaminant transport,

as contaminants can migrate through fractures in the shale saprolite and micropores in the limestone saprolite (Van der Hoven et al., 2003).

For colloids (under Brownian motion), interactions are determined by the solution's interfacial characteristics. The role of ionic strength and composition in colloids is well-established (McCarthy and McKay, 2004). Flury and Aramrak noted that most subsurface colloids and the air-water interface carry a negative charge, causing electrostatic repulsion (Flury and Aramrak, 2017). They concluded that air-water interfaces can either mobilize or immobilize colloids, based on hydrodynamics and surface chemistry. Colloid-sized particles include mineral matter, humic substances, various microorganisms, and insoluble organic fluids (McCarthy and Zachara, 1989). Colloids may contain microbes (Frimmel et al., 2007), which may enter groundwater through the vadose zone or flow from lakes or rivers. Factors such as infiltration rate and dispersive mixing influence the transport of microorganisms through the vadose zone. The transport of colloid-sized microbes in saturated porous media was first examined in the 1970s, with a focus on enhancing packed-bed filters (Saiers and Ryan, 2006). Colloid transport dynamics between wells are affected by hydrodynamic, geochemical, and contaminant factors that influence particle mobility and distribution (McCarthy and Zachara, 1989). Colloid transport accelerates the relocation of contaminants and can alter soil composition and flow paths (de Jonge et al., 2004).

Study Area

ENIGMA (Ecosystems and Networks Integrated with Genes and Molecular Assemblies) is a multi-disciplinary, multi-institutional research initiative aimed at closing fundamental knowledge gaps in groundwater and sediment microbiomes in the shallow subsurface at the U.S. Department of Energy Field Research Center (eFRC) within the Y-12 National Security Complex in Oak Ridge, Tennessee, USA. Area 1 is located just south and down dip from the S-3 ponds. Area 2 lies several hundred feet southwest of the S-3 ponds. Lastly, Area 3 is situated west of the S-3 ponds, directly down strike. The ENIGMA team has most recently concentrated on Area 3.

The 100 well survey (Smith et al., 2015), cone penetrometer survey (Putt et al., 2022) (**Figure 2**), and 27 well survey (Walker, 2024) were focused on the biogeochemistry and hydrology of the shallow, unconsolidated residuum at the Department of Energy ENIGMA Field Research Center (eFRC). These studies revealed that groundwater in Area 3 flows southward

toward Bear Creek. The most recent campaign is called Subsurface Observatory Wells (SSO) (**Table 1**), which were installed in 2022 in a 3x3 rows in the Vadose Zone (VZ), the Variably Saturated Zone (VSZ), Saturated Zone 1 (SZ1), Saturated Zone 2 (SZ2), and the Saturated Zone 3 (SZ3). It is divided into three sections: Upper (U), Middle (M), and Lower (L) wells (**Figure 3-6,**). In our study, we focused specifically on Saturated Zone 2 (SZ2): the U2-SZ2, M5-SZ2, and L8-SZ2 wells. SSO well depths from which samples were collected are as follows: U2-SZ2: 21-25' depth, M5-SZ2: 21-25' depth, L8-SZ2: 21-25' depth. In this study, we also examined EFP01 groundwater wells (outside SSO wells). The EFP01 well was sampled at a depth of 15-25'. The EFP01 well coordinates are at 35°58'38.3"N 84°16'24.2"W, and SSO wells at 35°58'37.7"N 84°16'24.0" W.

Problems

Contamination from uranium and nitrate linked to nuclear weapons production and waste is a significant environmental risk. Nitrate concentrations in drinking water in the United States affect the health of millions of people. Radionuclides, heavy metals, and organic pollutants readily sorb onto colloids suspended in water, acting as carriers of contaminants. Adsorption of several heavy metals and radionuclides to the surface of colloids poses a significant threat to the subsurface environment. Underestimating the migration of colloids and colloid-facilitated dissolved pollutants increases the risk of degradation of the groundwater system quality.

Knowledge gaps

1) Colloids in extreme environments are poorly understood. Most contaminant transport studies emphasize dissolved solutes and overlook the role of colloids as carriers of metals and microbes in high-stress, acidic, nitrate-rich aquifers.

2) Linkages between microbial communities and geochemical gradients are unexplored. While geochemistry is known to shape microbial ecology, there is limited work on how depth-related gradients (nitrate, Mn, pH) drive distinct microbial communities in saturated zone wells at contaminated legacy sites.

3) The connection between colloids, metals, and microbes remains unclear. It is not established how colloids associate with both abiotic (U, Mn, Fe) and biotic (microbes) material, and whether these interactions explain stealth transport beyond dissolved-phase models

4) Integrated frameworks are lacking. There is no comprehensive approach that links microbial ecology, geochemical gradients, and colloidal-mediated transport into a unified explanation of contaminant mobility.

5) While current models describe colloid transport in idealized porous media, their applicability to extreme nitrate environments, where geochemical and biological colloid behaviors may differ, has not been tested, to the best of our knowledge.

Research objectives

Objective 1-Microbial Community Structure

Determine whether microbial community composition and functional potential differ among the 3 studied wells in Saturated Zone 2 and evaluate how differences are explained by geochemical gradients (nitrate, Mn, Na, pH, conductivity).

Objective 2-Colloidal Associations with contaminants and microbes

Quantify how colloidal abundance relates to metal concentrations (U, Mn, Fe), microbial cell counts, ion chemistry, and pH, to test whether colloids act as carriers for both biotic and abiotic material in the study area.

Objective 3-Integrated role of colloids in subsurface transport

Assess whether colloids serve as primary vectors of stealth transport in Area 3 by linking geochemistry, microbial community data and colloidal abundance into a unified framework for contaminant mobility

Two focuses:

Patescibacteria, also known as the Candidate Phylum Radiation (CPR), are distinguished by their ultra-small size, typically 100-300 nanometers in diameter. This makes them among the smallest bacteria known to exist. Ultra-small bacteria and archaea showed adaptations for attached or planktonic lifestyles (Gios, E.*et al.*, 2023).

Rhodanobacter denitrificans spp. has garnered global scientific interest due to its resistance to extreme conditions and its denitrification capabilities.

Hypotheses

Overarching dissertation hypothesis: Colloid mobility in contaminated subsurface systems depends on geochemical gradients and microbial interactions. Colloids serve as carriers for both abiotic (metal) and biotic (microbial) transport, thereby linking biological and chemical transport

in extreme groundwater environments. Thus, colloids are positioned as a mechanistic bridge between biology and chemistry.

H_1 hypothesis: Microbial communities in the three wells differ significantly in composition and function among the studied wells. These differences are linked to geochemical gradients.

H_2 hypothesis: Colloidal abundance is significantly correlated with metals, pH, ASV data, Ions and microbial cell counts. These associations are influenced by pH and ion chemistry, indicating that colloids serve as carriers for both biotic and abiotic materials.

Dissertation significance

Understanding how colloids influence the fate of contaminants in groundwater is very important for advancing scientific knowledge and improving site management at legacy waste facilities. Traditional dissolved-phase transport models often fail to account for colloid-facilitated mobility, which can allow heavy metals and microbial populations to persist and spread in the environment. By explicitly linking microbial community dynamics to geochemical gradients-such as nitrate levels, metals, and pH-and to colloidal abundance, this research provides a mechanistic explanation of how biology and chemistry interact to control subsurface mobility. Demonstrating that colloids serve as stealth carriers of both biotic and abiotic materials fills a key knowledge gap in environmental microbiology and contaminant hydrogeology.

Dissertation overview

This dissertation is organized into 5 chapters, each addressing different but interconnected aspects of contaminant transport, microbial ecology, and colloid dynamics in contaminated subsurface environments.

Chapter I: Introduction to the Overall Dissertation

Chapter II: Colloidal modeling and data review

This chapter reviews conceptual and mathematical models of colloid transport, including colloid filtration theory (CFT), Derjaguin-Landau-Verwey-Overbeek (DLVO) frameworks, and pore-continuum-scale approaches. The chapter demonstrates how colloid-contaminant interactions challenge traditional dissolved-phase models, particularly under the extreme geochemical conditions observed at DOE legacy sites. By synthesizing prior modeling efforts and finding critical knowledge gaps, this chapter provides the theoretical foundation for subsequent empirical research. This gap motivates Chapters III and IV, which explore colloid-facilitated movement of

contaminants and minerals, alongside biological colloids, under nitrate-rich conditions. This chapter also outlines the data needs for understanding subsurface colloids in the study area.

Chapter III Colloid Impact On the Transport of Contaminants, Minerals and Biological Materials At The S-3 Ponds Y-12 Site

This chapter presents experimental and field-based analyses of colloidal characterization and its impact on transport at the DOE ENIGMA Oak Ridge Field Research Center (eFRC). Colloidal abundance (number of particles), compositions, and associations with metal were statistically quantified across all SSO wells and zones. We used colloidal borescope data, metals data, and ion chromatography data. Results are compared with prior studies at the eFRC and with published research from other contaminated field sites. This comparison allows evaluation of whether colloid-mediated transport at eFRC follows generalizable trends or reflects site-specific conditions. This chapter advances understanding of colloids as a carrier of contaminants in real-world aquifer systems.

Chapter IV Microbial Characterization at the eFRC Site

This chapter investigates microbial community composition and potential function across three studied wells in saturated zone 2, focusing on linkages with geochemical gradients (nitrate, manganese, pH, sodium, and conductivity). Particular interest includes *Rhodanobacter denitrificans*, which thrives under nitrate-and metal-rich conditions, and Patescibacteria, also known as the Candidate Phylum Radiation (CPR), whose size places them within the colloidal fraction. We used 16S rRNA and metagenomic data. Results are contextualized against previous microbiological surveys at eFRC and compared to findings from other nitrate and uranium-contaminated aquifers. This chapter demonstrates how geochemistry structures microbial communities and explores potential linkages between microbes, colloids, and contaminants.

Chapter V Conclusion

The final chapter synthesizes insights from three core research chapters. It emphasizes how modeling perspectives (Chapter II), colloid and transport trends (Chapter III), and microbial community ecology (Chapter IV) converge to demonstrate that colloids act as a mechanistic bridge between geochemical and biological processes. The conclusion reflects the dissertation's contribution to the field: an integrated framework that positions colloids not as secondary features, but as primary vectors of contaminant transport in extreme groundwater environments.

It also outlines implications for predictive modeling, risk assessment, and site management at DOE sites and other contaminated aquifers.

Appendix 1: Figures

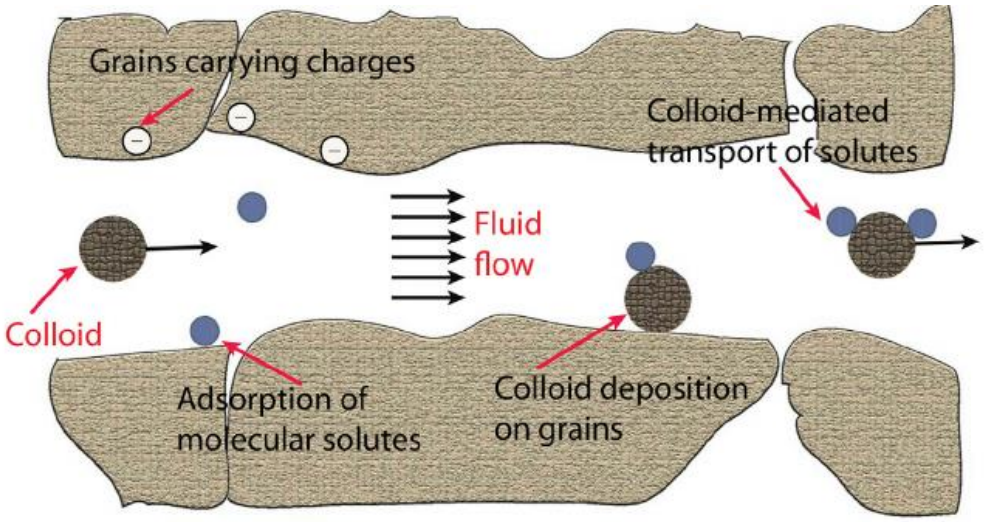

(Sharma et al, 2012)

Figure 1. Colloidal behavior in subsurface.

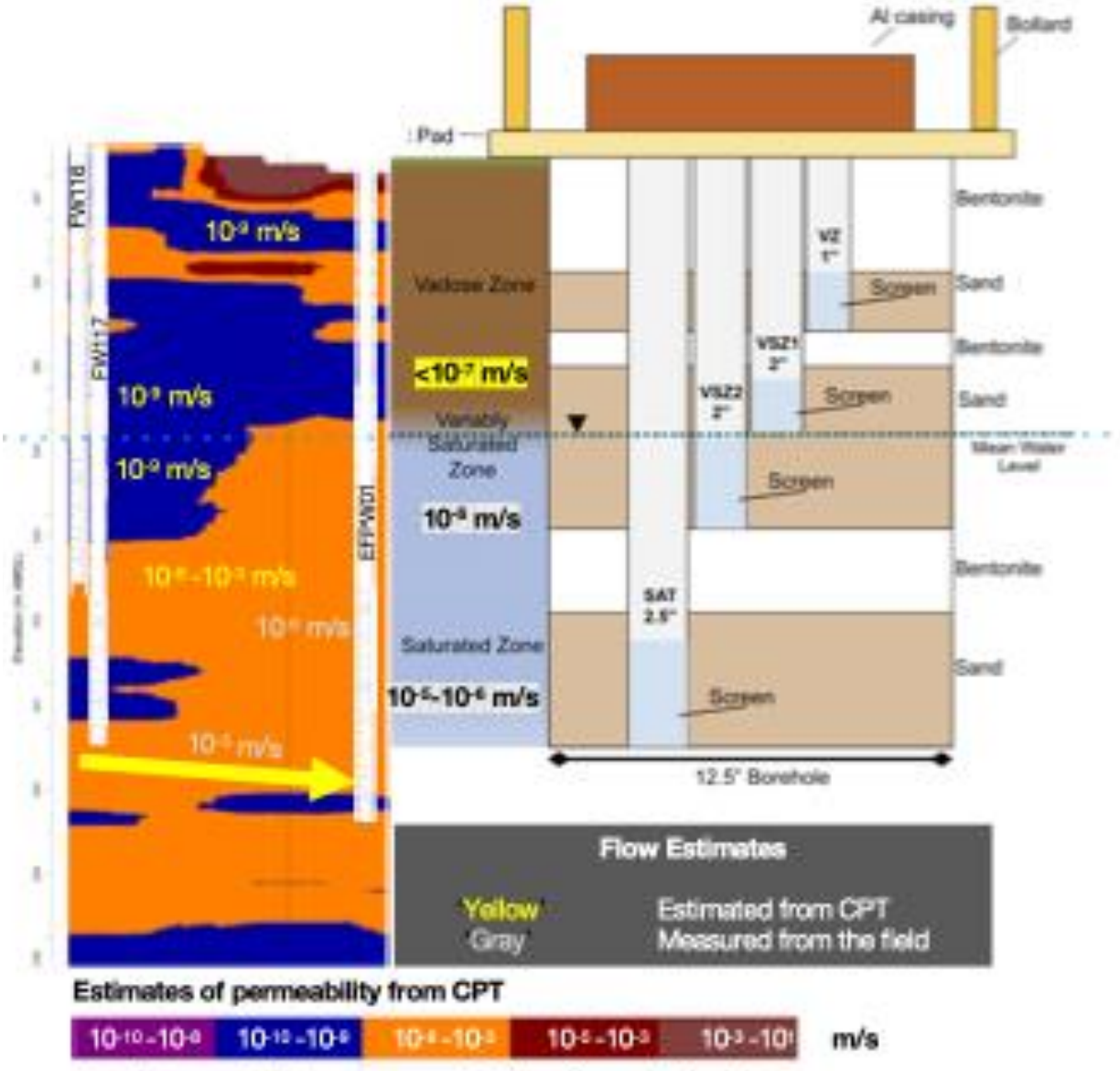

Figure 2. A quick dissection of localized flow in Area 3. Estimates of flow from CPT and field measurements as they relate to the SSO well placement.

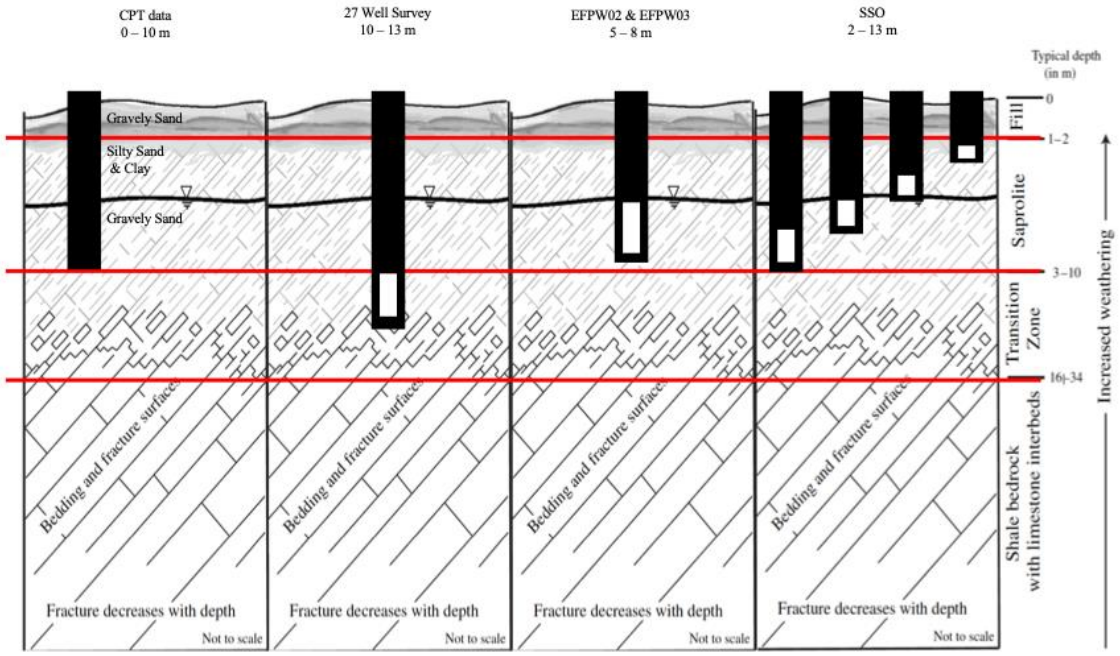

A

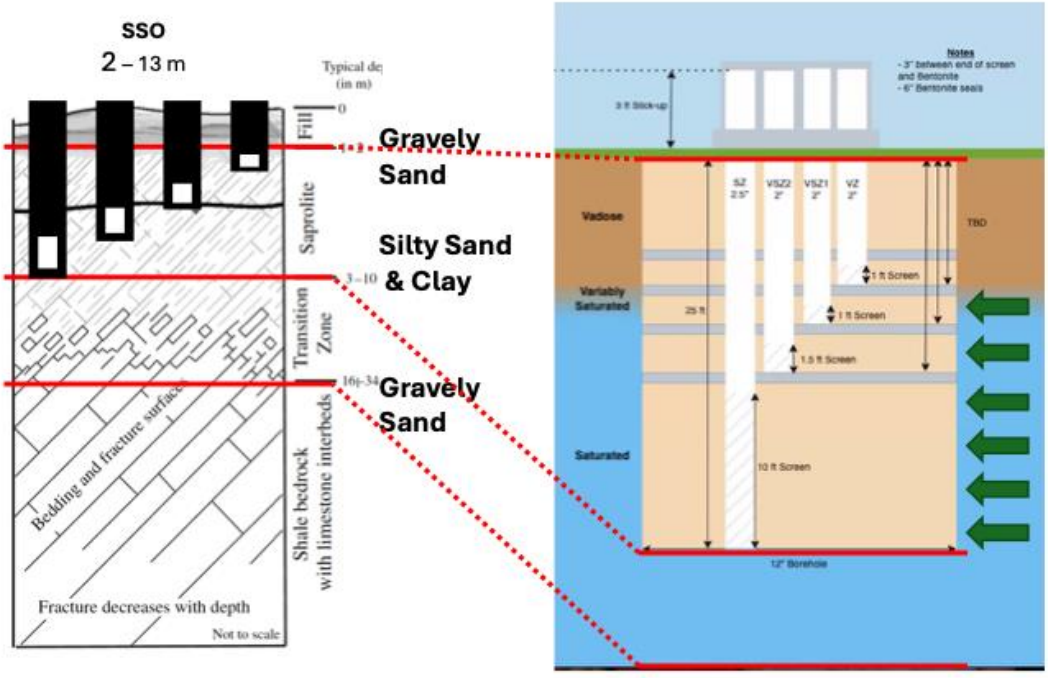

B C

(Revil et al., 2013).

Figure 3. A. Previous Surveys at Enigma FRC (eFRC). B. Subsurface Observatory (SSO) wells. C. Different zones of SSO wells.

A

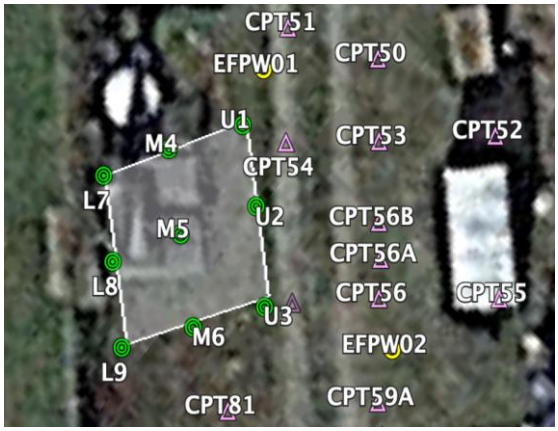

B

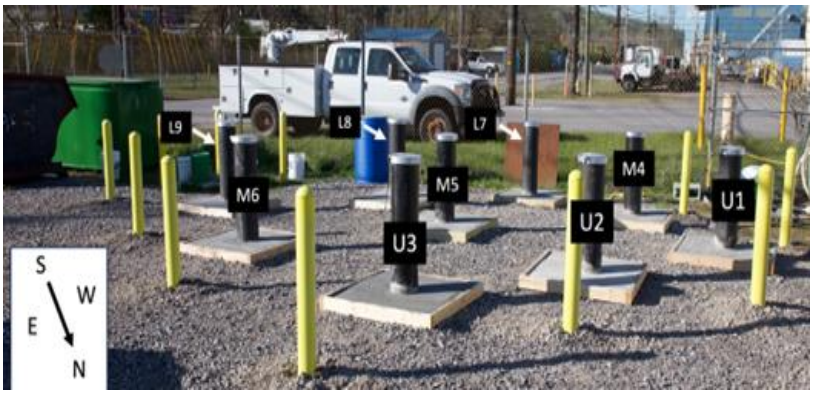

C

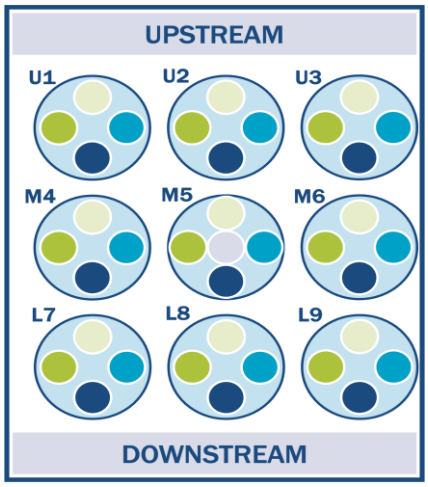

D

Figure 4. A Map of the Department of Energy ENIGMA Field Research Center (eFRC) S-3 ponds USA. B. The view of the SSO wells zoomed in. C. The surface view of SSO wells. D. A scheme of SSO wells order.

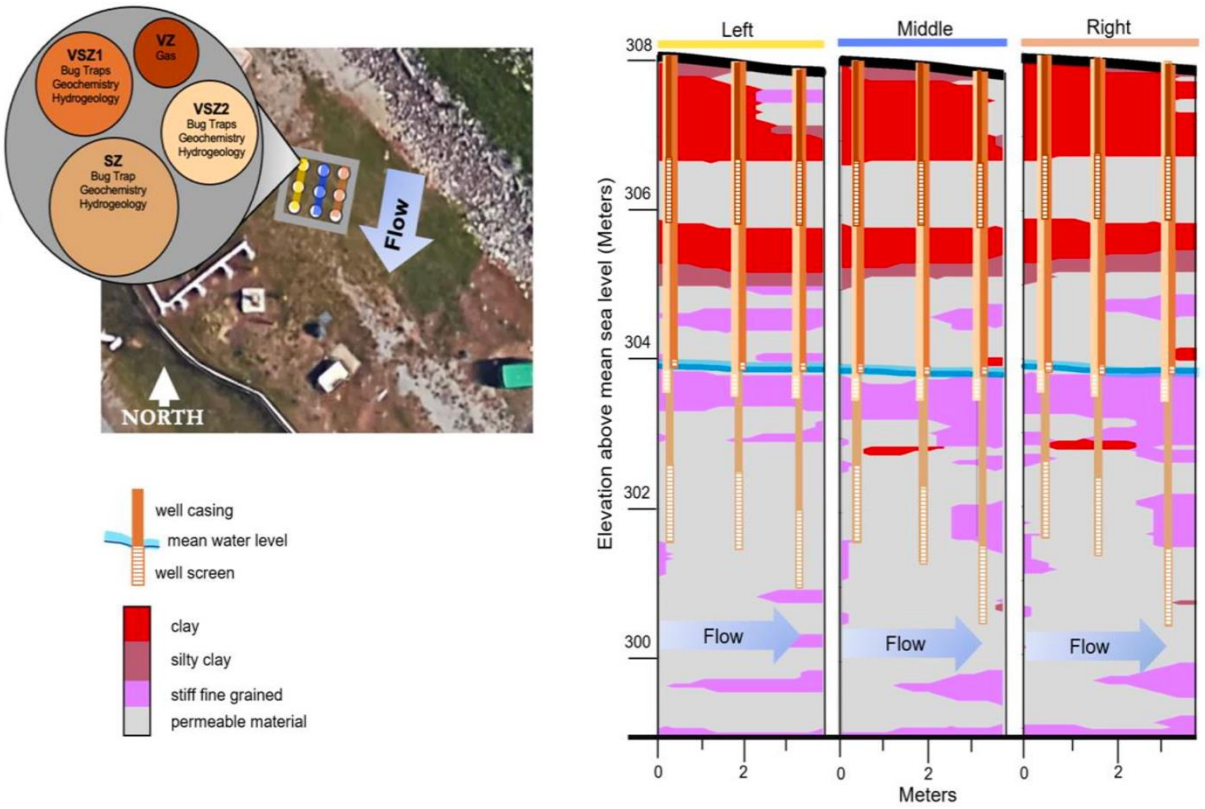

(Putt, 2022)

A B

Figure 5. A. Configuration of SSO wells built to investigate material transport from groundwater base flow and subsurface-level infiltration. B. Cone Penetrometer data of SSO wells.

Appendix 1: Tables

Table 1. Subsurface Observatory Wells location.

Name	Latitude	Longitude	Easting	Northing
U1	35.977253°N	84.273397°W	745841.79	3984863.42
U2	35.977241°N	84.273378°W	745843.54	3984862.13
U3	35.977225°N	84.273356°W	745845.57	3984860.41
M4	35.977236°N	84.273411°W	745840.58	3984861.49
M5	35.977222°N	84.273392°W	745842.33	3984859.99
M6	35.977208°N	84.273369°W	745844.45	3984858.49
L7	35.977219°N	84.273422°W	745839.64	3984859.58
L8	35.977206°N	84.273403°W	745841.39	3984858.19
L9	35.977192°N	84.273383°W	745843.24	3984856.68

CHAPTER II Colloid Modeling And Data Review

Introduction

Colloids have been recognized as key players in transporting substances through groundwater environments. Compared to dissolved solutes, colloids can carry metals, microbes, and viruses through the soil. Also, colloids influence how long contaminants persist in ways that traditional hydrological models can't fully capture (Flury and Aramrak, 2017; McCarthy and Zachara, 1989; Ryan and Elimelech, 1996). Colloidal behavior is highly responsive to local conditions (pore size, water chemistry, surface roughness, and biological activity). These conditions can influence how colloids act: attach, detach, aggregate, or remain suspended. As a result, predicting how colloids move through the soil has become a challenge for hydrogeology, environmental engineering, and risk assessment at contaminated sites.

To address this complexity, researchers have developed a wide range of modeling approaches over the past 30 years. Colloidal filtration theory (CFT) was one of the earliest frameworks, and it assumed uniform flow fields (Nelson and Ginn, 2005; Yao et al., 1971). While CFT provided a foundation, it made simplifying assumptions, such as pore-scale heterogeneity at field conditions (Bradford et al., 2006). This chapter reviews the development and application of colloid transport models, with particular attention to conceptual assumptions, calculations and critical parameter variables. This chapter also considers how these models have been extended to include colloid-facilitated transport of radionuclides, microbes and viruses. Finally, this chapter outlines the types of data required to understand subsurface colloids characteristics. Collectively, these elements provide a synthesis of the state of the field.

Literature Review

Various models for colloid transport exist, including both conceptual and mathematical approaches. Traditional models primarily focus on advection, dispersion, and filtration processes (Molnar et al., 2019). This literature review compared models for colloid and colloid-facilitated contaminant transport. We examined the model type, colloidal critical parameter variables, zone, and the most significant potential difference in the results.

Continuum-based models

Continuum-based models are partial differential equations that rely on the continuity principle across the system's spatial and temporal domains, whether the system is continuous or discretized. In contrast, pore-scale models represent solids and fluids with distinct configurations. While continuous models are effective for describing nanoparticle transport, they

are often seen as more descriptive than predictive. Additionally, these models can be used even when the mathematical representations do not fully align with the actual physical mechanisms of the nanoparticles (Babakhani et al., 2017).

Colloid filtration theory models

Colloid filtration theory is often used to predict colloid transport through porous media (Cullen et al., 2010; Nelson and Ginn, 2005). However, filtration theory has many limitations. Since it was developed based on a study of a single spherical grain collector, it does not account for pore structure and surface roughness on straining deposition (Bradford et al., 2006).

Given the complex nature of colloid systems, numerous parameters can be considered critical variables. Several authors identified the concentration of suspended colloids as a critical parameter. Several authors identified the concentration of suspended colloids as a crucial parameter. The following authors (Abdel-Salam and Chrysikopoulos, 1995; Bradford et al., 2009; Bradford et al., 2011; Contardi et al., 2001; Kheirabadi et al., 2017; Saiers and Hornberger, 1996; Sen et al., 2004; Sun et al., 2001b) classified colloidal deposition as a critical parameter variable (Chrysikopoulos and Abdel-Salam, 1997; Sun et al., 2001a). Colloid attachment and detachment were ranked as the third most frequently cited critical parameter variable (Babakhani, 2019; Bradford and Torkzaban, 2008; Flury and Qiu, 2008; Katzourakis and Chrysikopoulos, 2014; Oudega et al., 2021; Šimůnek et al., 2006). A few authors considered collision efficiency as a crucial parameter for their models (Cullen et al., 2010; Morales et al., 2007; Oudega et al., 2021).

Some models identified several parameters that greatly influenced the results. Sorption was among the most significant potential differences in the outcomes (Abdel-Salam and Chrysikopoulos, 1995; Contardi et al., 2001; Corapcioglu and Jiang, 1993; Šimůnek et al., 2006). Additionally, the rate constants of colloid capture were identified as the most critical factor influencing potential differences in results (Corapcioglu and Jiang, 1993). A few authors considered colloidal size to be the most significant factor affecting results (Babakhani, 2019; Bradford et al., 2011; Chrysikopoulos and Abdel-Salam, 1997). Some studies considered maximum retention concentration and reversible and irreversible retention (Bedrikovetsky et al., 2011; Leij and Bradford, 2013). Changes in linear isotherm coefficients and equilibrium distribution coefficients were also examined (Kheirabadi et al., 2017). Transverse dispersivity, overall hydraulic gradient, and velocities, as well as collision efficiency factors, blocking factors,

and heterogeneity, were also analyzed (Cullen et al., 2010). Some studies have concluded that soil structure and preferential flow are critical factors influencing colloid transport during transient flow conditions (Wang, C. et al., 2020).

Kaolinite particles on the Cesium-137 transport model

An interesting study created a model for kaolinite-facilitated transport of cesium-137 in a water-saturated porous medium (Saiers and Hornberger, 1996). They investigated how kaolinite particles affect the movement of cesium-137 in sand columns. They discovered that an irreversible, first-order kinetic process explained the deposition of kaolinite onto sand. Additionally, they observed that linear equations described the retention of Cesium-137 by clay particles for a two-site sorption model. A study introduced a model that features reversible and irreversible retention of colloids (Leij and Bradford, 2013). They found that larger colloids (3.2 μm) enhance dispersity and retention, while finer sand increases irreversible retention.

Dissipative particle dynamics model

Another interesting study (Pan and Tartakovsky, 2013) presented a dissipative particle dynamics model. They found that the contact efficiency of colloids increases with decreasing flow rate and increasing concentration. Other researchers (Katzourakis and Chrysikopoulos, 2014) developed a colloid and virus cotransport model in porous media. They studied individual viruses, colloids, and viruses attached to colloids. They solved governing coupled differential equations using the finite difference method. Other authors (Chrysikopoulos and Abdel-Salam, 1997; Cullen et al., 2010; Kheirabadi et al., 2017) used the same finite difference method for their models.

Vadose zone models

The presence of an air-water interface in the vadose zone influences the mobility of the colloids (Deb and Chakma, 2023; Flury and Qiu, 2008). Several researchers have studied models in the vadose zone (Bradford et al., 2004; Bradford and Torkzaban, 2008; de Jonge et al., 2004; Flury and Qiu, 2008; S˘imunek et al., 2006; Şengör and Ünlü, 2023) and noted that straining can sometimes be necessary for colloid retention. In particular, one study (Şengör and Ünlü, 2023) found that colloidal transport is sensitive to the electrostatic double layer under low-flow-velocity advective transport conditions. A model was built based on the physics of Escherichia coli cytoplasm (Maheshwari et al., 2023). In that model, the Brownian motion and diffusion raised due to physical interactions between individual molecules of finite size, density, and

physiological abundance. A new formulation of particle transport in 3D anisotropic porous media was developed in a model (Russell and Bedrikovetsky, 2023). They included the sink-source term in Boltzmann's equation, enabling exact upscaling.

Radionuclide transport models

Several researchers developed models for colloid-facilitated radionuclide transport. For instance, a study (Nair and Thampi, 2010) presented a colloid transport model in sets of parallel fractures with fracture skin. They found that the presence of skin greatly influenced colloid transport through a fractured medium. Additionally, they discovered that linear kinetic sorption isotherms govern the irreversible deposition onto fracture skin surfaces and rock formation. Other authors (Natarajan and Kumar, 2010) also studied radionucleotide and colloid co-transport in coupled fracture-skin matrix systems. They investigated that when colloid velocity increases, the diffusion of colloids into the fracture skin decreases.

Other models

Modeling reactive chemical transport of contaminants involving nonlinear equilibrium or kinetic reactions has received less attention than linear reactions (Bekhit and Hassan, 2007). That is why they investigated nonlinear reactions. They noticed that strongly sorbing contaminants may travel much farther and faster than expected by traditional solute-transport models.
One author (Sun et al., 2001b) tried to identify key parameters for a two-dimensional model of colloid transport in geochemically heterogeneous porous media. Based on sensitivity analysis, they found six parameters: hydraulic conductivity, longitudinal dispersivity, geochemical heterogeneity (favorable (fast) deposition rate coefficient), colloid release rate coefficient, unfavorable (slow) deposition rate coefficient, and injection duration (**Table 2.1)**.

Data needs for understanding subsurface colloids

To understand subsurface colloids, several data sources were needed:
1) Colloidal borescope measurements of all wells in 2023 (04/11/23,04/18/2023, 04/25/23) and in 2024 wells U3-SZ1, L9-SZ1, L9-SZ2, M4-SZ2, M4-SZ1, M5-SZ1, M5-SZ2, M5-SZ3. For 2023, 20 different depths were measured with a colloidal borescope: (14, 15, 18, 19, 20, 21, 22, 23, 24, 25, 26, 27, 28, 30, 31, 32, 33, 34, 35, 36 feet. 14 feet: ['L7' 'L8' 'L9' 'M4' 'M5' 'M6' 'U1' 'U3' wells]; 15 feet: ['U2' 'U3' wells], 18 feet: ['L8' 'L9' 'M4' 'M5' 'U1' wells]; 19 feet: ['L9' 'M4' 'M5' 'M6' 'U1' 'U2' 'U3' wells]; 20 feet: ['L7' 'L8' 'L9' 'M4' 'M5' 'M6' 'U1' 'U2' 'U3' wells]; 21 feet: ['M4' 'M5' 'M6' 'U3' wells]; 22 feet: ['L8' well]; 23 feet: ['L8' 'M4' wells]; 24 feet: ['L7' 'L9' 'M4'

'M5' 'U1' wells]; 25 feet: ['L7' 'L8' 'L9' 'M4' 'M5' 'M6' 'U1' 'U2' 'U3' wells]; 26 feet: ['L7' 'L9' 'M4' 'M5' 'M6' 'U1' 'U2' 'U3' wells]; 27 feet: ['L7' 'L9' 'M5' 'M6' 'U3' wells]; 28 feet: ['M5' well]; 30 feet: ['M5' well]; 31 feet: ['M5' well]; 32 feet: ['M5' well]; 33 feet: ['M5' well]; 34 feet: ['M5' well]; 35 feet: ['M5' well]; 36 feet: ['M5' well]. We used data with colloid counts at various depths, as well as data on flow directions and speeds.

2) We also needed native sediment from the EFP01 well to understand kinetic sorption using an ion chromatograph.

3) We needed metal data, pH, and ion chromatography data for all SSO wells collected in September 2024 (**Figure 2.1, Figure 2.2**).

4) We needed 16S and metagenomic data collected in February 2024, as well as transmission electron microscopy for three wells in Saturated Zone 2.

Conclusion

Predicting colloidal transport in porous media is essential to many natural and engineered processes. This includes wastewater treatment, natural filtration of pathogens in the subsurface, and transport of contamination by colloids. While current models describe colloid transport in idealized porous media, their applicability to extreme nitrate environments, where geochemical and biological colloid behaviors may differ, has not been tested, to the best of our knowledge. This gap motivates Chapters III and IV, which explore colloid-facilitated movement of contaminants and minerals, alongside biological colloids, under nitrate-rich conditions. Our research interest was in heterogeneous extreme nitrate system.

Appendix 2: Figures

Figure 2.1. Faceted bar plots showing variability in key hydrological and microbial variables across wells and zones

Each panel represents a different variable: pH, cell abundance (Cells per mL), mean speed, mean particle count, and calculated flux index. These variables are for each sound zone sample (x-axis). Bars are colored by well identity using a consistent color palette across panels. This layout enables direct comparison of the magnitude and distribution of multiple variables across the SSO sampling network, showing zones with distinct physicochemical or transport characteristics.

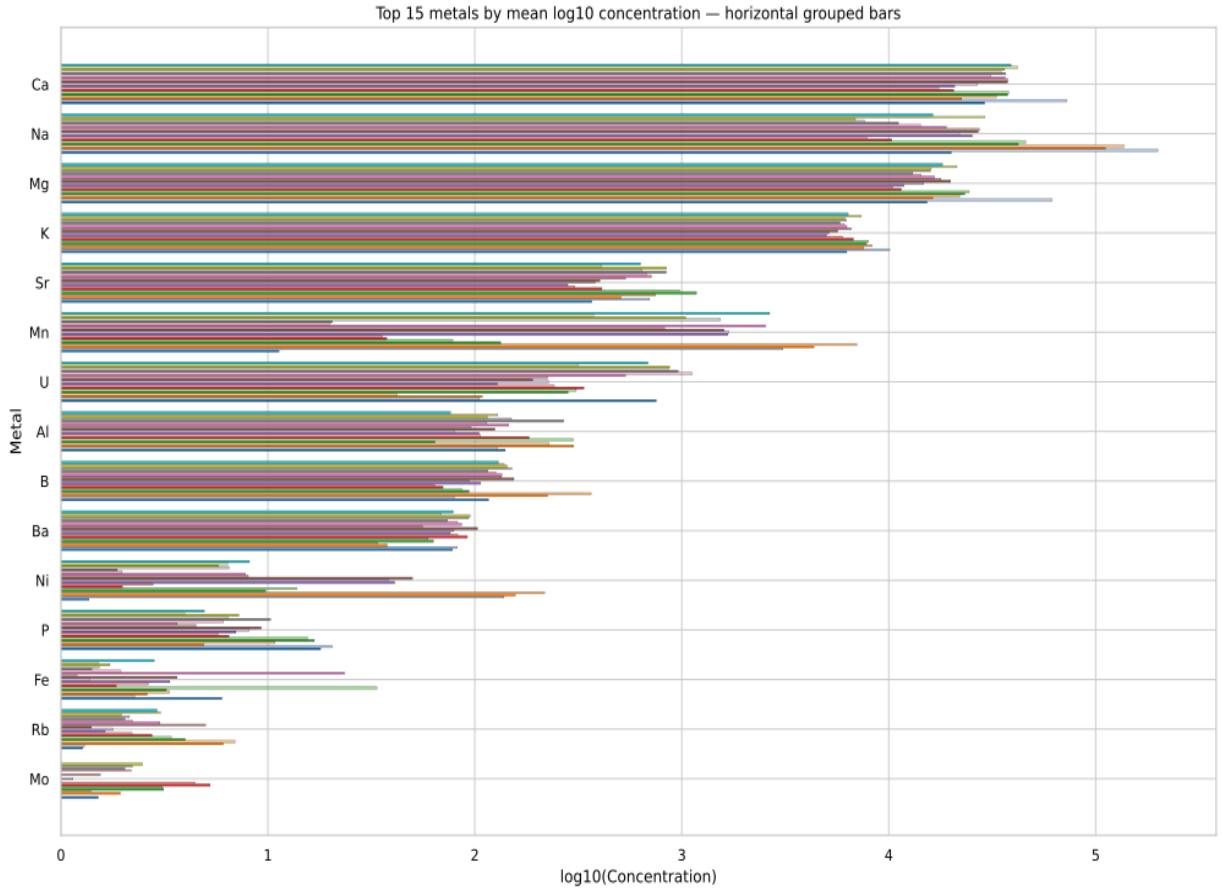

A

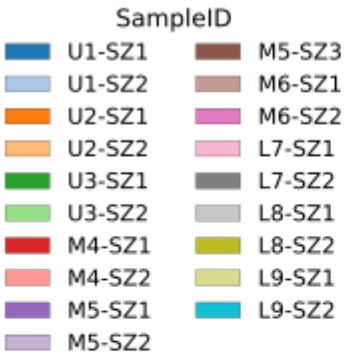

B

Figure 2.2. Top 15 metals by mean $\log_{10}$ concentration across all wells

A. Horizontal grouped bar plot showing the distribution of $\log_{10}$-transformed metal concentrations for each Sample ID, ordered by average concentration from lowest (bottom) to highest (top). Major cations (Ca, Na, Mg, K) dominate the concentration profiles, while trace metals (Ni, Fe, Mo) occur at lower levels. B. Bars are grouped by sample and color-coded by well ID.

Appendix 2: Tables

Table 2.1. Existing models review.

Source (Year)	Model type	Zone
Abdel-Salam and Chrysikopoulos (1995)	One-dimensional contaminant transport	Saturated rock fractures
Saiers and Hornberger (1996)	Model for Kaolinite-Facilitated transport of Caesium-137	Water-saturated porous medium
Chrysikopoulos and Abdel-Salam (1997)	Finite difference method	Saturated fracture with a spatially variable aperture
Sun et al (2001)	Two-dimensional model	Heterogeneous subsurface porous media
Contardi et al (2001)	Enhanced radionuclide transport by colloids model (mechanistic sorption model)	Saturated porous media
Sen et al (2004)	One-dimensional three-phase model based on colloidal induced release, migration and finally capture of these colloidal fines at pore constrictions	Saturated
Simunek et al (2006)	One-dimensional numerical model based on the HYDRUS-1D software	Variably saturated porous media (vadose zone)
Morales et al (2007)	Colloid transport through porous media	Saturated
Bradford and Torkzaban (2008)	Pore-scale model	Vadose zone
Flury and Qiu (2008)	A general model for colloid-facilitated contaminant transport in the vadose zone	Vadose zone

Table 2.1 Continued

Bradford et al (2009)	Clean bed transport micromodel	Saturated porous media
Cullen et al (2010)	Two-dimensional finite element model (nanoparticles)	Saturated porous media
Bradford et al (2011)	Dual permeability model	Saturated porous media
Bedrikovetsky et al (2011)	Modified particle detachment model	Saturated porous media
Pan and Tartakovky (2013)	Dissipative particle dynamics	Saturated porous media
Leij and Bradford (2013)	Reversible and irreversible retention of colloids and first-order exchange between the aqueous phases of two regions	Dual-permeability media
Katzourakis and Chrysikopoulos (2014)	Finite difference method, virus-colloid cotransport model	Saturated porous media
Kheirabadi et al (2017)	Fully implicit finite difference method	Saturated homogeneous porous medium
Babakhani (2019)	3D transport model MT3D-USGS	Saturated porous media
Oudega et al (2021)	3D colloidal transport model using HYDRUS software	Saturated porous media

CHAPTER III Colloid Impact On the Transport of Contaminants, Minerals and Biological Materials At the S-3 Ponds Y-12 Site

Authors: Diliya U. Murtazina[1,2], Andrew D. Putt[4], Michael P. Thorgersen[6], Farris L. Poole[6], Peter J. Walian[5], Lucy Zeng[5], Romy Chakraborty[5], Michael W. Adams[5], Dominique C. Joyner[3], Daniel E. Williams[3], Kathleen F. Walker[3], Terry C. Hazen[1,2,3*]

Target Journal for Submission*: *Frontiers in Environmental Science

[1]Bredesen Center-Energy Science and Engineering, University of Tennessee, Knoxville, TN, USA

[2]Biosciences Division, Oak Ridge National Laboratory, Oak Ridge, TN, USA

[3]Department of Microbiology, University of Tennessee, Knoxville, TN, USA

[4]Department of Earth and Planetary Sciences, University of Tennessee, Knoxville, TN, USA

[5]Lawrence Berkeley National Laboratory, Berkeley, CA, USA

[6]University of Georgia, Athens, GA, USA

Author Contributions: DM: Data curation, Formal analysis, Investigation, Methodology, Software, Validation, Visualization, Writing - review & editing, Writing - original draft; AP: Data curation, Investigation, Methodology, Software, Writing - review & editing; MT: Data curation, Investigation, Methodology, Software, Resources, Writing - review & editing;: FP: Data curation, Investigation, Methodology, Software, Resources, Writing - review & editing; PW: Data curation, Formal analysis, Investigation, Methodology, Software, Validation, Visualization, Writing - review & editing; RC: Data curation, Investigation, Methodology, Software, Resources; MA: Data curation, Investigation, Methodology, Software, Resources, Writing - review & editing; DJ: Data curation, Software, Validation, Writing - review & editing, Funding acquisition, Project administration, Supervision; DW: Data curation, Investigation, Methodology, Software; KW: Data curation, Investigation, Methodology, Software; TH: Investigation, Methodology, Resources, Validation, Writing - review & editing, Conceptualization, Formal analysis, Funding acquisition, Project administration, Supervision, Visualization.

Abstract

Area 3 at Y-12 National Security Area is known for having the highest groundwater nitrate contamination in the world. Colloids can accelerate subsurface transport of metals and biological material, yet their roles in nitrate- and metal-impacted fractured saprolite remain poorly constrained. We quantified colloid-transport relationships at the Department of Energy ENIGMA Field Research Center (eFRC) located at the Y-12 National Security Complex in Oak Ridge, Tennessee. We focused on SZ2 wells U2-SZ2, M5-SZ2, and L8-SZ2, with supplemental tests at EFP01. We combined colloidal borescope measurements (speed, direction, counts of particles) with circular statistics and 2,000-permutation tests, distributional comparisons via pairwise Kolmogorov-Smirnov (KS) tests, batch bromide sorption experiments, ion chromatography, and transmission electron microscopy (TEM). Directional analyses resolved strong vertical stratification and lateral heterogeneity: within-well zone contrasts were significant in 26 and 28 unweighted comparisons ($p<0.05$) and 21 and 28 when flux-weighted (velocity x count). The SZ2 lateral contrasts were significant for 35 and 36 pairs, indicating divergent transport orientations across the field site. KS tests showed structured distributional differences in colloid counts, with L8 (the uranium maximum) emerging as the most distinctive endmember (KS $D\approx0.27$-0.46 vs most wells; all $p<0.001$). Batch experiments showed no appreciable bromide sorption over 200 h (plateau ~120-140 mg L^{-1}). TEM provided rare in situ visualization of virus-colloid interactions (n=18 viruses total): the proportions of attached vs. free viruses differed among wells ($\chi^2=14.26$, df=3, $p=0.0026$). These results are preliminary, image-based evidence given n=18. L7-SZ2 showed higher attachment than L8-SZ2 (Fisher's exact $p=0.0128$) and M5-SZ2 ($p=0.0088$). Overall, hydrologic, chemical, and microscopic lines of evidence support our hypotheses that (H1) geochemical gradients structure colloid mobility and (H2) colloids associate with metals, ions, pH, and cells, acting as carriers that mechanistically link contaminant geochemistry and microbiology in SSO wells at Y-12.

Introduction

The 100 well survey (Smith et al., 2015), cone penetrometer survey (Putt et al., 2022), and 27 well survey (Walker, 2024) were focused on the biogeochemistry and hydrology of the shallow, unconsolidated residuum at the Department of Energy ENIGMA Field Research Center (eFRC). These studies revealed that groundwater in Area 3 flows southward toward Bear Creek. The most recent campaign is called Subsurface Observatory Wells, which were installed in 2022

in a 3x3 rows in the Vadose Zone (VZ), the Variably Saturated Zone (VSZ), Saturated Zone 1 (SZ1), Saturated Zone 2 (SZ2), and the Saturated Zone 3 (SZ3). It is divided into three sections: Upper (U), Middle (M), and Lower (L) wells. In our study, we focused specifically on Saturated Zone 2 (SZ2): the U2-SZ2, M5-SZ2, and L8-SZ2 wells. SSO well depths from which samples were collected are as follows: U2-SZ2: 21-25' depth, M5-SZ2: 21-25' depth, L8-SZ2: 21-25' depth. In this study, we also looked at EFP01 groundwater wells (outside of SSO wells). The EFP01 well was sampled at a depth of 15-25'. The EFP01 well coordinates are at 35°58'38.3"N 84°16'24.2"W, and the SSO wells are at 35°58'37.7"N 84°16'24.0" W.

The hydrology of the SSO aquifer system is highly heterogeneous, with hydraulic conductivity (K) values spanning more than two orders of magnitude depending on depth and zone. High-resolution Cone Penetration Testing (CPT) revealed strong stratification in the subsurface at Area 3 (Putt, 2022). Across 82 soundings with 0.02 m vertical resolution, Soil Behavior Types (SBTs) were mapped to permeability classes, delineating laterally persistent but vertically heterogeneous units. Sandy and gravelly materials dominate the shallow surface, perched silt-clay lenses extend from roughly 0.3 m to 6 m (spanning the water table), and coarse sandy layers resume below this interval. This layering is consistent across the 150 x 30 m site and reflects typical sedimentary anisotropy: horizontal connectivity is high within sand layers. By comparison, vertical flow is restricted by intervening fine-grained lenses. These silt-clay lenses act as perched zones that modulate infiltration and restrict vertical advective transport. Hydraulic gradients measured in the field indicate that under ambient conditions, groundwater flows are aligned with the regional gradient, primarily moving horizontally through the permeable sandy units beneath the perched lenses. Stratification results in distinct hydrologic zones: shallow perched intervals with limited connectivity, a variably saturated middle section influenced by infiltration events, and deeper saturated zones with well-aligned flow paths. Rainfall infiltration periodically perturbs this structure by raising the water table and promoting temporary convergence and divergence of flow paths around the clay-silt layers. Overall, transport in this system is governed by horizontal flow through high-permeability sands and retardation or storage within fine-grained units, establishing the physical background against which colloidal mobilization and retention occur (Im et al., 2023).

We tested two hypotheses in this chapter. H0 (Null hypothesis): Colloidal abundance is not significantly correlated with metals, microbes, or geochemical variables. H1 (Alternative

hypothesis): Colloidal abundance is significantly associated with metals and microbial cell counts. These associations are influenced by pH and ion chemistry, indicating that colloids serve as carriers for both biotic and abiotic materials.

The primary objectives of this study were to quantify the relationships among colloidal abundance, metal concentrations, microbial cell counts, ion chemistry, and pH, and to test whether colloids act as carriers for both biotic and abiotic material in the study area. The second objective was to assess whether colloids serve as primary vectors of stealth transport in Area 3 by linking geochemistry, microbial community data, and colloidal abundance into a unified framework for contaminant mobility. The investigation also focused on identifying microbial cells, viruses, and extracellular substances attached to colloids using transmission electron microscopy (TEM), providing the first evidence of ultra-small cells attached to colloids at the Y-12 site. Lastly, the research planned to evaluate tracer mobility and adsorption behavior through bromide tracer experiments to determine groundwater connectivity between wells and confirm bromide's role as a conservative tracer (non-sorbing) in the eFRC Y-12 subsurface environment.

Materials and Methods

Given ENIGMA's efforts at both long-distance and localized scales, two phases for tracer studies were proposed. The first phase included single-well push-pull and push-drift tests to analyze local characteristics. These tests involved injecting a tracer into one well and tracking its movement. Although similar in impact, the tests differed depending on whether the tracer was recovered or remained within the aquifer. In a push-pull test, tracer is injected into the aquifer and then pulled back, with recovery being optional. Conversely, a push-drift test uses the tracer's drifting tail after injection, providing similar data without recovery. These techniques help measure groundwater velocity, effective porosity, and dispersivity in a small area. Drift tests, which analyze tracer recovery or detection in nearby wells, are beneficial for understanding transport in neighboring wells. The second phase of the tracer test involved performing a natural-gradient injection to establish flow paths over a greater distance. Besides parameters from the local well, recovery mass and rate can help identify flow paths, connectivity, longitudinal dispersion, and the effects of heterogeneous materials and transport rates across a broader area of the aquifer. These tests require larger volumes of injectate and can remain measurable for weeks or even months after injection. Non-reactive tracers have been selected because they provide the most accurate estimates of physical hydrologic flow conditions. Bromide is a non-reactive ion

that dissociates in water, allowing for the monitoring of mass transport over distance and time. Bromide can be detected in the field by changes in specific conductivity. With TempHion continuous logging bromide probes (Seametrics, Kent, WA), it can measure bromide concentrations ranging from 0.1 to 100 ppm. The reliable detection limits for laboratory chromatography quantification of bromide range from 0.01 to 200 ppm (1 ppm was our target). To our knowledge, the measurement and reliability of this tracer are largely unaffected by pH, turbidity, or salinity; however, laboratory tests have been suggested to examine this directly. To test the applicability of this tracer in the field, we proposed conducting laboratory tests before injection and assessing tracer recovery to determine its conservative behavior. Enigma Flow Path well (EFP01) (outside of SSO wells) from the Y-12 site was used as a study well for this experiment. It was chosen for several reasons to compare to SSO wells: it has a similar depth, is only 10 feet away, was drilled by the same company, and was created one year before SSO wells were installed.

Bromide Sorption Experiments

Laboratory experiments help assess the stability and baseline sorption and desorption of the bromide tracer in Area 3 sediment. Bromide can exchange with anions in aquifer materials, particularly those with high iron content (Brooks et al., 1998). Consequently, we performed batch experiments to evaluate tracer stability during mixing, kinetic uptake, isotherms, and desorption, using laboratory methods previously established (Yu-chen Lin et al., 2003; Hellerich et al., 2003).

Kinetic Uptake Experiment

To further test the kinetics and sorption of the tracers, we used native material collected from EFP01 and EFP03 (outside of SSO wells) from the Y-12 site. The EFP01 sediment was used to test tracer sorption for the FW116 and EFP01 injections (**Figure 3.1, Table 3.1**). Six liters of groundwater were collected from EFP01 using a graduated cylinder. The pH of the water was recorded as 4.1. The specific conductivity of the water at the time of collection was about 1790 µs/cm as assessed using an In-Situ AquaTROLL 600 with data reported on HydroVu. After being evaluated by radiological protection, the water was released and stored at 4°C. A 400-gram sample of sediment was dried at 105°C for ten days. The dried sediment was pulverized and sieved to remove large debris (>2mm). The fine sediment was then weighed and placed into 125 mL serum bottles at ratios of 1:2, 1:4, and 1:10 sediment-to-water, using water from the injection

well. The final volume was 100 g, with 0.01 g of KBr added. Controls include spiked groundwater and a control of the tracer stock solution. Duplicate serum bottles were prepared for each trial type and shaken at 2 RPM, with 10 mL sampled at 1, 5, 10, 50, 100, and 200 hours. The experiment was repeated with 0.001 g of KBr, and measurements were obtained by ion chromatography. The data analysis includes all reported values (**Figures 3.3**).

Transmission Electron Microscopy of Colloid-containing Groundwater

The samples were obtained from the SSO wells U2-SZ2, M5-SZ2, and L8-SZ2, as well as the EFP01 well (outside of SSO wells) in Area 3 at the eFRC site of the Y-12 National Security Area. SSO well depths from which samples were collected are as follows: U2-SZ2: 21-25' depth, M5-SZ2: 21-25' depth, L8-SZ2: 21-25' depth. The EFP01 well, which is outside of the SSO wells, was sampled at a depth of 15-25'. The study area coordinates are 35°58'38.3"N 84°16'24.2"W. In Oak Ridge, TN, the climate is broadly classified as humid subtropical, characterized by abundant rainfall and significant temperature variations across seasons. On the day of sample collection, May 29, 2024, the morning temperature was 57°F, rising to a high of 75°F later in the day. It was a cloudy day. There was no rainfall that week that could change water table. Three liters of groundwater from the wells were first purged before collecting fresh incoming water. 5 ml samples of colloid-containing SSO groundwater were concentrated to increase the likelihood of locating and imaging the particles and individual microorganisms present. Concentration of groundwater samples was achieved using centrifuge-based concentration devices with a molecular weight cut-off of 100,000 (Amicon Ultra-4, Millipore). Concentrators were spun at 700 x g at a temperature of 4°C until the initial 5 mL samples were reduced to volumes of approximately 100 mL. For electron microscopy specimen preparation, 4 ml of concentrated groundwater was deposited onto a glow-discharged carbon-coated grid (Formvar-carbon, 200 mesh copper, Electron Microscopy Sciences). After five minutes, some of the sample on the grid was blotted away, leaving approximately 1 ml, which was then enriched with 2 ml of 1% uranyl acetate. After a ten-second pause, the grid was blotted dry. A JEOL JEM-1200EX electron microscope, operated at 80 kV, was used to analyze the grids at magnifications ranging from 5,000X to 30,000X. A 2k x 2k pixel CCD camera (Ultrascan, Gatan) was used to capture images, which were operated through the Digital Micrograph software package.

Colloidal borescope studies

We used the 52 colloidal borescope measurement data samples to do the following:

- Each sample has between zero and several thousand data points. Each data point contains the speed, direction, and number of colloids for that time point. While n=1 for each well and zone, the high number of data points can be used as pseudo-replicates. We used mean values.
- Use colloidal borescope data to compare colloid counts, speed, and direction between SSO wells using statistical tests, correlation analyses, and clustering techniques.
- Use colloidal borescope data to compare colloid counts, speed, and direction over time within each SSO wells using statistical tests, correlation analyses, and clustering techniques.
- Compare the 2024 cell count data for each well and zone (n=1 for each well and zone) to the 2024 colloidal borescope data for each well and zone with statistical tests and correlation analyses to see if any trends are suggested.
- Compare the 2024 ion chromatography (ENIGMA Chakraborty Lab) and 2024 metals data (ENIGMA Adams Lab) during Pilot series campaign for each well and zone (n=1 for each well and zone for both datasets) to the 2024 colloidal borescope data for each well and zone with statistical tests and correlation analyses to see if any trends are suggested.

Rose Diagrams

Directional rose diagrams were generated in Python (v3.13) using pandas, numpy, matplotlib, and the windrose library to visualize flow directions and transport magnitudes (velocity, colloid counts, flux). Directions (0-360°) were cleaned and wrapped to valid ranges, and non-physical values were removed. Data were binned into 16 directional classes (22.5°) and 4-5 magnitude classes (quantiles). Frequency roses show the proportion of observations per direction. At the same time, weighted roses display the sum of magnitudes per bin, normalized to percentages. Plots were created using WindroseAxes.bar.

Uniform Manifold Approximation and Projection (UMAP) Ordination

We used Uniform Manifold Approximation and Projection (UMAP) to visualize multivariate structure in the dataset. All continuous variables were standardized (zero mean, unit variance) with StandardScaler (sklearn.preprocessing) to prevent variables with large ranges from dominating the embedding. A 2D UMAP embedding was generated using the umap-learn library with n_neighbors = 15, min_dist = 0.1, n_components = 2, and metric = 'euclidean'. These parameters balance local neighborhood preservation with global structure. The resulting UMAP

coordinates were plotted using matplotlib, with sample groups (wells and/or zones) colored by category. Custom legends were created using Line2D for clear group labeling. UMAP plots were used to identify clustering and gradients across wells, zones, and geochemical regimes without assuming linear relationships.

Kolmogorov-Smirnov test

Differences between distributions were evaluated using the Kolmogorov-Smirnov (KS)test, implemented in Python (scipy. stats). The KS statistic reflects the maximum divergence between the two cumulative distribution functions. To assess whether colloid count distributions differed significantly between wells, we applied two-sample Kolmogorov-Smirnov (KS) tests. The KS test compares the empirical cumulative distribution functions of two samples and quantifies the maximum distance between them, providing a nonparametric test of distributional differences without assuming normality. A custom Python function (ks_all_wells) iterated over all unique well pairs for a given depth zone and or year. For each pair, colloid count distributions were extracted and compared using scipy.stats.ks_2samp. The function returned KS statistics and p-values for each pair, indicating whether distributions differed significantly.

Directional Flow Analysis

Directional flow data were analyzed to quantify both the prevailing orientation and the degree of directional concentration across wells and depth zones. All computations were carried out in Python (v3.13) using custom scripts based on circular statistics and permutation testing. Flow directions were expressed in degrees, with 0° corresponding to north and increasing clockwise. These values were then transformed to a circular statistical framework, allowing calculation of both the mean flow direction and the degree of directional clustering within each group.

For each well and depth zone, a circular mean direction was calculated to represent the dominant flow orientation, while the resultant vector length was used to describe how tightly the individual observations clustered around that mean. Higher values of the resultant length indicate stable, well-defined flow pathways, whereas lower values reflect diffuse or weakly oriented flow. In addition to unweighted analyses, a flux-weighted approach was used in which the product of flow velocity and colloid count weighted each directional observation. This weighting emphasized high-flux events and allowed identification of dominant transport directions rather than simple orientation trends.

To assess whether differences in mean flow direction between groups were statistically significant, a permutation-based approach was applied. This involved repeatedly shuffling group labels to generate a null distribution of directional differences, against which the observed difference between two groups was compared. This approach does not rely on distributional assumptions, making it well-suited for the heterogeneous and sometimes multimodal directional data observed at the site. A total of 2,000 permutations were used for each comparison, and statistical tests were performed only when both groups contained more than 30 observations to ensure robust results.

Two types of comparisons were performed. First, differences between zones within the same well were tested to evaluate vertical variability in flow direction. Second, differences between wells within the same zone (particularly SZ2) were tested to examine lateral variability across the field site. Both unweighted and flux-weighted analyses were conducted in parallel. The permutation test approach was chosen over traditional parametric methods because it is robust to deviations from the von Mises distribution and compatible with modern Python environments. R unit is the Rayleigh resultant length.

Calculation of Colloidal Flux Index

Colloidal transport was quantified using borescope data collected across wells and zones. The borescope provides two primary outputs: flow speed (μm/s) representing local groundwater velocity at the point of measurement, and particle count, representing the number of colloidal particles detected within the instrument's optical field of view per unit time (counts). To integrate these two metrics, we defined a flux index as: Flux index = speed x count

This index provides a relative measure of colloid transport intensity, expressed in instrument units rather than absolute flux. Because the borescope does not directly record the cross-sectional discharge area or sampling volume. Nonetheless, the metric is internally consistent across wells and zones, enabling direct comparisons of colloid transport variability within the study system. Flux index distributions were summarized by well, zone, and depth, and descriptive statistics (median, interquartile range, 90th percentile) were calculated to characterize central tendency and variability.

Statistical Analysis of Attached vs. Free Viral States

Differences in the distribution of attached and free viral particles among wells were evaluated using contingency table-based statistical tests. A Pearson's Chi-square test of independence was

applied to assess whether the proportion of attached versus free viruses differed significantly among wells. Observed frequencies were obtained from direct counts of viruses classified as attached or free within each well (L7-SZ2, L8-SZ2, M5-SZ2, and U2-SZ1). Expected frequencies were calculated for each cell in the contingency table as the product of the row and column totals, divided by the total, representing the values expected if well and viral state were independent. The Chi-square statistic was then computed as the sum of squared deviations between observed and expected frequencies, normalized by the expected frequencies. The degrees of freedom were determined by (r-1) x (c-1), where r and c are the number of rows and columns, respectively. Statistical significance was evaluated using the Chi-square distribution. To identify specific pairwise differences between wells, Fisher's exact tests were performed on all pairwise 2 x 2 contingency tables. Fisher's exact test is more appropriate than the Chi-square test for small sample sizes or when expected cell counts fall below 5. We computed a Pearson χ^2 test across wells as an exploratory summary, because several cells had expected counts <5. So, these p-values are indicative only. Odds ratios and exact p-values were calculated for each pairwise comparison to determine whether the proportion of attached versus free viruses differed significantly between individual wells. Tests yielding odds ratios of infinity or zero corresponded to cases in which one or both categories contained only attached or only free viruses. All statistical tests were two-tailed, and significance was assessed at $\alpha = 0.05$. Analyses were conducted in Python using the scipy.stats module (functions chi2_contingency and fisher_exact).

Results

Ion chromatography after a kinetic uptake experiment.

We conducted a kinetic experiment to determine the time required to reach equilibrium and to study the percentage uptake of bromide by the sediments. This suggests that bromide did not adsorb significantly to the solid surfaces under laboratory conditions, even after 200 hours, when the concentration was relatively constant (between 120 and 140 mg/L). The ion chromatography results are presented in **Figure 3.2** and **Figure 3.3.**

Electron microscopy.

The colloids observed in our wells can be divided into three groups. Biotic colloids (organic or biological material) included the L8-SZ2 sample, which exhibited the highest biological diversity, comprising full-sized cells, ultra-small cells, viruses, and various biological particles. A bacteriophage and an ultra-small cell were identified in this sample (**Figure 3.5A**). The M5-

SZ2 sample was primarily composed of ultra-small cells (**Figure 3.5**). It contained a possible Vibrio bacterium (**Figure 3.8)**, as well as virus particles that appeared to associate with cells (**Figures 3.5, Figure 3.6 Top,** and **Figure 3.7 B, C**). The L7-SZ2 sample displayed cells entangled in extracellular polymeric substances (EPS) or pili, surrounded by organic necromass (**Figures 3.7A, Figure 3.6 Bottom, Figure 3.12)**. **Figure 3.12** also contained vesicles, extracellular fibers, and virus particles, indicating active microbial processes such as biofilm formation or cell lysis. Aggregates composed solely of biological material, without sediment, were also observed in L7-SZ2.

Abiotic colloids (inorganic or sediment particles), such as in the EFP01 sample, contained very few microbes, and its particles resembled sand grains more than clay. The L7-SZ2 sample included sediment-only particles measuring 1-2 μm in size (**Figure 3.9).**

Mixed (biotic-abiotic associations): The L7-SZ2 sample contained sediment particles with attached biological material, including cells, viruses, and vesicles, embedded in mineral aggregates (**Figures 3.6 (Bottom) and 3.7A**). Virus particles were frequently found attached to sediment in multiple samples. In M5-SZ2, a colloidal particle (about 0.6 x 0.85 μm) appeared to host a lone virus (**Figure 3.5B**), indicating a direct mineral-viral interaction. Both L8-SZ2 and M5-SZ2 samples contained viruses attached to either sediment or bacteria, either freely floating or bound to mineral surfaces. Some aggregates in U1 and U2 appeared to be composed of amorphous organic material mixed with abiotic colloids, further emphasizing the presence of mixed organic-inorganic colloids. The U2-SZ2 sample contained no detectable microbes and very few particles, primarily consisting of stacked, plate-like clay minerals (**Figure 3.11**). Both U-SZ2 and U2-SZ2 samples contained abiotic particles, including plate-like clay fragments (**Figures 3.11B, C, and D),** which were classified as primary colloids resulting from sediment fragmentation. Secondary colloids, such as nanospheres formed by mineral precipitation, were observed in U2 wells (**Figure 3.11A)**.

The samples varied significantly in composition, with L8-SZ2 showing the highest microbial diversity and EFP01 and U2-SZ2 being predominantly abiotic. Virus-mineral associations were recurrent in L7, L8, and M5 samples. We found that clay fragments (primary colloids) were the main type present in U1, U2, and EFP01. In addition, U2 contained secondary colloids that appeared as tiny, precipitated spheres. This mix suggests that both mineral processes and biological activity are shaping the colloid population.

Distribution of Attached vs. Free Viruses

TEM provided rare in situ visualization of virus-colloid interactions in fractured aquifers. A total of 18 viruses were observed across wells. Attachment frequencies were highly heterogeneous: L7-SZ2 was dominated by attached viruses (9.5 attached vs. 1.5 free), L8-SZ2 contained only free viruses (n = 2), M5-SZ2 exhibited a mix but was free-dominated (3 free, 1 attached), and U2-SZ1 contained only attached viruses (n = 1).

The distribution of attached versus free viruses differed significantly among wells (χ^2 = 14.26, df = 3, p = 0.0026). An exploratory χ^2 suggested that heterogeneity, but inference relies on the exact pairwise Fisher tests reported above. L7-SZ2 contained more attached viruses and fewer free viruses than expected under a random distribution, whereas L8-SZ2 and M5-SZ2 were enriched in free viruses. U2-SZ1 contained only attached viruses, similar to L7-SZ2.
Pairwise Fisher's exact tests identified significant differences between specific wells. L7-SZ2 had a significantly higher proportion of attached viruses compared to L8-SZ2 (odds ratio = ∞, p = 0.0128) and M5-SZ2 (odds ratio = ∞, p = 0.0088). No significant difference was detected between L7-SZ2 and U2-SZ1 (p = 1.0000), consistent with both being dominated by attached viruses. Comparisons between L8-SZ2 and M5-SZ2, L8-SZ2 and U2-SZ1, and M5-SZ2 and U2-SZ1 were not significant (p > 0.3), likely reflecting the small sample sizes in these groups **(Table 3.5)**

Pairwise Fisher's Exact Test Results

Pairwise Fisher's test results were following: L7-SZ2 vs L8-SZ2: odds ratio=inf, p=0.0128. L7-SZ2 vs M5-SZ2: odds ratio=inf, p=0.0088. L7-SZ2 vs U2-SZ1: odds ratio=nan, p=1.0000. L8-SZ2 vs M5-SZ2: odds ratio=0.00, p=1.0000. L8-SZ2 vs U2-SZ1: odds ratio=0.00, p=0.3333. M5-SZ2 vs U2-SZ1: odds ratio=0.00, p=0.4000

Ion chromatography pilot test results

For pilot series studies, there were two time points: T1 = September 9, 2024, and T2 = September 18, 2024. Romy Chakraborty's ENIGMA lab did the measurements. U1 is the extreme outlier with very high nitrate (about 482 ppm) and moderately elevated sulfate. U2 shows both high sulfate (about 231 ppm) and high nitrate (about 236 ppm), reflecting strong redox gradients. M5 has moderate sulfate but elevated nitrate (about 140 ppm), a mixed redox environment. L wells (L7, L8, L9) and M4 and M6 show low nitrate (<10 ppm) but moderate

sulfate, consistent with reduced oligotrophic zones. U3 is intermediate, with moderate sulfate (about 155 ppm) and low nitrate (about 17 ppm).

We made Spearman correlations among chloride, sulfate, and nitrate across all samples to see if redox-sensitive ions co-vary across the dataset. Chloride and sulfate are strongly correlated (ρ (rho) = 0.89). It suggests these ions often co-occur, possibly due to shared sources (legacy waste inputs or mineral dissolution) or conservative transport. Sulfate and nitrate show a moderate correlation (ρ (rho) = 0.52). It indicates that higher nitrate often coincides with elevated sulfate, consistent with redox stratification, where both serve as electron acceptors. Chloride and nitrate are weakly correlated (ρ (rho) = 0.42). This provides both statistical and visual evidence that: chloride and sulfate behave conservatively together, likely reflecting shared sources. Nitrate is more dynamic, reflecting both contamination loading and microbial consumption, with extreme enrichment in U1 and U2. Chloride's conservative behavior suggests that its correlation with sulfate reflects common contamination sources rather than redox coupling. Chloride and sulfate co-vary, whereas nitrate varies more independently. In U1 and U2, all three remain high, consistent with mixed waste inputs. In M5, high nitrate but moderate sulfate, which reflects selective nitrate loading and partial decoupling of sulfur cycling. In L wells, low nitrate despite moderate sulfate indicates zones where nitrate has been consumed, leaving sulfate as the dominant electron acceptor.

Directional Flow Analysis and Statistical Comparisons

Wind rose diagram (**Figure 3.21**) showed the fasted speed (μm/s) is in M5 well. Flow directions vary strongly by well and by depth. Dominant orientations span nearly the full compass-from near-north in U1-SZ2 (354°) and U3-SZ2 (351°) to south and south-west in several background and M-series wells (M4-VSZ ≈ 6°, M5-SZ1 ≈ 270°). R is the Rayleigh resultant length. Directional concentration also differs sharply: shallow zones are typically diffuse (L7-SZ1 R=0.020; U2-SZ1 R=0.057; M5-SZ1 R=0.145), whereas deeper zones are stable and well aligned (L9-VSZ R=0.978; U1-VSZ R=0.943; U3-VSZ R=0.775). Overall, these results indicate weak, variable surface flow and coherent flow paths at depth.

We used a non-parametric permutation test on differences in circular mean direction (2,000 permutations), applied to both vertical (within-well) and horizontal (between-well) comparisons. These statistical tests confirm these depth-wise shifts. In the unweighted analysis, 26 of 28 zone-pair comparisons were significant ($p<0.05$), with mean directional differences

averaging ~83° and reaching ~170° (M4 SZ1 vs VSZ). When weighting observations by flux (velocity x count), the number of significant contrasts decreased slightly (21 of 28), but the average separation increased to ~91°. Thus, transport-relevant directions (those carrying higher velocities and particle counts) diverge even more across depth than unweighted orientations. Wells M5 and M6 illustrate this trend: shallow flows are weakly oriented, while deeper layers show strongly aligned transport vectors.

Lateral contrasts are pronounced within SZ2. Almost all well pairs differ significantly in the unweighted tests (35 and 36, mean separation ≈ 99°), and flux weighting yields a similar picture (32 and 36, mean ≈ 99°). The clearest contrasts occur between U-series wells and L and M wells: U1-SZ2 (354°) and U3-SZ2 (351°) trend northward. M5-SZ2 (261°) trends west-southwest, M6-SZ2 (304°) northwest, and L8-SZ2 (144°) southeast. These clusters reveal coherent directional regimes within subsets of wells and sharp divergence between them. Flux-weighted analyses further show that these differences are statistically robust (permutation test, $p < 0.05$ for 32 of 36 pairs; $p < 0.01$ for 28), with many pairwise orientation differences exceeding 90°. Directional concentration (Rayleigh R) varied systematically, with some wells exhibiting tightly aligned transport vectors while others were more diffuse.

Overall, the results resolve a two-part structure of the flow field: vertical stratification, with deeper zones showing stable, high-concentration flow while shallow zones remain diffuse and variable. Our results also pronounced horizontal heterogeneity within SZ2, where wells in different hydrogeologic settings display nearly opposite dominant orientations. Flux weighting demonstrates that the most consequential transport directions (those carrying the most significant flux) are vertically distinct within wells and laterally divergent across the site (**Table 3.6, Figure 3.23-3.25**).

UMAP results

We applied UMAP (n_neighbors = 15, min_dist = 0.1, metric = euclidean; all variables z-scored) to explore the multivariate structure of the 2023 borescope dataset. The resulting two-dimensional embedding reveals clear spatial organization when colored by particle count, flow speed, and flow direction (**Figure 3.18-3.20**). Observations with high particle counts form a compact central region of the manifold, while low-count observations are distributed more diffusely toward the periphery. The smooth color transitions across the embedding indicate that particle abundance varies continuously rather than forming discrete clusters. A similar trend

emerges when the data are colored by flow speed: fast observations occupy the same central region as high counts, whilst slower observations are scattered toward the edges. This overlap shows that episodes of elevated particle abundance coincide with higher groundwater velocities, defining a coherent set of transport states within the embedding. Flow direction varies smoothly across the manifold as well, forming broad directional bands with opposite headings positioned on opposite sides. The apparent break near 0 and 360° is a colormap artifact rather than a true discontinuity. Areas of highest point density also exhibit narrower directional spreads, reflecting greater directional coherence during high-flux episodes. These trends are robust across different UMAP parameter choices (n_neighbors 10-30; min_dist 0.05-0.3). These trends persist even when particle count is excluded, confirming that the central enrichment of high counts reflects real co-variation with flow speed and direction rather than a modeling artifact (**Figure 17-19**).

Pairwise Distribution Comparisons Using the Kolmogorov-Smirnov Test (also K-S test or KS test)

KS dissimilarity analysis grouped most wells (L9, M4-M6, U1, U2), with L7 and U3 in intermediate positions and L8 as an outlier. Every well-pair shows significant differences ($p < 0.0001$). Pairwise Kolmogorov-Smirnov (KS) tests revealed clear and statistically significant differences in the empirical distributions of colloid counts across wells (all $p < 0.001$). Dissimilarity values ranged from 0.04 to 0.46, reflecting varying degrees of divergence in the underlying distributions of colloidal abundances and transport behaviors (**Table 3.7, Figure 3.22).**

The largest dissimilarities were observed in well L8, which consistently exhibited higher KS distances than other wells (like L8 vs M4 = 0.46, L8 vs U3 = 0.43, L8 vs L9 = 0.39; all $p < 0.001$). Similarly, L7 and L8 displayed a substantial dissimilarity of 0.38, indicating that even adjacent or laterally close wells can support markedly different colloid distributions. These trends reinforce the distinct hydrodynamic and geochemical conditions at L8, which is already identified as the uranium concentration maximum in the system. In contrast, comparisons among the M-series wells (M4-M6) and among U-series wells (U1-U3) yielded relatively low dissimilarities, typically between 0.04 and 0.20, suggesting broadly similar colloid count distributions within these groups. For example, M4 vs U3 showed the lowest overall dissimilarity (0.04), while M5 vs U2 and M6 vs U2 showed similarly low values (0.05-0.08). These results point to a shared distributional structure among mid-gradient and upgradient wells, consistent with more homogeneous hydrological regimes. Intermediate dissimilarities were

observed between L7 and the M- or U-series wells (0.12-0.22), reflecting a moderate shift in distribution shape and location. Notably, L7 vs U3 exhibited a particularly low dissimilarity (0.05), indicating that in some cases, distributions between wells in different zones can converge.

Overall, the KS test results reveal a structured trend of distributional differences, with L8 emerging as the most distinctive well, L7 occupying an intermediate position, and the M- and U-series wells forming more cohesive groups. These findings demonstrate the heterogeneous hydrodynamic and colloidal transport regimes across the field site and provide quantitative support for subsequent clustering and multivariate analyses.

Colloidal flux results

We created colloidal Flux-index profiles with depth across 9 SSO wells (**Figure 3.23-3.26**). Flux indices, calculated as the product of flow speed and particle count, revealed pronounced spatial and temporal heterogeneity across wells and zones. Among all sites, L7-SZ1 exhibited the highest mean flux index (5, 459) in the static dataset, corresponding to exceptionally fast borescope-measured velocities and elevated colloid counts. This zone stands out as a persistent active mobilization spot, likely reflecting the intersection of transmissive fractures and geochemical conditions that favor particle detachment. Time-series data supported these observations. Across 2023-2024, L8-SZ2 showed consistently elevated flux values, peaking at ~9, 694 in April 2023, coinciding with high flow velocities and moderate to high conductivity. L8-SZ1 also maintained above-average fluxes but with greater temporal variability. In contrast, L9-SZ1 and SZ2 displayed intermediate flux levels (~1, 300-1, 900), indicative of stable but less intense mobilization dynamics. M4-SZ1 maintained lower flux values overall, consistent with lower conductivity and fewer high-flow events. Temporally, flux peaks were concentrated in spring 2023, suggesting seasonal hydrological forcing, possibly linked to recharge events. Zones with sustained high flux generally overlapped with high flow speed measurements (>1000 μm/s), demonstrating the strong influence of hydraulic gradients on colloid mobilization. These spatial "hot spots" and temporal peaks demonstrate a non-uniform flux landscape, where specific fractures or well-zone combinations dominate colloid transport potential across the network.

Additionally, hydrological flux calculations and statistical modeling revealed substantial spatial variability in the relationship between conductivity and colloid mobilization across the SSO wells (**Figure 3.20**). After aligning HydroVu conductivity with borescope-derived velocity and particle counts, we computed a flux index (velocity x particle count rate) and analyzed the

native time-series resolution (15-60 min merges). Across 14 well-zone pairs, ordinary least squares (OLS) regressions and random-slopes mixed-effects models showed that conductivity often exerts a measurable influence on colloid flux. Still, the effect is highly heterogeneous across sites, producing distinct mobilization "hot spots" and "cold spots."

Positive conductivity-flux slopes were concentrated in the upper wells, particularly U3-SZ2, U3-SZ1, U1-SZ1, and U2-SZ1. In these zones, increases in conductivity were strongly associated with increased log-transformed flux, with slope magnitudes from 0.12 to 2.85 Δlog(flux) per 100 $\mu S\ cm^{-1}$ and R^2 values up to 0.15. These wells represent geochemical and hydraulic settings where ionic strength promotes colloid detachment and transport, consistent with double-layer compression and enhanced mobilization in transmissive fractures.

Conversely, negative slopes were observed in U2-SZ2, U1-SZ2, L9-SZ1, M4-SZ1, and L8-SZ1. These wells exhibited significant inhibitory effects, with slopes as low as -1.70 Δlog(flux) per 100 $\mu S\ cm^{-1}$ and R^2 up to 0.16, indicating that higher ionic strength corresponded to reduced colloid flux. Other wells, such as L9-SZ2 and L8-SZ2, displayed weak, non-significant associations, indicating little or no conductivity control on flux in those zones.

Mixed-effects models using a within-between (REWB) specification produced slope patterns consistent with the OLS results, confirming that conductivity effects are governed primarily by local well-zone characteristics rather than a single aquifer-wide relationship. The inclusion of random slopes revealed substantial between-site variability, emphasizing the fractured system's patchy hydrogeochemical structure.

Overall, these results showed conductivity as a key but context-dependent driver of colloid mobilization. Zones with positive slopes function as mobilization "hot spots," where increases in ionic strength trigger enhanced transport. On the other hand, negative slopes correspond to "cold spots," where conductivity suppresses flux. This spatial heterogeneity aligns with conceptual models of fractured aquifers, where geochemical and hydraulic factors interact to produce localized zones of high and low mobilization potential. This interaction links conductivity dynamics to colloid transport, fracture flow, and microbial/viral dispersal in the subsurface.

Discussion

Laboratory experiments showed no bromide sorption in EFP01 sediments, which aligns with its well-established use as a conservative groundwater tracer. Bromide is generally non-reactive,

exhibiting negligible sorption or transformation under typical aquifer conditions (Davis et al., 1980; Fetter Jr, 2001). Minor deviations from ideal conservativeness have been reported in organic-rich surface soils due to organobromine formation, but such effects are not expected in the saprolitic aquifer tested here (Flury and Qiu, 2008).

Similarly, nitrate (NO_3^-) behaved largely conservatively across the system, which is consistent with its well-known mobility and low sorption affinity in groundwater (Rivett et al., 2008). Nitrate typically migrates with advective flow due to its high solubility and negative charge, and significant retardation is uncommon unless redox conditions favor biological denitrification (Rivett et al., 2008). Depth profiles showed elevated nitrate concentrations in upper wells (U1 and U2) and accumulation in deeper zones (M5-SZ3). Such trend can be explained by a combination of recharge-driven flow in the variable saturated zone (VSZ) and density-driven transport in deeper layers (Fetter Jr, 2001; Scanlon and Cook, 2002). Deep zones showed strong chemical extremes but limited flow detection, suggesting solute accumulation in disconnected zones disconnected from rapid advective pathways.

Colloid transport in this system is strongly controlled by ionic strength and anion composition, consistent with colloid filtration theory. Increased ionic strength compresses the electrical double layer, enhancing deposition and reducing mobility (Ryan and Elimelech, 1996; Stumm and Morgan, 1996). Both NO_3^- and SO_4^{2-} can destabilize colloids. The latter is particularly effective at collapsing the double layer around iron (III) oxides, thereby promoting aggregation and retention (Stumm and Morgan, 1996). These mechanisms explain why colloid mobility is highest in the upper SSO wells, where ionic strength is lower, and deposition dominates at depth.

TEM imaging revealed that most mobile colloids fell within a 0.5-1 μm size range, which corresponds closely to field tracer studies in fractured saprolite at Oak Ridge. Cumbie and McKay (1999) and McKay et al. (2000) showed that colloidal tracers of this size traveled tens of meters through fractured shale saprolite. The saprolite's fine-grained matrix and fracture network provide a continuous supply of mobile particles, particularly under contaminant-enhanced weathering (Putt et al., 2022). These results support the interpretation that saprolite zones in the SSO wells act as both sources and conduits for colloid transport, especially under advective conditions. Numerous studies have documented colloids enhancing the mobility of both cationic and anionic metals, including uranium, plutonium, and technetium, in contaminated aquifers

(Deb and Chakma, 2023; Flury and Qiu, 2008; Kersting et al., 1999; McCarthy and Zachara, 1989). Uranium in these systems is typically present as the uranyl cation (UO_2^{2+}) or as uranyl-carbonate complexes, both of which exhibit mobility that depends strongly on solution chemistry (Stumm and Morgan, 1996; Fetter, 2001).

Colloids in the SSO wells can be grouped into abiotic, biotic, and mixed assemblages, a classification widely used in environmental colloid research. Abiotic colloids (such as clays, silts, and iron oxides) can act as nucleation sites for biofilm development, anchoring microbial communities and extracellular polymeric substances (EPS) (Geesey et al., 1988; Morales et al., 2007). This interaction is ecologically significant: biofilms can alter redox microenvironments, facilitate denitrification, and mediate contaminant retention or release.

Abiotic colloids can serve as a foundation for biofilm formation (Secchi et al., 2022). Viruses attached to both cells and minerals could affect nutrient cycling and change community composition in SSO wells (Wang et al., 2024). Electron microscopy (TEM) images reveal that some ultra-small cell types we've observed at the site exhibit a smooth, oval, or egg-like morphology and occasionally display very fine pili. There has been considerable discussion about the presence and activity of ultra-small cells in the sediment, with speculation that these long, delicate pili may serve to anchor the cells to other cells or sediment particles. In the L7 water, we found a colloid aggregate containing what appeared to be vesicles or necromass, a bacteriophage, other virus particles, and an ultra-small cell seemingly tethered to the aggregate by at least one, and possibly three, fine pili (**Figure 3.6 Bottom).** To the best of our knowledge, this is the first evidence showing an ultra-small cell directly attached to sediment at Y-12 Area.

The viral and microbial associations with colloids observed in our TEM images provide a novel mechanistic layer. Viruses are known to adsorb to mineral surfaces, especially clays and oxides, in a pH- and ionic strength-dependent manner (Bales et al., 1989; Bales et al., 1991). Under changing chemical conditions, such as recharge events, previously attached viruses can detach and be transported (Bales et al., 1991). At Oak Ridge, groundwater viromes include auxiliary metabolic genes that may influence nitrogen and sulfur cycling (Wang et al., 2024). Our direct visualization of ultra-small cells tethered by pili to colloidal aggregates represents the first in situ evidence at Y-12 of microbial and viral colonization of mobile particles, bridging pore-scale interactions with field-scale transport. Finally, bioremediation experiments elsewhere have shown that microbial activity can immobilize metals through biogenic colloids. One study

(Safonov et al., 2022) detected uranium, neptunium, and plutonium associated with microbial cells and EPS after laboratory treatment, demonstrating how colloids can switch roles from transport facilitators to sinks under different conditions. Overall, our findings fit within established theories of conservative solute movement and colloid physics, while extending them by showing how biotic-abiotic interactions shape transport in fractured saprolite.

Pairwise Kolmogorov-Smirnov (KS) tests revealed a clear and structured trend in the distribution of colloid counts across wells. Effect sizes (D) ranged from 0.04 to 0.46 (all $p < 0.001$), indicating statistically robust differences in both the shape and location of colloid count distributions. The largest dissimilarities consistently involved well L8. Well L7 occupied an intermediate position, and the upper and middle wells exhibited comparatively low dissimilarities. This stratified structure reflects underlying geochemical gradients and hydraulic connectivity at the site and resonates strongly with both theoretical expectations and empirical observations from decades of colloid transport research.

The pronounced distributional divergence at L8, including a maximum KS distance of 0.46 (L8 vs M4), aligns closely with classical filtration and deposition theory (Elimelech and O'Melia, 1990; Yao et al., 1971) and early colloid-facilitated transport models (Corapcioglu and Jiang, 1993) Flury and Qiu, 2008; (Šimůnek et al., 2006) Bradford, 2006, 2014; (Natarajan and Kumar, 2010). These studies demonstrate that attachment efficiencies are strongly controlled by solution chemistry, particularly pH and ionic strength, as well as by surface charge interactions. Zones with reduced attachment efficiency promote broader, heavy-tailed colloid distributions, precisely as observed at L8. L8 well represents the maximum uranium concentration and an extreme geochemical anomaly within the site. More recent syntheses have expanded these frameworks by incorporating nanoparticle aggregation and dynamic detachment phenomena (Molnar et al., 2019; (Babakhani, 2019); (Şengör and Ünlü, 2023). Those studies showed that chemically heterogeneous zones produce distinctive, intermittent transport regimes. The elevated KS distances involving L8 reflect this chemically modulated mobility, consistent with theoretical predictions.

Comparable behavior has been documented in field tracer studies examining colloid and virus transport in variably saturated media (Bales et al., 1989; 1991), where attachment efficiency decreased under low ionic strength and neutral pH, resulting in extended breakthrough curves. Radionuclide transport studies (McCarthy and Zachara, 1989; (Malkovsky, V. and Pek,

A., 2009); (Malkovsky, V.I. and Pek, A.A., 2009) Deb and Chakma, 2022) similarly demonstrate that metal-colloid co-migration is favored under geochemical conditions that suppress attachment, paralleling the distinct distributions observed in the L8 well.

In contrast to L8, the middle and upper wells showed lower KS dissimilarities ($D \approx 0.04$-0.20), reflecting more homogeneous transport regimes. This trend is consistent with field tracer experiments in fractured saprolite, which have demonstrated rapid and stable colloid migration along well-connected preferential pathways (McKay et al., 1993; (McKay et al., 2000); (Zhang et al., 2015); (Baumann et al., 2010). Hydrogeophysical imaging studies at Oak Ridge have resolved fracture networks that facilitate uniform flow across specific portions of the aquifer (Revil, Andre et al., 2013). Fracture network modeling (Lee et al., 1999) and recent site investigations (Putt et al., 2022; Walker dissertation, 2024) indicate that hydraulic connectivity can homogenize colloid transport across upgradient zones. The KS structure also parallels well-established trends of microbial community differentiation along geochemical gradients at the Oak Ridge site. Metagenomic and population genomic studies have repeatedly shown that microbial communities in highly contaminated zones differ strongly in both composition and function from those in less contaminated wells (Hemme et al., 2010; Hemme et al., 2016; Hemme et al., 2015; Peng et al., 2022; Tian et al., 2020; Waldron et al., 2009). Deterministic community assembly dominates under strong geochemical forcing (Fan et al., 2025; Ning et al., 2024), and functional traits related to metal resistance and nitrate metabolism track these gradients (Goff et al., 2022; Paradis et al., 2022). The fact that L8 well exhibits both the strongest geochemical anomalies and the greatest KS dissimilarities provides independent, distribution-level evidence that hydrological and colloidal processes are structured by the same geochemical forces that shape microbial communities. This directly supports H1, which posits that microbial communities differ significantly among wells in association with geochemical gradients. Moreover, the correlations between colloid mobility and geochemical parameters implied by the KS trends are consistent with H2, which predicts significant associations between colloids, metals, ions, pH, microbial abundance, and community structure. Virus tracer studies (Bales (Bales et al., 1989; Bales et al., 1991) and research on biofilm-EPS interactions (Bradford and Torkzaban, 2008; Geesey et al., 1988; Morales et al., 2007) show that biological factors further modulate colloid mobility, often amplifying chemical effects.

UMAP analysis shows that colloidal transport at the site is best described as a continuum of states, with high particle counts, high flow speeds, and coherent flow directions clustering in a compact core, and low-flux, variable observations scattered at the periphery. This organization indicates that episodes of intense particle transport occur along stable pathways, while more retentive behavior dominates under variable conditions. Wells overlap strongly in the embedding, suggesting that transport is shaped by shared hydraulic and geochemical forcing rather than well identity (Smith et al., 2015). Depth exerts clearer influence, with deeper intervals more often aligned with high-flux states, consistent with greater directional stability. These findings align with colloid filtration and DLVO theory (Elimelech and O'Melia, 1990; Yao et al., 1971), as mobility varies continuously with chemistry and flow. Similar transport shifts have been observed in field studies (Grolimund and Borkovec, 2005), demonstrating the coupled controls on colloid mobility in fractured saprolite. The structured colloid transport regimes observed here are not unique to Oak Ridge. At Hanford's 300 Area, uranium and technetium plumes have been shown to drive deterministic microbial assembly and structured transport trends (Lin et al., 2012; Zachara et al., 2007). At the Savannah River Site, colloid-facilitated plutonium transport was documented in situ (Kersting et al., 1999). By comparison, at Rifle IFRC, microbial community succession closely tracked redox and contamination gradients (Anantharaman et al., 2016a).

Flux indices varied strongly across wells and time. L7-SZ1 showed the highest mean flux (5 459), marking it as a persistent mobilization hot spot. L8-SZ2 exhibited consistently elevated flux, peaking at ~9 694 in April 2023, likely driven by high flow velocities and seasonal recharge. L9 zones showed intermediate flux, while M4-SZ1 remained low. Overall, flux peaks clustered in spring 2023 and aligned with zones of high flow (> 1000 μm/s), showing localized hydraulic control on colloid mobilization. The elevated flux indices observed in this study reflect the combined effects of high fracture velocities and abundant mobilizable particles in specific well-zone intervals. Frame-level borescope measurements show flow speeds frequently exceeding 1000 μm/s in zones such as L7-SZ1 and L8-SZ2, which are among the most transmissive intervals in the network. These velocities comparable to those typically reported for ambient flow in fractured aquifers (McCarthy and Zachara, 1989). Elevated particle counts (3-7 particles per frame) recorded concurrently suggest that these zones not only transmit water rapidly but also act as sources of mobilizable colloids, likely through detachment processes

driven by hydraulic pulses or geochemical shifts (Ryan and Elimelech, 1996). Because the flux index is calculated as the product of speed and particle count, these two factors amplify each other, producing values in the 5,000-10,000 range, which are higher than those observed in many ambient field studies and approach levels typically associated with recharge events or engineered injections (McKay et al., 2000; Molnar et al., 2015). These results indicate that a limited number of hydraulic hot spots dominate colloid transport at the site, consistent with previous observations in fractured systems where preferential flow paths control both advective and particle flux (Borgman et al., 2022; Zvikelsky and Weisbrod, 2006).

The conductivity-flux analysis demonstrates how ionic strength can act as both a mobilizing and inhibitory force in fractured subsurface systems, depending on local geochemical and hydrological conditions. Positive conductivity-flux relationships observed in U3-SZ2, U3-SZ1, U1-SZ1, and U2-SZ1 indicate zones where increased ionic strength enhances colloid mobilization. This pattern aligns with established colloid transport theory, in which increased ionic strength compresses electrostatic double layers, weakens repulsive forces, and promotes detachment of particles from mineral surfaces (Elimelech and O'Melia, 1990; Ryan and Elimelech, 1996; Torkzaban et al., 2015). Similar conductivity-driven mobilization has been documented in fractured saprolite aquifers and other contaminated sites, where salinity fluctuations triggered sharp increases in colloid-bound contaminant transport (Grolimund and Borkovec, 2005; Haliena et al., 2016). The magnitude of slopes in U3-SZ2 ($\beta = 2.85$ log units per 100 µS cm^{-1}) and U3-SZ1 ($\beta = 0.86$), combined with moderate R^2 values, suggests that conductivity is a dominant control on mobilization in these zones, reflecting open, transmissive fractures where geochemical changes propagate effectively. Conversely, strong negative slopes in U2-SZ2, U1-SZ2, L9-SZ1, M4-SZ1, and L8-SZ1 show zones where elevated ionic strength suppresses colloid flux. This inhibition may result from increased attachment due to double-layer compression in regions already near the attachment threshold, or from co-occurring increases in metals and sulfate that promote colloid aggregation and deposition. Such processes are well documented in metal-rich aquifers, where high ionic strength can stabilize colloids through enhanced bridging and precipitation reactions (Saiers and Lenhart, 2003; Shen et al., 2008; Spielman-Sun et al., 2024). The magnitude of inhibition in U2-SZ2 ($\beta = -0.37$, $R^2 = 0.16$) and L9-SZ1 ($\beta = -1.70$) indicates that conductivity changes can strongly constrain flux in specific geochemical contexts, creating “cold spots” where transport is effectively dampened. The

coexistence of mobilization and inhibition within the same aquifer illustrates the patchwork structure of transport heterogeneity in fractured systems. Mixed-effects modeling confirmed that these conductivity effects are well explained by local well-zone characteristics rather than a uniform aquifer-wide relationship, with substantial random slope variance reflecting site-specific fracture geochemistry and hydrodynamics. U3 wells, for example, likely correspond to high-permeability fractures with low surface coatings or biofilms, which enable conductivity changes to destabilize attached particles rapidly. In contrast, wells such as U2-SZ2 and L9-SZ1 may intersect chemically reactive or constricted fractures where geochemical extremes dominate particle behavior. These results demonstrate that conductivity is a powerful but context-dependent predictor of colloid transport. It can reveal underlying fracture-scale geochemical regimes that either enhance or suppress mobilization. It has practical implications for contaminated site management: conductivity monitoring can identify zones with high mobilization potential, inform targeted sampling, and improve transport modeling by incorporating heterogeneity explicitly. Moreover, conductivity-driven flux changes may also influence the co-transport of microbial and viral assemblages, linking geochemical triggers to ecological and contaminant dispersal processes in the subsurface.

Conclusion

This study demonstrates that both hydrologic variability and strong geochemical gradients structure colloid transport at the S-3 ponds Y-12 site. Bromide behaved conservatively, confirming that advective flow pathways can be probed without sorption effects. Ion chemistry revealed nitrate and sulfate enrichment in upper wells and extreme anomalies at depth. At the same time, colloid distributions reflected these chemical regimes: L8 stood out as a chemically forced, high-mobility spot. L7 showed intermediate behavior. The middle and upper wells clustered with more stable transport. Colloids were not only physical carriers but also biological substrates. TEM imaging revealed biotic, abiotic, and mixed aggregates, with viruses and ultra-small cells attached to minerals and EPS. Viral states varied by well, with L7 enriched in attached viruses and L8 dominated by free viruses, showing how microbial interactions reflect geochemical forcing. Overall, these results confirm that colloids link chemical and biological transport. Geochemistry shaped microbial community differences, and colloid abundance correlated with metals, ions, pH, and cell counts. Colloids thus emerge as a mechanistic bridge

between contaminant chemistry and microbial ecology, validating the overarching hypothesis and providing strong support for both H1 and H2.

Acknowledgments

We thank our ENIGMA project team members: we are grateful to Dr. Peter Walian and Dr. Lucy Zeng for creating the electron microscopy images for our samples; we thank Dr. Michael Thorgersen, Dr. Farris Poole, and Dr. Michael Adams for providing the metal analysis data of the groundwater; we thank Dr. Romy Chakraborty for the ion chromatography data.

Appendix 3: Figures

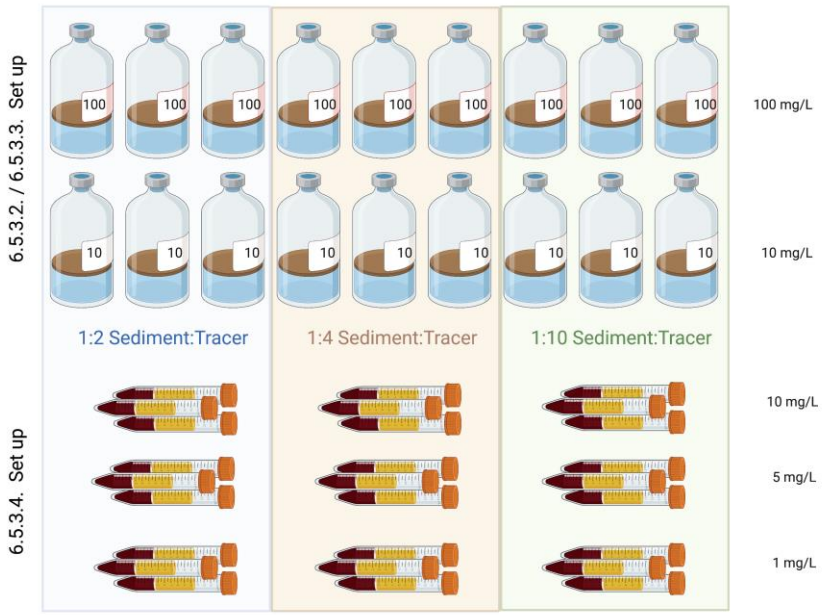

Figure 3.1. Experiment set-up. Sediment to trace ratio and concentration during the setup of the kinetic uptake experiment.

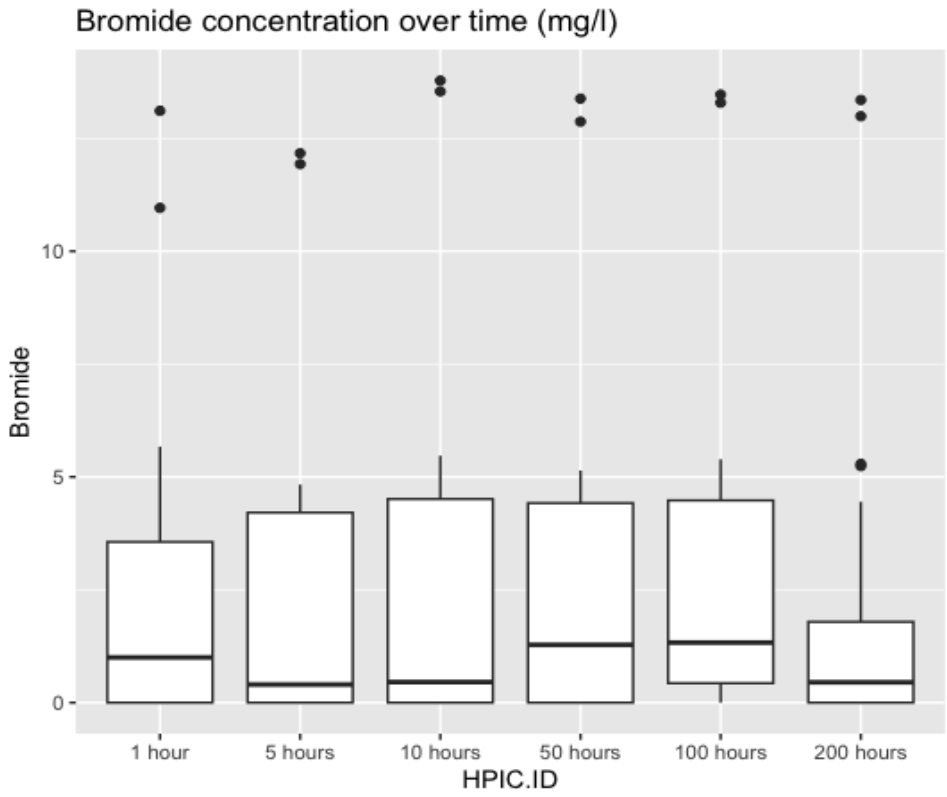

Figure 3.2. Box Plot Ion Chromatography results after 200 hours. After 200 hours, the concentration remained relatively constant, with a slight increase at each time point.

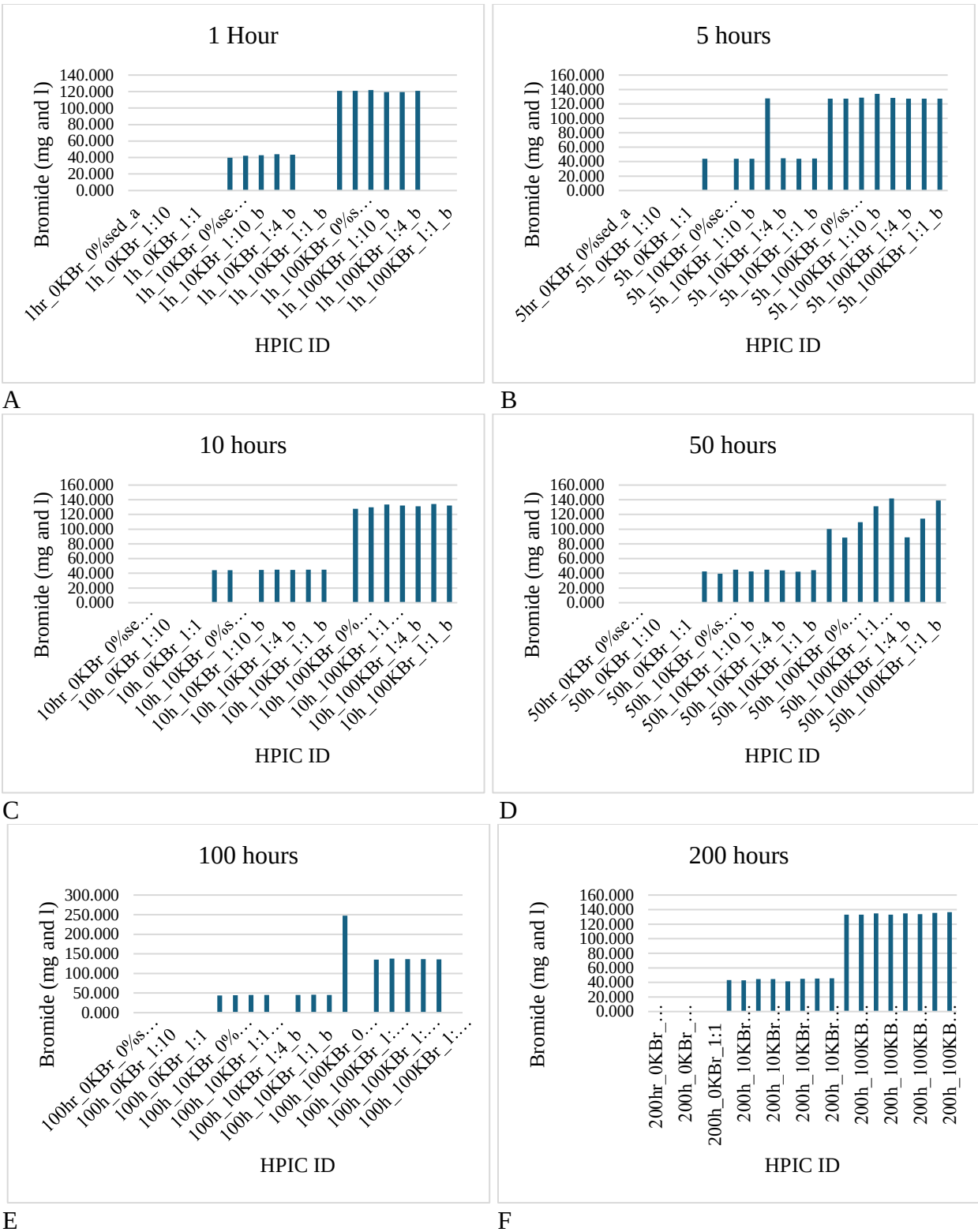

Figure 3.3. Ion Chromatography (IC) results (all values reported) **A**. Ion Chromatography (IC) results after 1 hour. **B**. IC results after 5 hours. **C**. IC results after 10 hours. **D**. IC results after 50 hours. E. IC after 100 hours. F. IC results after 200 hours.

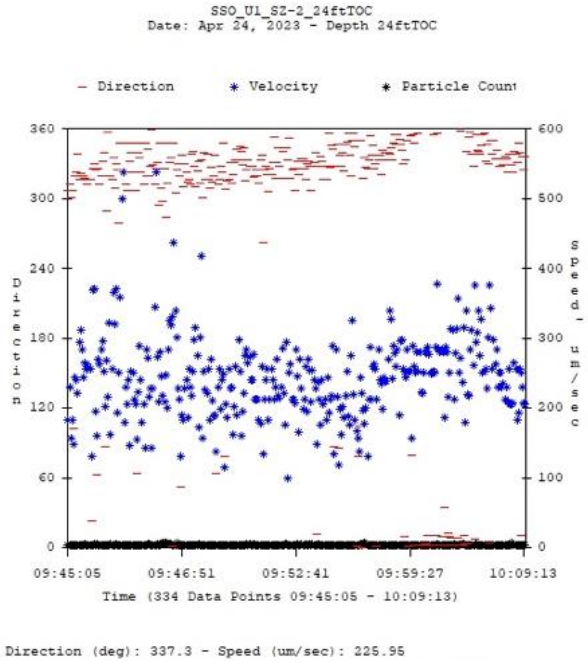

A

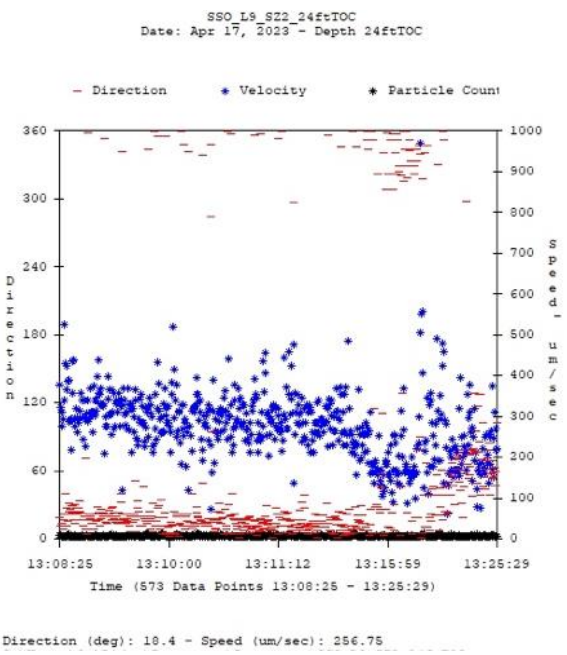

B

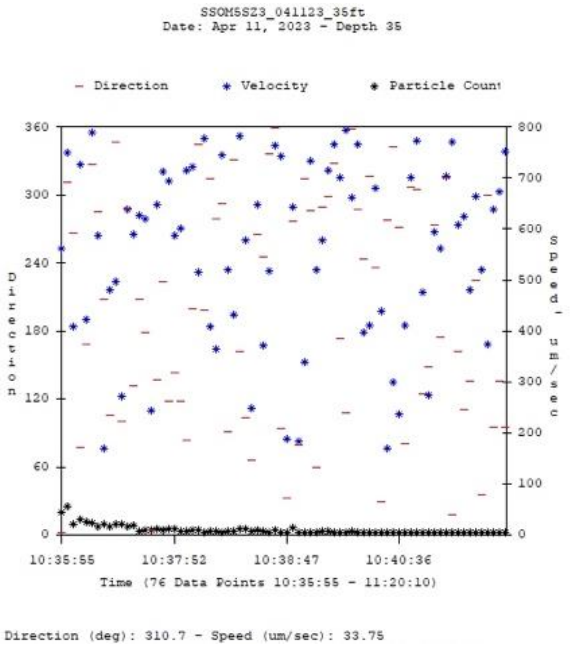

C

Figure 3.3. Colloidal borescope results. A. Colloidal borescope measurements of U1_SZ2_24 ft TOC well. B. Colloidal borescope measurements of SSO_L9-SZ2_24 ft TOC well. C. Colloidal borescope measurements of SSO_M5-SZ3_35 ft TOC well.

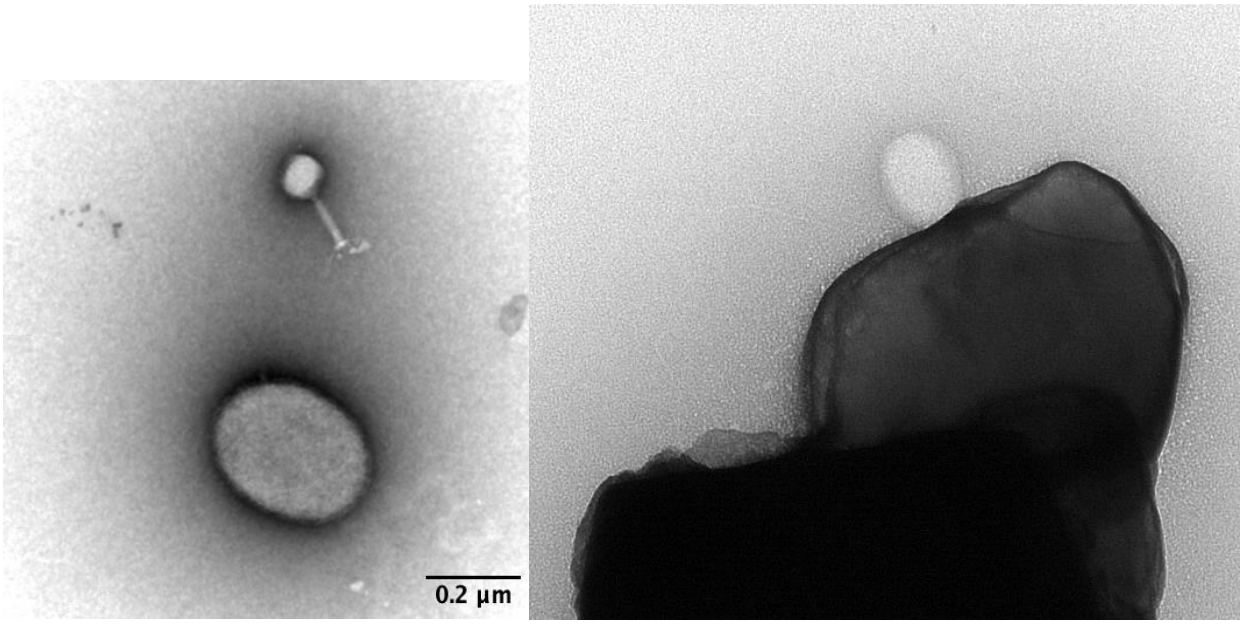

(A) (B)

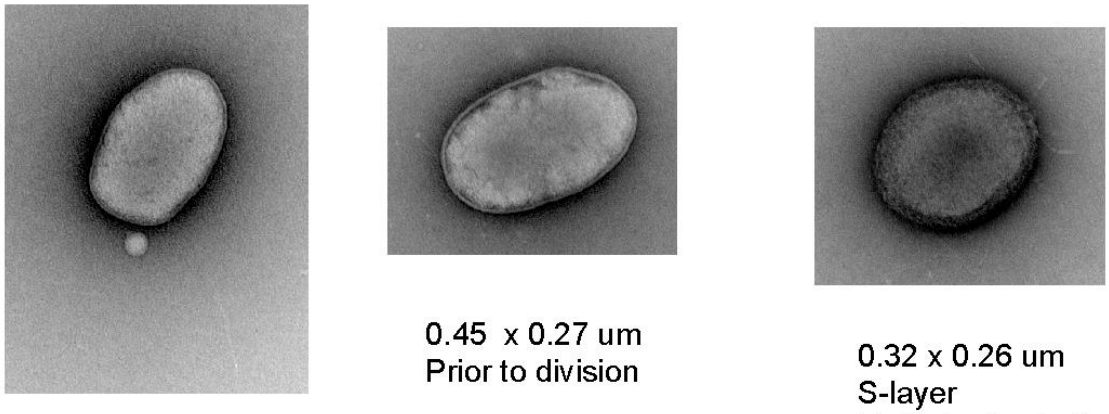

(C)

Figure 3.4. Viruses found using electron microscopy in L8-SZ2 and M5-SZ2 wells.

A. L8-SZ2 well sample. In addition to the bacteriophage in the top half of the figure, there is what is likely to be an ultra-small cell located in the bottom half of the image. **B.** One of the few M5-SZ2 well's particles (0.6 x 0.85 µm) we observed that may be "hosting" a lone virus particle (about 100 x 70 nm). **C.** M5-SZ2 well sample. Has a significant population of ultra-small cells, but relatively few colloidal particles were noted in this sample. Courtesy of Dr Peter Walian and Dr Lucy Zeng.

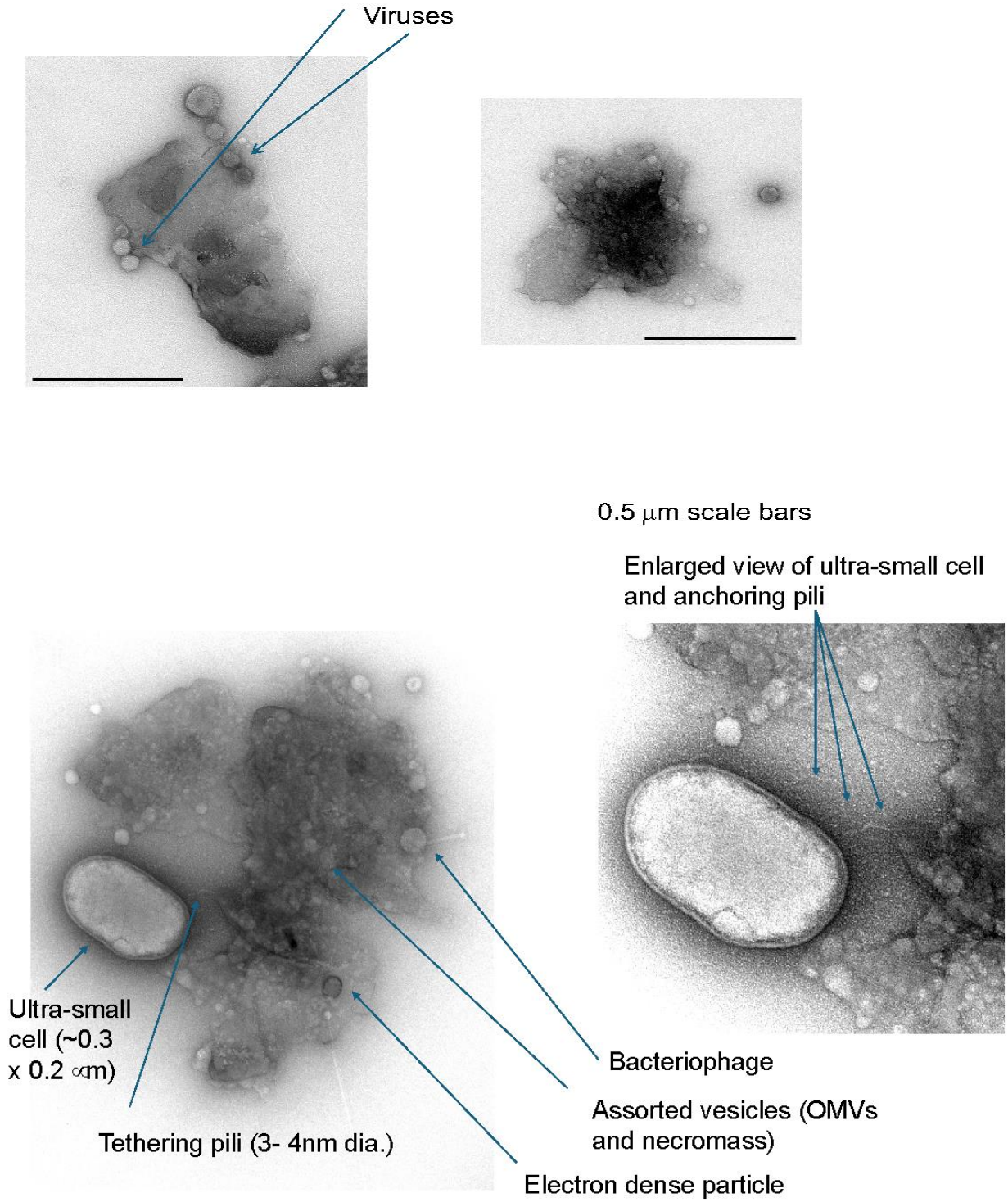

Figure 3.5. Electron microscopy images of L7-SZ2 well. Top: Aggregates of sediment and low levels of biological material in L7-SZ2 well. Bottom: L7-SZ2 well's aggregate of sediment and biological material - including vesicles, secondary mineral particles, virus particles, and what appears to be a pili-tethered ultra-small cell. Courtesy of Dr Peter Walian

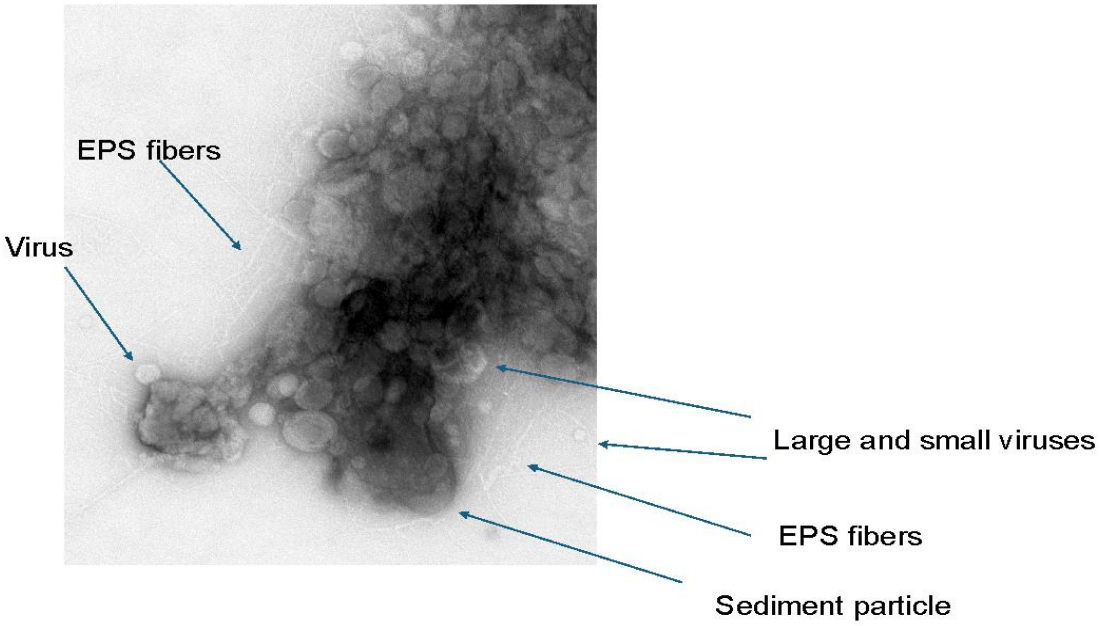

(A)

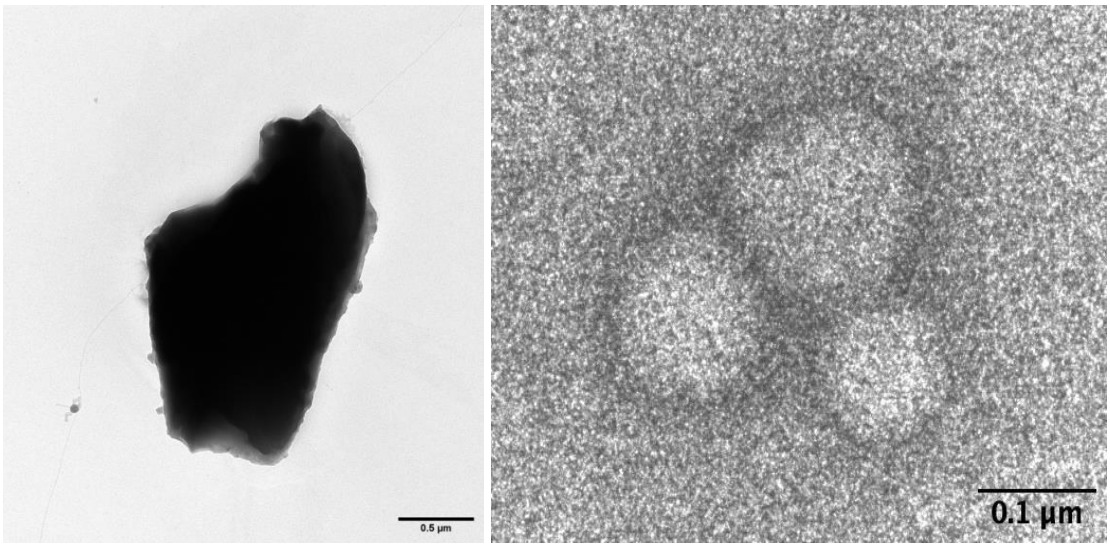

(B) (C)

Figure 3.6. Electron microscopy images of L7-SZ2, U2-SZ1, and M5-SZ2 well samples.

A: Sediment particles heavily coated with various forms of biological material (L7-SZ2 well). This aggregate appears to be more organic in nature than sediment. Large composite of potential necromass fragments and omvs, virus particles, and an assortment of extracellular polymeric fibers coating small pieces of sediment particle. **B**: U2-SZ1 well sample: very clean particle typical of the few others observed in this sample, the long fiber with phage attached. **C**. M5-SZ2 well sample: There are at least two objects that are likely to be virus particles and what might be a bacterium. Courtesy of Dr Peter Walian

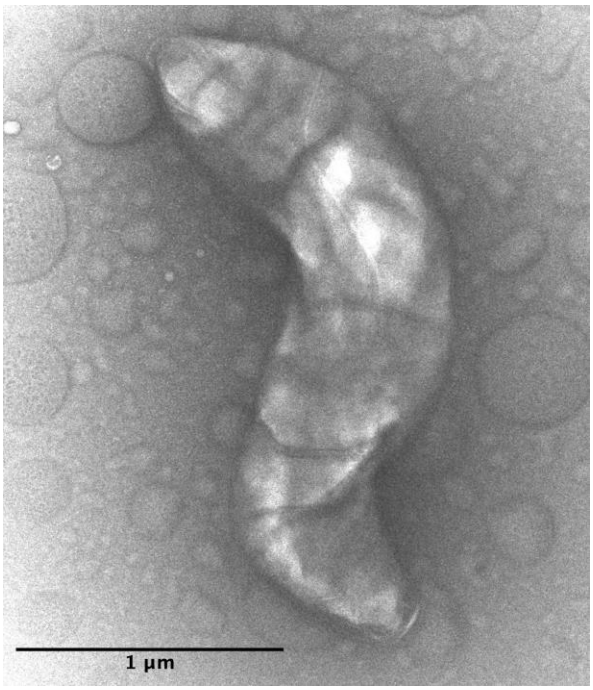

Figure 3.7. Electron microscopy image of M5-SZ2 well sample.

A shape that might be a *Vibrio* bacterium
Courtesy of Dr Peter Walian.

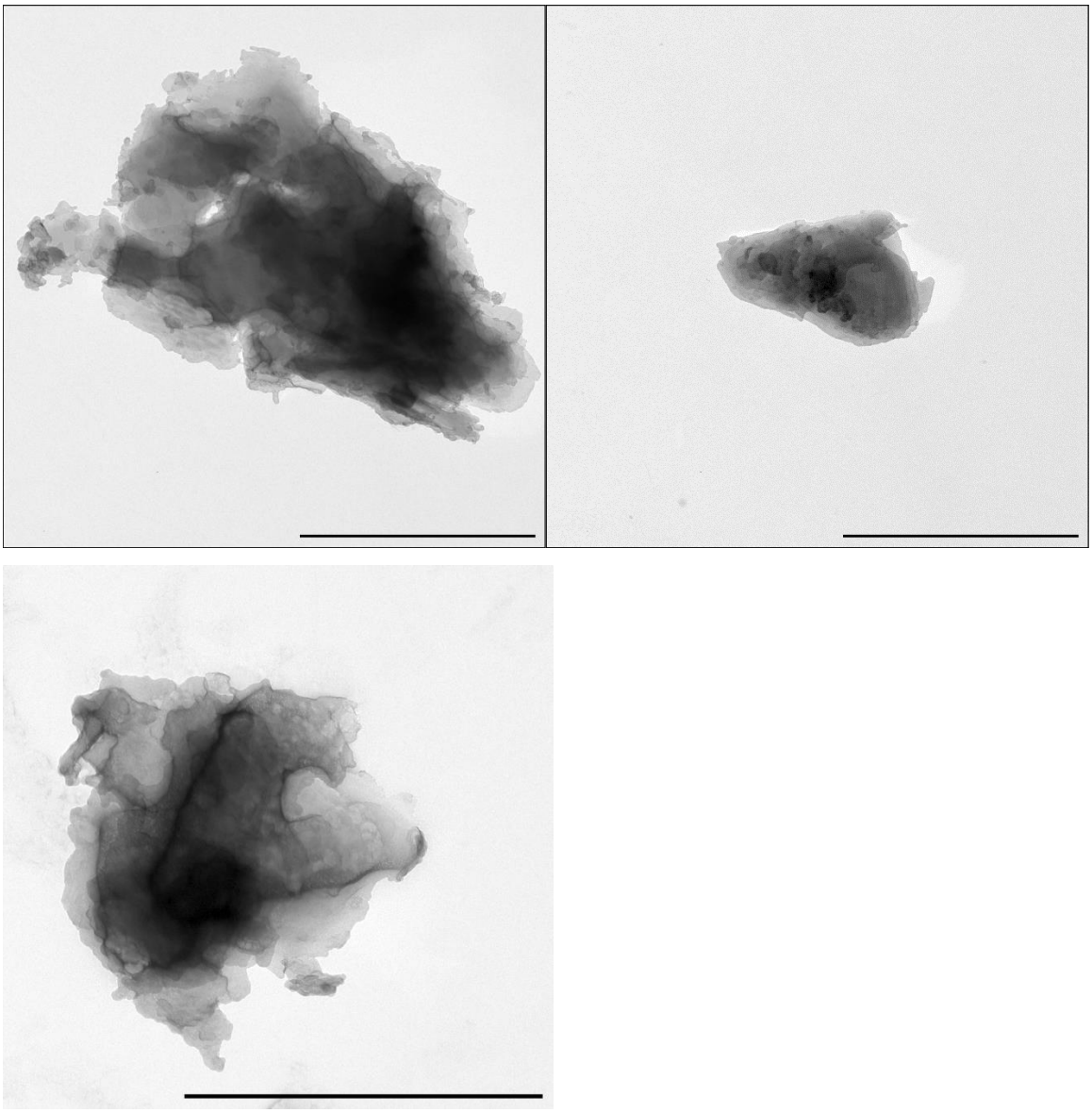

Figure 3.8. Electron microscopy images of L7-SZ2 sample

Sediment-only particles from L7-SZ2 water, (1-2 μm) size range, 1 μm scale bars
Courtesy of Dr Peter Walian.

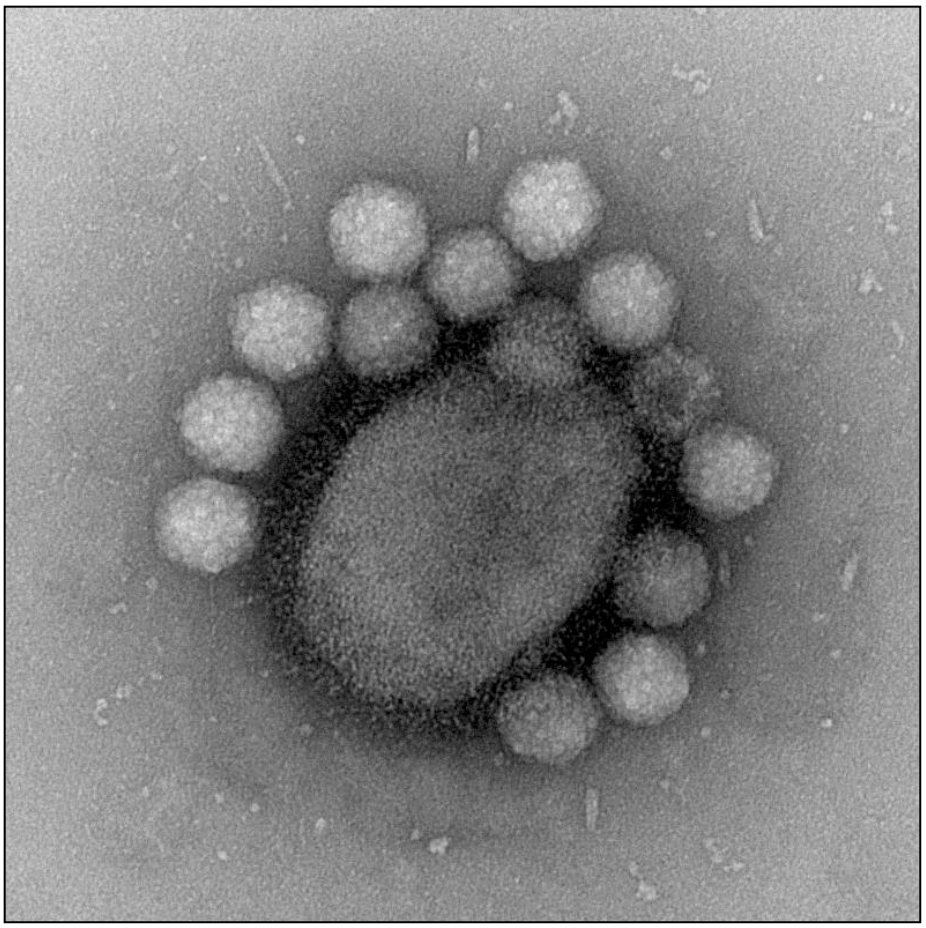

Figure 3.9. Electron microscopy image of MLS B6 well sample (Area 2).

Ultra-small cell with viruses: Cell - about 1.0 μm x 0.8 μm
Viruses - about 60 nm capsid
Courtesy of Dr Peter Walian

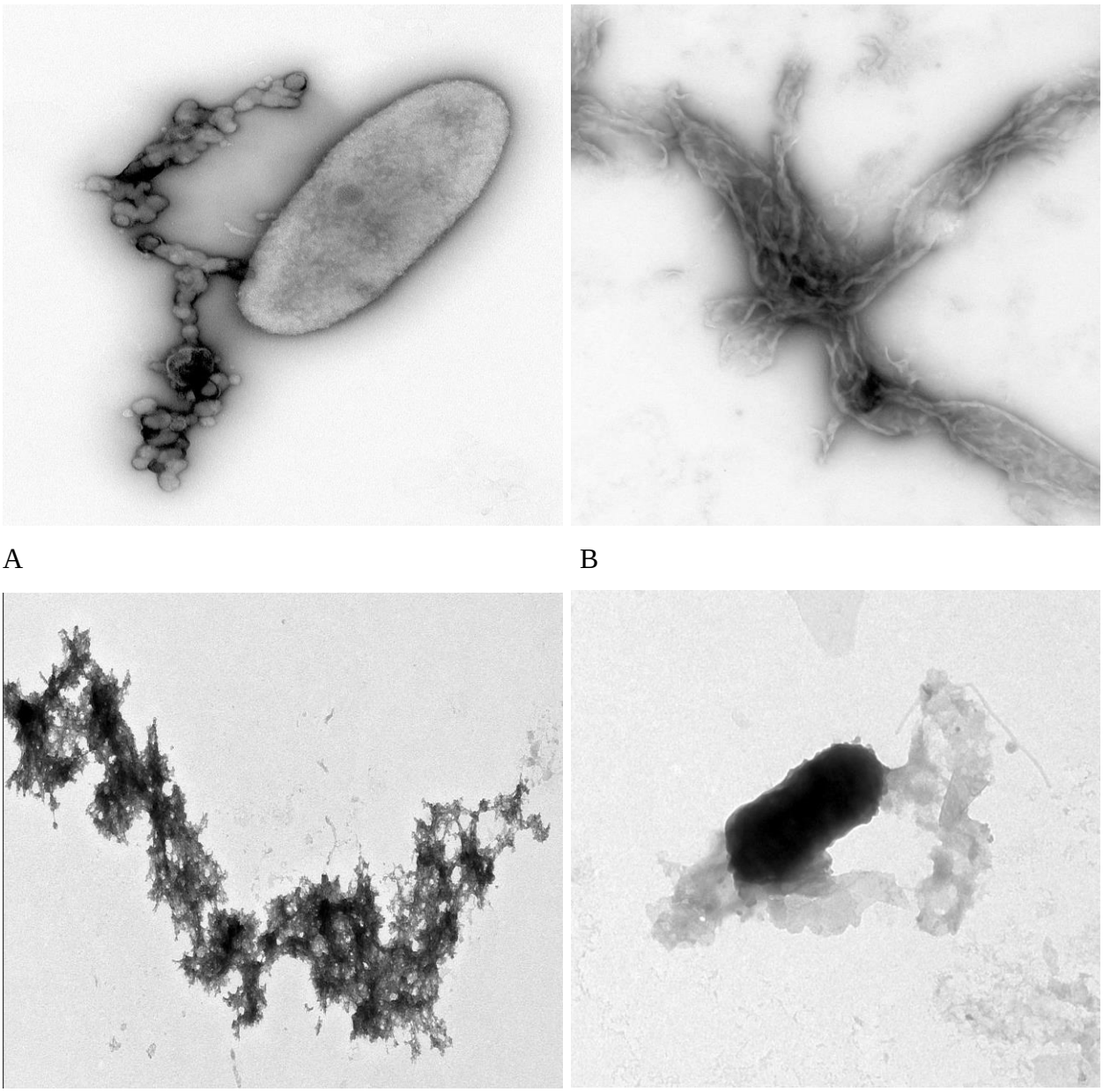

A B

C **D**

Figure 3.10. Electron microscopy images of U1 and U2 samples.

A. U2-SZ2 colloid rvs 0004 @10kx Secondary colloid, potentially cell-associated Spheres about 60 - 80 nm diam. **B**. U-1 0005 @ 10kx Lots of amorphous material, possibly plant and fungal in this view. **C**. U-2 0001 @10kx Sediment and bio aggregate**. D.** U-2 0005 @ 10kx Possible cell and sediment aggregate.
Courtesy of Dr Peter Walian.

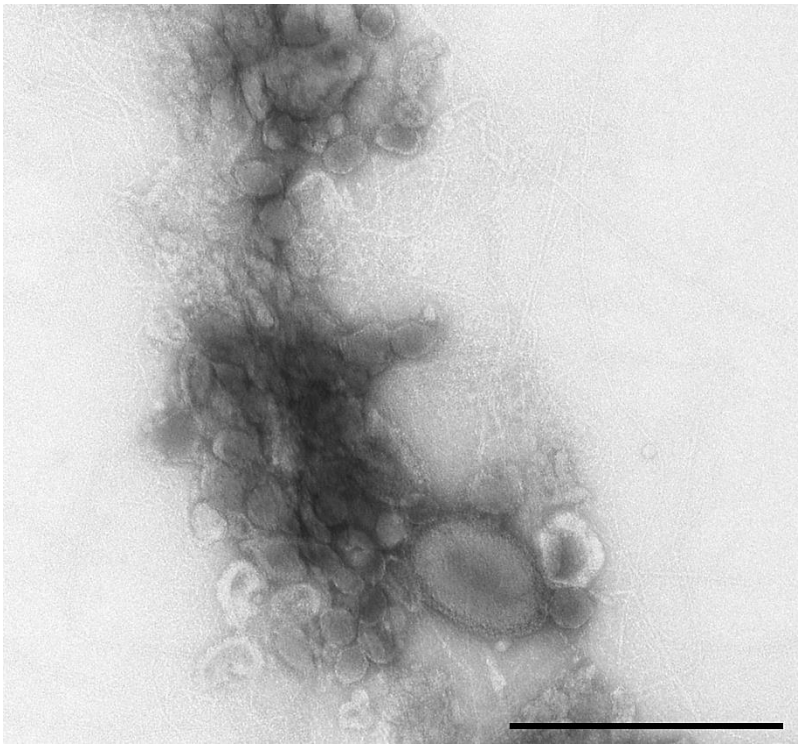

Figure 3.11. Electron microscopy image of L7-SZ2 well sample.

Bio only aggregate- in this case, the cell body is directly up against and surrounded by other vesicles and viruses within the aggregate. 0.5 μm scale bars showing that ultra-small cells can get entangled with or even incorporated into these aggregate types (L7 images).
Courtesy of Dr Peter Walian.

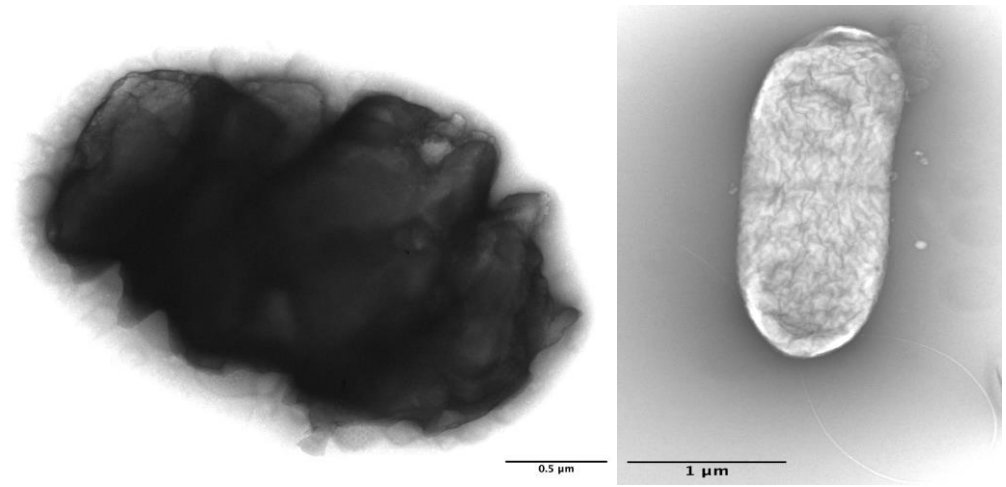

A **B**

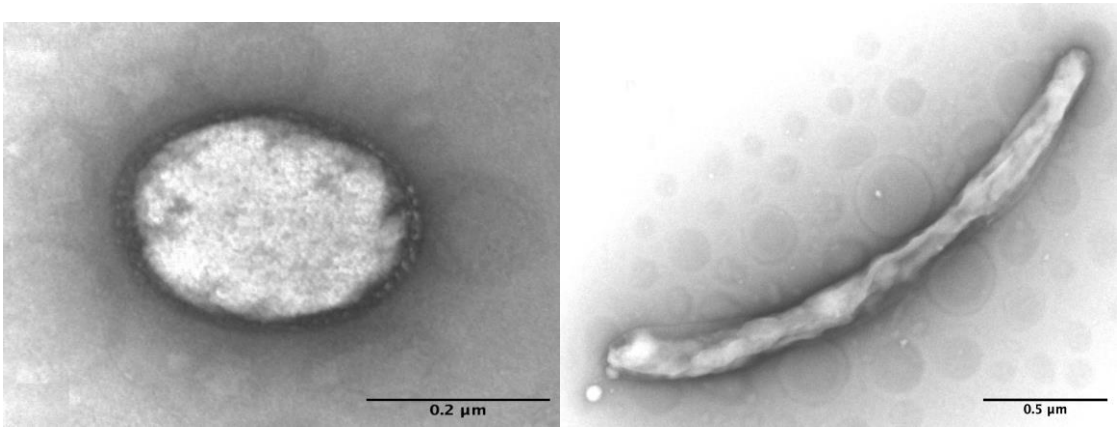

C **D**

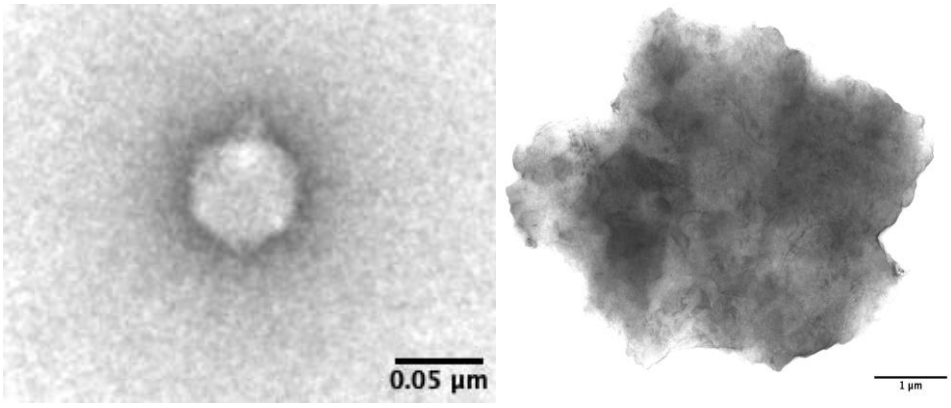

E **F**

Figure 3.12. Electron microscopy image of the L8-SZ2 well sample.

A. Relatively thick sediment particle (about 2.5 x 1.5 µm) with no discernible associated biological material. **B.** Large cell (about 2 x 0.7 µm) apparently preparing for division. **C**. Ultra-small cell (about 0.3 x 0.25 µm). **D.** Long narrow cell (about 3 x 0.2 µm). **E.** Putative podovirus (about 70 nanometers). **F.** Sediment particle (about 5 x 5 µm) with no associated biological material.

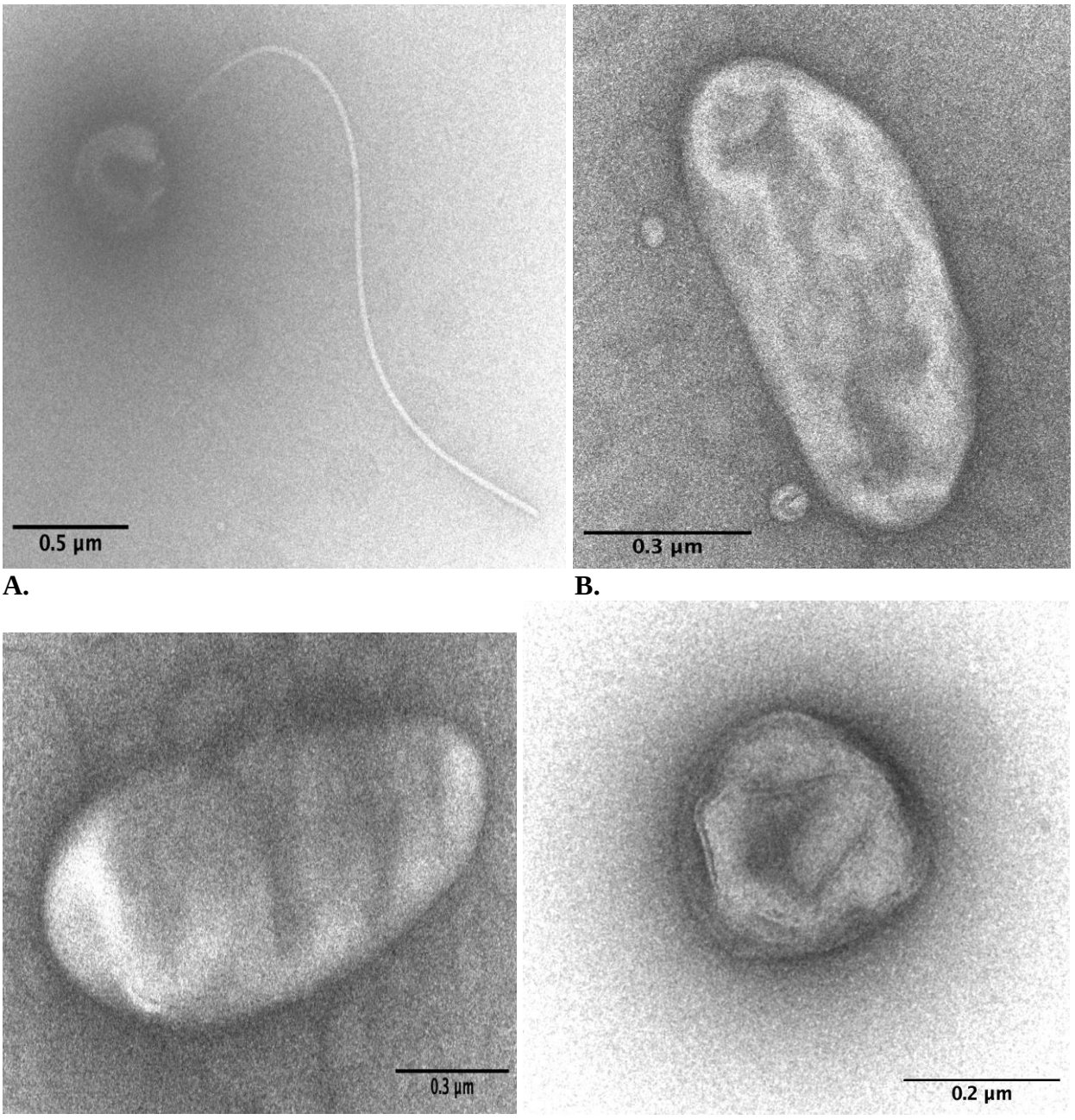

A. **B.**

C. **D.**

Figure 3.13. Electron microscopy image of the M5-SZ2 well sample.

A. Small cell (about 0.4 µm) with a single flagellum. **B.** Mid-range cell (about 0.8 x 0.4 µm). **C.** Large cell (about 1.2 x 0.7 µm). **D.** Ultra-small cell (about 0.25 µm).

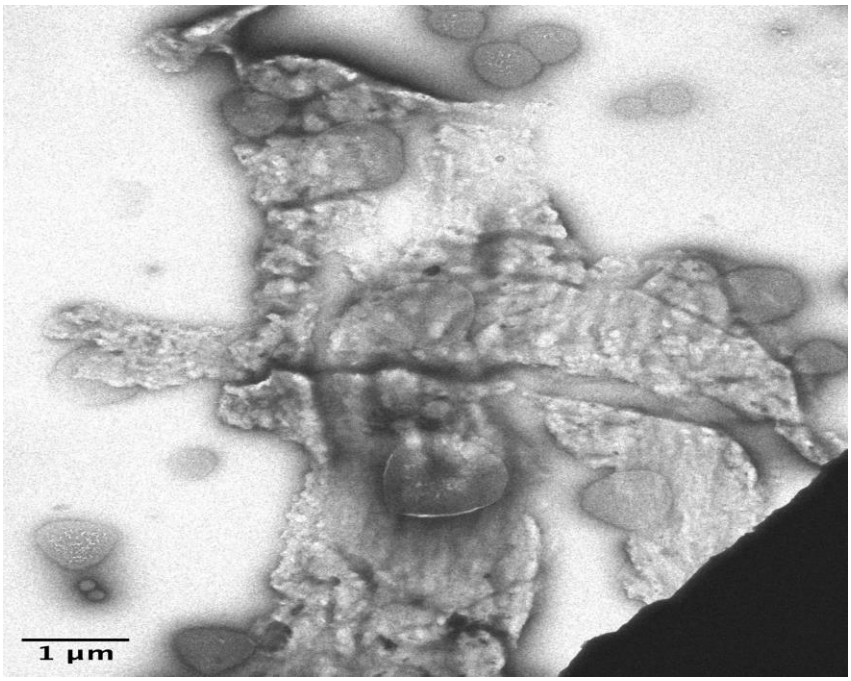

A.

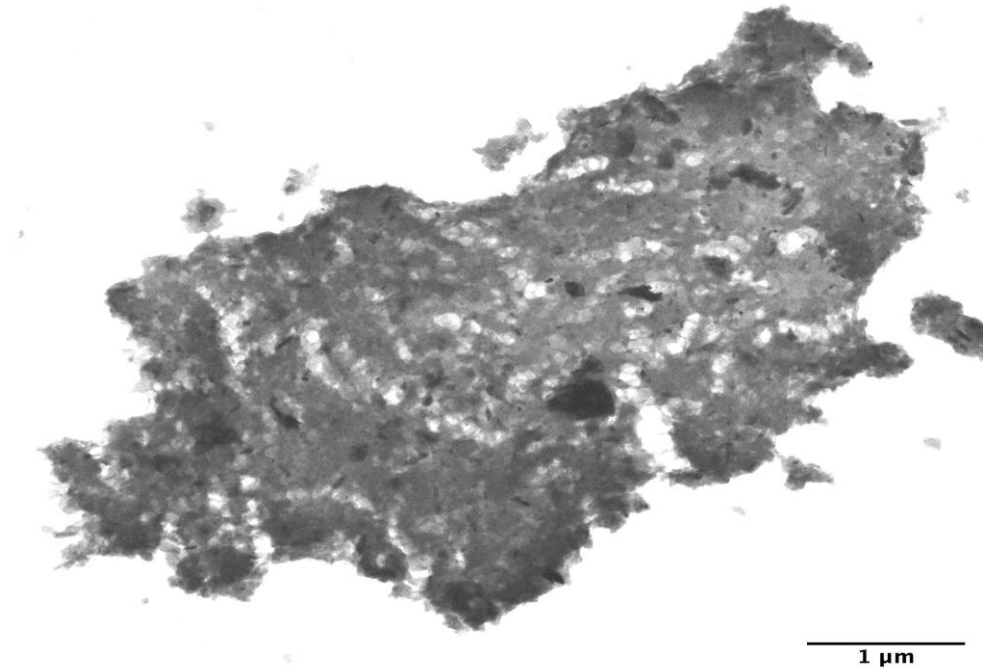

B.

Figure 3.14. Electron microscopy image of the U2-SZ2 sample.

A. Sediment particle with stain artifacts (triangle-like) with no associated biological material. **B.** Sediment fine particle aggregate about 6 x 4 µm with no biological material.

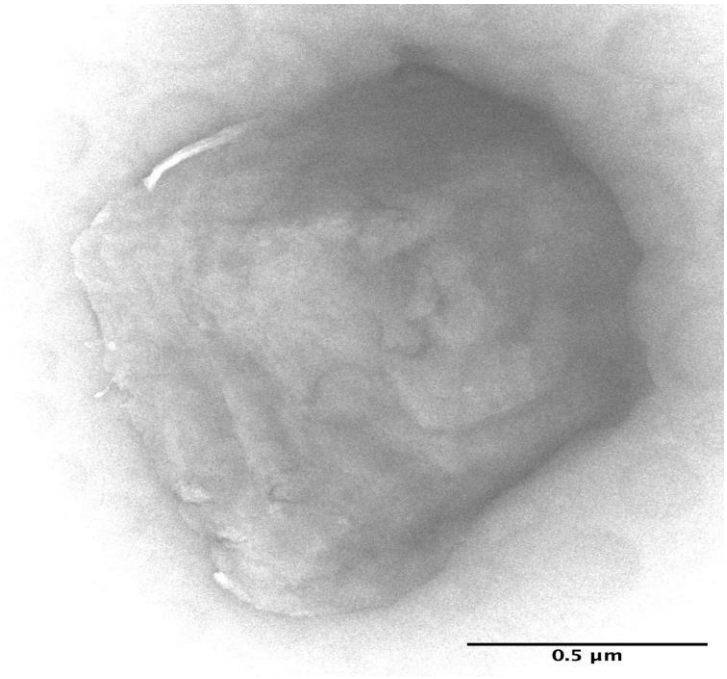

A.

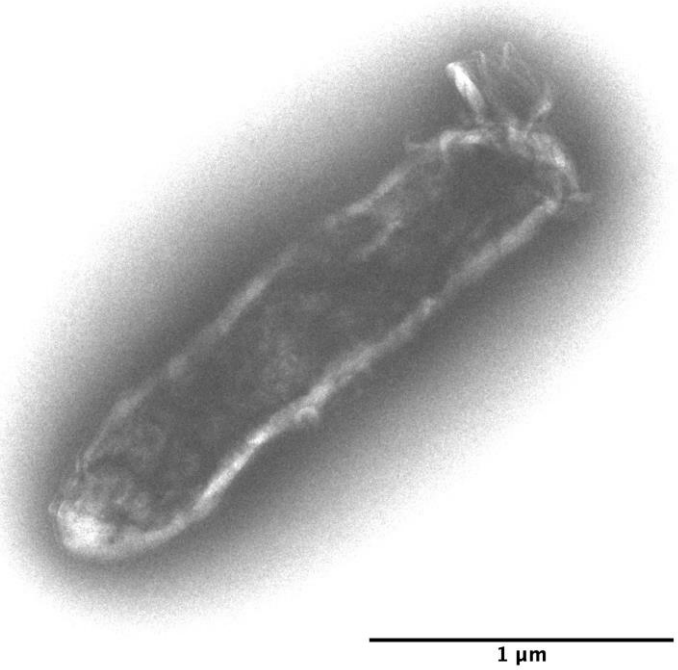

B.

Figure 3.15. Electron microscopy image of the EFP01 sample.

A. Likely a very small particle aggregate about 1 x 1 µm in size. **B.** Heavily stained, collapsed bacterial cell about 2.2 x 0.5 µm

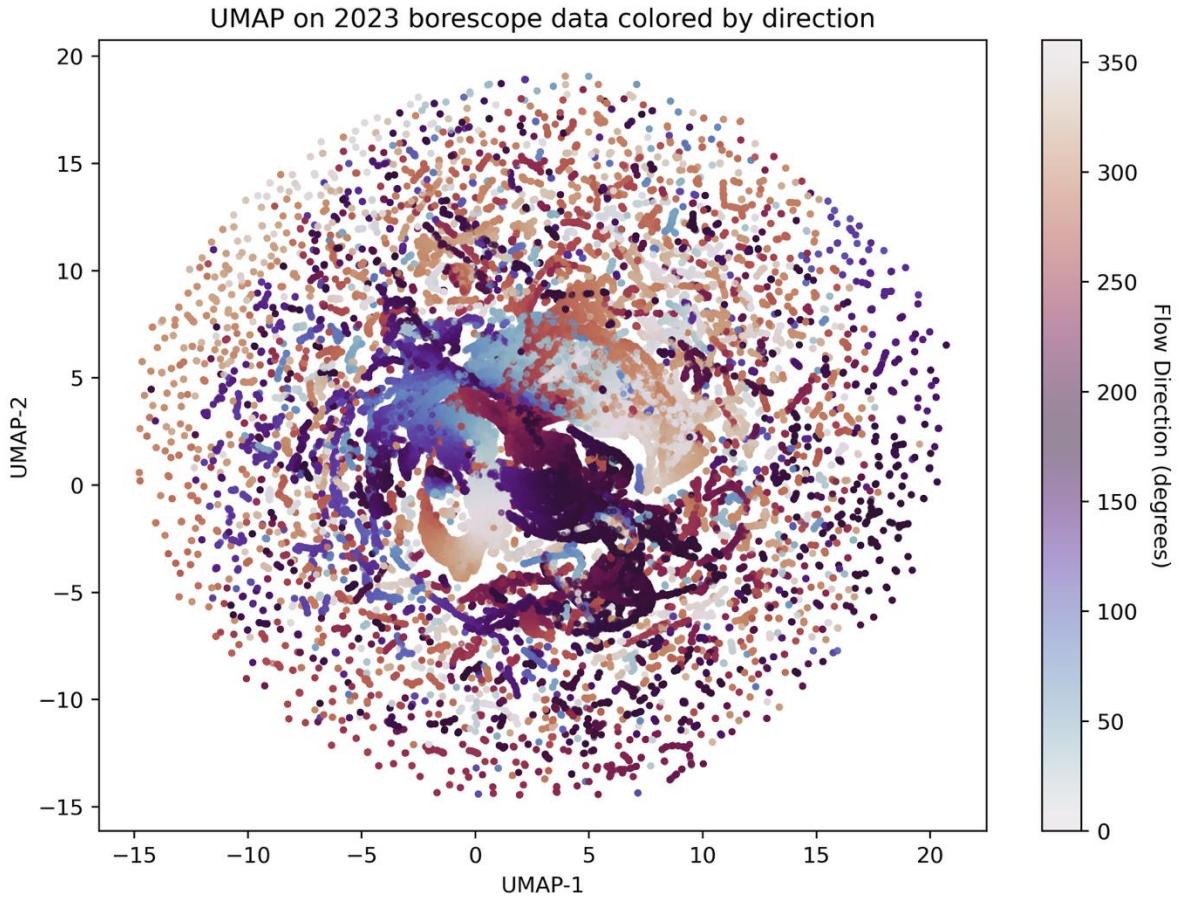

Figure 3.16. UMAP on 2023 borescope data colored by direction.

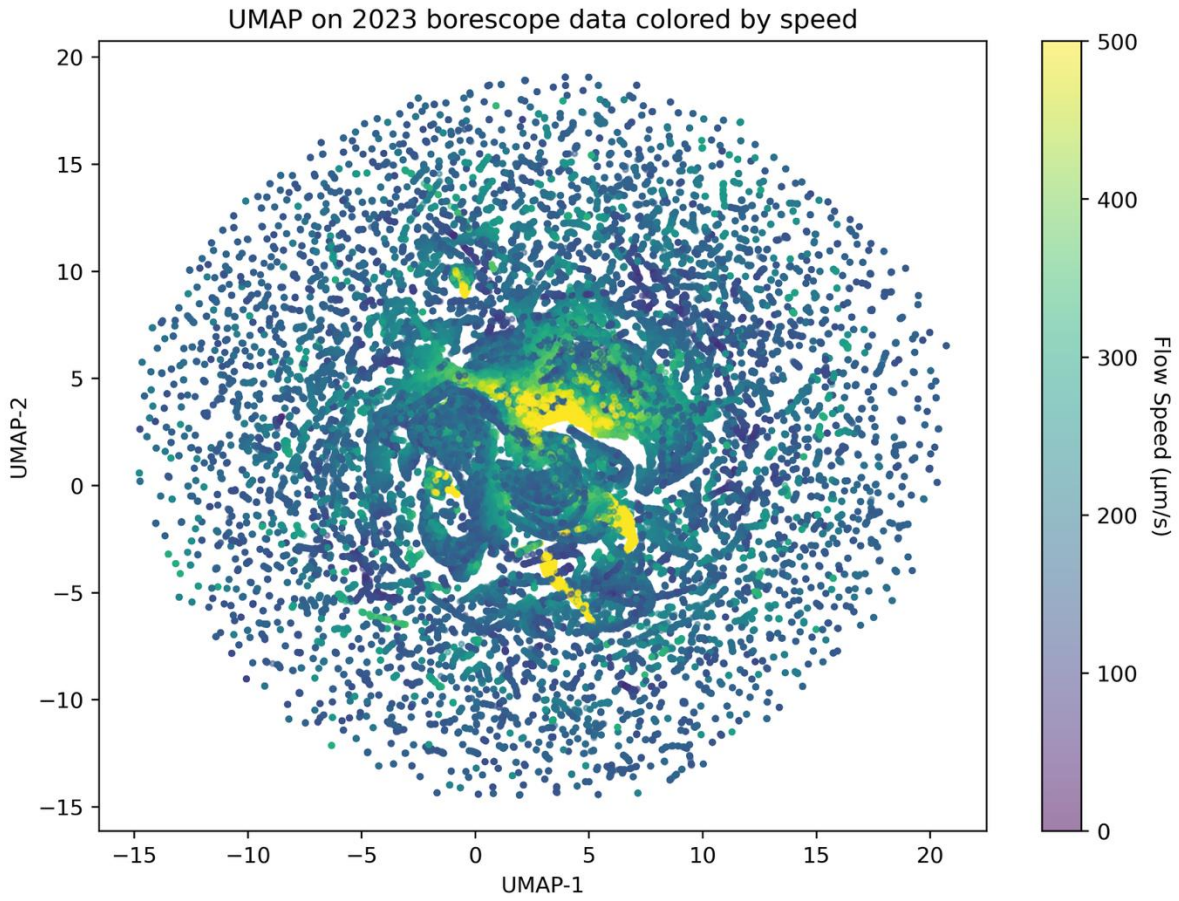

Figure 3.17. UMAP on 2023 borescope data colored by speed.

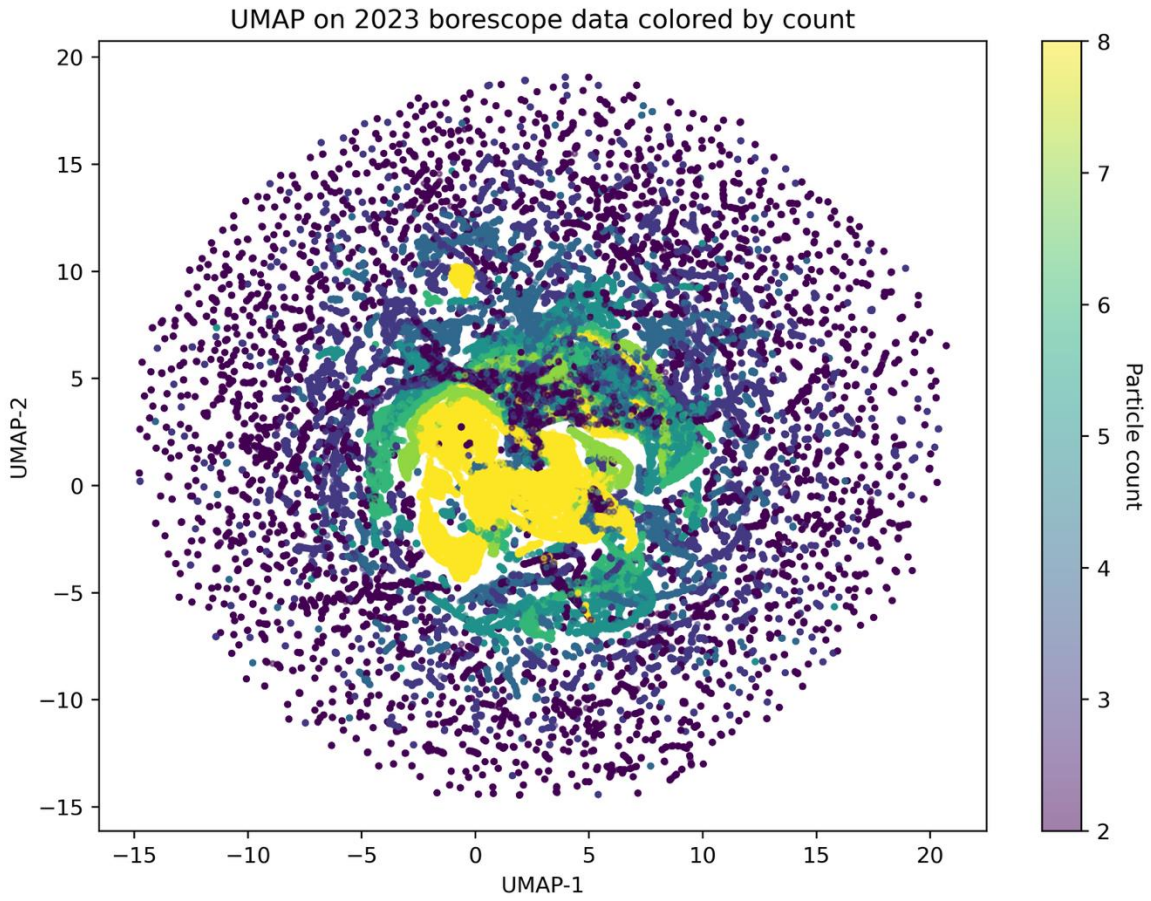

Figure 3.18. UMAP in 2023 borescope data colored by count.

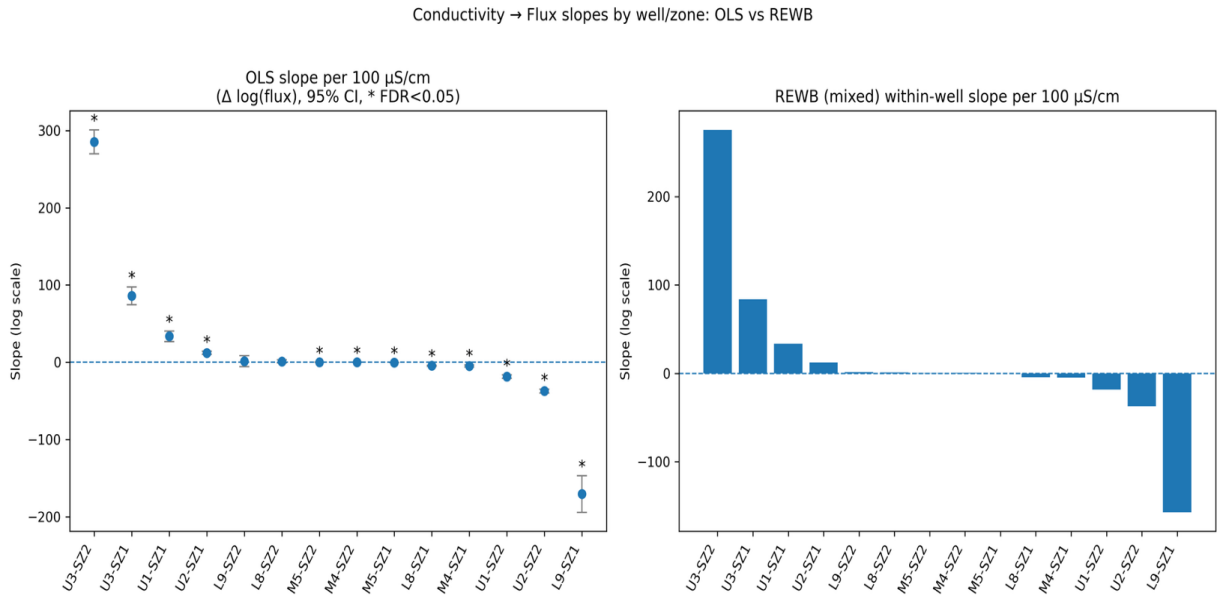

Figure 3.19. Flux slopes by well/zone: OLS vs REWB.

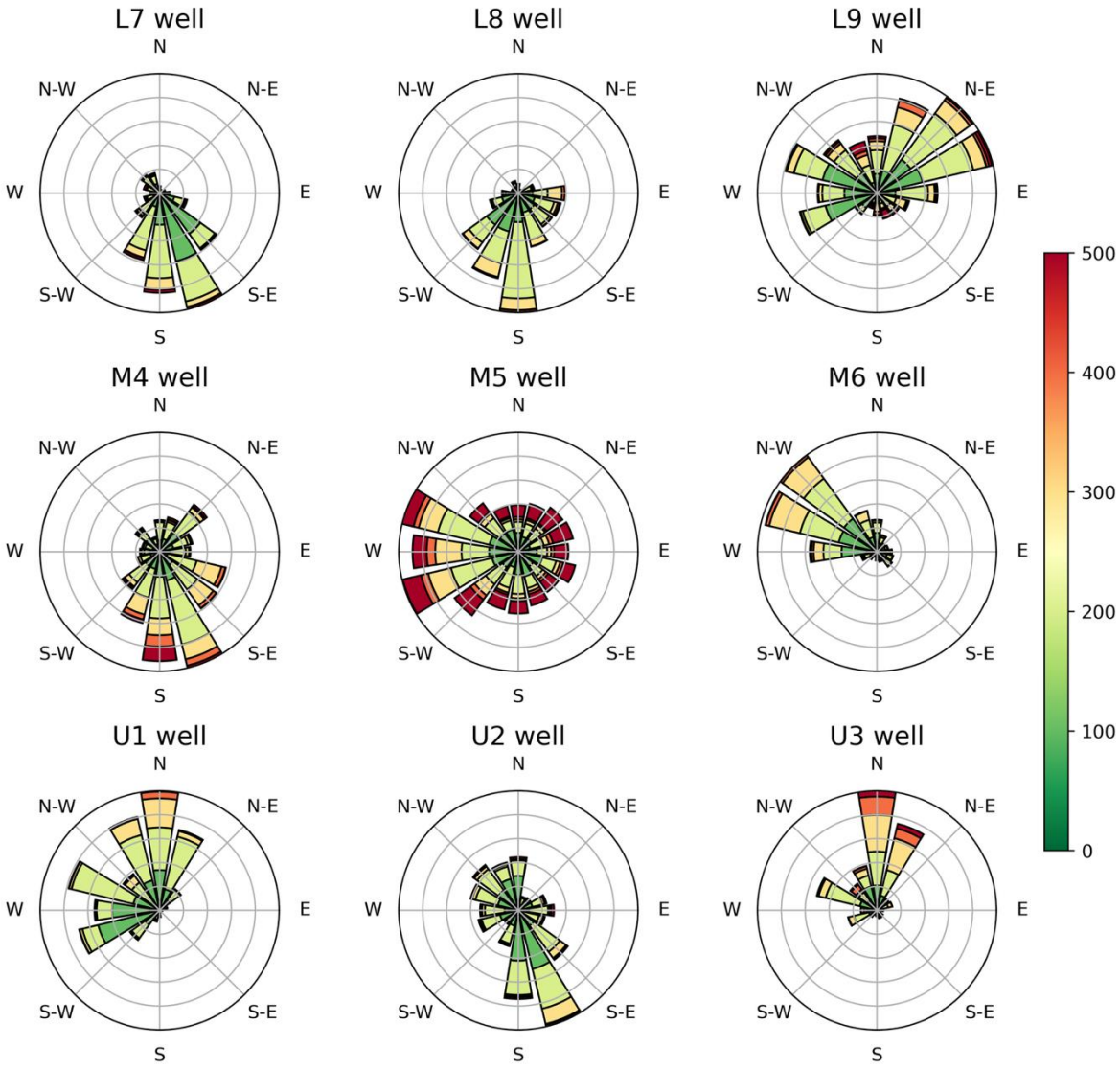

Figure 3.21. Wind Rose diagram of direction and speed in all 9 wells, all zones in SSO wells based on colloidal borescope, 2023. Flow velocity (µm/s) legend is on the right side.

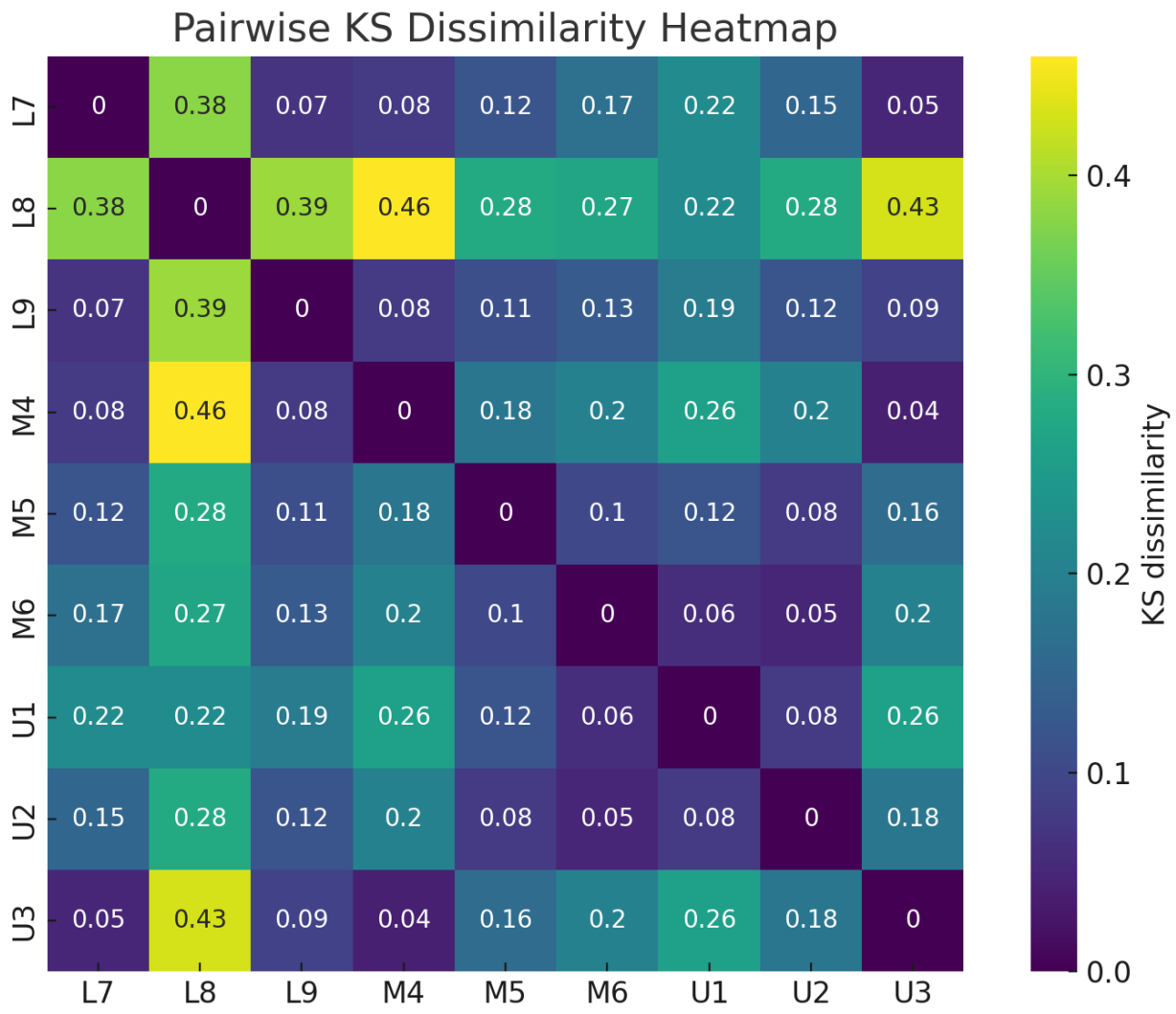

Figure 3.22. Pairwise KS Dissimilarity heatmap.

Pairwise dissimilarity values (darker=more dissimilar) L8 well has the highest dissimilarities (0.27-0.46) across most wells. The block of low dissimilarities (<0.15) is concentrated among L9, M4-M6 and U1-U2, indicating high similarity.

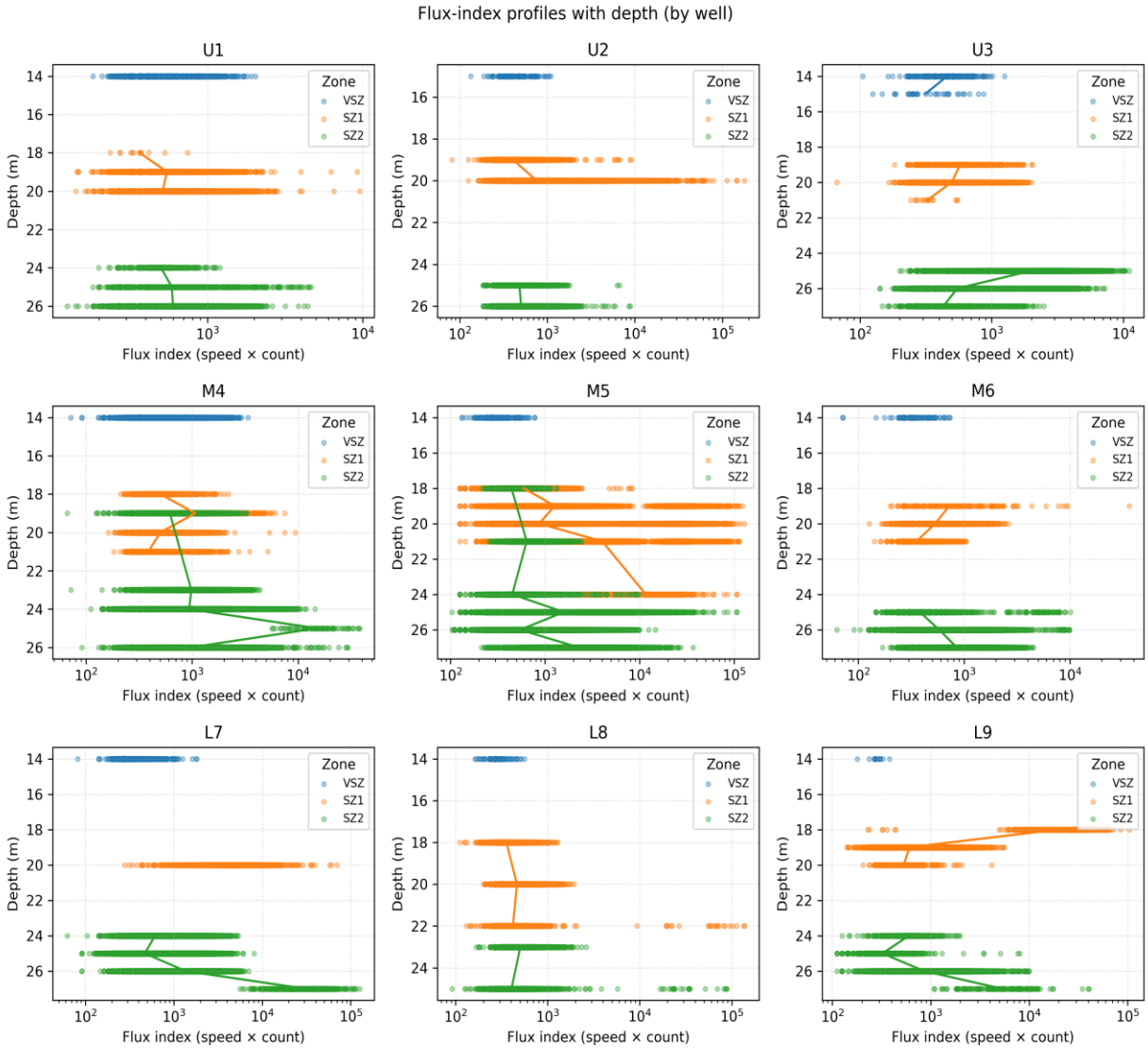

Figure 3.23. Flux-index profiles with depth across 9 SSO wells.

Colloidal borescope data 2023-2024. Flux index (speed of flow x colloid count) is plotted on a log scale against depth (m), with zones distinguished by color: VSZ (blue), SZ1 (orange), and SZ2 (green).

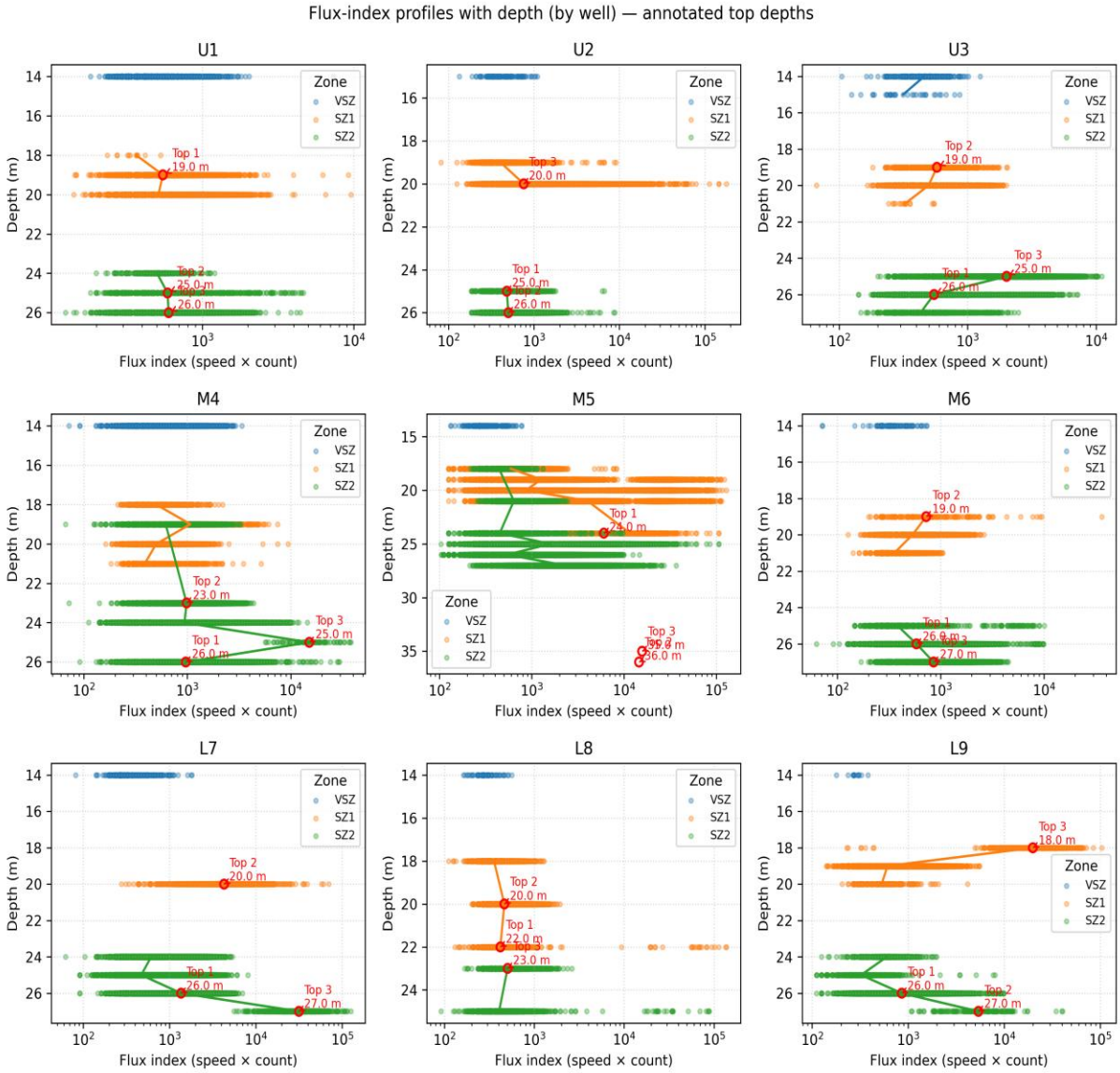

Figure 3.24. Flux-index profiles with depth across 9 SSO wells with annotated top depths.

Colloidal borescope data 2023-2024. Flux index (speed of flow x colloid count) is plotted on a log scale against depth (m), with zones distinguished by color: VSZ (blue), SZ1 (orange), and SZ2 (green).

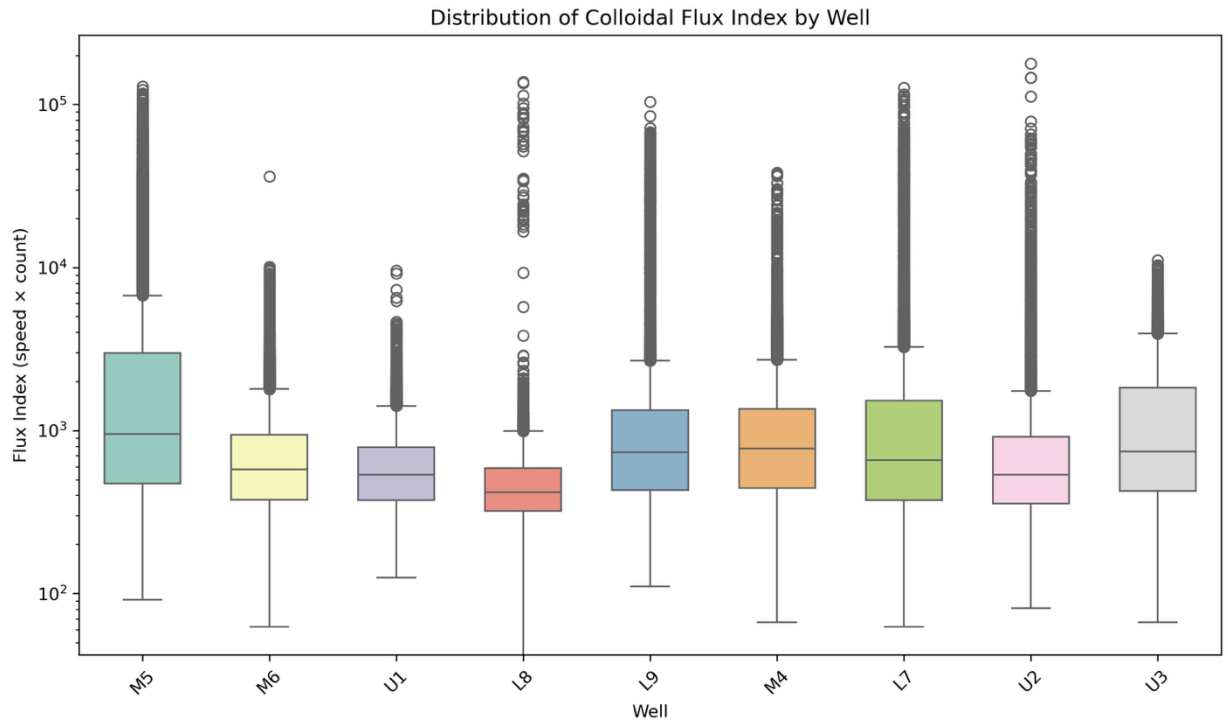

A

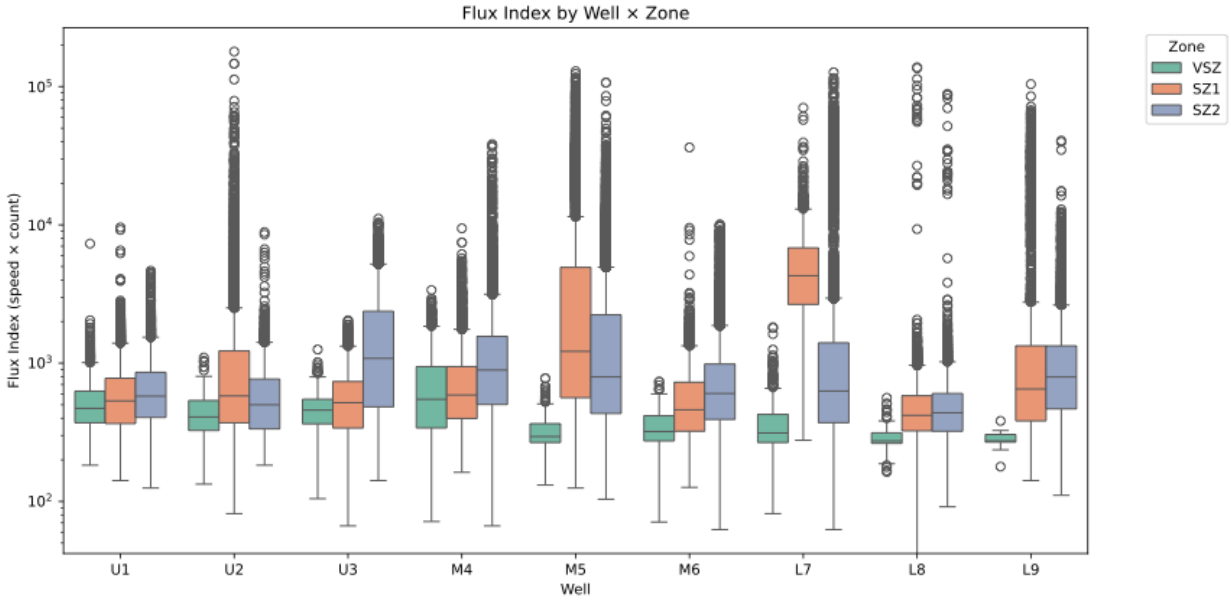

B

Figure 3.25. A: Distribution of colloidal flux index (speed x count) by well. B: Distribution of colloidal flux index (speed x count) by well and zone.

Appendix 3: Tables

Table 3.1. Total water and sediment collected and bottle preparation

		1:10 (10%sed.)	1:10 (10%sed.)	1:4 (25%sed.)	1:4 (25%sed.)	1:1 (50% sed.)	1:1 (50%sed.)	0% sed.
KBr conc.	Material	Bottles	Amount and bottle	Bottles	Amount and bottle	Bottles	Amount and bottle	Water for 2 bottles
10 mg and L	Sed. (g)	2	10	2	25	2	50	
10 mg and L	Tracer (ml)		90		75		50	200
100 mg and L	Sed. (g)	2	10	2	25	2	50	
100 mg and L	Tracer (ml)		90		75		50	200
0 mg and L	Sed. (g)	1	10	1	25	1	50	0
0 mg and L	FRC water (ml)		90		75		50	200
Total 125ml bottles	21	5		5		5		6
Total FRC sed.	425 g		50		125		250	

Table 3.1 Continued

Total FRC water	1675 ml		450		375		250	600

Table 3.2. Concentration and mass of KBr.

Concentration of KBr	Volume of FRC H_2O (ml)	Mass of KBr to add (grams)
0 mg and L	1000	0
10 mg and L	1000 (990)	10 mg
100 mg and L	1000 (900)	100 mg

Table 3.3. Natural Gradient Injection Wells

Bore	Area	Screen Interval (m)	Injectate volume (L)	Natural-gradient designation	Down-gradient wells
EFP02	3	3	500	Injection	EFP03, EFP04, EFP05, EFP06, FW012, FW013,
EFP03	3	3	500	Injection	EFP04, EFP05, EFP06, FW012, FW013

Table 3.4. Number of SSO wells at each depth (in feet) that have colloidal borescope data.

14 feet: ['L7' 'L8' 'L9' 'M4' 'M5' 'M6' 'U1' 'U3']
15 feet: ['U2' 'U3']
18 feet: ['L8' 'L9' 'M4' 'M5' 'U1']
19 feet: ['L9' 'M4' 'M5' 'M6' 'U1' 'U2' 'U3']
20 feet: ['L7' 'L8' 'L9' 'M4' 'M5' 'M6' 'U1' 'U2' 'U3']
21 feet: ['M4' 'M5' 'M6' 'U3']
22 feet: ['L8']
23 feet: ['L8' 'M4']
24 feet: ['L7' 'L9' 'M4' 'M5' 'U1']
25 feet: ['L7' 'L8' 'L9' 'M4' 'M5' 'M6' 'U1' 'U2' 'U3']
26 feet: ['L7' 'L9' 'M4' 'M5' 'M6' 'U1' 'U2' 'U3']
27 feet: ['L7' 'L9' 'M5' 'M6' 'U3']
28 feet: ['M5']
30 feet: ['M5']
31feet: ['M5']
32 feet: ['M5']
33 feet: ['M5']
34 feet: ['M5']
35 feet: ['M5']
36 feet: ['M5']

Table 3.5. Viruses on TEM images.

well	state	number of viruses per image
L8-SZ2	free	1
M5-SZ2	attached	1
M5-SZ2	free	1
L7-SZ2	attached	1
L7-SZ2	attached	5
L7-SZ2	both	3
U2-SZ1	attached	1
M5-SZ2	free	2
L7-SZ2	attached	2
L8-SZ2	free	1

Table 3.6. Pairwise flux-weighted directional contrasts between wells within SZ2, showing differences in mean transport orientation, directional concentration (R), and permutation test significance.

Well 1	Well 2	n1	n2	mean_dir_1_deg	mean_dir_2_deg	abs_delta mean_deg	R1	R2	P value
L7	L8	27380	3038	190.6	145.3	45.36	0.359	0.188	0.0005
L7	L9	27380	9002	190.6	348.4	157.76	0.359	0.265	0.0005
L7	M4	27380	15614	190.6	156.5	34.1	0.359	0.491	0.0005
L7	M5	27380	27841	190.6	346.4	155.75	0.359	0.022	0.0005
L7	M6	27380	23240	190.6	305.4	114.77	0.359	0.665	0.0005
L7	U1	27380	5293	190.6	356.3	165.64	0.359	0.752	0.0005
L7	U2	27380	4613	190.6	172.4	18.24	0.359	0.365	0.01949
L7	U3	27380	7551	190.6	356.3	165.7	0.359	0.805	0.0005
L8	L9	3038	9002	145.3	348.4	156.88	0.188	0.265	0.0005
L8	M4	3038	15614	145.3	156.5	11.26	0.188	0.491	0.003
L8	M5	3038	27841	145.3	346.4	158.89	0.188	0.022	0.04898
L8	M6	3038	23240	145.3	305.4	160.13	0.188	0.665	0.0005
L8	U1	3038	5293	145.3	356.3	149	0.188	0.752	0.0005
L8	U2	3038	4613	145.3	172.4	27.12	0.188	0.365	0.02799
L8	U3	3038	7551	145.3	356.3	148.94	0.188	0.805	0.0005
L9	M4	9002	15614	348.4	156.5	168.14	0.265	0.491	0.0005
L9	M5	9002	27841	348.4	346.4	2.01	0.265	0.022	0.92304
L9	M6	9002	23240	348.4	305.4	43	0.265	0.665	0.0005
L9	U1	9002	5293	348.4	356.3	7.88	0.265	0.752	0.0035
L9	U2	9002	4613	348.4	172.4	176	0.265	0.365	0.0005
L9	U3	9002	7551	348.4	356.3	7.94	0.265	0.805	0.0005
M4	M5	15614	27841	156.5	346.4	170.15	0.491	0.022	0.0005
M4	M6	15614	23240	156.5	305.4	148.87	0.491	0.665	0.0005
M4	U1	15614	5293	156.5	356.3	160.26	0.491	0.752	0.0005
M4	U2	15614	4613	156.5	172.4	15.86	0.491	0.365	0.0005
M4	U3	15614	7551	156.5	356.3	160.2	0.491	0.805	0.0005
M5	M6	27841	23240	346.4	305.4	40.99	0.022	0.665	0.0005
M5	U1	27841	5293	346.4	356.3	9.89	0.022	0.752	0.6007
M5	U2	27841	4613	346.4	172.4	173.99	0.022	0.365	0.03848
M5	U3	27841	7551	346.4	356.3	9.95	0.022	0.805	0.13643
M6	U1	23240	5293	305.4	356.3	50.88	0.665	0.752	0.0005

Table 3.6 Continued

M6	U2	23240	4613	305.4	172.4	133	0.665	0.365	0.0005
M6	U3	23240	7551	305.4	356.3	50.94	0.665	0.805	0.0005
U1	U2	5293	4613	356.3	172.4	176.12	0.752	0.365	0.0005
U1	U3	5293	7551	356.3	356.3	0.06	0.752	0.805	0.93253
U2	U3	4613	7551	172.4	356.3	176.06	0.365	0.805	0.0005

Table 3.7. Pairwise Kolmogorov-Smirnov test.

L7 and L8 have a KS dissimilarity of 0.38 with a $p < 0.001$
L7 and L9 have a KS dissimilarity of 0.07 with a $p < 0.001$
L7 and M4 have a KS dissimilarity of 0.08 with a $p < 0.001$
L7 and M5 have a KS dissimilarity of 0.12 with a $p < 0.001$
L7 and M6 have a KS dissimilarity of 0.17 with a $p < 0.001$
L7 and U1 have a KS dissimilarity of 0.22 with a $p < 0.001$
L7 and U2 have a KS dissimilarity of 0.15 with a $p < 0.001$
L7 and U3 have a KS dissimilarity of 0.05 with a $p < 0.001$
L8 and L9 have a KS dissimilarity of 0.39 with a $p < 0.001$
L8 and M4 have a KS dissimilarity of 0.46 with a $p < 0.001$
L8 and M5 have a KS dissimilarity of 0.28 with a $p < 0.001$
L8 and M6 have a KS dissimilarity of 0.27 with a $p < 0.001$
L8 and U1 have a KS dissimilarity of 0.22 with a $p < 0.001$
L8 and U2 have a KS dissimilarity of 0.28 with a $p < 0.001$
L8 and U3 have a KS dissimilarity of 0.43 with a $p < 0.001$
L9 and M4 have a KS dissimilarity of 0.08 with a $p < 0.001$
L9 and M5 have a KS dissimilarity of 0.11 with a $p < 0.001$
L9 and M6 have a KS dissimilarity of 0.13 with a $p < 0.001$
L9 and U1 have a KS dissimilarity of 0.19 with a $p < 0.001$
L9 and U2 have a KS dissimilarity of 0.12 with a $p < 0.001$
L9 and U3 have a KS dissimilarity of 0.09 with a $p < 0.001$
M4 and M5 have a KS dissimilarity of 0.18 with a $p < 0.001$
M4 and M6 have a KS dissimilarity of 0.2 with a $p < 0.001$
M4 and U1 have a KS dissimilarity of 0.26 with a $p < 0.001$
M4 and U2 have a KS dissimilarity of 0.2 with a $p < 0.001$
M4 and U3 have a KS dissimilarity of 0.04 with a $p < 0.001$
M5 and M6 have a KS dissimilarity of 0.1 with a $p < 0.001$

Table 3.7 Continued

M5 and U1 have a KS dissimilarity of 0.12 with a $p < 0.001$
M5 and U2 have a KS dissimilarity of 0.08 with a $p < 0.001$
M5 and U3 have a KS dissimilarity of 0.16 with a $p < 0.001$
M6 and U1 have a KS dissimilarity of 0.06 with a $p < 0.001$
M6 and U2 have a KS dissimilarity of 0.05 with a $p < 0.0010$
M6 and U3 have a KS dissimilarity of 0.2 with a $p < 0.001$
U1 and U2 have a KS dissimilarity of 0.08 with a $p < 0.001$
U1 and U3 have a KS dissimilarity of 0.26 with a $p < 0.001$
U2 and U3 have a KS dissimilarity of 0.18 with a $p < 0.001$

Chapter IV Microbial Characterization at eFRC Site

Abstract

Analyzing the microbial community structure in groundwater at the Y-12 National Security Complex, a historic nuclear site associated with the Manhattan Project, is essential for understanding contaminant behavior and the impacts of contamination on microbial geochemical cycling, predicting groundwater geochemistry, and supporting environmental monitoring. Currently, the microbial community in contaminated areas at this legacy site attracts significant attention in the U.S. DOE Science Focus Area ENIGMA (Ecosystems and Networks Integrated with Genes and Molecular Assemblies) - a multidisciplinary, multi-institutional research effort addressing foundational knowledge gaps in groundwater and sediment microbiomes at the U.S. Department of Energy ENIGMA Field Research Center (eFRC) at the Y-12 National Security Complex in Oak Ridge, Tennessee. We used *Rhodanobacter denitrificans* and Patescibacteria *spp.* as key case studies. We hypothesized that microbial communities differ among ENIGMA subsurface observatory wells (SSO wells), arranged in a 3x3 grid, designated as Upper (U), Middle (M), and Lower (L) from north to south. To our knowledge, this study represents the first metagenomic analysis of saturated Zone 2 SSO wells, including the identification and taxonomic classification of viral contigs using geNomad. We examined three wells (U2-SZ2, M5-SZ2, L8-SZ2) representing contrasting contamination gradients, integrating 16S rRNA amplicon data, metagenome-assembled genomes (MAGs), and geochemical measurements. Microbial communities exhibited significant compositional differences among wells (PERMANOVA pseudo-F = 9.74, p = 0.001) and were closely linked to geochemical gradients (Mantel r = 0.628, p = 0.001). Random forest models accurately captured ordination structure (PC1 cvR^2= 0.93), with tungsten, zirconium, boron, cadmium, magnesium, manganese, and uranium emerging as the strongest predictors. Colloids, by themselves, were only weakly related to community composition; however, a partial Mantel test revealed a significant, independent positive association when geochemistry was controlled for (p = 0.016). Mobile genetic elements were abundant, and viromes were dominated by *Caudoviricetes*, pointing to high potential for horizontal gene transfer and colloid-facilitated dispersal.

Introduction

Groundwater microorganisms perform essential ecological functions, including nutrient cycling, the breakdown of organic matter, and the degradation of pollutants (Griebler and Lueders, 2009). However, human activities introduce harmful contaminants that disrupt these microbial systems, threatening aquifer integrity and long-term water quality. Subsurface aquifers store nearly one-third of the planet's accessible freshwater, a critical resource. Yet groundwater is highly vulnerable to pollution, which degrades drinking water safety, reduces supply availability, increases treatment costs, and poses health risks. Among contaminants, nitrate is particularly widespread and problematic. In nitrate-polluted aquifers, microbial diversity becomes severely depleted, especially when combined with low pH and other toxins. In the U.S., millions are exposed to groundwater exceeding the EPA's 10 mg and L nitrate safety limit, a concentration linked to acute health effects.

Nuclear legacy sites can represent significant sources of contamination. From 1951 to 1983, nuclear waste from the Y-12 heavy metals processing plant was deposited in unlined S-3 ponds. This waste was acidic (pH < 2) and contained uranium and other metals dissolved in nitric acid. In June 1983, the S-3 ponds were neutralized. Despite this, the surrounding area still has the highest groundwater nitrate concentrations globally, ranging from 0 to 14,000 mg and L (Pettenato, 2014), which is ten thousand times above the U.S. EPA's drinking water standards. Since the groundwater in the S-3 ponds Area 3 is near the contamination source, it can contain high concentrations of radionuclides (uranium), salts, organics, and metals (Ni, Cu, Al, Mn, Fe, Co, Cd) (Thorgersen et al., 2019). Under these conditions, the microbial community is minimal and lacks diversity.

To address these issues, understanding *in situ* biogeochemical cycling processes and developing effective *in situ* action plans to improve and protect groundwater are essential (Smith et al., 2015). *Rhodanobacter* sp. has garnered global scientific interest due to its resistance to extreme conditions and its denitrification capabilities (Cardenas et al., 2010; Chakraborty et al., 2014; Deutschbauer et al.; Green et al., 2010; Hemme et al., 2015). *Rhodanobacter denitrificans* and Patescibacteria were used as a case study.

Overview of *R. denitrificans* Bacteria

Rhodanobacter sp. was first studied by Nalin and others (Nalin et al., 1999). It belongs to the family Xanthomonadaceae, order Xanthomonadales, and class Gammaproteobacteria

within the phylum Proteobacteria. It is a Gram-negative, oxidase- and catalase-positive, rod-shaped bacterium that serves as an indicator of site contamination (Carlson et al., 2018; Koh et al., 2015). *R. denitrificans* has been observed in the most contaminated wells at the eFRC site, where pH is low and nitrate and uranium concentrations are higher than those of other contaminants (Green et al., 2012). In their research, Prakash and colleagues (Prakash et al., 2021) studied the stress tolerance of the *Rhodanobacter* genus. The studied strains tolerated low pH, high uranium (1 mmol/L), and high nitrate levels (400 mmol/L). They found that these extreme conditions are likely responsible for the presence and dominance of *Rhodanobacter* at the eFRC site. High nitrate levels, high metal presence, low pH, and anoxic conditions create the best environment for *Rhodanobacter* abundance. Under less extreme conditions, the abundance of *Rhodanobacter* decreases significantly (Green et al., 2012). Also, shallow wells in porous media are the most sensitive to contamination, like the SSO wells. Similarly, high nitrate levels, the presence of metals, low pH, and anoxic conditions favor the abundance of *R. denitrificans*.

R. denitrificans in eFRC Area 3 compared to other sites

Rhodanobacter bacteria dominate the most contaminated wells at the S-3 ponds in the Y-12 National Security Complex 1, 2, and 3, which are characterized by low pH, high nitrate, and high uranium concentrations. *Rhodanobacter* is recognized as an indicator of contamination at the site (Carlson et al., 2018). An overabundance of recombination and DNA repair processes was found in the FW-106 well at the eFRC site, suggesting that the development of resistance and stress response genes is a key survival strategy for the microbial community (Hemme et al., 2010). The availability of anaerobic terminal electron acceptors (nitrate), the absence of fermentation communities, and extremely low but detectable dissolved oxygen levels (0.26 mg/L) indicate that the respiratory community primarily derives energy from denitrification (Hemme et al., 2010). Our primary focus was on *Rhodanobacter's* denitrification capabilities at the eFRC compared to those at other locations. (Lycus et al., 2017) found that *Rhodanobacter* isolates decreased nitrous oxide at low pH. They also noted that all knowledge of denitrification is based solely on studies of a few model organisms, including *Rhodanobacter*. They also discovered that *Rhodanobacter* possesses a wide range of regulatory mechanisms involved in denitrification. Their study revealed that *Rhodanobacter* could act as both a sink and a source for nitrous oxide. The site of their study was on two agricultural peat soils with pH levels of 3.7 and 7.4. Interestingly, none of their *Rhodanobacter* isolates had nitrate reductase genes. The

denitrification process is generally affected by four main genes: nitrate reductase, nitrite reductase, nitric-oxide reductase, and nitrous oxide reductase (Peng et al., 2022). *R. denitrificans* isolates from two agricultural peat sites (pH 3.7 and 7.4) were found to decrease nitrous oxide at low pH (Lycus et al., 2017).

We searched the Integrated Microbial Genomes and Microbiomes (IMG and M) system (U.S.DOE, 2022), specifically for protein-coding genes associated with KEGG pathways and examined energy metabolism and nitrogen metabolism. We found the following: IMG and M contains 11 *R. denitrificans* genomes extracted from the uranium- and nitrate-contaminated subsurface at the eFRC, each containing genes for nitrate reductase. Among 34 *Rhodanobacter* genomes, only 3 genome names have nitrate reductase genes: *Rhodanobacter sp.* KS-T3 (lab-enriched sediment microbial communities from Bremen, Germany), *R. thiooxydans* LCS2 (agricultural, isolated from biofilm in South Korea), *Rhodanobacter sp.* genome from NDFO enrichment metagenome (UT) (draft genomes from nitrate-dependent iron-oxidizing enrichment culture). These findings indicate that all 11 *Rhodanobacter spp.* genomes from the eFRC (IMG) contain nitrate reductase genes (Berks et al., 1995). Lateral gene transfer has been identified as the main evolutionary mechanism facilitating rapid adaptation in stressed soil communities. An evolutionary assessment of groundwater from many wells in Area 3 at eFRC revealed that lateral gene transfer contributes to rapid adaptation to contamination. Heavy metal-resistant genes are known to transfer readily among species. Gene transfer may occur via plasmids, which can expedite bacterial evolution by promoting the development of plasmid-encoded genes, thereby enhancing the adaptation of their host chromosomes (Rodríguez-Beltrán et al., 2021). Nitrate reductase is a flavoprotein enzyme that requires molybdenum as its only metal requirement (Berks et al., 1995; Campbell, 1996). While nitrate reductase requires molybdenum at its active site, iron and copper are involved in other enzymes that catalyze the reduction of nitrate to nitrite and then to nitrogen gas (Thorgersen et al., 2015).

Hemme and others (Hemme et al., 2010) additionally found that DNA recombination and repair are overabundant in Area 3 at the eFRC site. Therefore, establishing resistance and stress response genes is a fundamental survival strategy for the microbial community. The availability of anaerobic terminal electron acceptors (nitrate), the absence of a fermentation community, and an extremely low but detectable dissolved oxygen level (0.26 mg/L) indicate that the respiratory community primarily obtains energy from denitrification (Hemme et al., 2010).

Previous ENIGMA surveys were conducted to evaluate microbial communities at the Y-12 National Security Complex, specifically in Areas 1, 2, and 3, including the 100-well survey (Smith et al., 2015) and 27-well survey (Walker, 2024). The 100-well survey indicated that, among the studied wells, *Rhodanobacter* has the highest relative abundance in the FW106 well, at 111.267 cells/ml (**Figures 4.1** and **4.2**). The 27-well survey results (Walker, 2024) correlated with those of the 100-well survey (Smith et al., 2015). The 100-well survey showed significant variability in abundance levels across the samples. The data exhibit extreme variability, with some wells showing very high Rhodanobacter abundance, while others show minimal or no detection. Patescibacteria in the Y-12 area were studied previously (Putt, 2022). This phylum has been suggested to correlate positively with coarse material, indicating preferential mobility associated with macropores and fractures.

The Subsurface Observatory (SSO), which was installed in 2022 with wells in 3x3 rows, each with depths in the Vadose Zone (VZ), the Variably Saturated Zone (VSZ), Saturated Zone 1 (SZ1), Saturated Zone 2 (SZ2), and the Saturated Zone 3 (SZ3). The SSO is divided into three sections: Upper (U), Middle (M), and Lower (L). In our study, we focused specifically on Saturated Zone 2 (SZ2): the U2-SZ2, M5-SZ2, and L8-SZ2 wells.

Viruses in the groundwater from the SSO wells at Y-12 have not been studied before. Only one author (Kothari et al., 2021; Kothari et al., 2019a; Kothari et al., 2019b) has addressed the distribution of phages and plasmids in the groundwater system at the eFRC site, and also there are no existing studies on the colloidal microbial ecology at this site.

Methods

16S Amplicon Sequencing and Analysis

Groundwater samples were obtained from the Y-12 National Security Complex. These samples were obtained from the SSO wells U2-SZ2, M5-SZ2, and L8-SZ2, as well as the EFP01 well in Area 3 at the eFRC site of the Y-12 National Security Complex. SSO well depths from which samples were collected: U2-SZ2: 21-25' depth, M5-SZ2: 21-25' depth, L8-SZ2: 21-25' depth. EFP01 well, which is outside of SSO wells: 15-25' depth. Three liters of groundwater from the wells were first purged before collecting fresh incoming water. Five liters of groundwater were sequentially filtered through 8 µm and then 0.1 µm filters to collect biomass. The filters were stored at -20 °C before being transferred to Zhou's lab at the University of Oklahoma. The members of ENIGMA team at Jizhong Zhou's lab at the University of Oklahoma

conducted DNA extraction, 16S PCR, NanoDrop, PicoGreen, data preprocessing, MiSeq sequencing, and extracted metagenomic raw sequencing files (Fan et al., 2025). They also created 16S plots. They used previously established protocols (Bolyen et al., 2019; Callahan et al., 2016; Caporaso et al., 2012; Katoh et al., 2002; Ludwig et al., 2021; Price et al., 2009, 2010; Quast et al., 2012; Wang et al., 2007; Wu et al., 2015), and the DNA quality and concentration presented in **Table 4.1.**

Library preparation and sequencing

The PCR product library was prepared using a two-step amplification approach, following Wu et al. (2015b). The first step targeted the V4 hypervariable region of prokaryotic 16S rRNA genes, with universal primers 515F (5'-GTGCCAGCMGCCGCGGTAA-3') and 806R (5'-GGACTACHVGGGTWTCTAAT-3'). The second step incorporated phasing primers to enhance nucleotide diversity, with all procedures performed as described in Wu et al. (2015a). Final sequencing was conducted on the Illumina MiSeq platform (Illumina, San Diego, CA, USA), using validated protocols (Caporaso et al., 2012), ensuring consistency from amplification to sequencing.

Data processing

The bioinformatics analysis utilized QIIME2 (version 2021.2) (Bolyen et al., 2019) based on an Amplicon Sequence Variant (ASV) approach. The initial step included trimming barcode and primer sequences with zero error tolerance and denoising and ASV identification using DADA2 (Callahan et al., 2016). Chimeric sequences were eliminated using the 'consensus' method, which processed samples independently and applied quality filtering by truncating forward reads at position 253 and reverse reads at position 203, guided by a quality score threshold of 2. The expected maximum error for paired-end sequence merging was set to 2.0. Taxonomic classification was conducted with the RDP Naive Bayesian Classifier algorithm (Wang et al., 2007) as implemented in DADA2, using a confidence threshold of 0.5 and referencing the Silva database (Quast et al., 2012) (v. 138.1). After classification, ASVs associated with Chloroplast, Mitochondria, Eukaryota, or those not classified at the kingdom level were excluded from subsequent analysis. Further quality filtering eliminated operational taxonomic units (OTUs) present in control samples or water blanks at abundances equal to or exceeding those in any of the eight experimental samples. The remaining prokaryotic ASV sequences were aligned using MAFFT (Katoh et al., 2002) in the QIIME2 environment without

sequence masking. These aligned sequences were then used as input for phylogenetic tree construction using FastTree (Price et al., 2009, 2010), which included topological constraints from a prokaryotic guide tree sourced from the All-Species Living Tree Project (Ludwig et al., 2021). A shotgun sequencing depth of 20 Gbp (PE150) was used for our samples.
Analysis of Microbial Cell Counts (Cells/mL) in Groundwater Samples is based on the Initial characterization of SSO wells using Acridine Orange Direct Count (AODC) protocols (Hazen et al., 1991) (**Table 4. 2).**

Metagenomic analysis

Bioinformatics analysis in KBase

We conducted bioinformatics analysis using applications on the KBase online platform, following the metagenome-assembled genome (MAG) extraction protocol described by Chivian (Chivian et al., 2023). The process unfolded as follows: initially, large, compressed files were uploaded to KBase through the Globus platform (Allen et al., 2012; Foster, 2011) and uncompressed in the staging area (v1.0.12). The data were imported as FASTQ reads, with the initial read quality assessed using FastQC (Simon Andrews et al., 2010). Quality trimming was performed using Trimmomatic (v0.39) with the following parameters: Sanger and Illumina 1.9 encoding (Phred33), Nextera PE-PE adaptor clipping (allowing for up to 2 bp mismatches), a 30 bp palindromic clip threshold, and a 10 bp simple clip threshold. Additional configurations included a sliding window size of 4 (minimum quality score: 15), a head crop length of 20, leading and trailing minimum quality scores of 3, and a minimum read length of 36 (Bolger et al., 2014). After trimming, read quality was evaluated again using FastQC. Taxonomic classification was performed using Kaiju and GOTTCHA2 (Freitas et al., 2015; Menzel et al., 2016). Metagenomic assembly was performed using metaSPAdes (v3.15.3) (Nurk et al., 2017) with a minimum contig length >= 2000 bp. Contig binning was carried out using CONCOCT (v1.1), MaxBin2 (v2.2.4), and MetaBAT2 (v1.7) (Alneberg et al., 2014; Kang et al., 2015; Wu et al., 2016; Wu et al., 2014). Finally, the bacterial and archaeal genome bins were refined using dereplication, aggregation, and scoring with the DAS Tool (v1.1.2) (Sieber et al., 2018). We filtered the bins with Filter Bins by Quality using CheckM - v1.0.18 (set manually to greater than 90% completeness and under 2% contamination) (Parks et al., 2015). Then, we used BinUtil (v1.0.2) to extract assembled bins for downstream processes. The next step was to annotate the assembled bins, assigning taxonomic classifications at the lineage level. Genomes often have

high similarity, including functional similarities, across samples. To compare this within bins, functional gene comparisons are performed in 'Classify Microbes with GTDB-Tk' (v2.3.2) (Chaumeil et al., 2022; Chivian et al., 2023; Parks et al., 2022). Alternatively, similar genomes can be compared at a higher level using ANI. MSA% (Marker Set Alignment) indicates the completeness estimate from GTDB-Tk (Genome Taxonomy Database), which is based on 120 bacterial markers. Finally, we ran FastANI (v. 0.1.3) (Jain et al., 2018) to determine bin similarities, particularly for genomes from similar conditions. Lastly, we ran the Set of Genomes Into Species Tree v2.2.0 (Price et al., 2010) to see evolutionary distances.

Virus and Plasmid Analysis using geNomad

We ran geNomad via the Bash command line to identify viral contigs and classify their taxonomy with metaSPAdes assemblies. This included annotating proteins using MMseq2 and the geNomad database (v.1.9) (Camargo et al., 2024). We executed the full geNomad pipeline, which involves gene prediction (identifying open reading frames (ORFs) in contigs with Pyrodigal-gv for viruses), marker detection, and classifying sequences into viral, plasmid, and chromosomal categories. geNomad uses a machine learning model (neural network) for scoring. The first step was running geNomad annotate (v1.11.0), which performed gene calling and annotated predicted proteins with geNomad's markers. Next, we ran geNomad find-proviruses (v1.11.0) to identify potential proviral regions in the input sequences. After that, we executed geNomad marker classification (v1.11.0) to categorize sequences into chromosomes, plasmids, or viruses based on geNomad markers and gene-related features. Then, we proceeded with geNomad nn-classification (v1.11.0), which classified sequences into chromosomes, plasmids, or viruses based on nucleotide sequences. Lastly, we executed geNomad aggregated classification (v1.11.0), which combined results from marker classification and neural network classification to classify the input sequences into chromosomes, plasmids, or viruses.

The functional characteristics of the MAGs

Metabolic potential analysis.

This discussion synthesizes results from the ASV Pilot Time Series (n = 40), genome-resolved metagenomic data (n=8), and plasmid and viral inventories from geNomad (n=8), alongside detailed geochemical, ion, and colloid datasets. The goal is to evaluate these hypotheses, interpret the statistical results, and determine findings within the broader literature on colloid-facilitated transport, microbial ecology, and hydrological processes in contaminated aquifers.

Data processing and statistical analyses were conducted in Python (v3.13) using pandas, *numpy*, *scikit-bio*, and *statsmodels* within controlled conda environments (McKinney (Harris et al., 2020; McKinney, 2010; Seabold and Perktold, 2010) using Jupyter Lab notebook (Kluyver (Kluyver et al., 2016).

Metabolic pathway reconstruction was performed using the DRAM pipeline on assembled metagenomes from all wells and depth zones. Annotated modules and pathways were aggregated at the functional category level. Pathway abundance was quantified as the number of annotated gene hits per pathway normalized by sample sequencing depth. To enable cross-sample comparison, data were merged into a pathway x sample matrix. A heatmap of pathway abundance across samples was constructed in Python using *Pandas* and *Matplotlib and Seaborn*. Prior to visualization, abundances were log-transformed [$\log_{10}$ (x+1)] to reduce the influence of highly abundant pathways and clustered by both sample (columns) and pathway (rows) using hierarchical clustering with Bray-Curtis dissimilarity. This approach shows both the distribution of core metabolisms (glycolysis, TCA cycle, amino acid biosynthesis) and niche-specialized pathways (denitrification, sulfate reduction, CRISPR defense).

To assess similarity in metabolic potential between samples, pairwise Spearman's rank correlation (ρ (rho)) was calculated across all pathways using the *scipy.stats.spearmanr* function in Python (v3.13). This nonparametric approach assesses whether samples with high abundance of specific pathways exhibit consistent ranking trends across other pathways. Correlation matrices were visualized as clustered heatmaps, and significance was assessed with Benjamini-Hochberg FDR correction of p-values. Microbial community composition and functional potential were evaluated using a multi-tiered statistical and genome-resolved framework. Amplicon-derived 16S rRNA sequences were clustered into amplicon sequence variants (ASVs) and subjected to Hellinger transformation to minimize the influence of dominant taxa.

Pairwise dissimilarities were computed using Bray-Curtis distances and used as input for both unconstrained principal coordinates analysis (PCoA) and constrained ordination with distance-based redundancy analysis (dbRDA). To assess group-level differences, permutational multivariate analysis of variance (PERMANOVA; 999 permutations) was conducted across wells and depth zones. To ensure that significant results reflected centroid differences rather than unequal dispersion, homogeneity of dispersion was verified with betadisper. Alpha diversity metrics were calculated using scikit-bio; Beta diversity matrices were ordinated with PCoA.

Mantel tests (Spearman, 999 permutations) were applied to quantify correlations between microbial community dissimilarities and environmental predictor matrices. Predictor matrices were constructed for metals only, metals plus colloid counts, metals plus colloid flux (particle counts x flow velocity), metals plus anions (nitrate, sulfate, chloride), and all predictors combined. In total, 53 predictors were considered, of which 50 were retained after filtering for non-constant values with coverage ≥ 3. Partial Mantel tests were further conducted to understand the unique contributions of geochemistry versus colloids.

Univariate regression was conducted using ordinary least squares (OLS), with significance evaluated through t-statistics and adjusted p-values corrected for false discovery rate (Benjamini-Hochberg). To account for multicollinearity among predictors, partial least squares (PLS) regression was employed, and model performance was evaluated using cross-validated R^{2} (cvR^2), residual mean square error (RMSE), and diagnostic plots. Random forest (RF) regression (with 1000 trees and stratified 5 x 5 cross-validation) was employed to capture nonlinearities and assess variable importance. Classification models, including RF and k-nearest neighbors (kNN), were trained to predict uranium and nitrate contamination class, well identity, and depth zone. Viral and plasmid elements were annotated with geNomad to capture the contribution of mobile genetic elements.

Functional Categorization of Metabolic Potential

The analysis was implemented in Python (v3.13) using the built-in libraries with NumPy (numerical arrays), pandas (dataframe manipulation, de-duplication, aggregation, pivoting), and Matplotlib for visualization. Metabolic functions identified from DRAM-annotated bins were classified into nine broad categories using a two-stage keyword-matching procedure. To avoid ambiguous assignments, categories were applied in a fixed priority order: Transporters, Organic Nitrogen, Energy, Carbon Utilization, Defense and CRISPR, Translation and Ribosome, Nucleotide Metabolism, Motility and Flagella, and Other Degradation.

1. *Carbon utilization* included central carbon pathways (glycolysis, Entner-Doudoroff, pentose phosphate, TCA cycle, gluconeogenesis, glyoxylate shunt), carbon fixation (Calvin cycle, reverse TCA, Wood-Ljungdahl), fermentation and short-chain fatty acid metabolism (acetate, propionate, butyrate, lactate, ethanol, acetone), carbohydrate-active enzymes (CAZy), fatty acid degradation and β-oxidation, and biosynthesis of cofactors and electron carriers

(cobalamin and vitamin B12, folate, biotin, riboflavin, thiamine, pyridoxine, niacin, NAD and NADP, heme, porphyrins, tetrapyrroles, ubiquinone, menaquinone).

2. *Organic Nitrogen* included denitrification (nar, nap, nir, nor nosZ), dissimilatory and assimilatory nitrate and nitrite reduction, DNRA, anammox (hzs, hdh), nitrogen fixation (nifH, nifD, nifK), urea metabolism (urea, urease, urtA-E), nitrification (amoA, hao), ammonium assimilation and transport (glnA, gltB and D, gdh, amtB), and glutamine and glutamate synthesis pathways.
3. Energy included electron transport chain complexes (I-V; nuo, ndh, SDH, bc1), respiratory cytochromes and oxidases (ubiquinol and quinol oxidase, bo3, aa3), RNF and Ech complexes, hydrogenases, and ATP synthase and ATPase.
4. *Transporters* covered a wide range of systems, including ABC, MFS, SMR, MATE, and RND efflux families; peptide and oligopeptide transporters (LIV, OPP, DPP); phosphate and sulfate transporters; phosphotransferase systems (PTS); and ion and metal uptake or resistance loci (znu, mnt, sit, feo, fep, fhu, tonB, cop, cus, czc, ars, mer, nik, amtB).
5. *Defense and CRISPR* comprised CRISPR arrays and associated proteins (cas0-9, cse, csd, cascade).
6. Translation and Ribosome included ribosomes, ribosomal proteins, and information-processing systems.
7. *Nucleotide metabolism* covered purine and pyrimidine metabolism, adenine and guanine and pyrimidine ribonucleotides, and nucleotide-sugar pathways.
8. *Motility and Flagella* captured terms associated with flagella, flagellar proteins, and motility.
9. *Other degradation* pathways were also present, including glucuronate, salicylate, and hydrocarbon degradation. Each function was restricted to a single category, with assignment based on the first match in the precedence order above. Rows without matches were excluded. To prevent double-counting, a unique function identity was generated as the concatenated string of module, subheader, header, and gene description. Counts were aggregated at the level of unique functions per sample per category, considering only those functions with presence (any Bin > 0).

Identification of Metal-Responsive Taxa

All analyses of taxon-specific responses were performed in Python, using pandas and numpy for data management, scipy and statsmodels for statistical testing and regression, and matplotlib and

seaborn for visualization. To identify taxa most responsive to geochemical gradients, we integrated ASV-level regression analyses with taxonomic annotations. Amplicon sequence variants (ASVs) from the 16S rRNA dataset were tested for their associations with environmental variables, including uranium, manganese, rubidium, boron, nitrate, sulfate, and colloid counts. Univariate regressions were performed for each ASV relative to individual predictors, and statistical significance was assessed after false discovery rate (FDR) correction. ASVs with adjusted p-values < 0.05 and regression coefficients (β) of large magnitude (typically $|\beta| > 3$) were considered significant responders.

Taxonomic assignments for significant ASVs were drawn, which provided classifications at the phylum, class, order, family, and genus levels. To ensure consistency, results were cross-referenced with the summarized outputs. This allowed us to quantify the number of responsive ASVs at each taxonomic rank and determine whether particular lineages were disproportionately represented among the significant results.

Counts of responsive ASVs per well and per depth zone were extracted and enabled the identification of site-specific trends, such as the strong uranium-linked responses in U2-SZ2 compared to the lower frequencies of responsive ASVs in L8-SZ2. Finally, to show the most reproducible responders, taxa were ranked by recurrence across wells, strength of regression coefficients, and the number of ASVs consistently associated with a given predictor. This integrative approach allowed us to identify both well-known uranium- and nitrate-adapted lineages (like Acidobacteria Subgroup 1, Rhizobiales) and novel or poorly classified ASVs that consistently responded to geochemical stressors.

Results

16S analysis results (n=8)

The highest DNA concentration (using Qubit) was found in sample M5-SZ2F01, at 69.8 ng and µL. By comparison, the lowest was in sample L8-SZ2.F8, measuring only 0.713 ng and µL. Using Nanodrop, DNA concentrations were measured at 71.4 ng and µL and 1.4 ng and µL, respectively (**Table 4.1, Figure 4**). The sequencing coverage was nearly 100%, with a sequencing depth of 37579 across all samples. The highest number of ASVs was found in the L8-SZ2 wells, at approximately 2000, while the lowest was observed in the EFP01 wells, at around 500 (**Figure 4.5**).

The abundance distribution was also estimated. The cumulative relative abundance (%) of U2-SZ2, EFP01 with a 0.1 µm and an 8 µm filter, exhibited a steep early rise, indicating low evenness and high dominance. The potential cause of this outcome is likely the extreme environment of the study area and its proximity to the contaminating source (which has a lower pH). Both curves suggest a community dominated by a small number of highly abundant species. All other samples demonstrated a gradual rise, indicating high evenness and low dominance, which implies a lesser level of disturbance from the extreme environment (**Figure 4.6**).

Alpha diversity, as measured by 16S richness, was highest in the L8-SZ2 and M5-SZ2 wells, and lowest in the U2-SZ2 well (**Figure 4.7**). The alpha diversity Shannon index demonstrated the same trend, indicating high diversity and evenness of abundance in those 2 wells (**Figure 4.8).** Beta diversity based on 16S Bray PCoA indicated that the L8-SZ2 and M5-SZ2 wells formed closely clustered groups, suggesting they may share similar communities. In comparison, the U2-SZ2 sample exhibited a microbial composition that differed significantly from the others (**Figure 4.9**).

At the phylum level, *Proteobacteria* (class Gammaproteobacteria***)*** were most abundant. Then, *Bdellovibrionota*, which showed the second-highest abundance (**Figure 4.10).** The relative abundance of *Rhodanobacter* was highest in EFP samples, followed by U2-SZ2 samples. The lowest relative abundance of *Rhodanobacter* was found in L8-SZ2 well (**Figure 4.11**). Sulfate-reducing bacteria have the highest relative abundance in the M5-SZ2 and L8-SZ2 wells. Interestingly, sulfate-reducing bacteria were not detected in the EFP01 or U2-SZ2 wells. *Thermodesulfovibrio* was identified as the most abundant type of sulfate-reducing bacteria. By comparison, Desulfovibrionales recorded the lowest abundance (**Figure 4.12**).

The U2-SZ2 well had the highest abundance of nitrifiers (more than 50%). By comparison, the EFP01 well had the lowest abundance (**Figure 4.13**). Based on 16S data, the *Rhodanobacter spp.* has the highest relative abundance (almost 50%) in EFP01 compared to the downgradient wells U2-SZ2, M5-SZ2, and L8-SZ2. That correlates with the fact that EFP01 is closer to Area 3 and has higher nitrate concentrations.

Metagenomic analysis results (n=8)

M5_SZ2_F01_S2_paired retained 98.0% of read pairs (77.6M), with 2.0% as single-direction reads and only 0.03% discarded. Similarly, M5_SZ2_F8_S1_paired retained 97.8% (80.5M), with 2.2% single reads and 0.04% lost. Sample L8_SZ2_F8_S4_paired showed 97.2% retention

(90.8M), 2.8% single reads, and 0.04% loss. L8_SZ2_F01_S7 kept 98.0% (56.4M), with 1.9% single reads and 0.03% discarded. U2_SZ2_F01_S8 retained 97.9% (84.8M), 2.1% single reads, and 0.03% loss. Samples U2_SZ2_F8_S5 and EFP_01_F8_S6 had slightly lower retention at 97.6% (94.9M) and 97.4% (95.7M), respectively, with 2.4-2.6% single reads and minimal losses (0.04% each). In general, Trimmomatic maintained high read retention while discarding a very few number of reads.

Proteobacteria are the only phylum found in every sample, with 90% completeness and 2% contamination bins. Actinobacteria are almost universal. Viruses (Microviridae, *Caudoviricetes*) are surprisingly abundant but do not represent true bacterial phyla. The 10 most common phyla were found: Proteobacteria, Actinobacteria, Bacteroidetes, Verrucomicrobia, Nitrospirae, *Microviridae* (viral), *Caudoviricetes* (viral), Acidobacteria, Spirochaetes, and Planctomycetes. Rhodanobacter denitrificans was detected in all four wells within the bins, with 90% completeness and 2% contamination, as determined by the quality assessment of the filter bins. The medium-quality bins, set to 50% and contamination at 10% (**Figures 4.25-4.30),** showed Patescibacteria in all samples (U2-SZ2, M5-SZ2, L8-SZ2), but only for the 0.1-µm filter (F01). It did not show up in 8-µm filters (F8).

Species trees for bins with 50% completeness indicated that EFP01F8_S6 has the shortest evolutionary distance to *Pseudomonas*. The EFP01F01_S3 is most closely associated with *Pusillimonas sp T7-7*, *Paraburkholderia symbiotica*, and *Burkholderia pseudomallei K96243.* The U2_SZ2_F01_S8 sample shows strong confidence in its closest relationship with *Rhodanobacter* fulvus Jlip2, *Rhodanobacter denitrificans*, which was isolated from Area 3 at Y-12, and *Rhodanobacter thiooxydans*. In comparison, the U2_SZ2_F8_S5 sample is most closely linked to various *Mycobacterium* species, along with *Methylocystis rosea sv97* and *Thiobacillus denitrificans DSM 12475*. The M5_SZ2_F8_S1 sample displayed the closest evolutionary distance to *Methylomonas methanica MC09* and *Methyloglobulus morosus KoM1*. The M5_SZ2_F01_S2 is most closely related to *Sulfuritalea hydrogenivorans sk43H*. The L8_SZ2_F8_S4 sample is most closely related to *Brevundimonas viscosa* and *Brevundimonas DS20*. Meanwhile, L8_SZ2_F01_S7 shares its closest relatives with *Halothermothrix orenii H 168*, *Paenibacculus sp. P1XP2* and *Borrelia parkeri SLO.*

Cell count results

The Acridine Orange Direct Count (AODC) measurements ranged from 8.51 x 10^4 to 4.73 x 10^5 cells/mL. It is typical for groundwater to reflect moderate microbial activity across the site. The highest was in well M6-VSZ (4.73 x 10^5 cells/mL). Next were U1-SZ1 (3.43 x 10^5, highest among upper wells) and M5-SZ1 (3.36 x 10^5, high for middle wells). The lowest values were observed in L9-SZ2 (8.51 x 10^4), M4-SZ1 (6.85 x 10^4, the lowest among the middle wells), and L7-SZ1 (9.22 x 10^4, the lowest among the lower wells) **(Table 4.2, Figure 4.39).**

geNomad results (n=8)

Overall viral families across the samples are illustrated in **Figure 4.42.** geNomad software helped to detect exact viruses and plasmid names with more than 90% confidence. In the upper U2 well, the 0.1 µm fraction (F01_S8) contained 148 plasmids and 105 viruses, predominantly *Caudoviricetes*, with a few rare Microviridae and Corticoviridae. Most viral scores exceeded 0.95. The 8 µm fraction (F8_S5) was richer, containing 383 plasmids and 275 viruses, including several rare groups such as Autographiviridae and Smacoviridae, as well as a single eukaryotic Iridoviridae sequence. Proviruses ranged up to nearly 40 kb, and most contigs scored confidently.

The middle M5 well followed the same trend. The 0.1 µm fraction (F01_S2) contained 97 plasmids and 92 viruses, nearly all of which were phages, with a few giant viruses and ssDNA phages. Confidence was mixed, but strong viral signatures supported most sequences. In the 8 µm fraction (F8_S1), richness increased to 248 plasmids and 254 viruses, still ~95% *Caudoviricetes*, with only minor representation of eukaryotic and ssDNA groups.

The lower L8 well showed the most even viral diversity. In the 0.1 µm fraction (F01_S7), only 10 plasmids but 73 viruses were found, including *Caudoviricetes*, giant Mimiviridae and Phycodnaviridae, Microviridae, and a potentially novel virus. The 8 µm fraction (F8_S4) contained 78 plasmids and 200 viruses, primarily phages, with contributions from Iridoviridae, Mimiviridae, and Tectiviridae. Several sequences remained unclassified.

In the EFP01 well, the 0.1 µm fraction (F01_S3) contained the richest community, comprising 1,155 plasmids and 594 viruses, including 500 viral contigs that *Caudoviricetes* dominated. Only a few sequences represented other groups such as Microviridae, Inoviridae, and Nucleocytoviricota. Families such as Zobellviridae, Autographiviridae, and Straboviridae were identified, and most sequences scored above 0.98, indicating high confidence. In comparison, the

8 µm fraction (F8_S6) was significantly less diverse, comprising only 82 plasmids and 52 viruses, still dominated by phages but also including 12 integrated proviruses.

Across all wells and fractions, bacteriophages (*Caudoviricetes*) dominated, typically accounting for over 90% of the detected viruses. Smaller filters captured far greater richness, while larger filters revealed more proviruses and occasional enrichment of rare eukaryotic or novel viruses. The lower well (L8) stood out for its broader viral diversity. By comparison, the EFP01 well was exceptional for plasmid abundance.

Metabolic Pathway Distributions Across Wells

DRAM outputs from KBase can be seen on **Figures 31-36**. Metagenome-assembled genomes (MAGs) from the SSO wells revealed distinct functional capacities when binned into nine major pathway categories: carbon utilization, organic nitrogen, energy, transporters, defense and CRISPR, translation and Ribosome, nucleotide metabolism, motility and Flagella, and other degradation. These categories collectively capture the major axes of microbial metabolism and provide insight into how microbial consortia respond to the combined stresses of uranium, nitrate, sulfate, and colloid-rich groundwater chemistry. The following results describe both the absolute counts of unique functions recovered in each well and their relative contributions as percentages of total encoded pathways.

Carbon utilization functions were among the most abundant across all wells, but their prominence varied with depth and geochemistry. M5 (SZ2) encoded the most extensive repertoire with 2,093 functions (30.6% of its total functional profile), reflecting the central role of glycolysis, the pentose phosphate pathway, and fermentation processes in this nitrate- and metal-rich aquifer. EFP01 (shallow F01 filter) encoded 1,117 functions (28.9%), dominated by CAZy carbohydrate-active enzymes and short-chain fatty acid metabolism. In contrast, L8 (SZ2) had fewer carbon pathways (798 functions, 22.7%), consistent with its oligotrophic, uranium-rich conditions. Pathways included the Calvin cycle, reverse TCA, Wood-Ljungdahl acetogenesis, and β-oxidation, pointing to metabolic flexibility under redox stress.

Organic nitrogen metabolism displayed strong signatures of nitrate reduction and urea cycling. U2 (SZ2) carried 954 functions (27.1%), the highest relative proportion across wells, dominated by nar, nap, nir, and nosZ genes for denitrification, as well as nifH-encoded nitrogen fixation. M5 (SZ2) also contained extensive nitrogen potential (1,542 functions, 22.5%), reflecting denitrification paired with DNRA. In contrast, L8 (SZ2) showed only 596 functions

(17.0%), suggesting limited nitrogen turnover in the uranium hot spot, where strong geochemical controls may constrain nitrogen availability.

Energy pathways centered on electron transport chains and respiratory versatility. EFP01 encoded 976 functions (25.3%), the highest relative contribution, featuring abundant cytochromes, complex I-V subunits, and hydrogenases. M5 contained 1,398 functions (20.4%), supporting its role as a redox-active transition zone. L8 exhibited the fewest energy pathways (674 functions, 19.2%), but these included complete ATP synthase and terminal oxidase systems, suggesting resilience under oxidative stress from uranium and nitrate.

Transport capacity was widespread, but trends reflected geochemical niches. M5 encoded 1,221 transporter functions (17.8%), including ABC, MFS, RND efflux, phosphate and sulfate uptake, and TonB-dependent siderophore systems. EFP01 contained 851 transporters (22.1%), a high relative contribution, featuring nutrient acquisition in shallower flow paths. L8 (SZ2) exhibited 722 transporters (20.3%), many linked to metal resistance (czc, ars, cop, cus) and ammonium uptake, directly relevant to its uranium-rich context.

Defense systems were less abundant but consistently represented. U2 (SZ2) carried 154 CRISPR and cas functions (4.4%), higher than L8 (101 functions, 2.9%) or M5 (189 functions, 2.7%). This suggests viral pressure and adaptive immunity are more pronounced in U2, consistent with viral inventories showing enriched *Caudoviricetes* in this well.

Translation machinery was universally abundant, with ribosomal proteins and information-processing genes forming a conserved backbone. M5 encoded 897 functions (13.1%). By comparison, EFP01 carried 766 (19.9%), the highest proportional share. This reflects a robust protein synthesis capacity across all wells, regardless of environmental stress.

Nucleotide metabolism, including purine and pyrimidine synthesis, as well as nucleotide-sugar pathways, was strongly represented. U2 encoded 433 functions (12.3%), compared to M5 (612 functions, 8.9%) and L8 (301 functions, 8.5%). High nucleotide turnover in U2 is consistent with elevated cell counts and active microbial replication under nitrate stimulation.

Motility pathways were minor but informative. EFP01 (shallow) exhibited the strongest representation, with 233 functions (6.0%), indicating active chemotaxis and biofilm dispersal near inflow zones. M5 and L8 contributed 142 (2.1%) and 101 (2.8%) functions, respectively, consistent with particle-associated lifestyles under subsurface flow.

Minor degradation pathways included glucuronate, salicylate, and hydrocarbon breakdown. These were uniformly low, ranging from 51 functions (1.4%) in L8 to 87 (1.3%) in M5, but their presence suggests a potential for xenobiotic or organic pollutant turnover, particularly in contaminated shallow zones.

Overall, M5 exhibited the most extensive functional inventory (6,852 total functions), reflecting its intermediate geochemical complexity and high colloid counts. U2 encoded 3,520 functions, dominated by nitrogen cycling and nucleotide synthesis, consistent with its nitrate-rich status. L8 carried 3,519 functions, with a distinctive emphasis on metal transporters and stress tolerance pathways, reflecting adaptation to uranium contamination. EFP01 encoded 3,867 functions, enriched in carbon metabolism, energy generation, and motility, emphasizing its role as a shallow, nutrient-rich entry point into the flow path. These results demonstrate that metabolic potential across wells is not evenly distributed but instead reflects environmental filtering by geochemistry and contaminants. Carbon and nitrogen pathways dominated shallow and mid-depth wells. By comparison, metal transporters and stress pathways characterized L8, the uranium hot spot (**Figure 4.43**-**4.44).**

Statistical analysis results

Alpha diversity

Alpha diversity differed strongly among wells. Shannon diversity was lowest at U2-SZ2 (≈3.0-3.2), intermediate at M5-SZ2 (≈3.6-3.8), and highest at L8-SZ2 (≈4.2-4.4). Richness showed a similar gradient. Within the broader dataset (n = 40), Shannon diversity ranged from 3.95 ± 0.39 at U2-SZ2 to 6.19 ± 0.46 at M6-SZ1 and 6.16 ± 0.06 at L7-SZ1, with intermediate values in the other wells.

Beta diversity

Beta diversity revealed strong between-well differences (Bray-Curtis dissimilarities 0.58-0.90), compared to within-well dissimilarities (<0.40). PERMANOVA confirmed significant differences among wells (pseudo-F = 9.74, p = 0.001, n = 40) but not between zones (pseudo-F = 1.07, p = 0.359). PERMDISP indicated these patterns reflected shifts in group centroids rather than heterogeneity of dispersion (p > 0.4) (**Table 4.3**).

A Principal Coordinates Analysis (PCoA) of Hellinger-transformed Bray-Curtis dissimilarities (**Figure 4.47**) further illustrate these differences. Samples cluster tightly by well,

with clear separation among groups. Axes 1 and 2 explain 22.8 % and 17.7 % of the variance, respectively, indicating strong spatial structuring of microbial communities across wells.

Environmental correlation of geochemistry onto the Bray-Curtis PCoA revealed clear structuring of communities by two main gradients. pH aligned strongly and positively with PCo1 (rightward), while nitrate loaded toward the upper-left (positive PCo2, negative PCo1) (**Figure 4.48**)

Mantel tests

Mantel tests revealed strong correlations between community structure and geochemistry, particularly with the combined pH, metal, and anion matrix ($r = 0.628$, $p = 0.001$, $n = 40$), whereas correlations with colloids alone were not significant ($r = 0.055$, $p = 0.221$, $n = 40$). Partial Mantel tests further confirmed that geochemistry remained a robust driver when controlling for colloids ($r = 0.638$, $p = 0.001$, $n = 40$), while colloids showed only a weak but statistically significant conditional effect when controlling for geochemistry ($r = 0.143$, $p = 0.005$, $n = 40$). All Mantel and partial Mantel tests were conducted using Spearman correlation with 999 permutations.

k-Nearest Neighbors (kNN) Classification

For both Smith-18 and all geochemistry, microbial communities could be classified with high accuracy (acc_mean = 1.0, acc_sd = 0) for the nitrate class, uranium class, well, and zone. High separability is consistent with strong geochemical gradients. However, n is modest, and we interpret classification with caution. Communities carry a strong and consistent signal of their geochemical environment and sampling context, enabling perfect classification in cross-validation. For the 18 metals suggested by the previous study (Smith et al., 2015) the adjusted R^2 reported was 0.279, with $p = 0.001$. For the full geochemistry set (all metals), the reported adjusted R^2 was also 0.279, $p = 0.001$, not higher. The Smith-18 dbRDA model explained 59.4% of constrained variance, but the adjusted R^2 was 0.279 ($p = 0.001$). Similarly, the full geochemistry model had an adjusted $R^2 = 0.279$ ($p = 0.001$), indicating that model complexity did not improve explanatory power beyond the Smith-18 predictor panel.

Univariate OLS regressions

Univariate OLS regressions linked microbial cell counts to multiple metals and ions. Strongest predictors included Mn ($\beta = 0.00036$, $t = 8.58$, $R^2 = 0.66$, $p = 2 \times 10^{-10}$), B ($\beta = 0.00941$, $t = 7.59$,

R^2 = 0.60, p = 3.9 x 10^{-9}), and Rb (β = 0.462, t = 7.35, R^2 = 0.59, p = 8.2 x 10^{-9}). Other significant predictors included Na, Ni, Co, Se, Zn, Cd, Be, and Ta (R^2 ≈ 0.49-0.55). Predictors were standardized for comparability of β.

Diversity indices responded strongly to anion chemistry. Shannon diversity declined with nitrate (β = -0.36, R^2= 0.803, p = 5.6x10^{-15}) and sulfate (β = -0.49, R^2 = 0.677, p = 7.3x10^{-11}). Richness and evenness showed parallel trends, with nitrate and sulfate consistently negative predictors. In multivariable models that included nitrate, sulfate, and chloride together, overall fits remained high (Shannon adjusted R^{-2} = 0.815, p = 7.0 x 10^{-14}), although chloride emerged as the only significant single predictor (p = 0.031).

Partial Least Squares (PLS) Regression

PLS regression confirmed that geochemistry (including ions) explained ~27% of community variance (cvR^2 = 0.27), while colloids contributed negligible explanatory power (cvR^2 < 0).

Random Forest (RF) regression

Random Forest (RF) regression achieved high predictive accuracy for ordination axes (cvR^2 = 0.93 for PC1, 0.78 for PC2). PC1 was most influenced by Mg, B, La, Mo, Cu, and W, while PC2 was shaped by K, Ge, Hf, Na, U, B, and Zr. While anion chemistry (nitrate, sulfate, and chloride) showed strong associations with microbial diversity, these results must be interpreted with caution. The strong fits may partly reflect covariance among predictors, leading to collinearity bias, where chloride appeared significant only in multivariable models. Moreover, restricting analysis to anions may overemphasize their role compared to metals, which also emerged as strong predictors in other models. Finally, the relatively modest sample size (n = 40) raises the possibility of overfitting and limits generalization across all aquifer zones (**Figure 4.49-4.50**).

Global feature importance

Across all RF runs, the strongest global predictors of ordination structure included tungsten (W, importance = 0.070), zirconium (Zr, 0.067), boron (B, 0.053), cadmium (Cd, 0.047), and magnesium (Mg, 0.045). These metals consistently ranked highest in raw RF importance metrics, indicating broad influence across multiple axes.

Axis-specific permutation importance

Permutation-based assessments provided a more nuanced view of axis-specific drivers:

- PC1 (n = 40 samples) was structured primarily by Mg, B, La, Mo, and Cu, with additional contributions from W and Zr. This axis reflects gradients dominated by

alkaline earths and trace metals, suggesting strong geochemical control over the dominant dimension of microbial variance. (**Table 4.4**.)

- PC2 was driven by K, Ge, Hf, Na, and U, with B again emerging as a secondary predictor. This axis emphasizes alkali elements, metalloids, and actinides as key drivers of secondary variation, consistent with uranium-rich zones exerting a selective influence. (**Table 4.5**).

Importances were averaged over CV folds and seeds. Overall, the global and axis-specific analyses demonstrate that multiple geochemical gradients jointly structure microbial communities. While PC1 is dominated by alkaline earth and transition metals (Mg, B, La, Mo, Cu, W, Zr), PC2 captures alkali and actinide contributions (K, Na, U, Ge, Hf). These results indicate that uranium is not the sole structuring force; rather, microbial community composition reflects integrated responses to a suite of metals spanning major ions, trace elements, and actinides.

Key Metals Driving Responses results

Among the strongest drivers, Mn was strongest in univariate fits, while U ranked highly across models and aligned with L8. In univariate regressions, uranium explained ~52% of variance (β = 0.42, t = 6.30, $R^2 \approx 0.52$, $p < 0.001$). Mantel correlations also revealed a significant correlation with uranium (r = 0.628, p = 0.001). Responses were particularly concentrated in L8, the well with the highest uranium concentration, where more than 40 ASVs showed significant uranium associations. Responsive groups included Acidobacteriota, Patescibacteria, Actinobacteriota, and families such as Holophagaceae and Rhizobiales. Genera such as *Occallatibacter* were repeatedly enriched under uranium stress.

Manganese was the strongest univariate predictor overall, explaining ~66% of variance (β = 0.00036, t = 8.58, R^2 = 0.66, p = 2.0 x 10^{-10}). Responses were particularly pronounced in M5, with ~30 ASVs enriched. Responsive lineages included the Comamonadaceae (Betaproteobacteria) and the genus *Sediminibacterium*, which is strongly associated with Mn cycling. The magnitude of the regression coefficient reflects differences in measurement units rather than biological effect size. Because β values are unit-dependent, they are not directly comparable across metals; instead, R^2 and significance levels provide the most reliable measure of relative strength. Responses to manganese were most evident in M5, where approximately 30 ASVs were enriched. These included Betaproteobacteria, especially Comamonadaceae, and the

genus *Sediminibacterium*, both of which are strongly linked to manganese cycling and adaptation to redox-active metals. Boron also showed a major role ($\beta = 0.0094$, $t = 7.59$, $R^2 = 0.60$, $p = 3.9 \times 10^{-9}$). Sensitive taxa included Acidobacteria Subgroup 1 and *Terracidiphilus*, both showing strong negative correlations with B. Effects were broadly distributed across U2 and M5, indicating system-wide sensitivity. Rubidium had significant predictive power ($\beta = 0.462$, $t = 7.35$, $R^2 = 0.59$, $p = 8.2 \times 10^{-9}$), particularly shaping communities in U2. Responsive groups included *Reyranella* and AKYH767 group taxa.

Several additional metals showed strong effects (all $p < 10^{-6}$, $R^2 = 0.49$-0.54): Ni: $\beta = 0.0099$, $t = 6.73$, $R^2 = 0.54$, $p = 5.7 \times 10^{-8}$. Co: $\beta = 0.025$, $t = 6.66$, $R^2 = 0.54$, $p = 7.1 \times 10^{-8}$. Se: $\beta = 1.65$, $t = 6.56$, $R^2 = 0.53$, $p = 9.8 \times 10^{-8}$. Zn: $\beta = 0.072$, $t = 6.49$, $R^2 = 0.53$, $p = 1.2 \times 10^{-7}$. These associations indicate a multimetal stress environment shaping communities through overlapping ecological filters.

Taxonomic Breadth of Responses:

1. Phylum (31 phyla): Most responsive phyla were Acidobacteriota, Actinobacteriota, Proteobacteria, and Patescibacteria, accounting for >60% of all significant associations.
2. Class (45 classes): Key responders included Acidobacteriae, Alphaproteobacteria, Gammaproteobacteria, and Holophagaceae-related lineages.
3. Order (63 orders): Prominent orders included Rhizobiales, Burkholderiales, and Holophagales, strongly tied to uranium and manganese.
4. Family (55 families): Frequent responders included Acidobacteriaceae (Subgroup 1), Chitinophagaceae, and Reyranellaceae.
5. Genus (44 genera): Occallatibacter - uranium-associated, especially in L8. *Sediminibacterium* - Mn-responsive, abundant in M5. Reyranella - enriched under Rb and Ni. *Terracidiphilus* - sensitive to B and nitrate stress.

L8 (uranium hot spot): >40 ASVs responsive to uranium, dominated by Acidobacteria and Actinobacteria. M5 (manganese-rich): ~30 ASVs enriched, dominated by Betaproteobacteria and Mn-adapted genera. U2 (multimetal diversity): the broadest range of responsive taxa, including lineages sensitive to Rb, Ni, Co, Se, Zn.

Across all analyses, metals consistently emerged as the primary ecological filter structuring microbial communities. Uranium-driven lineages dominated in L8, manganese-adapted groups prevailed in M5, and U2 hosted the broadest diversity of metal-responsive taxa.

Statistical convergence across PERMANOVA, Mantel, dbRDA, OLS regression, and Random Forest showed metals as the key predictors of community composition (R^2 up to 0.80). Colloids and zones contributed secondary or negligible effects, emphasizing that metal gradients are the dominant selective force in this extreme subsurface environment.

Discussion

This discussion synthesizes results from the ASV Pilot Time Series (n = 40 samples), genome-resolved metagenomic data (n=8), and plasmid and viral inventories from geNomad (n=8), alongside detailed geochemical, ion, cell count, and colloid datasets. The goal is to evaluate these hypotheses, interpret the statistical results, and situate the findings within the broader literature on colloid-facilitated transport, microbial ecology, and hydrological processes in contaminated aquifers.

AODC results (8.51×10^4 to 4.73×10^5 cells/mL) confirm moderate microbial activity, with peak cell counts in well M6-VSZ (4.73×10^5 cells/mL). This high cell abundance is due to the presence of more nutrients in the variably saturated Zone (Khurana et al., 2024). U2-SZ2 exhibits high cell counts, attributed to its unique geochemistry, which is rich in Na, Mn, and nitrate, rendering it a microbial hotspot influenced by its environment. Given that U2-SZ2 has high NO_3^- levels of 290.98 ppm, it hosts more *Rhodanobacter denitrificans* than other SSO wells in Saturated Zone 2 (**Figure 3.11**). This may be because of the upper wells being located near the surface and the contamination source.

Based on 16S data from the EFP01 well, we observe the highest relative abundance of *Rhodanobacter* (almost 50%) among the downgradient wells: U2-SZ2, M5-SZ2, and L8-SZ2. This finding correlates with the fact that EFP01 is closer to S3 ponds (contamination source) and has a higher nitrate concentration, according to HydroVu data. Patescibacteria are often classified as having 60-80% completeness by the CheckM tool in the KBase pipeline, even for circular genomes of these species (Lui and Nielsen, 2023). Patescibacteria were detected in all samples with 50% completeness (U2-SZ, M5-SZ2, L8-SZ2), but only for the 0.1-µm filter (F01). This phylum did not show up in 8-µm filters (F8). The 8-µm filter is probably too large to retain Patescibacteria. Only in EFP01 did Patescibacteria show up in both filters. geNomad analysis reveal high-confidence viral identification scores above 0.9, with *Caudoviricetes* being the most common, although the accompanying taxa vary. This implies that pore size has a significant

impact on virome composition, where finer filters are more favorable for smaller, free viruses, while coarser filters tend to capture larger or host-associated viral particles.

GTDB-Tk Genome Classification Analysis Summary study provides a comprehensive genomic characterization of bacterial communities across multiple environmental samples, revealing substantial taxonomic diversity and a high degree of novel microbial lineages. Metagenome-assembled genomes (MAGs) from the analyzed samples span 10 major bacterial phyla, with Pseudomonadota, Patescibacteria, Acidobacteriota, and Bacteroidota being the most prevalent. These findings show the important role of metagenomic sequencing in uncovering microbial dark matter, particularly in understudied environments.

The species trees built in KBase explored the evolutionary relationships among bacterial populations from various environmental samples using phylogenetic analysis of metagenome-assembled genomes (MAGs). Species trees built from bins with at least 50% completeness exhibit sample-specific clustering, revealing how environmental conditions shape microbial communities. Notably, EFP01F8_S6 is closely related to *Pseudomonas*, indicating possible metabolic diversity in its niche. In contrast, EFP01F01_S3 groups with *Pusillimonas, Paraburkholderia*, and *Burkholderia*, suggesting roles in symbiosis or pathogenicity. The strong link between U2_SZ2_F01_S8 and *Rhodanobacter species (R. fulvus, R. denitrificans, R. thiooxydans*) aligns with their known adaptation to environments contaminated with or rich in Nitrogen. Conversely, U2_SZ2_F8_S85 is closely related to *Mycobacterium*, *Methylocystis*, and *Thiobacillus*, suggesting a habitat that supports methylotrophic and sulfur-oxidizing processes. The clustering of M5_SZ2_F8_S1 with *Methylomonas methanica* and *Methyloglobulus morosus* shows methane-related microbial activity. On the other hand, M5_SZ2_F01_S2's association with *Sulfuritalea hydrogenivoran* points to sulfur and hydrogen cycling. The relationship between L8_SZ2_F8_S4 and *Brevundimonas species (B. viscosa, B. DS20*) may indicate adaptation to nutrient-poor environments. Finally, L8_SZ2_F01_S7's association with *Halothermothrix orenii*, *Paenibacillus*, and *Borreliaparkeri* suggests extremophilic traits or host-related interactions. Future research should combine metabolic pathway analysis with cultivation efforts to confirm these evolutionary connections and examine their biogeochemical significance. Overall, these findings enhance our understanding of microbial population structure in niche-specific settings and show the value of phylogenomics in unraveling complex environmental microbiomes.

Microbial adaptation to extreme nitrate and metal stress at the eFRC has been documented at multiple scales. Early metagenomic studies revealed strong taxonomic simplification and enrichment of denitrifying *Rhodanobacter* in highly contaminated wells, accompanied by a concurrent loss of respiratory diversity (Green et al., 2010; Green et al., 2012; Hemme et al., 2010; Hemme et al., 2016; Hemme et al., 2015). Genome-resolved work subsequently demonstrated that streamlined lineages, such as Patescibacteria, persist with minimal functions under stress (Tian et al., 2020). Enrichment experiments confirmed that denitrification remains active even under multimetal toxicity (Thorgersen et al., 2019) and deterministic community assembly processes dominate in highly contaminated zones (Ning et al., 2024). Other studies reported that while taxonomic diversity declines with stress, functional diversity is buffered (Fang et al., 2025), suggesting resilience at the metabolic level. Most recently, (Lui et al., 2024; Lui et al., 2025) started to expand genomic resources for the eFRC. Our results are currently used to map the ENIGMA isolate genomes to the SSO metagenomes. Our data will assist in determining which strains the ENIGMA team will phenotype.

Our analysis extends this framework by revealing that pathways within MAGs are not randomly distributed but form cohesive, co-occurring functional blocks. Pairwise pathway correlations revealed strong coupling between carbon and nitrogen utilization, energy metabolism and nucleotide and cofactor biosynthesis, transporters and CRISPR defenses, and motility and substrate degradation. Such functional linkage suggests that microbial genomes are structured around integrated ecological strategies rather than isolated traits. This provides genome-resolved support for the concepts of functional buffering and dependency (Braga et al., 2021), extending beyond taxonomic observations to demonstrate how stress-adapted microbes organize their genomes for survival.

Our results complement the dissertation of Putt (2022) on the eFRC, who demonstrated that Patescibacteria are heterogeneously distributed and transported preferentially through coarse aquifer material. We observed Patescibacteria in fine fractions, consistent with their episymbiotic lifestyles (Tian et al., 2020), which supports their persistence under contamination. Similarly, our findings align with Walker (2024) dissertation on the eFRC, who demonstrated that rainfall pulses drive rapid microbial succession. But while Walker (2024) emphasized temporal turnover, our results prioritize the internal structuring of genomes as adaptive modules. Overall, these

studies demonstrate that both physical transport and genomic coupling shape microbial responses in contaminated aquifers.

Functional stratification across wells further emphasizes this point. Flow-path EFP01 and upper U2-SZ2 wells carried expanded repertoires of polysaccharide-degrading enzymes, denitrification modules, and metal transporters, confirming their role as microbial "hot spots" (Kuzyakov and Blagodatskaya, 2015) under nitrate- and Mn-rich stress. In comparison, the lower L8-SZ2 wells exhibited reduced carbon degradation and denitrification, consistent with oligotrophic conditions and a trend of higher taxonomic but lower functional richness (Wang et al., 2023). This selective enrichment of nutrient assimilation and stress-response modules, alongside flexible energy metabolism and motility, aligns with broader frameworks of microbial stress adaptation, including the Integrated Stress Response. It is also aligned with the stringent response, a conserved bacterial program enabling survival under nutrient limitation and other environmental stresses (Urwin et al., 2024).

We observed clustered CRISPR subtypes within MAGs, consistent with a previous study (Ning et al., 2024), who identified viral pressure as a determinant of community assembly. *Caudoviricetes* dominated across wells, with niche-specific families (Corticoviridae, Smacoviridae) and integrated proviruses also detected, consistent with other eFRC viral studies (Kothari et al., 2021). A study (Wu et al., 2024) demonstrated that Patescibacteria are highly susceptible to viral infection, a finding that align with our detection of episymbionts in fine fractions. Collectively, these results support the central role of viruses as ecological drivers and demonstrate that microbial genomes maintain multi-layered defense systems in response. Multiple lines of evidence indicate strong and spatially structured viral pressure in the aquifer. Functionally, defense capacity clustered exactly where viral ecology appeared most intense, with high-defense counts in upper and flow-path wells and low-defense counts at depth. The co-enrichment of transporters and CRISPR suggests a practical pairing-rapid uptake and efflux alongside multilayer antiviral defense. It is consistent with membrane-associated CRISPR effectors (CorA-family, Csx28, Cam1) (Baca et al., 2024; VanderWal et al., 2023).

Functional results complement statistical findings. Enrichment of *Rhodanobacter* under high uranium and nitrate stress ($R^2 \approx 0.50$) directly supports prior observations at Oak Ridge (Hemme et al., 2010, 2015, 2016; Thorgersen et al., 2019). Conversely, Patescibacteria

enrichment in L8-SZ2 aligns with findings from Tian et al. (2020), featuring streamlined survival strategies under low-energy, low-stress conditions.

Mobile genetic elements were prolific. GeNomad annotated 383 plasmids and 275 viruses in U2-SZ2 (F8), dominated by *Caudoviricetes*. EFP01 stood out with >1,100 plasmids and ~600 viruses. EFP01 also included proviruses of up to 244 kb, featuring potential for horizontal gene transfer. Genomes from U2-SZ2 carried elevated transporter repertoires and CRISPR defenses, consistent with adaptation to extreme metal and viral stress (Thorgersen et al., 2019). Suppressed dsr genes in nitrate-rich zones aligned with shifts from sulfate reduction to denitrification (Anantharaman et al., 2016a; He et al., 2010; Michael et al., 2024). The abundance of plasmids and viruses in both contaminated and transitional wells reinforces the notion that resistance traits spread rapidly across aquifers (Kothari et al., 2019a, 2019b). The dominance of *Caudoviricetes* reflects global virome studies (Roux et al., 2021). At the same time, detection of diverse families emphasizes broad host-virus networks. Viral-colloid associations observed here and previously ((Xing et al., 2020) further demonstrate colloids as dispersal vehicles.

Carbon utilization functions showed clear stratification across wells, with the highest functional counts in L8SZ2F8_S4 (19 functions) and U2SZ2F8_S5 (19 functions), followed closely by EFP01F8_S6 (17 functions). In comparison**,** the lowest abundance was recorded in L8SZ2F01_S7 (9 functions), representing a more oligotrophic profile. These differences were statistically supported: PERMANOVA (n = 40 samples, pseudo-F = 8.47, R^2 = 0.231, p = 0.001) confirmed significant variation in carbon potential across wells, with betadisper testing (p = 0.42) indicating that the effect was due to centroid differences rather than variance heterogeneity.

These findings are consistent with the long-standing eFRC field studies. Michael et al. (2024) reported highly reproducible microbial successions following acetate amendments, indicating that carbon metabolism is a primary driver of community restructuring. Similarly, Smith et al. (2015) described eFRC bacterial communities as “quantitative biosensors,” with carbon functions tightly linked to contaminant concentrations. Our observations confirm these dynamics: U2-SZ2 and EFP01, characterized by hydrological mixing and elevated organic flux, supported broader carbon repertoires. The L8-SZ2 contracted to narrower functional sets under oligotrophic conditions. Global analogs support this interpretation. (Chaudhari et al., 2024) observed streamlined carbon repertoires in deep aquifer MAGs. This study features an ecological

strategy whereby deep, energy-limited environments favor minimalistic carbon-processing repertoires. Thus, the broader capacity of U2-SZ2 and EFP01 likely reflects higher dissolved organic carbon fluxes and transient substrates that select for metabolic versatility.

Organic nitrogen pathways paralleled carbon metabolism, with maxima in U2SZ2F01_S8 (16 functions) and EFP01F8_S6 (16), and reduced values in L8SZ2F01_S7 (11 functions) and M5SZ2F01_S2 (11 functions). These distributions align with nitrate-rich upper aquifer zones of the eFRC plume, often exceeding 10 mM, whereas the deeper L8-SZ2 shows much lower nitrate levels. PERMANOVA (n = 40, pseudo-F = 9.21, R^2 = 0.247, p = 0.001) confirmed significant nitrogen differences across wells, and Mantel correlations showed strong associations with nitrate concentrations (r = 0.54, p = 0.002). Genome-resolved data revealed enrichment of denitrification genes in U2-SZ2, including narGHI and napAB for nitrate reduction, and nirS and nirK for nitrite reduction. However, nosZ was often absent, indicating incomplete denitrification. This trend aligns with Hemme et al. (2010, 2015, 2016), who found *Rhodanobacter* dominance under extreme nitrate and metal stress, often accompanied by truncated respiratory chains, and Thorgersen et al. (2019), who observed the persistence of denitrification under multimetal toxicity but incomplete pathways. The absence of *nosZ* suggests potential for nitrous oxide accumulation, consistent with eFRC flux measurements. In comparison, sulfate reduction genes (*dsrAB*) were sparse across wells, especially in U2-SZ2, consistent with nitrate outcompeting sulfate as the terminal electron acceptor. This metabolic suppression parallels the Rifle IFC site, where nitrate redirection of respiratory capacity was documented (Anantharaman et al., 2016b). Our data extend this observation, confirming that nitrate-driven inhibition of sulfate reduction is a reproducible phenomenon in contaminated aquifers. The functional contrasts were particularly sharp in L8-SZ2, where reduced nitrate exposure corresponded with minimal nitrogen metabolism. This supports the interpretation of Ning et al. (2024) that deterministic assembly processes under contamination select for resilient nitrate-utilizing communities in upper zones, while deeper strata retain minimal nitrogen cycling. Collectively, these results confirm that nitrate and uranium stress jointly structure microbial nitrogen metabolism, with incomplete denitrification emerging as a hallmark of contaminated zones.

Energy-associated modules were relatively conserved, ranging from 7 in L8SZ2F01_S7 to 13 in M5SZ2F8_S1, with most wells encoding 11-12 modules. These included oxidative phosphorylation and hydrogenase systems. Although differences among wells were weaker than

for carbon or nitrogen, they were still statistically significant: PERMANOVA (n = 40, pseudo-F = 2.14, R^2 = 0.081, p = 0.031). Coupling between energy generation and biosynthesis was evident. Samples with elevated energy modules, such as U2SZ2F8_S5 (12) and M5SZ2F8_S1 (13), also showed high nucleotide and cofactor repertoires (>130 functions). Mantel testing confirmed this correlation (r = 0.47, p = 0.004). This co-occurrence features a metabolic strategy in redox-stressed environments: genomes that invest in energy capture also maintain biosynthetic pathways to sustain redox balance and growth.

These results align with prior studies. Fang et al. (2025) reported that while taxonomic diversity declines in nitrate- and metal-stressed environments, functional breadth is buffered by redundancy in energy and biosynthetic functions. Anantharaman et al. (2016) similarly observed that groundwater microbiomes retain oxidative phosphorylation across redox gradients. Our findings confirm this resilience at eFRC.

Nucleotide biosynthesis and cofactor pathways were abundant, ranging from 104 in L8SZ2F01_S7 to 134 in U2SZ2F8_S5. These included purine and pyrimidine synthesis and cofactors such as NAD, FAD, and heme. Their co-occurrence with energy modules reinforces the idea of linked metabolic strategies under geochemical stress. This observation is consistent with Hemme et al. (2016), who showed that core biosynthetic functions are retained despite environmental stress, and Fang et al. (2025), who emphasized buffering of nucleotide metabolism. Our results extend these findings by providing genome-resolved confirmation that nucleotide and cofactor biosynthesis co-varies with energy metabolism in contaminated aquifers.

Transporters dominated functional repertoires, consistently exceeding 100 across samples, with maxima in U2SZ2F01_S8 (131) and U2SZ2F8_S5 (127). L8SZ2 carried fewer (118). PERMANOVA (n = 40, pseudo-F = 11.62, R^2 = 0.291, p = 0.001) identified transporters as the strongest axis of functional separation. Fe (II) feoB transporters were abundant, while Fe (III) uptake systems were absent, consistent with reduced aquifer conditions. Mantel tests revealed significant correlations between transporter repertoires and uranium (r = 0.58, p = 0.001) as well as colloid flux (r = 0.49, p = 0.003), showing how both geochemistry and hydrology shape transporter inventories. These results are consistent with those of Kothari et al. (2019a, 2019b), who described plasmids enriched in efflux systems that carry multimetal resistance genes. Our genome-resolved data confirm that such transporter enrichment is not plasmid-restricted but pervasive across microbial communities. Similar redox-specific

transporter trends have been observed in groundwater and sediment microbiomes (Anantharaman et al. 2016, Zhang et al., 2023).

CRISPR defenses were highest in upper wells (27 in U2SZ2F01_S8, 26 in M5SZ2F8_S1, 25 in EFP01F8_S6) and lowest in L8SZ2 (8-9). PERMANOVA (n = 40, pseudo-F = 7.32, R^2 = 0.202, p = 0.001) confirmed these differences, and Mantel correlations linked CRISPR abundance with viral counts (r = 0.52, p = 0.002). These inventories feature the potential for horizontal gene transfer in contaminated and transitional zones. Mantel tests confirmed associations between plasmids and uranium (r = 0.44, p = 0.006). These results are consistent with eFRC plasmidome findings (Kothari et al., 2019a, 2019b) and global virome studies (Roux et al., 2021). The detection of *Caudoviricetes* dominance, alongside Zobellviridae and Autographiviridae, demonstrates broad host-virus networks. Viral-colloid associations observed in this study and microscopy work demonstrate that colloids function as vectors for dispersal and HGT, providing direct support for our overarching hypothesis.

Translation-associated functions were uniformly distributed, with no significant differences across wells (PERMANOVA n = 40, pseudo-F = 1.12, R^2 = 0.032, p = 0.21). Ribosomal proteins and RNA polymerase subunits remained intact in all MAGs, even those with streamlined metabolic repertoires. This result reflects the evolutionary conservation of translation as a non-negotiable genomic backbone. It aligns with Tian et al. (2020), who showed streamlined Patescibacteria retain translation. It also supports Lui et al. (2024), who emphasized the stability of information-processing functions across the eFRC MAGs.

Motility was enriched in U2SZ2 samples (such as U2SZ2F8_S5, which contained multiple FlgB-FlgF and FlgE proteins), but absent in L8SZ2. PERMANOVA (n = 40, pseudo-F = 5.89, R^2 = 0.174, p = 0.002) confirmed well-level differences. Motility likely supports persistence in dynamic zones where resource patches are transient. At the same time sessile strategies dominate in oligotrophic, stable aquifers. Ning et al. (2024) emphasized the importance of deterministic assembly in contaminated zones, where dispersal traits enhance survival under fluctuating environmental gradients. Our data supports this, showing that investment in motility is ecologically rational in U2-SZ2 but disadvantageous in L8-SZ2.

At the Hanford 300 Area (WA, USA), uranium mobility is strongly modulated by the Columbia River stage, which drives mixing and desorption processes in the hyporheic corridor. These hydrologic-geochemical controls are linked to deterministic (selection-dominated)

microbial assembly, with selection strongest where river-groundwater exchanges are most dynamic (Stegen et al., 2016; Zachara et al., 2016). In our dataset, colloids were only weakly related to ASV dissimilarities (Mantel r = 0.055, p = 0.26, n = 40). That demonstrated that community structure is primarily geochemically filtered, while colloids can still act as carriers in groundwater. The classic field demonstration of colloid-facilitated plutonium transport is (Kersting et al., 1999) at the Nevada Test Site. At that site, Pu traveled kilometers predominantly in the colloidal fraction. At the Savannah River Site (SC, USA), Pu is predominantly non-colloidal: size-fractionation showed <4% of ^{239}Pu, ^{240}Pu in the colloidal fraction (Dai et al., 2002). Similar low colloid association was observed at Hanford's 100K-Area (Dai et al., 2005), supporting the view that colloids were a minor Pu transport phase at these sites
At the Rifle Integrated Field Research Challenge (RIFRC) in Colorado, USA, repeated acetate amendments produced reproducible geochemical and microbial successions, and genome-resolved metagenomics identified MAG-encoded capacities for denitrification, carbon degradation, and transport systems (Anantharaman et al., 2016). These trends align with our DRAM annotations (U2-SZ2 MAGs carried 131 transporter genes and 27 CRISPR systems, compared to 118 transporters and 9 CRISPR systems in L8-SZ2). These findings show that when redox conditions fluctuate, microbes repeatedly invest in the same sets of functions that support survival. In the Zelenogorsk region of Russia, environmental monitoring near the Electrochemical Plant has documented nitrate-rich groundwater plumes and noticeable redox-controlled, including microbial, processes that influence actinide mobility (Boguslavsky et al., 2020). Subsequent work has assessed the risks of colloidal and pseudo-colloidal actinide transport in nitrate-contaminated groundwater and demonstrated that microbial activity can promote aggregation of colloids during and after bioremediation, thereby reducing their mobility (Safonov et al., 2022). At other Russian uranium-sludge sites, in-situ biogeochemical barriers employing denitrifying bacteria have been implemented under extremely high nitrate conditions to enhance contaminant immobilization (Boguslavsky et al., 2020). While these studies establish geochemical and microbial conditions that could facilitate colloid-associated contaminant transport, none provide direct evidence of virus-on-colloid movement within the Zelenogorsk system. In contrast, our analyses of the EFP01 well detected 1,155 plasmids and 594 viruses (including 491 classified as *Caudoviricetes*) in the operationally defined colloidal fraction obtained by size-based separation. While this does not directly prove physical attachment, it

indicates that genetic elements are concentrated in the colloid-associated size range, consistent with the potential for colloids to act as hidden vectors of genetic material, even where explicit viral co-transport has not yet been demonstrated. At the Semipalatinsk Nuclear Test Site (northeastern Kazakhstan), size-fractionation and ultrafiltration studies show that shows that Pu, Am, and U are present in filtered (<0.45 μm) waters from wells, streams, lake craters, and Degelen tunnel discharges. Size-resolved analyses identified sub-micron (including <3 nm) colloidal and pseudocolloidal carriers for actinide transport. Site-wide particle studies further document U- and Pu-bearing heterogeneous particles (Fe-oxyhydroxide/clay/organic matrices) whose behavior (and thus mobility) varies with redox conditions (Lukashenko et al., 2020; Toropov, 2020; Vintró et al., 2009). As at Zelenogorsk, no published studies exist for virus-on-colloid co-transport at Semipalatinsk.

Analyses of ASV-metal associations across n = 40 samples revealed several microbial lineages consistently enriched under uranium, manganese, nitrate, and rubidium stress ($\beta > 5$, FDR < 1×10^{-6}). *Terracidiphilus* and *Occallatibacter* (Acidobacteria Subgroup 1) were strongly enriched in the uranium-rich L8-SZ2 zone. *Sediminibacterium* (Chitinophagaceae) was found to track uranium, boron, and rubidium, particularly in M5-SZ2. Rhizobiales ASVs responded to uranium-nitrate interactions in U2-SZ2, and *Reyranella* (Reyranellaceae) was enriched with manganese and uranium in M5-SZ2. Additional uranium responders included Ilumatobacteraceae and Holophagaceae. At the same time, several unclassified ASVs also exhibited reproducible uranium-nitrate responses, suggesting the presence of novel lineages adapted to the contaminated aquifer. These results both confirm and extend the trends reported by Smith et al. (2015), who linked microbial communities across 93 eFRC wells to 26 geochemical parameters, identifying uranium and nitrate as the strongest predictors (Kendall's $\tau \approx 0.25$-0.55) and emphasizing uranium- and nitrate-enriched Acidobacteria and Rhizobiales. Like Smith (2015), we observed uranium and nitrate as core selective pressures. However, our regressions revealed additional strong predictors-manganese ($R^2 = 0.66$), boron (0.60), and rubidium (0.59) - that were not previously emphasized. These broader associations, coupled with higher explanatory power (uranium $R^2 \approx 0.52$ vs. Smith's $\tau \approx 0.5$), demonstrate that microbial communities function as biosensors not only for uranium and nitrate but also for a wider range of trace metals and metalloids, such as tungsten, zirconium, boron, and rubidium, in the eFRC.

Conclusion

This chapter shows how extreme geochemical gradients at the Y-12 eFRC structure affect groundwater microbiomes and their mobile gene pools. By combining 16S rRNA data, MAGs, viromes, colloid profiles, and detailed chemistry across SSO wells, we demonstrate that geochemistry is the primary filter, with colloids and mobile elements providing secondary but influential roles.

H1 fails to reject because microbial communities differ significantly among wells, track pH, nitrate, and metals, and display distinct ecological niches. For example, nitrate-rich at U2, redox-active at M5, and uranium-enriched at L8. Functional profiles reflect these gradients, with broader metabolic capacity in upper and transitional wells and specialized metal resistance at L8.

H2 also fails to reject because colloids explain slight variance alone but show an independent effect when controlling for chemistry. Colloid fractions concentrate plasmids and viruses, indicating potential for enhanced adaptation and horizontal gene flow. Case studies demonstrate *Rhodanobacter denitrificans* dominance under nitrate stress, streamlined Patescibacteria in fine fractions, and widespread enrichment of transporters and CRISPR defenses.

Overall, the results support a conceptual framework in which geochemistry sets community boundaries, colloids modulate the transport of cells and genes, and genomic plasticity under viral pressure enables adaptation. While limited in scope, this work establishes the first genome- and virome-resolved baseline for SZ2 wells at Y-12.

Acknowledgments

We thank our ENIGMA project team members: Jizhong Zhou ENIGMA's lab at the University of Oklahoma for extracting and processing 16S data files and preparing metagenomic shotgun sequencing files, as well as creating 16S plots. We also thank Dr. Lauren Lui at Berkeley National Laboratory ENIGMA team for advice and suggestions on metagenomic analysis.

Appendix 4: Figures

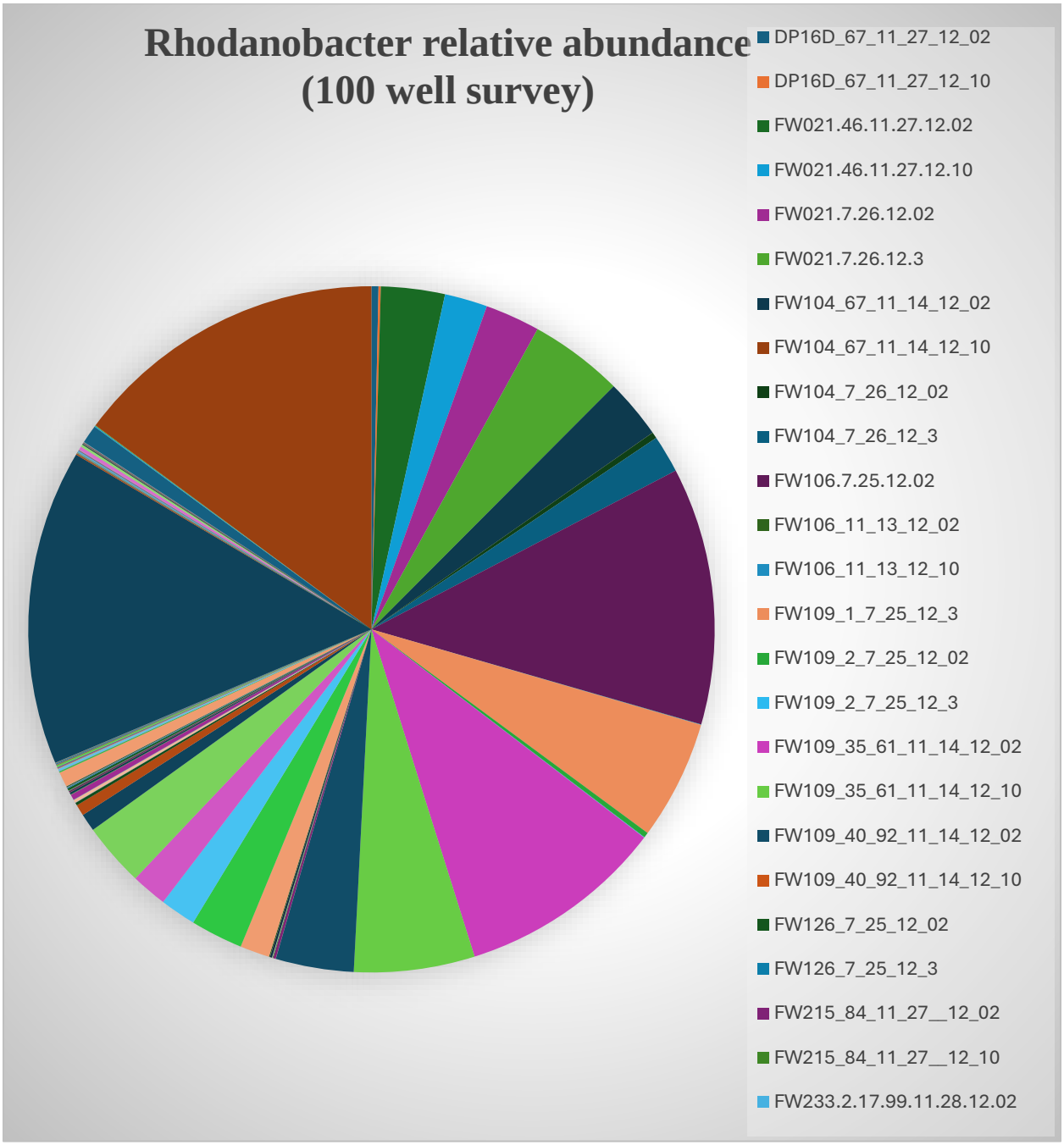

Data from (Smith et al., 2015)
Figure 4.1. *Rhodanobacter* relative abundance (100 well survey).

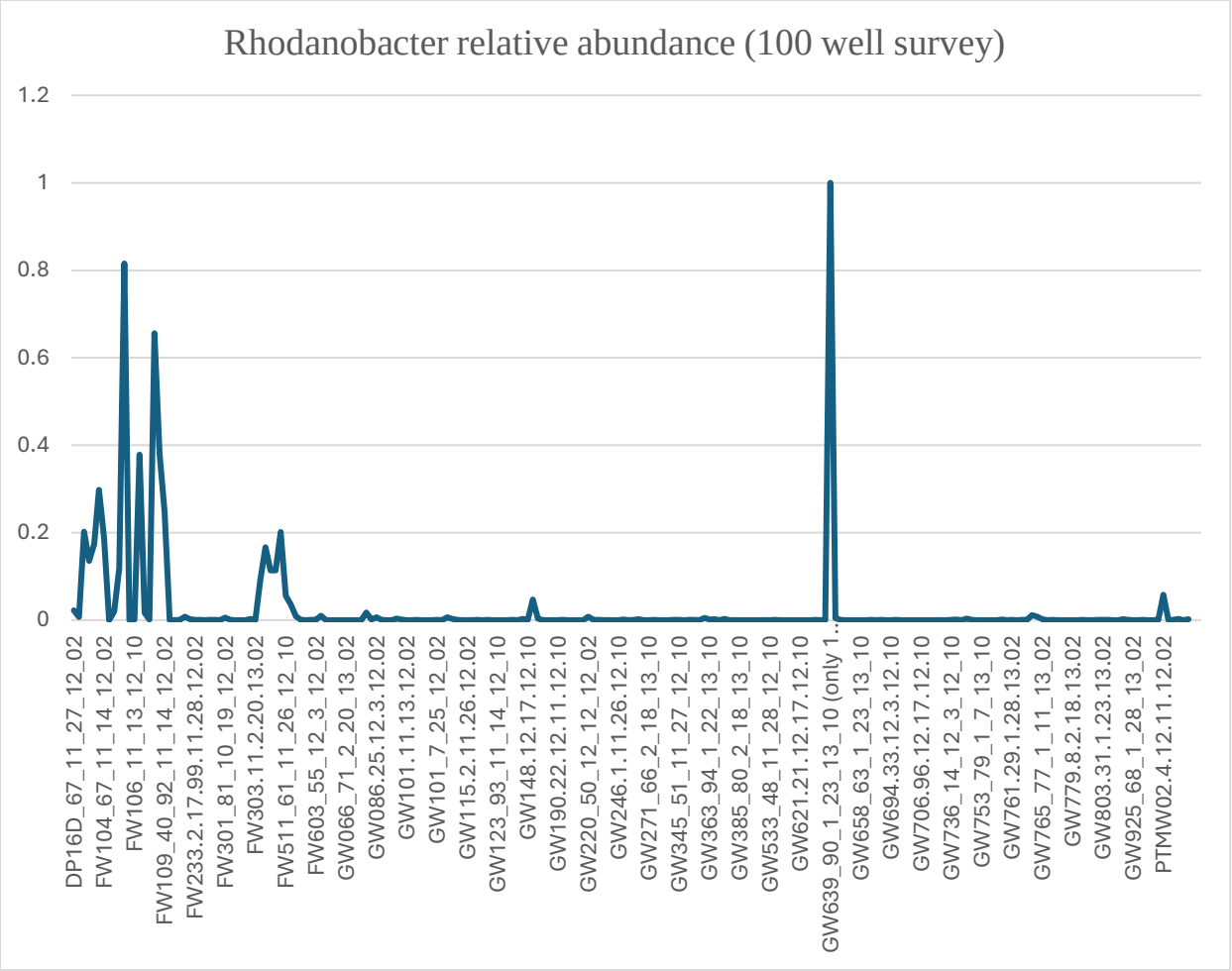

Data from (Smith et al., 2015)

Figure 4.2. *Rhodanobacter* relative abundance (100-well survey).

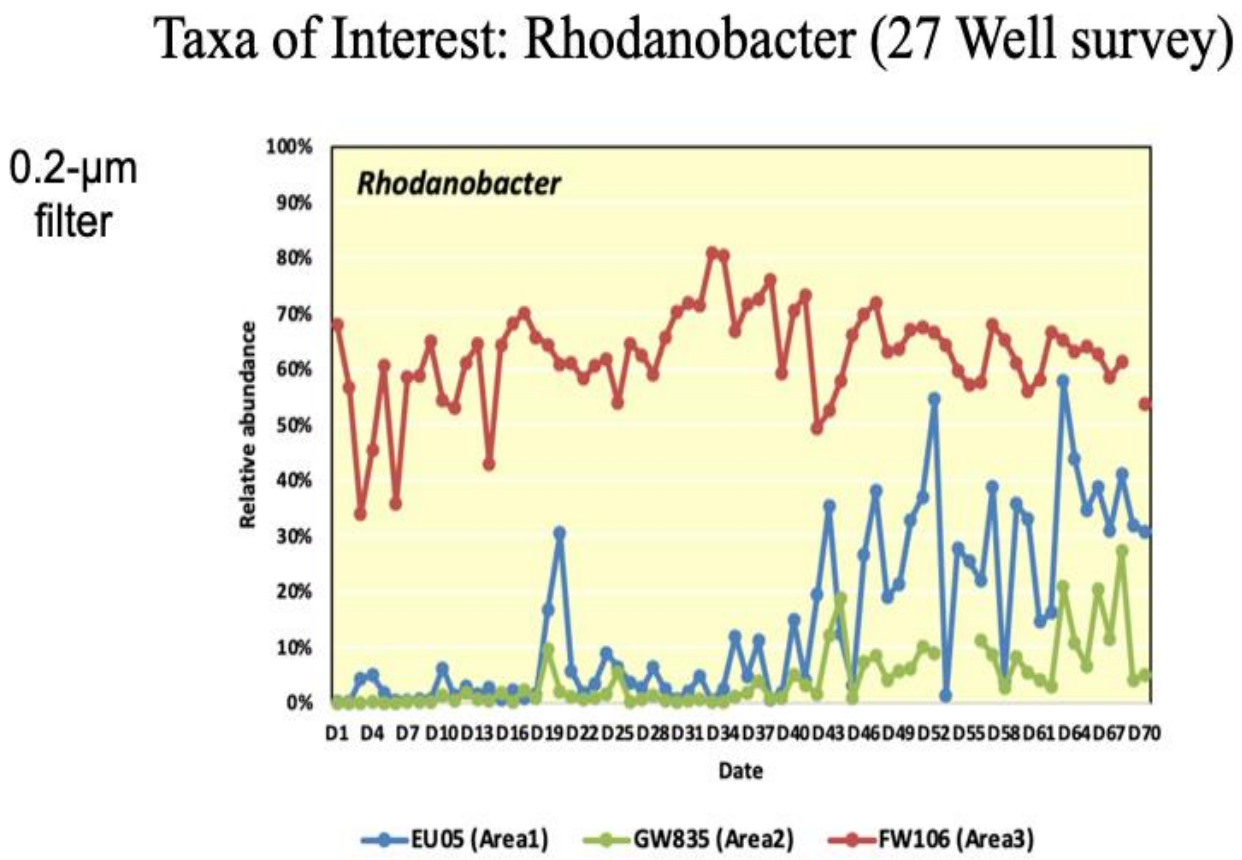

Data from (Walker, 2024)

Figure 4.3. *Rhodanobacter* relative abundance (27 well survey).

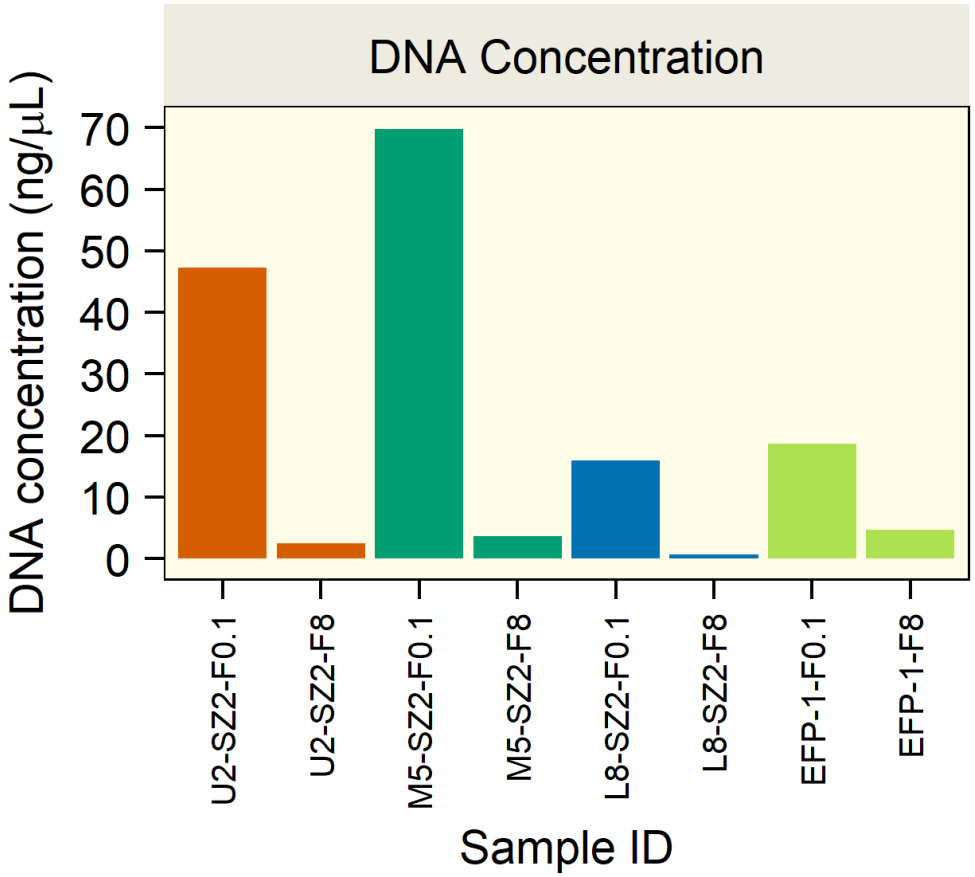

Courtesy of Zhou's lab

Figure 4.4. Environmental factors and DNA yield.

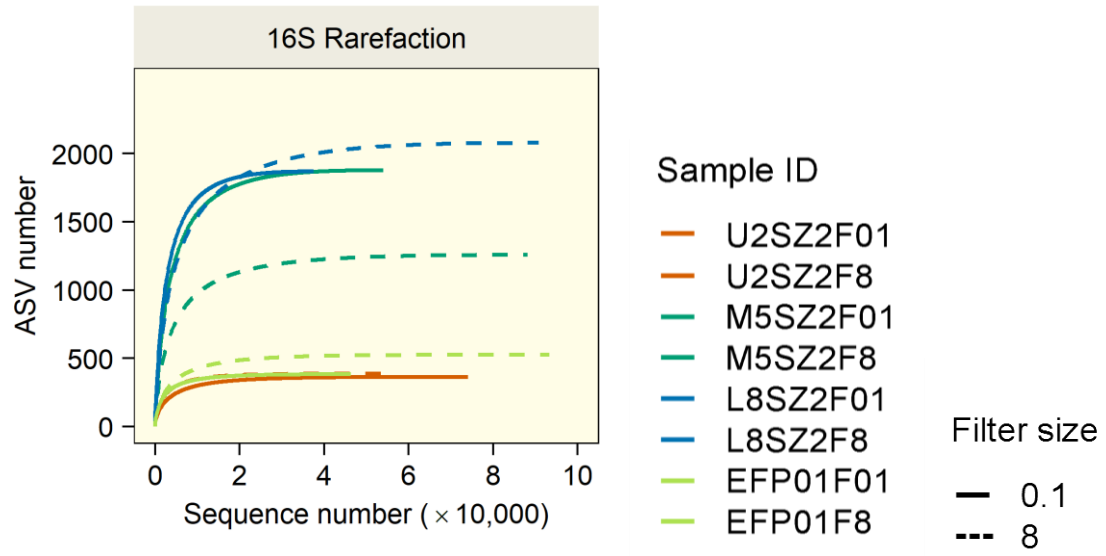

SampleID	Rarefied Sequencing Depth	Coverage
U2SZ2F01	37579	99.95%
U2SZ2F8	37579	99.98%
M5SZ2F01	37579	99.82%
M5SZ2F8	37579	99.75%
L8SZ2F01	37579	100.00%
L8SZ2F8	37579	99.48%
EFP01F01	37579	99.99%
EFP01F8	37579	99.92%

Courtesy of Zhou's lab

Figure 4.5. Sequencing efforts.

A. 16S Rarefication. B. Sequencing depth and coverage

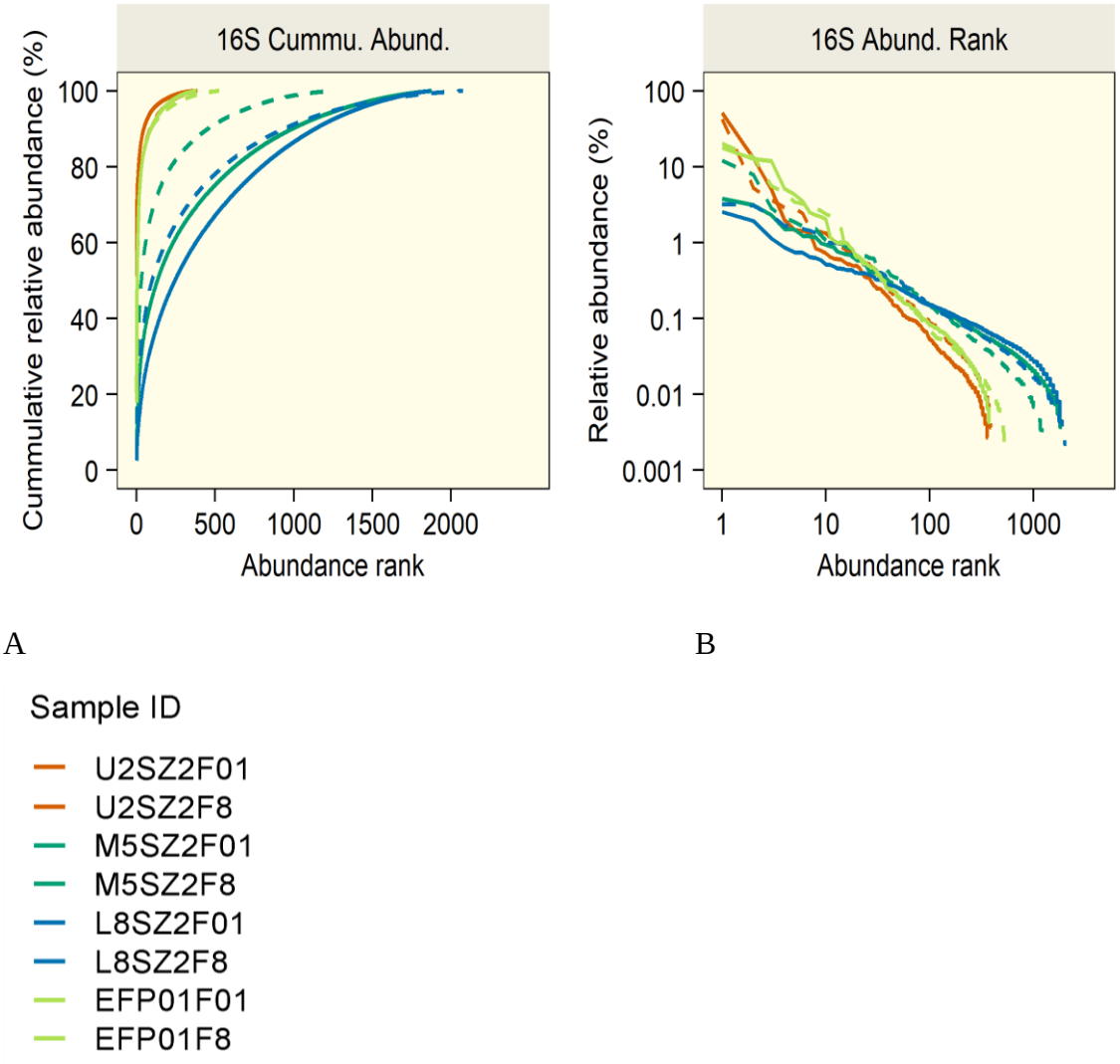

Courtesy of Zhou's lab

Figure 4.6. A. 16S Cumulative abundance. B. 16S Abundance rank.

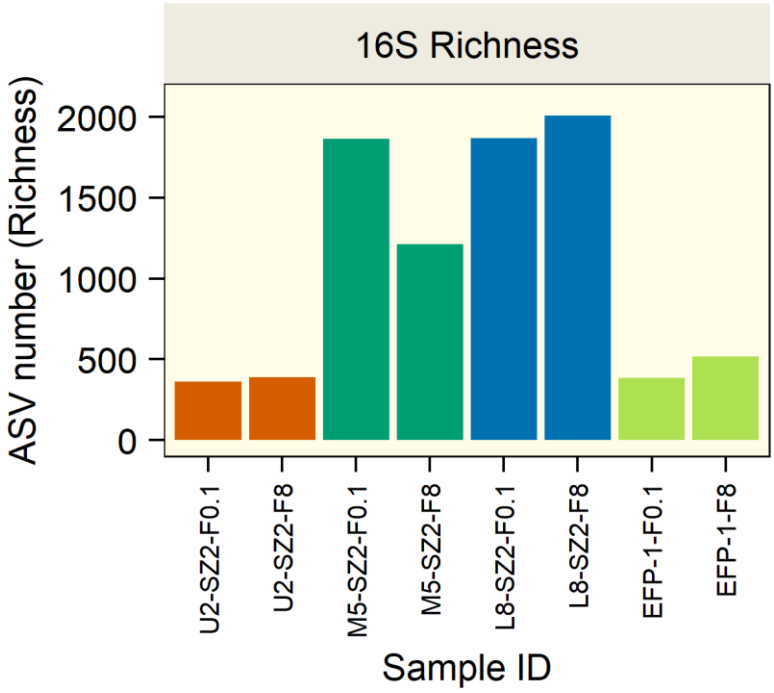

Courtesy of Zhou's lab

Figure 4.7. Alpha diversity 16S Richness.

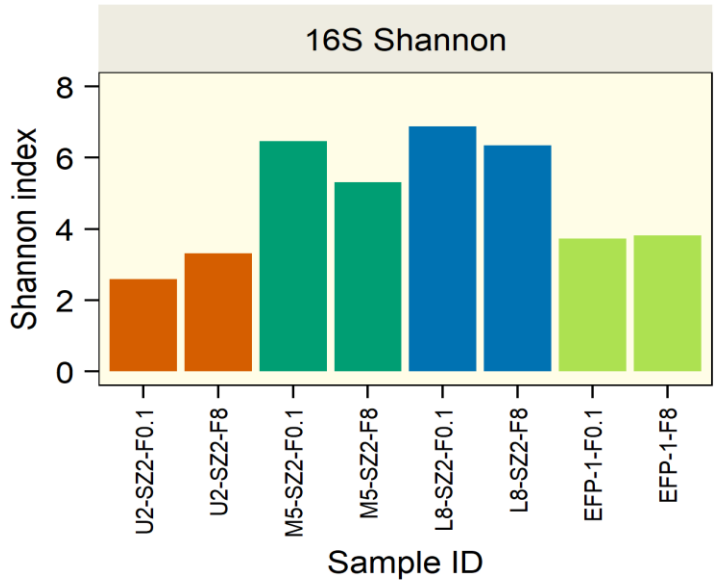

Courtesy of Zhou's lab

Figure 4.8 .Alpha diversity Shannon index.

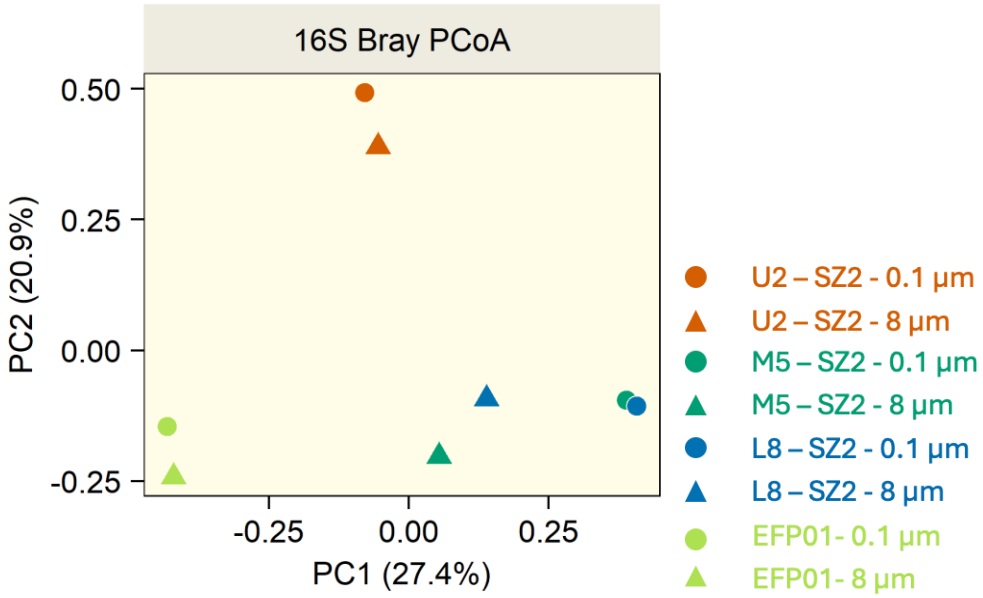


```
adonis2(formula = bc ~ Layer * FilterSize + Well, data = grp)
                Df SumOfSqs      R2      F Pr(>F)
Layer            1  0.63866 0.24549 2.5828  0.005 **
FilterSize       1  0.40325 0.15500 1.6308  0.072 .
Well             2  0.92492 0.35553 1.8702  0.046 *
Layer:FilterSize 1  0.14015 0.05387 0.5668  0.939
Residual         2  0.49455 0.19010
Total            7  2.60152 1.00000
---
Signif. codes:  0 '***' 0.001 '**' 0.01 '*' 0.05 '.' 0.1 ' ' 1
```

Courtesy of Zhou's lab

Figure 4.9. Beta diversity.

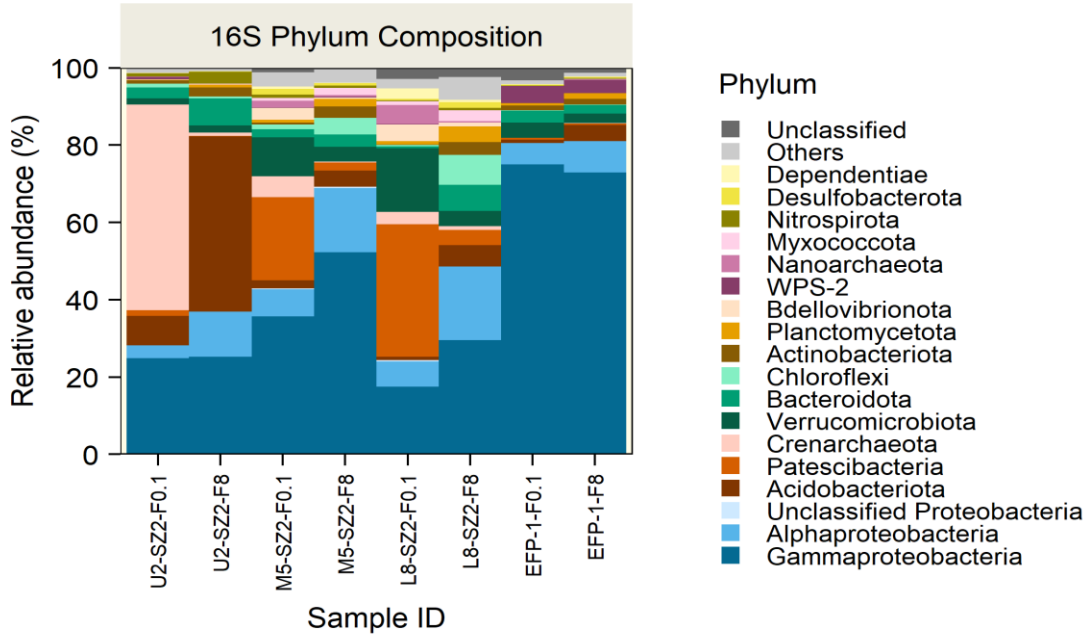

A

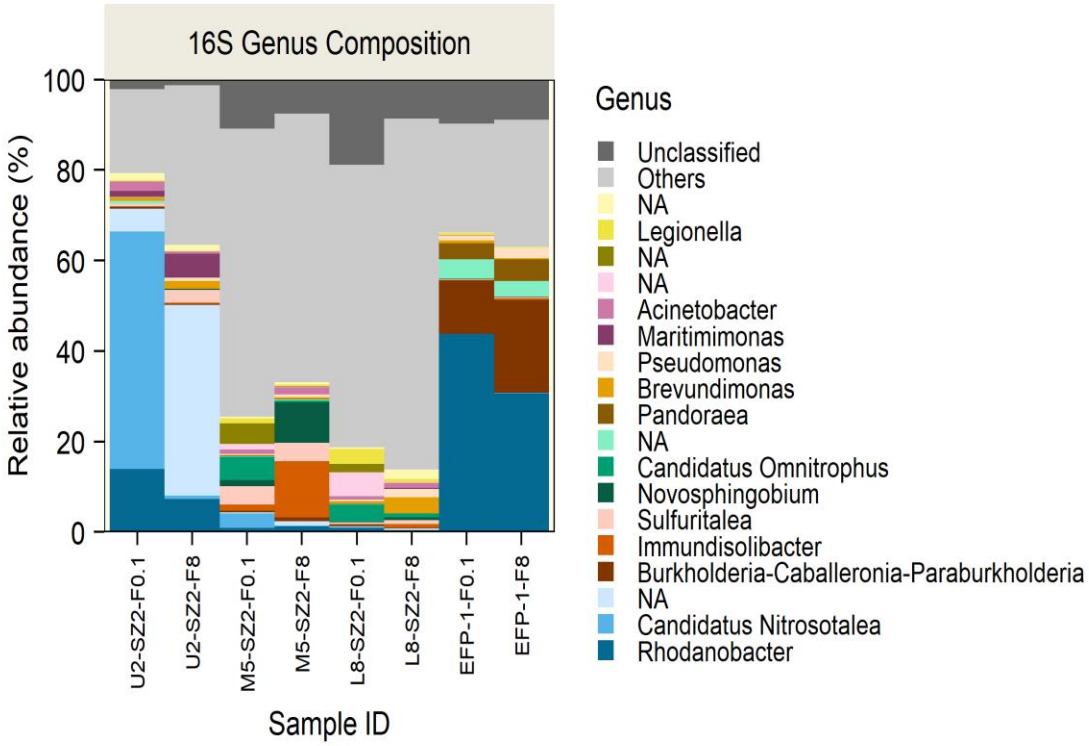

B

Courtesy of Zhou's lab

Figure 4.10. A. 16S Phylum composition. B. 16S Genus Composition.

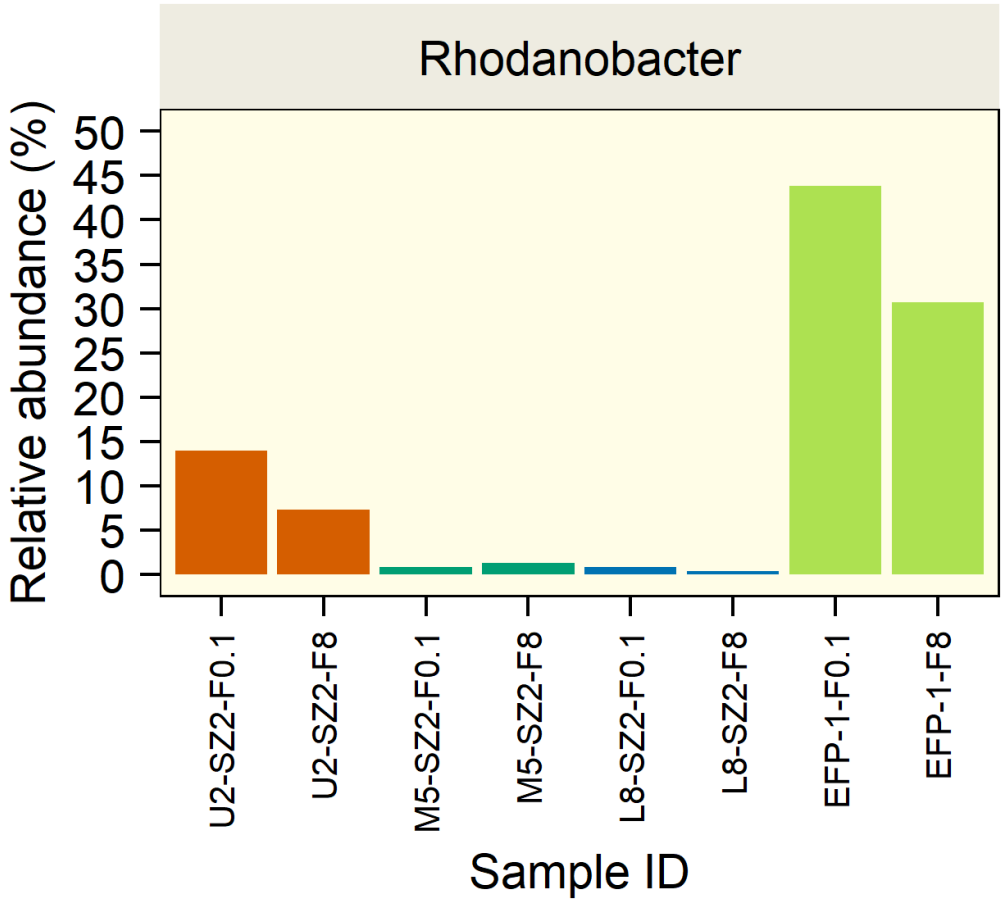

Courtesy of Zhou's lab

Figure 4.11. *Rhodanobacter* relative abundance.

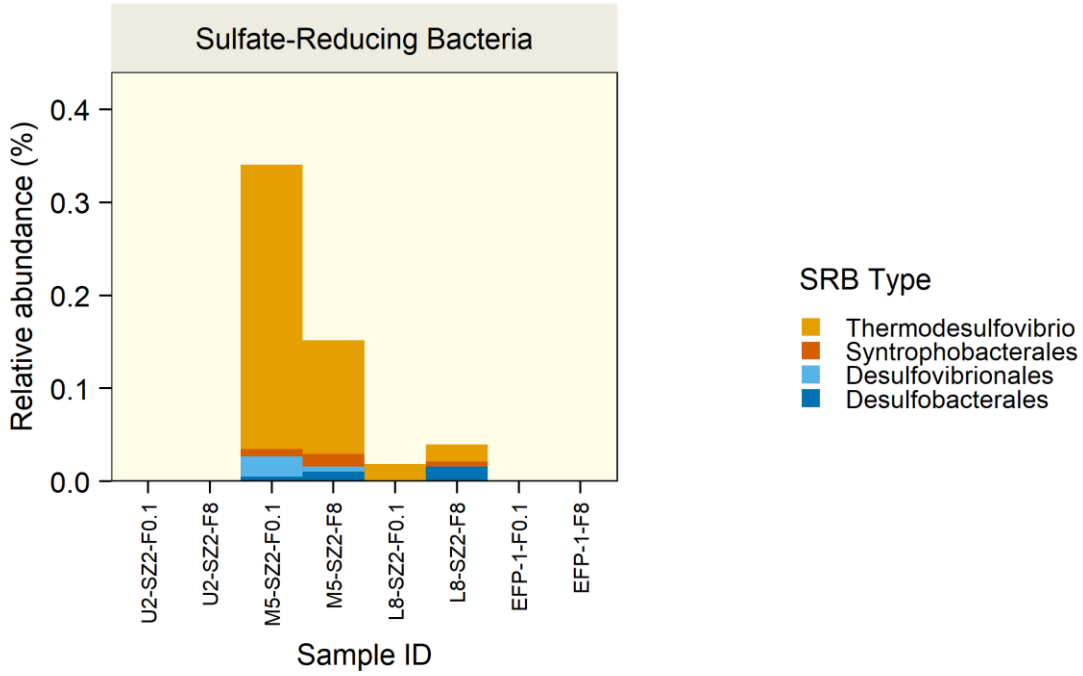

Courtesy of Zhou's lab

Figure 4.12. Sulfate-Reducing Bacteria.

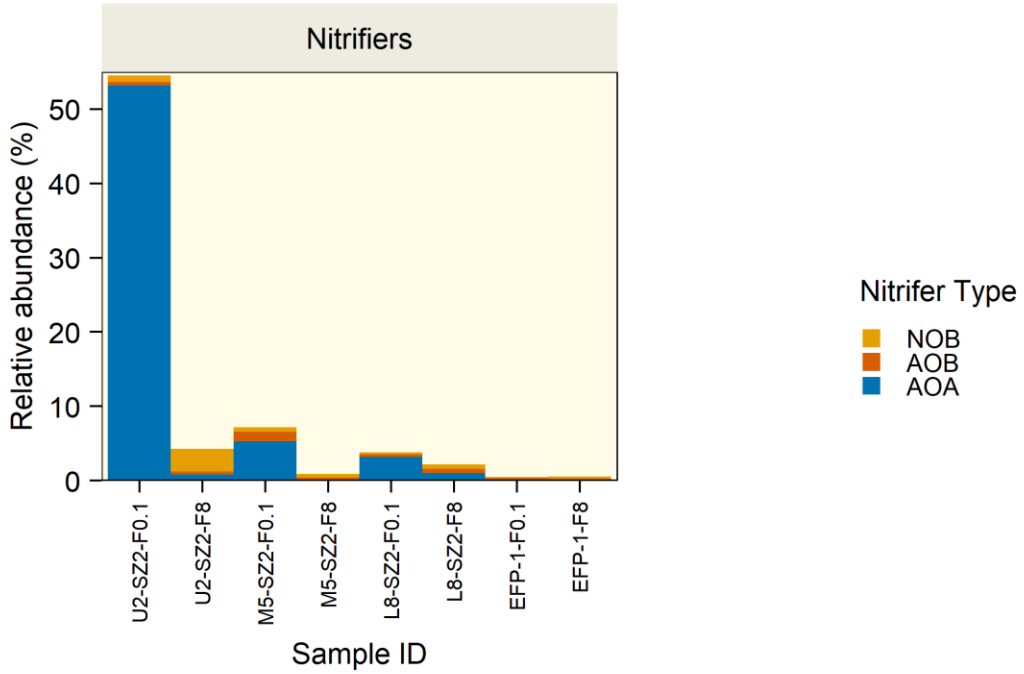

Courtesy of Zhou's lab

Figure 4.13. Nitrifiers.

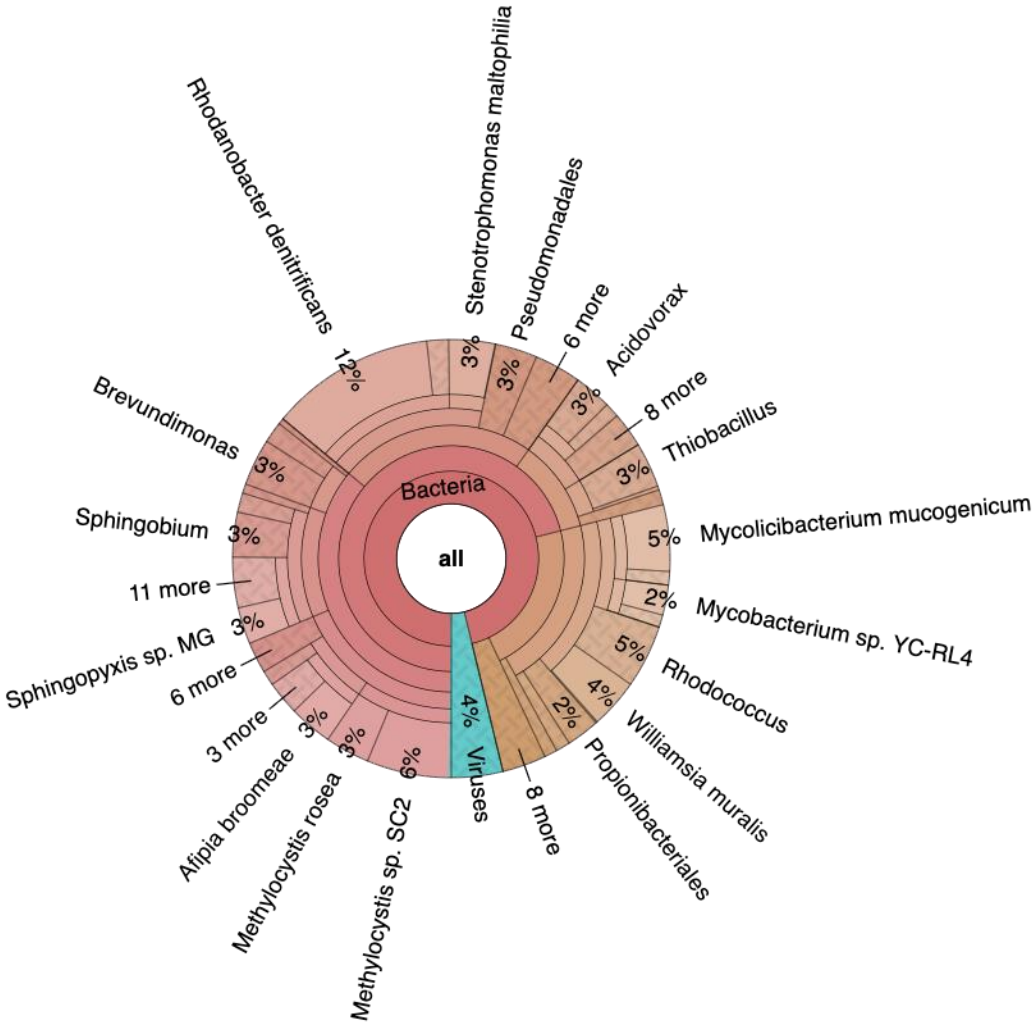

Figure 4.14. U2_SZ2_F8 GOTTCHA2 result.*Kbase.*

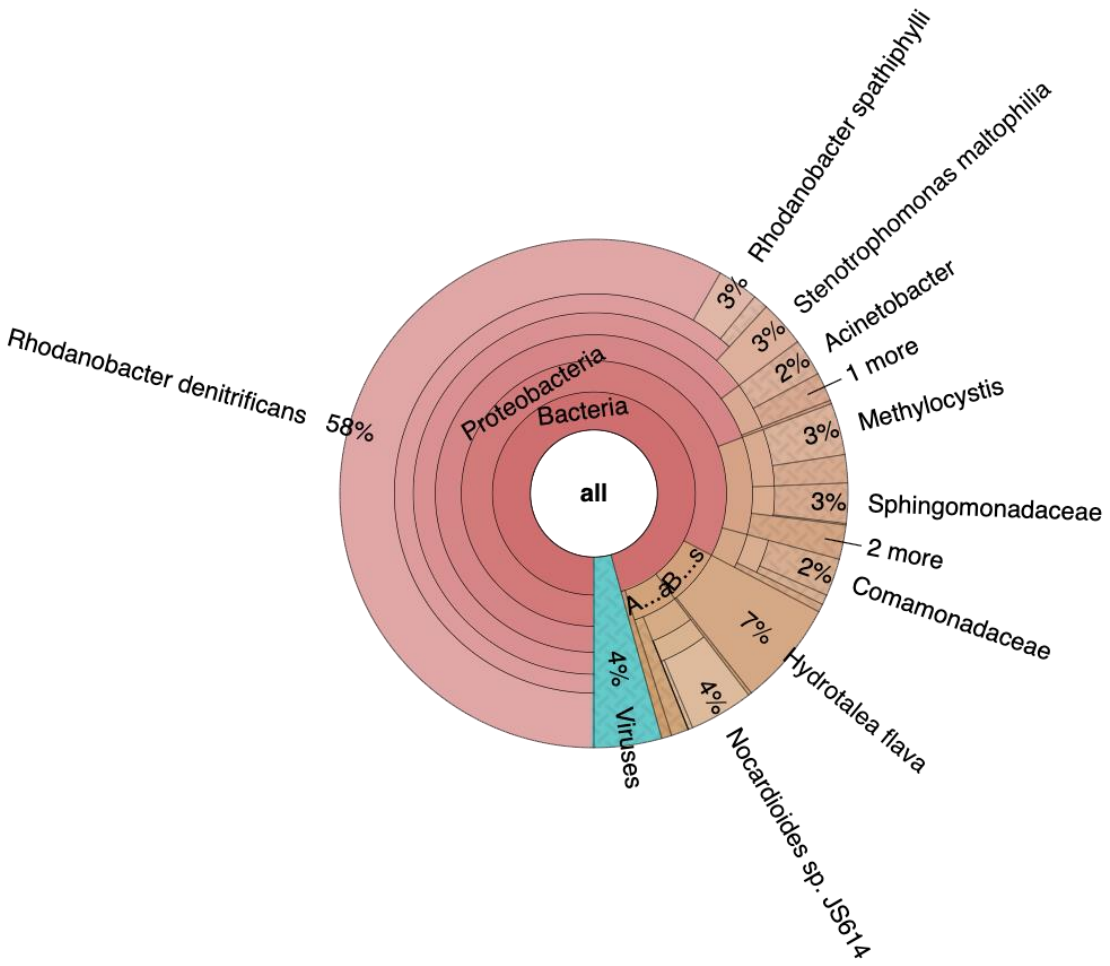

Figure 4.15. U2_SZ2_F01 GOTTCHA2 Result.

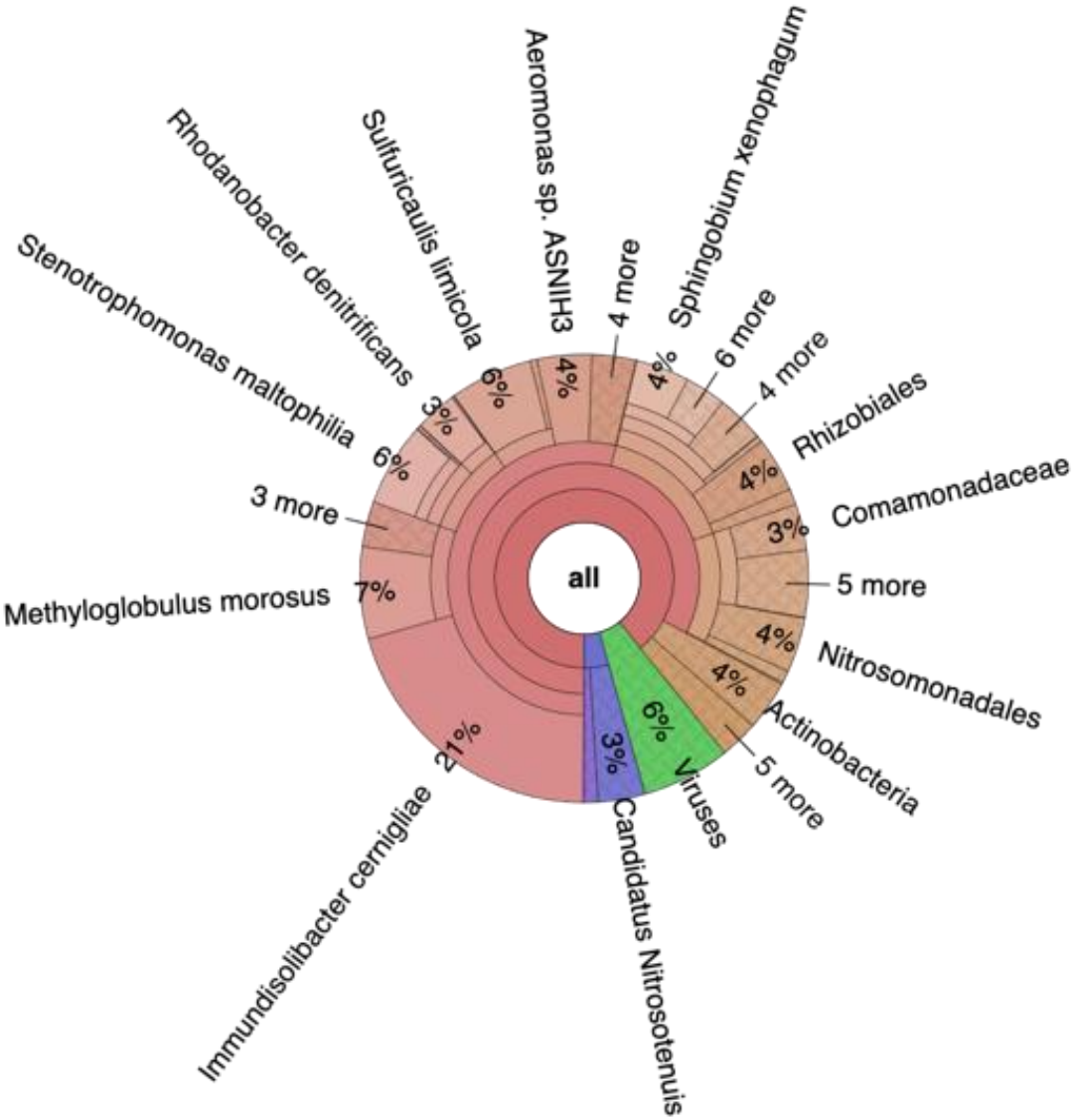

Figure 4.16. M5_SZ2_F01 GOTTCHA2 Result.

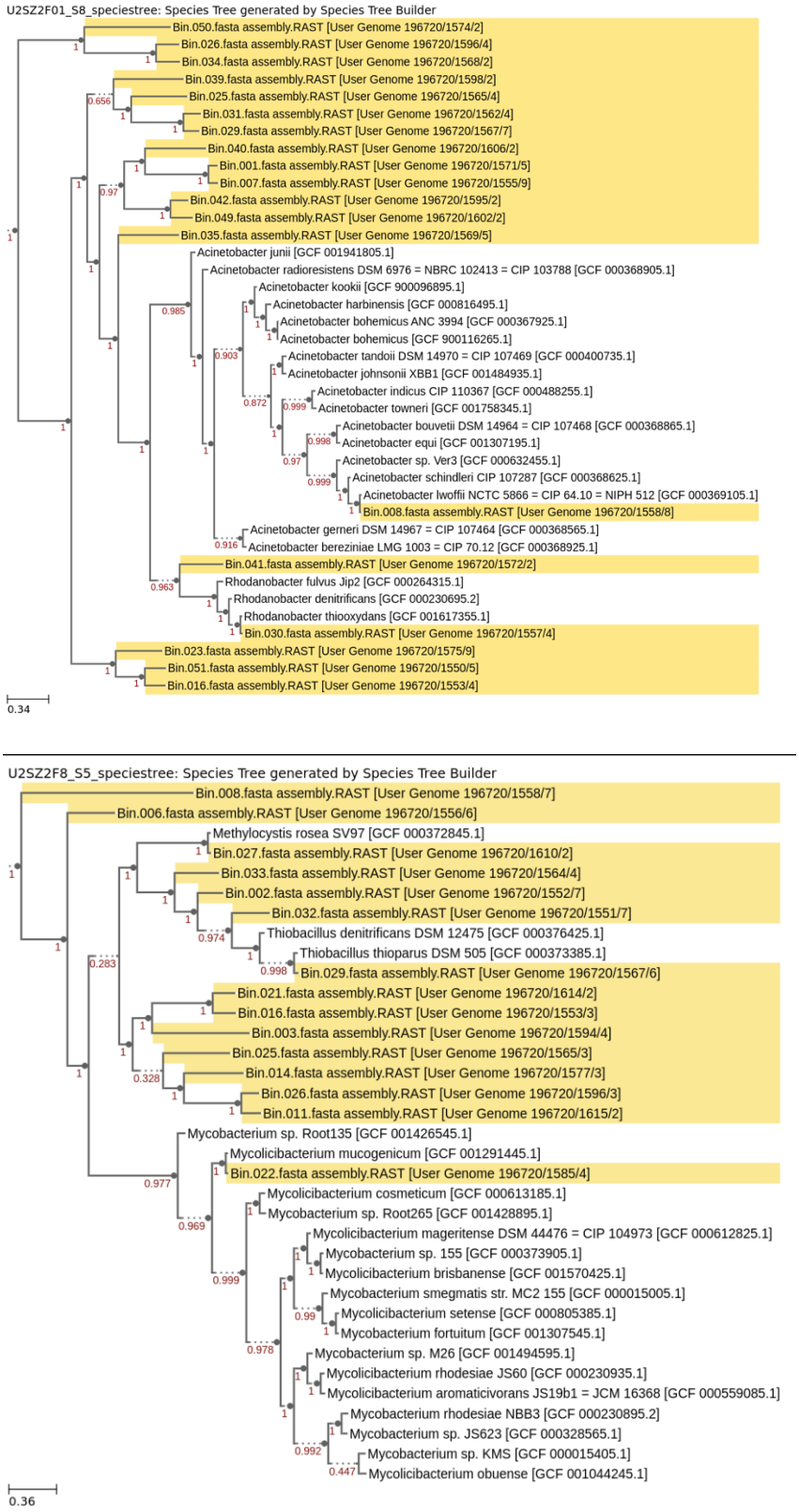

Figure 4.17. Top: U2_SZ2_F8_S5 Species Tree. Bottom: U2_SZ2_F01_S8 Species Tree. High-quality bins.

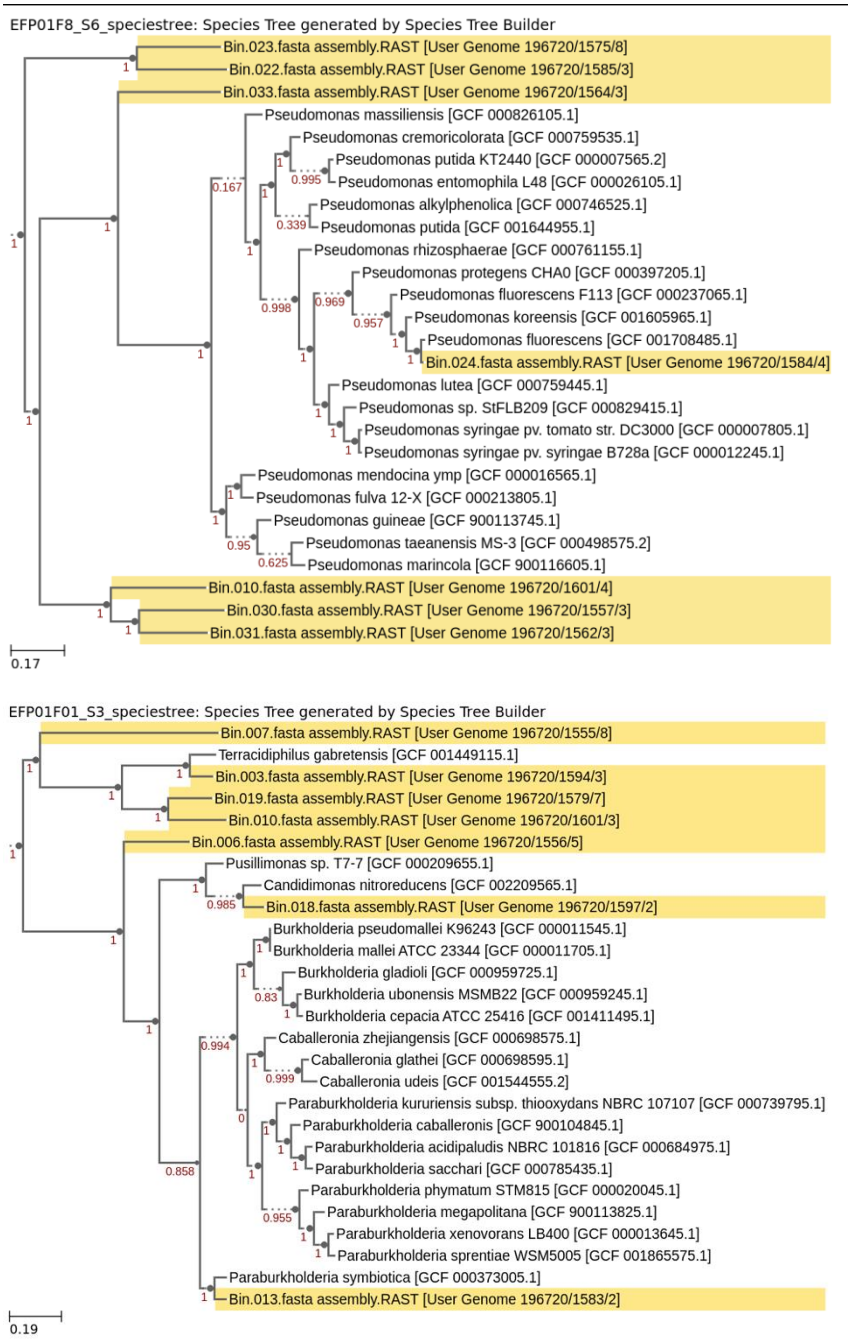

Figure 4.18. Top: EFP01_F8_S6 Species Tree. Bottom: EFP01_F01_S3 Species. High-quality bins.

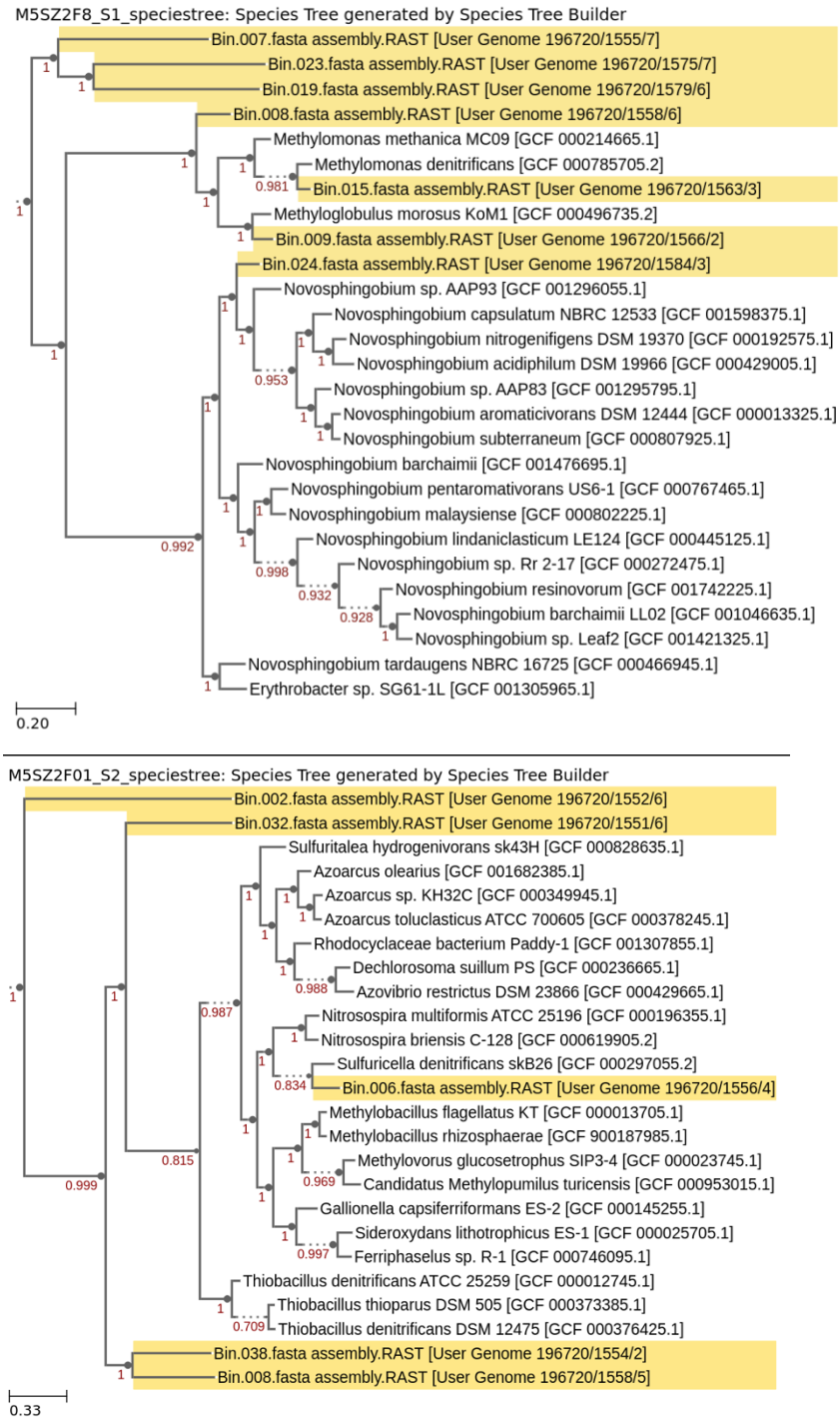

Figure 4.19. Top: M5_SZ2_F8_S1 Species Tree. Bottom: M5_SZ2_F01_S2 Species Tree. High-quality bins.

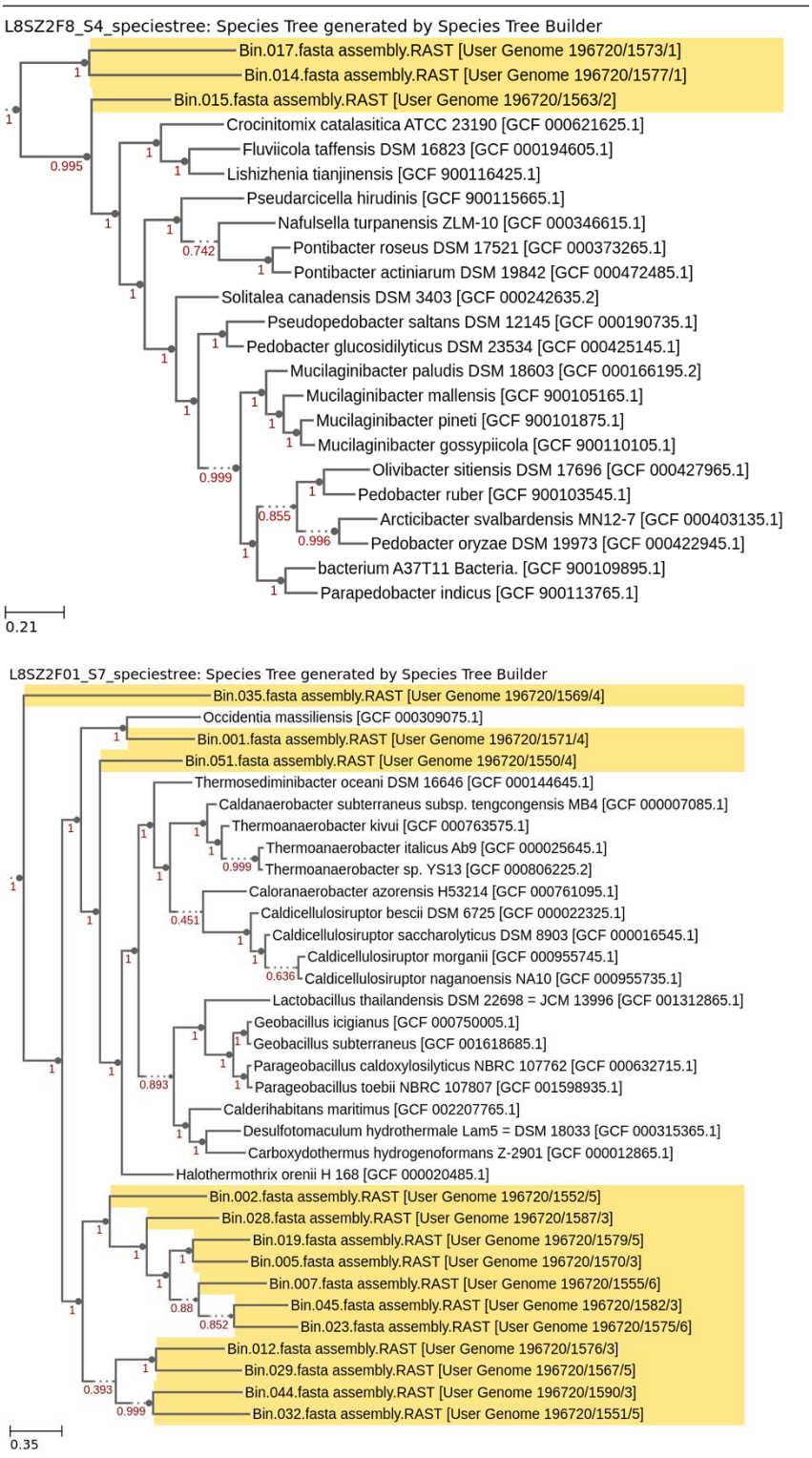

Figure 4.20. Top: L8_SZ2_F8_S4 Species Tree. Bottom: L8_SZ2_F01_S7 Species Tree. High-quality bins.

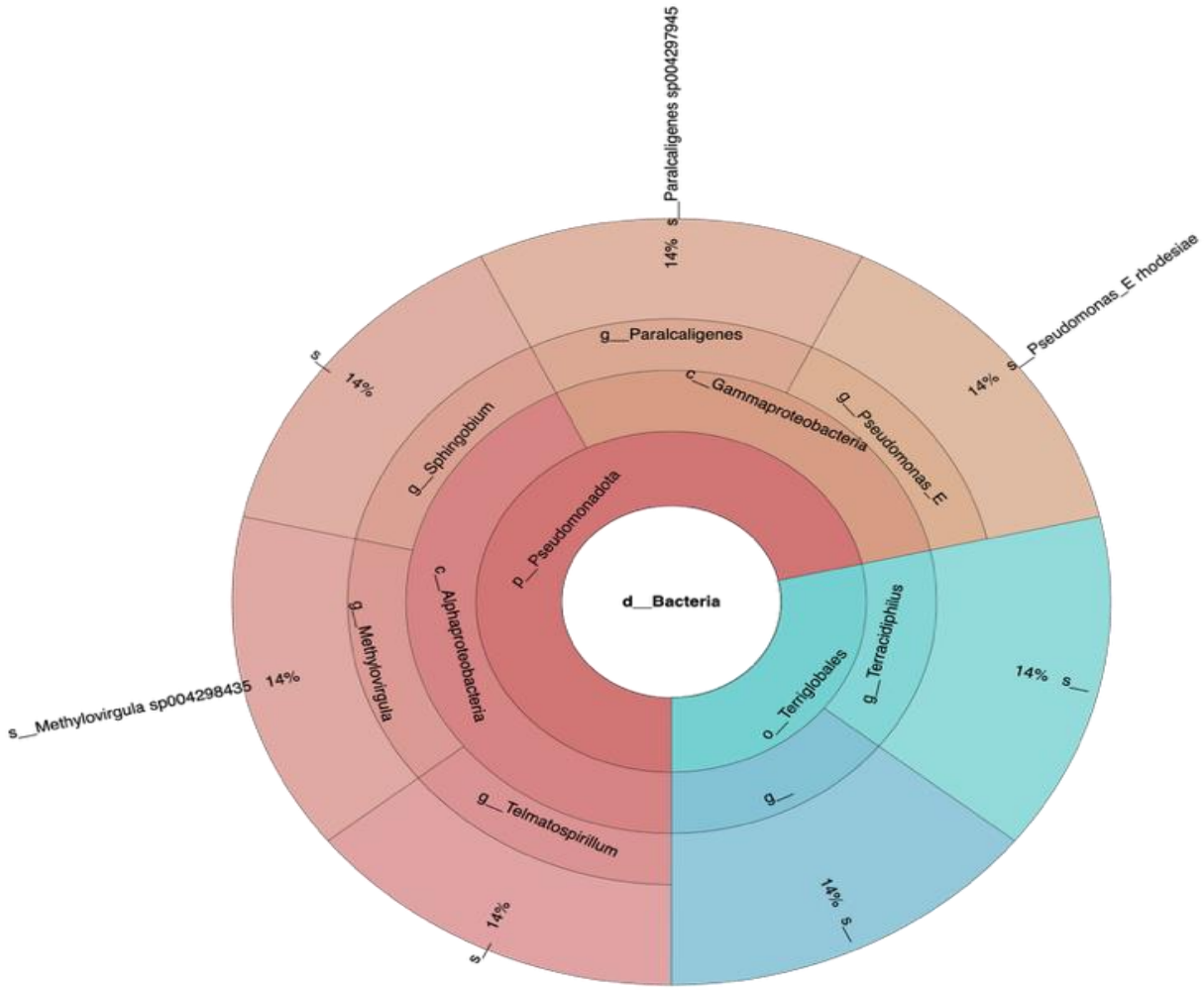

Figure 4.21. EFP01F8_S6 sample classified by GTDB-TK in KBase (8µm filter). High-quality bins.

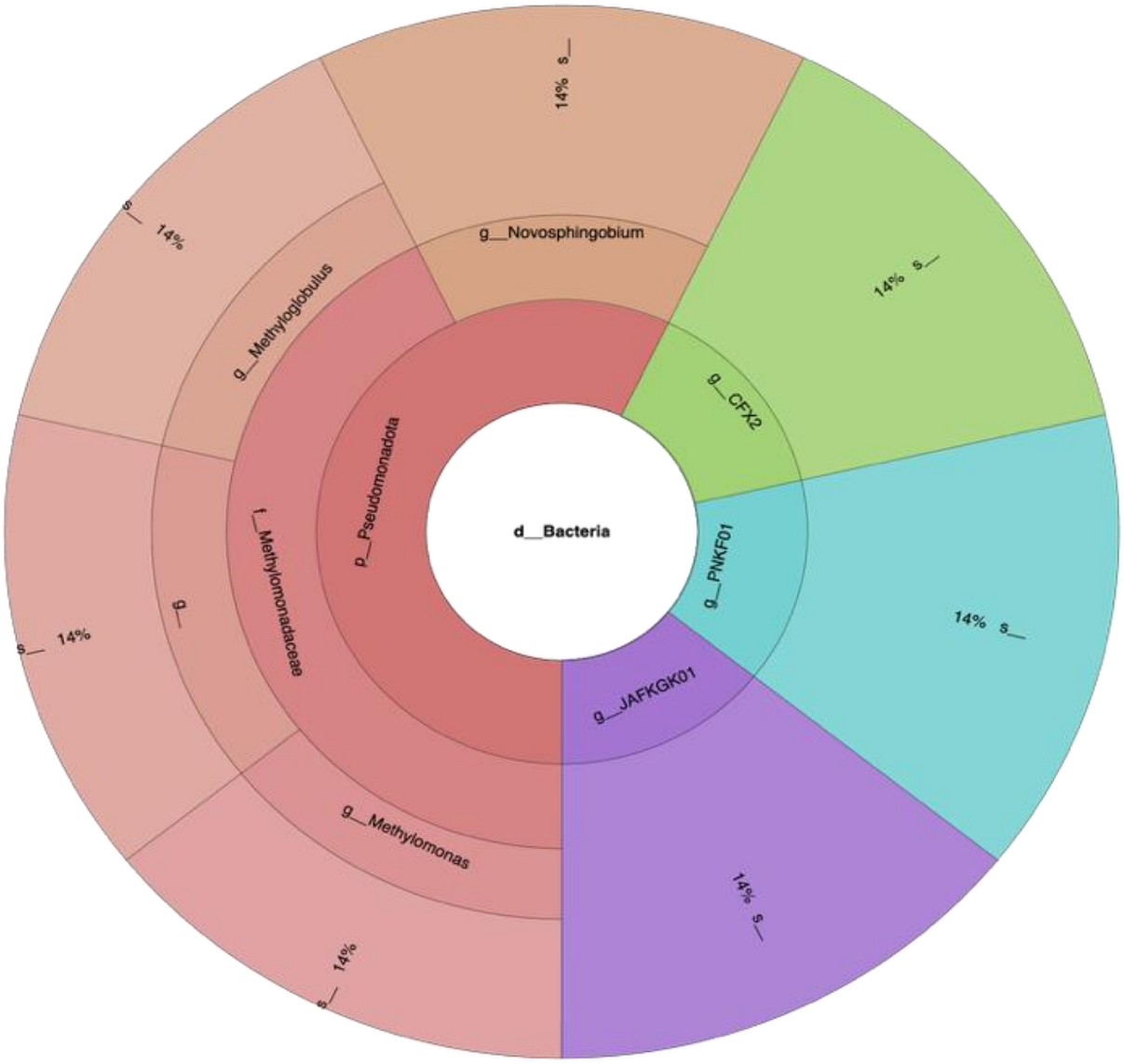

Figure 4.22. M5SZ2F8_S1 sample classified by GTDB-TK in KBase (8 µm filter). High-quality bins.

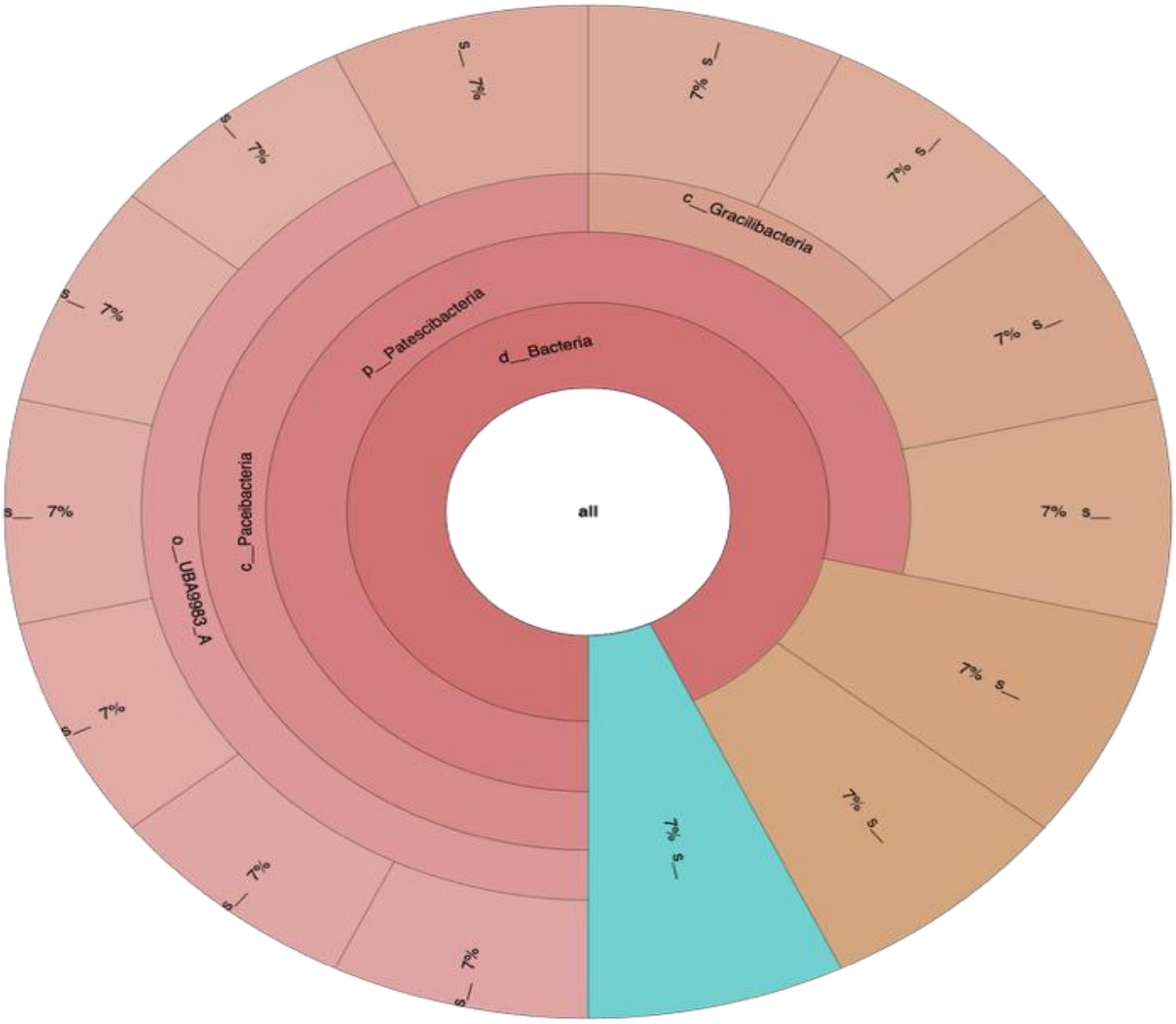

Figure 4.23. L8_SZ2_F01_S7 sample classified by GTDB-TK in KBase (0.1 µm filter). High-quality bins.

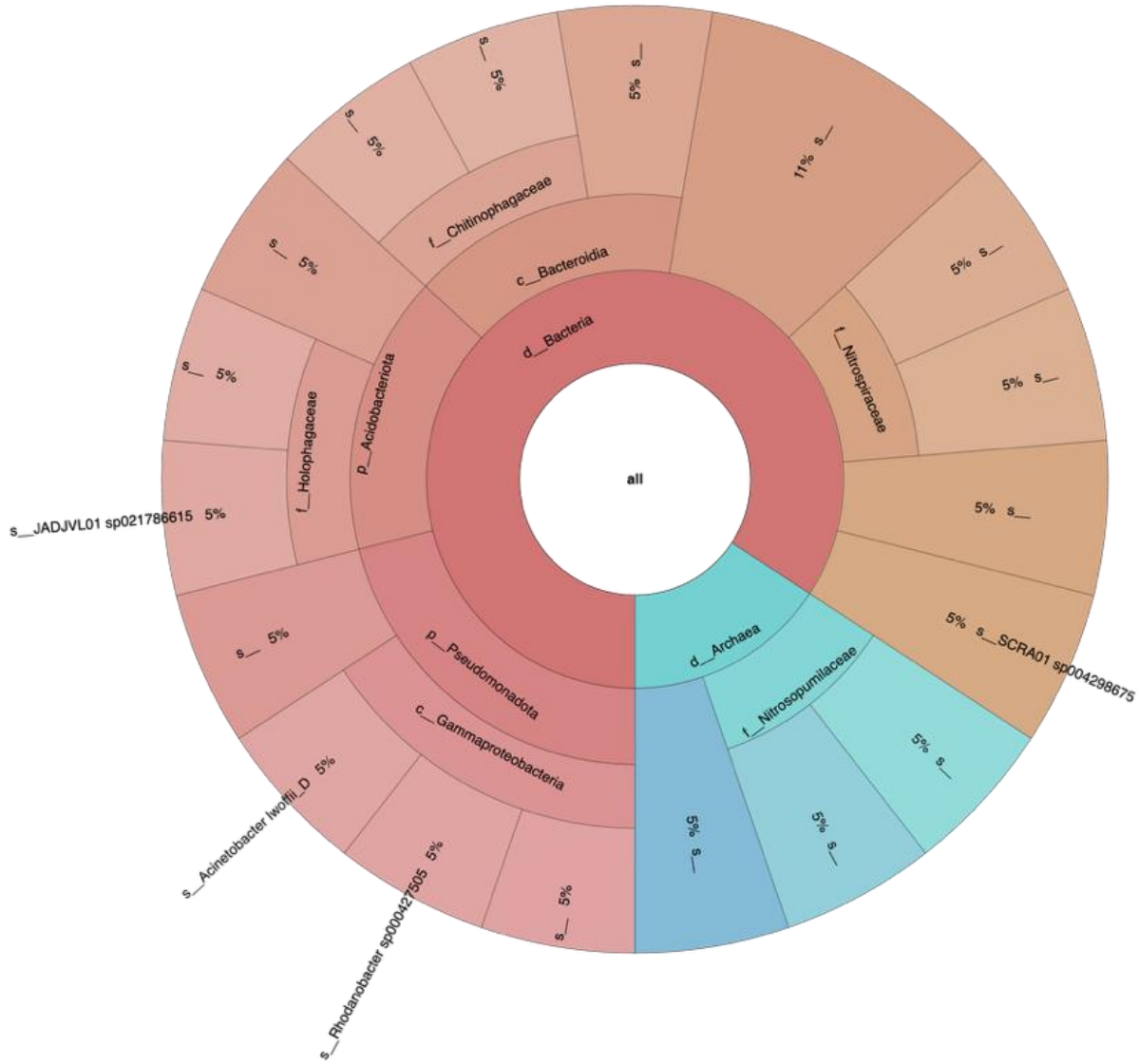

Figure 4.24. U2SZ2F01_S8 sample classified by GTDB-TK in KBase (0.1 µm filter). High-quality bins.

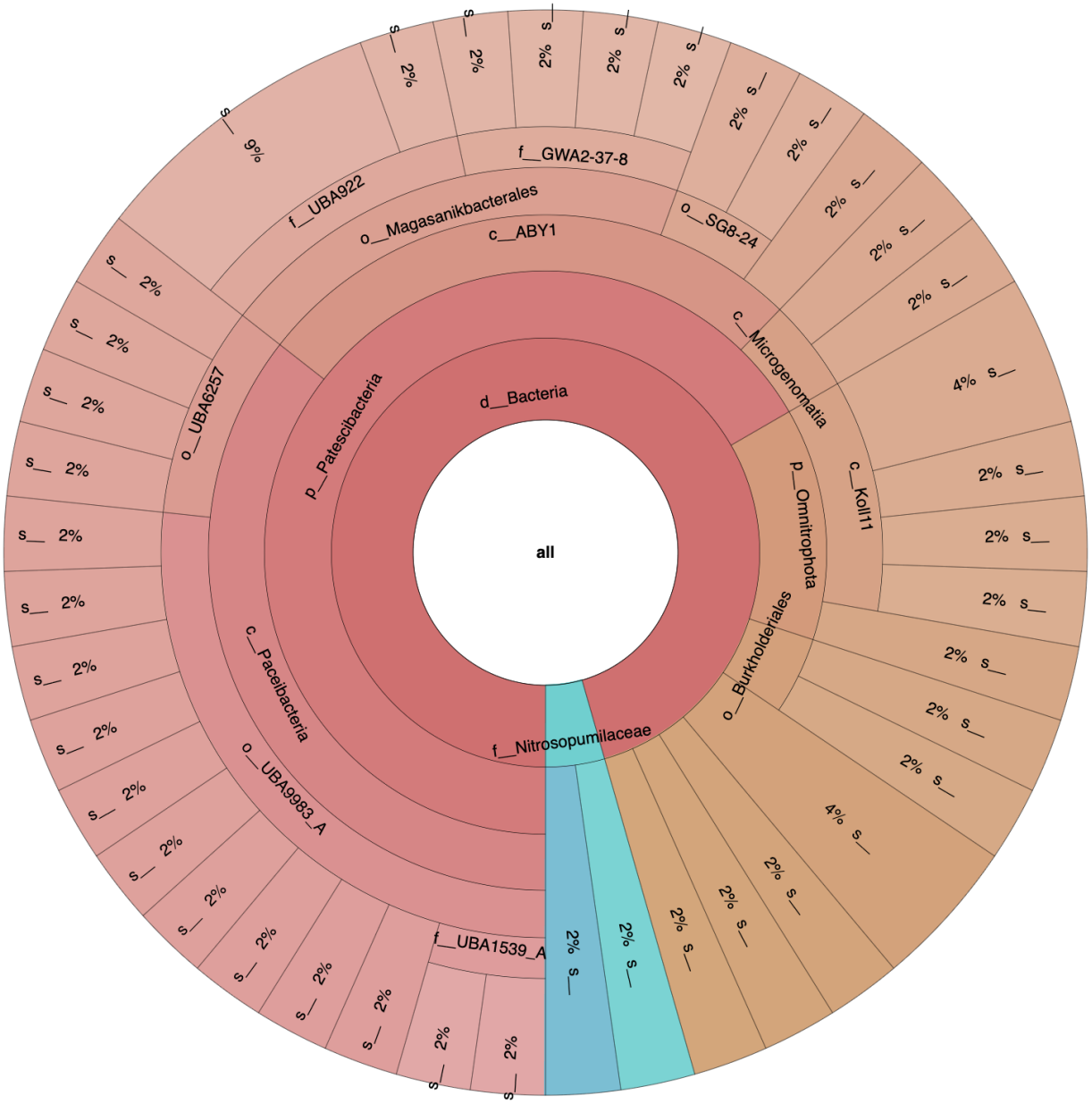

Figure 4.25. M5SZ2F01_S2 sample classified by GTDB-TK in KBase (0.1 µm filter). Medium-quality bins.

Figure 4.26. M5SZ2F8_S1 sample classified by GTDB-TK in KBase (8 µm filter). Medium-quality bins.

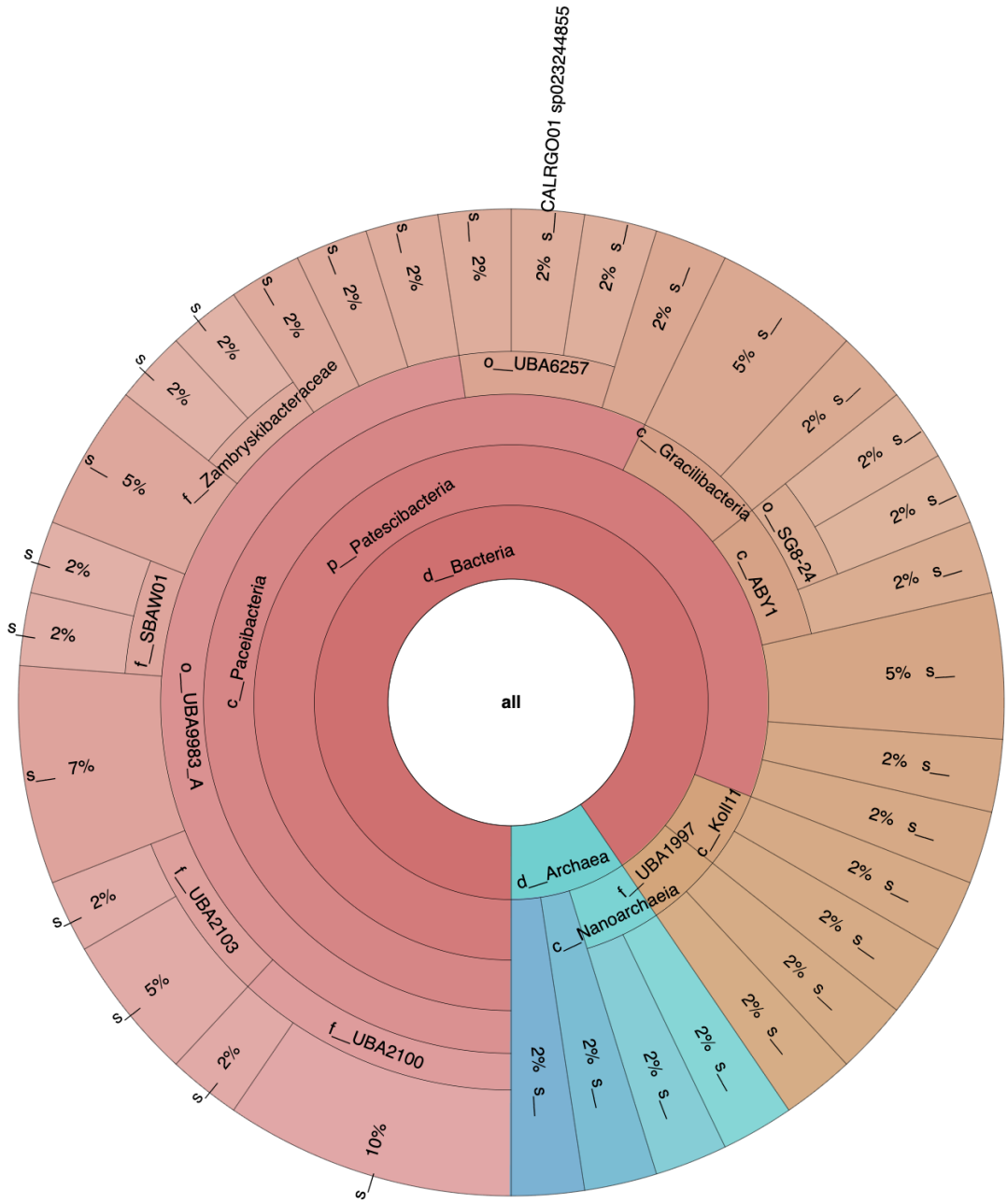

Figure 4.27. L8SZ2F01_S7 sample classified by GTDB-TK in KBase (0.1 µm filter). Medium-quality bins.

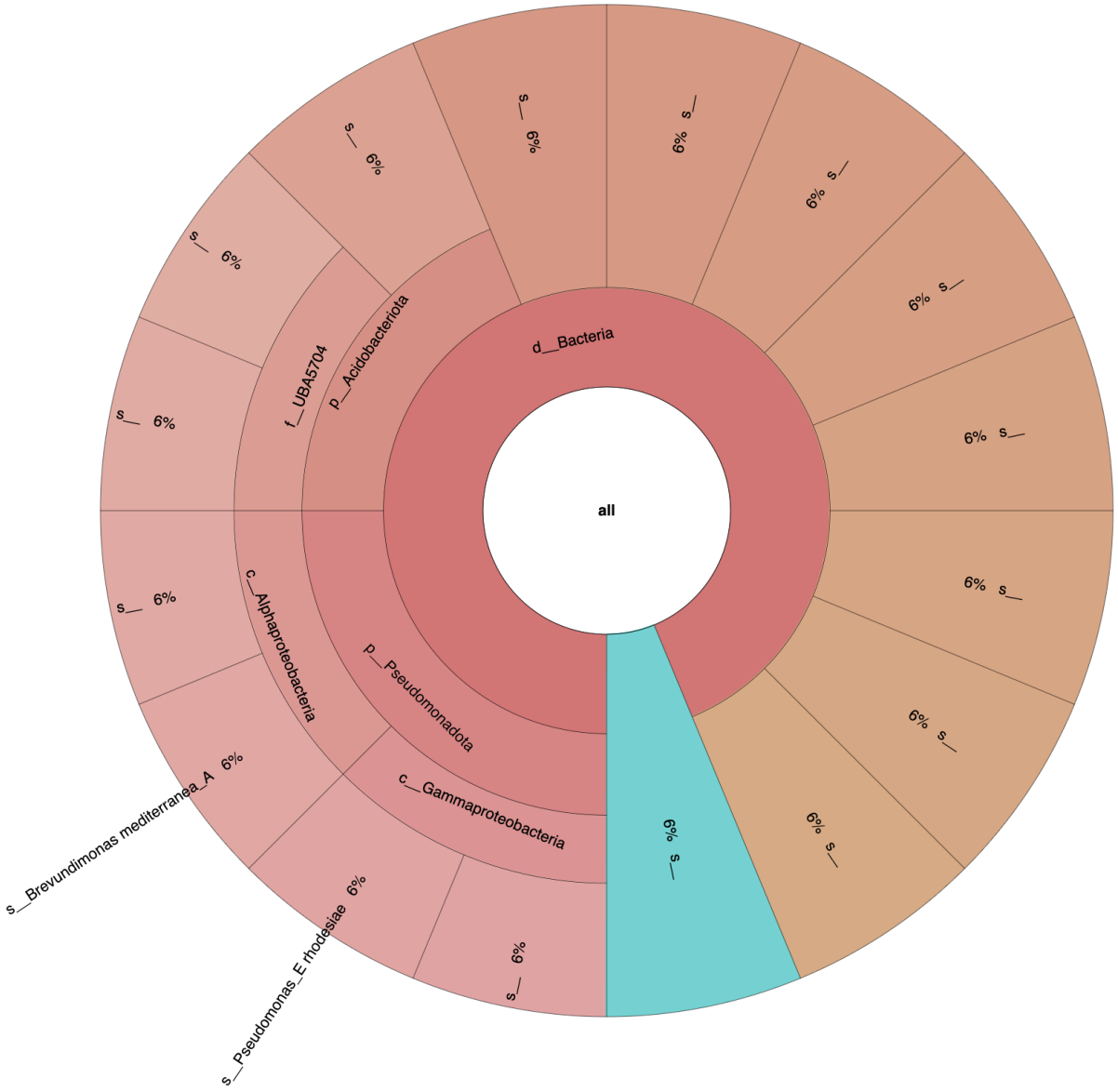

Figure 4.28. L8SZ2F8_S4 sample classified by GTDB-TK in KBase (8 µm filter). Medium-quality bins.

Figure 4.29. EFP01F8_S6 sample classified by GTDB-TK in KBase (8 µm filter). Medium-quality bins

Figure 4.30. EFP01F01_S3 sample classified by GTDB-TK in KBase (0.1 µm filter). Medium-quality bins.

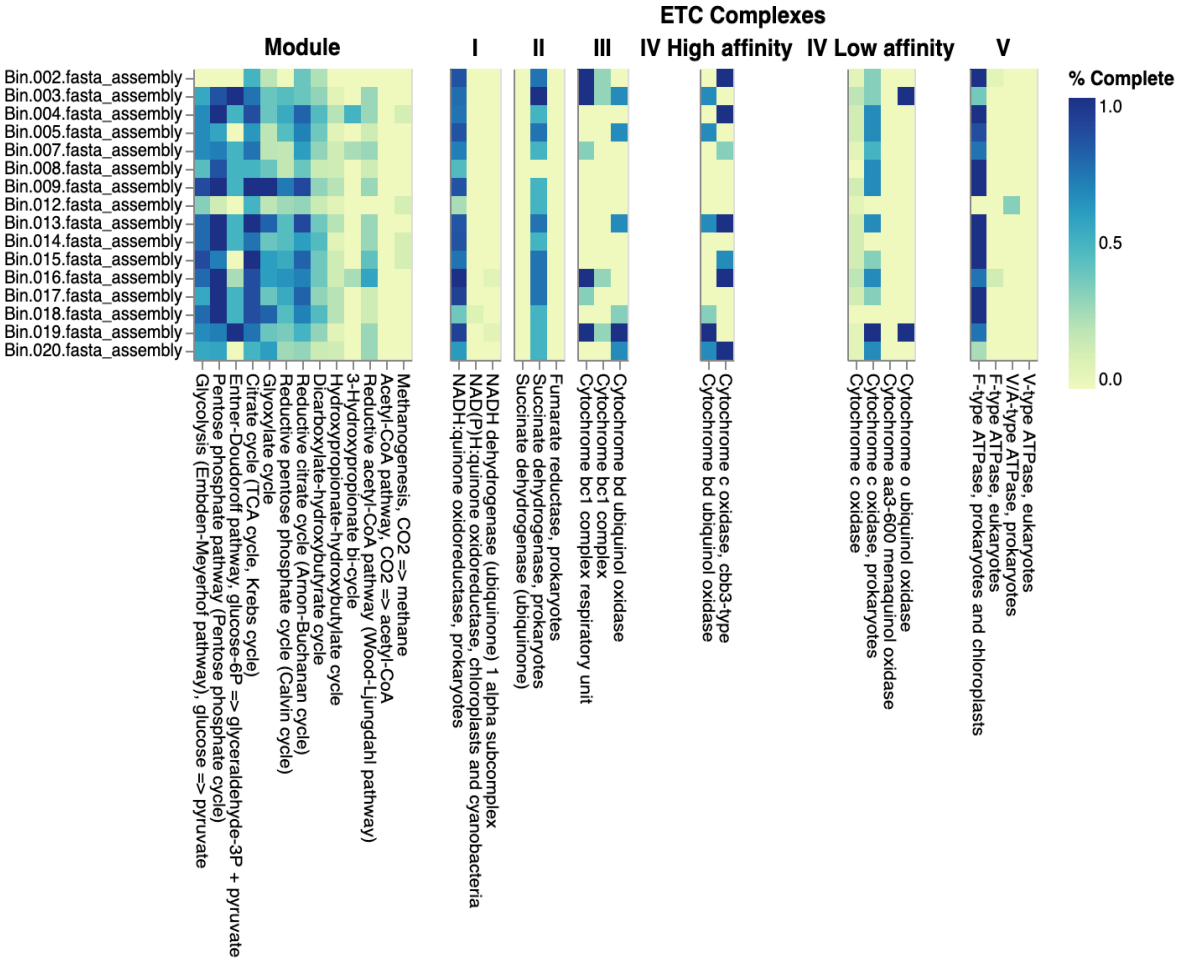

Figure 4.31. DRAM product output showing percentage completion of energy-deriving pathways and electron transport chain components in co-assembled microcosms of L8SZ2F8_S4 sample.

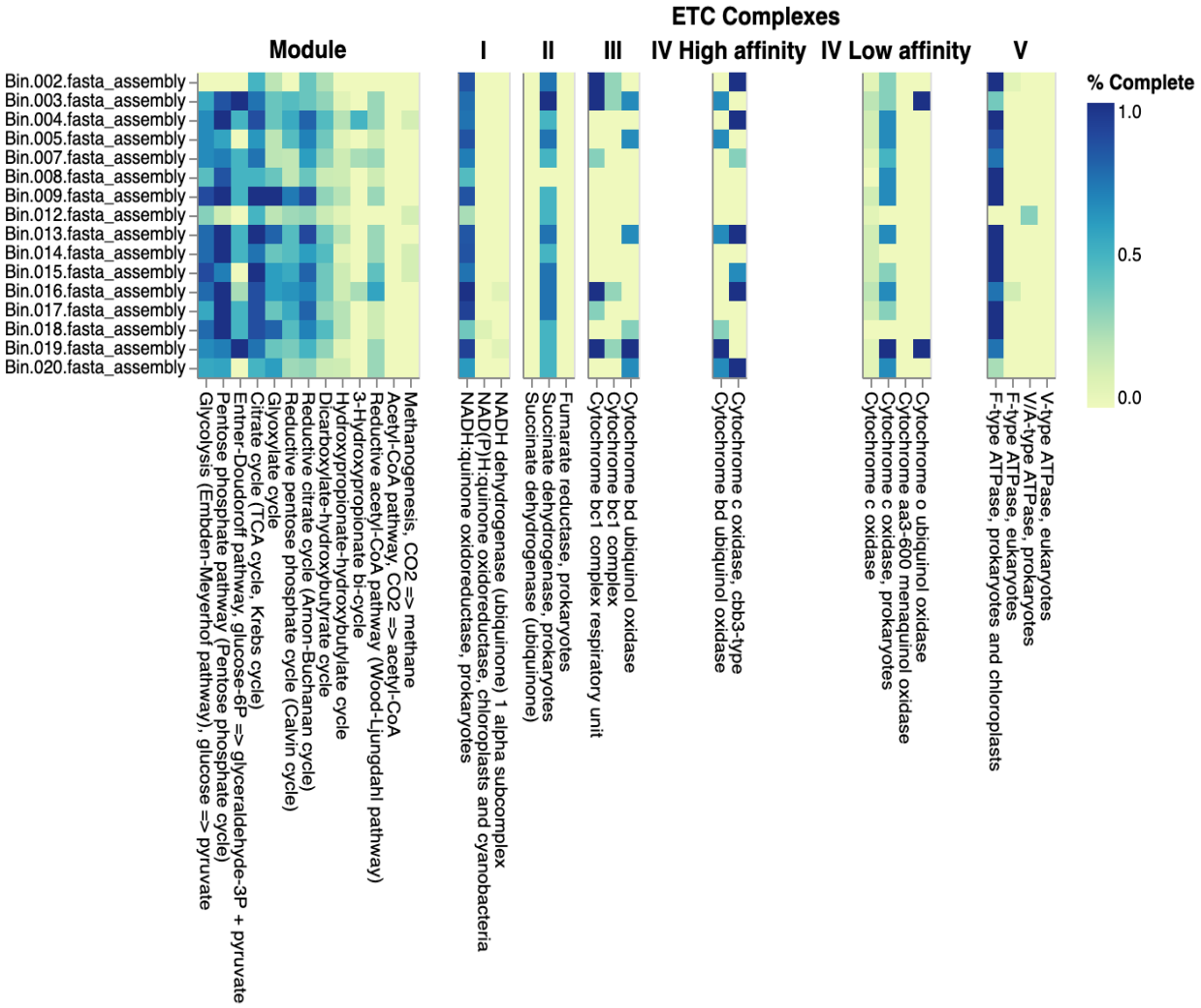

Figure 4.32. DRAM product output showing percentage completion of energy-deriving pathways and electron transport chain components in co-assembled microcosms of U2SZ2F8_S5 sample.

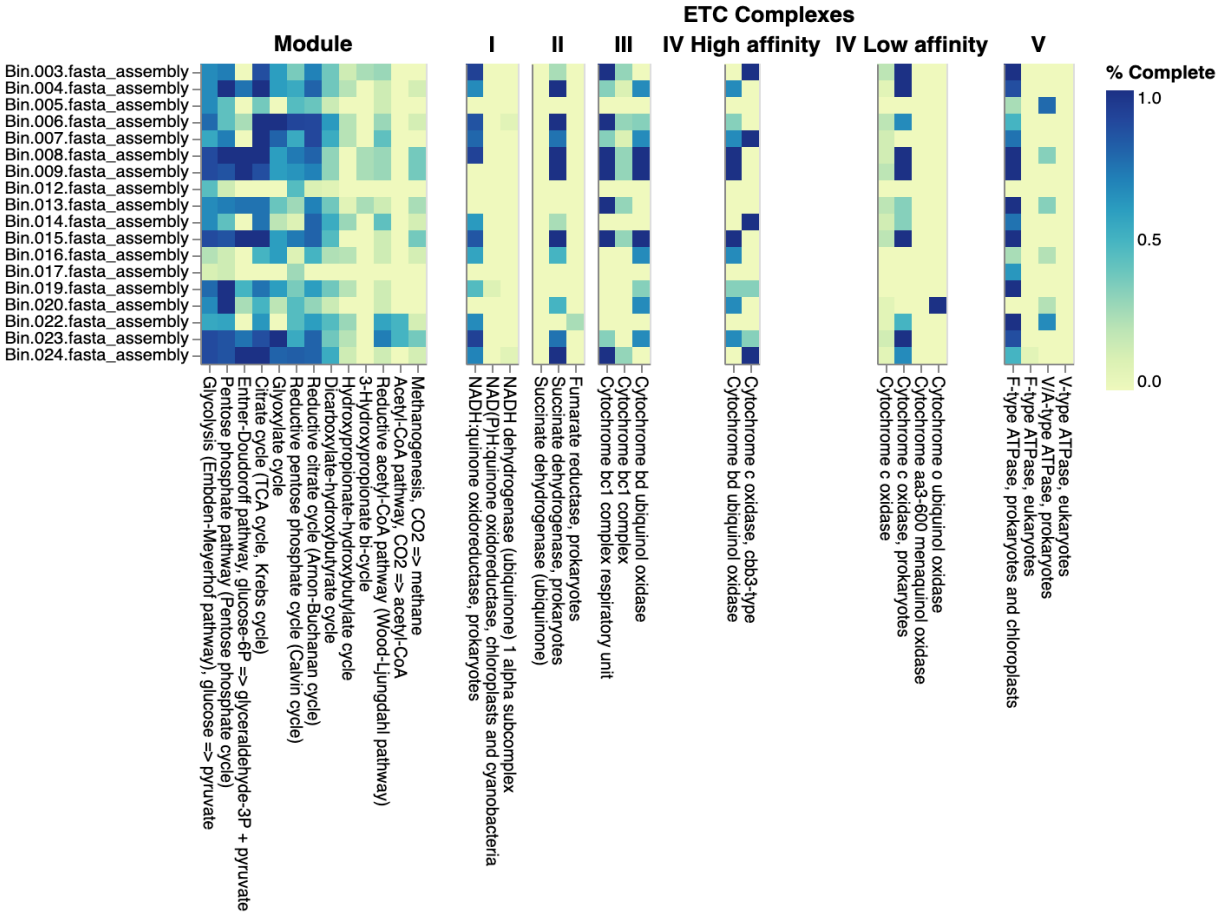

Figure 4.33. DRAM product output showing percentage completion of energy-deriving pathways and electron transport chain components in co-assembled microcosms of M5SZ2F8_S1 sample.

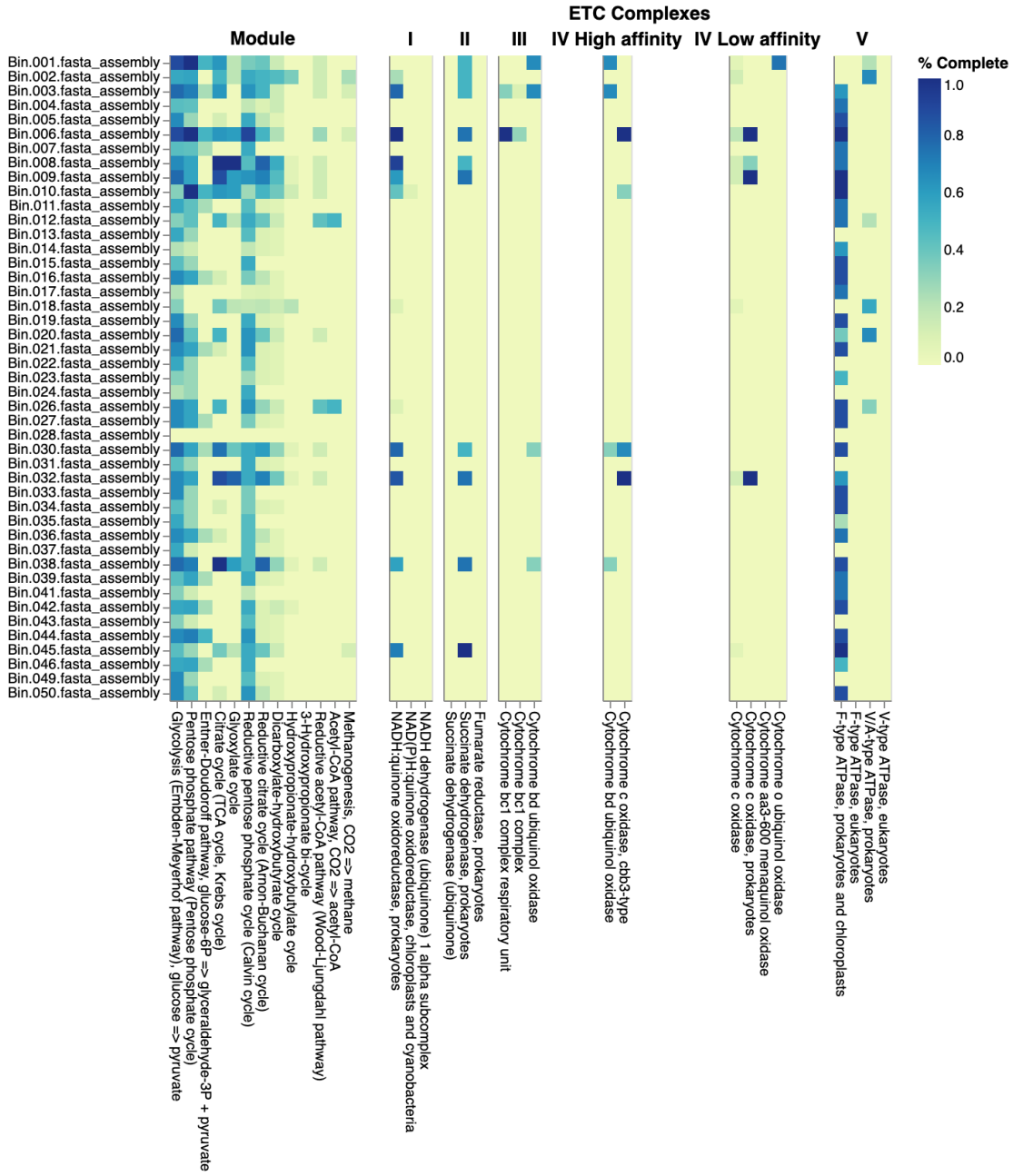

Figure 4.34. DRAM product output showing percentage completion of energy-deriving pathways and electron transport chain components in co-assembled microcosms of M5SZ2F01_S2 sample.

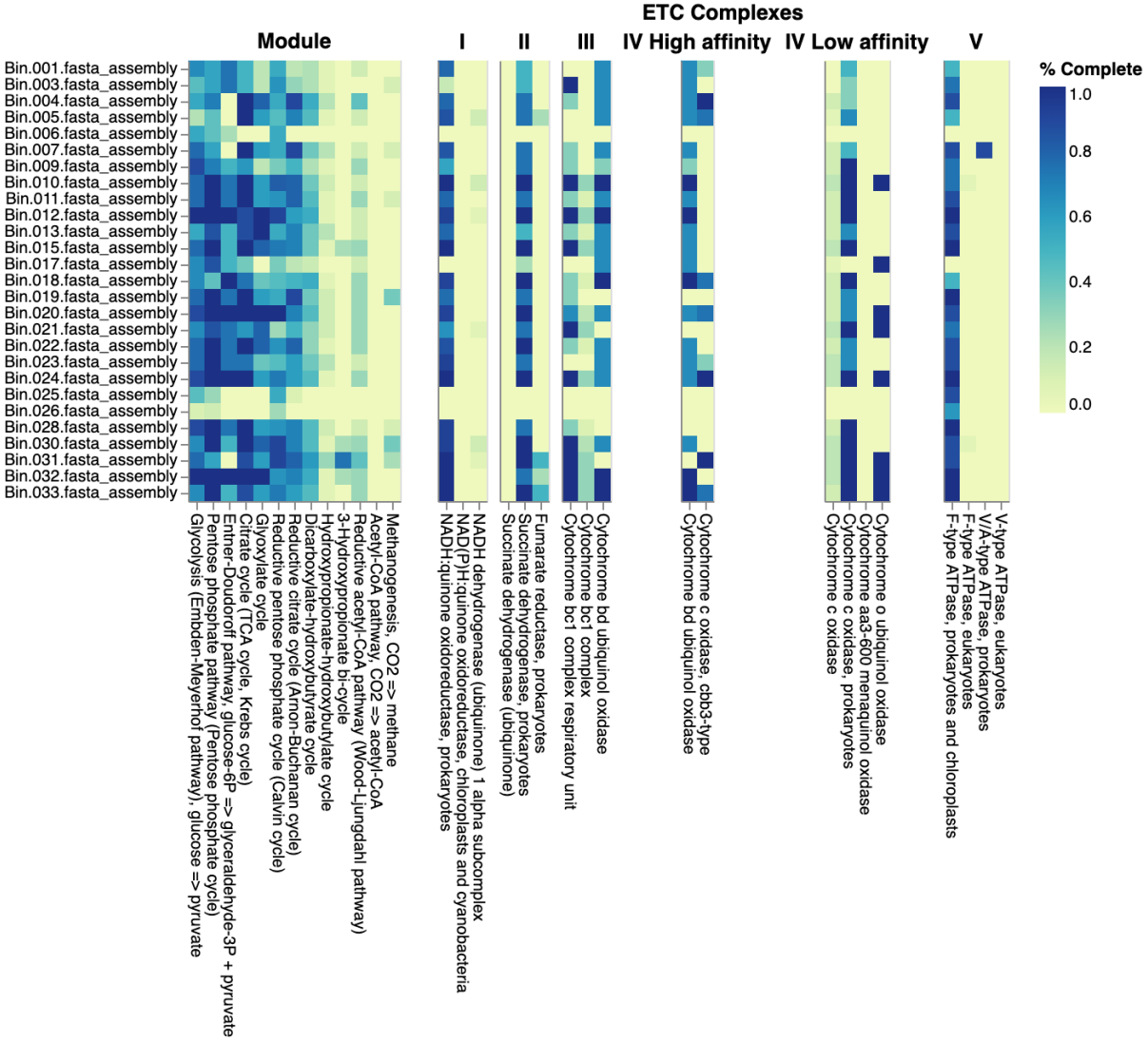

Figure 4.35. DRAM product output showing percentage completion of energy-deriving pathways and electron transport chain components in co-assembled microcosms of EFP01F8_S6 sample.

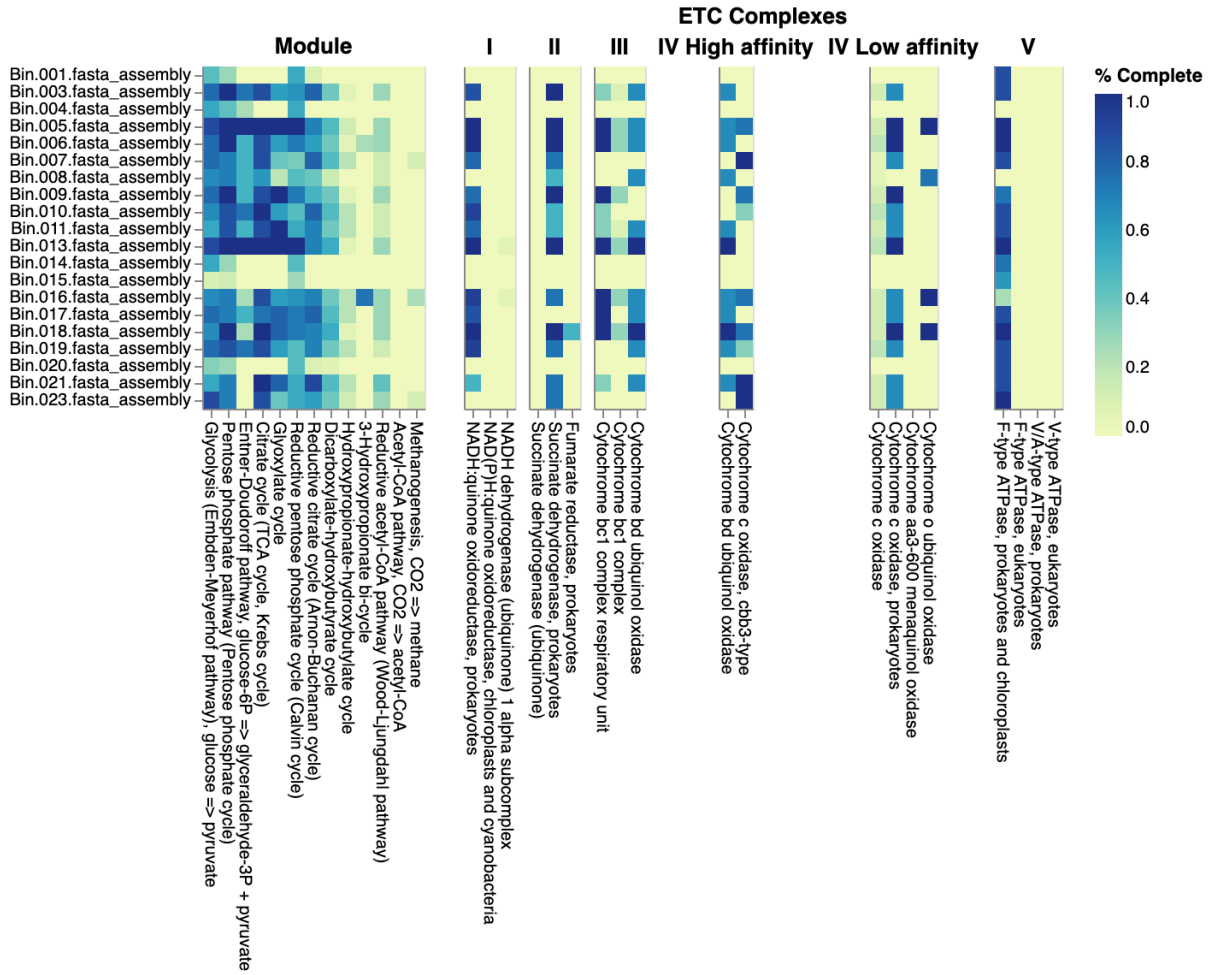

Figure 4.36. DRAM product output showing percentage completion of energy-deriving pathways and electron transport chain components in co-assembled microcosms of EFP01F01_S3 sample.

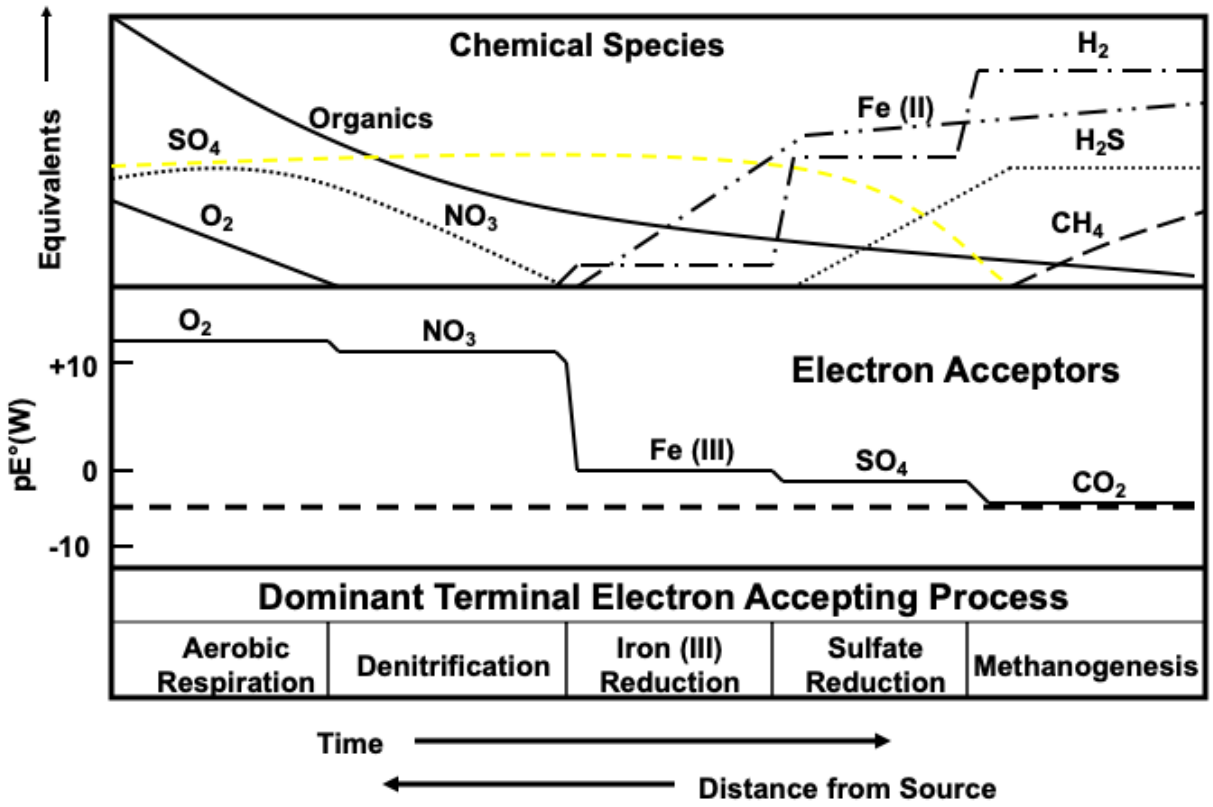

Figure 4.37. Electron acceptors based on time and distance from the source.

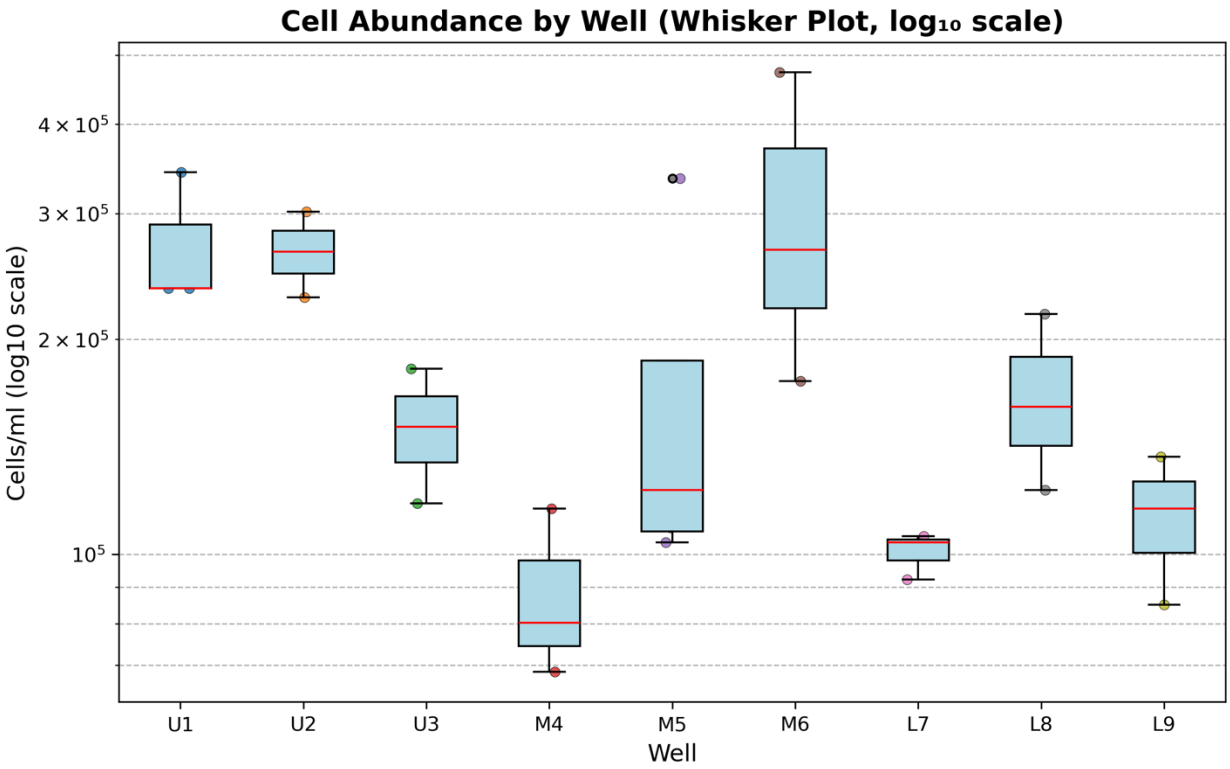

Figure 4.38. Cell abundance by well (Whisker Plot).

Figure 4.39. M5SZ2 F01 sample GeNomad viruses score.

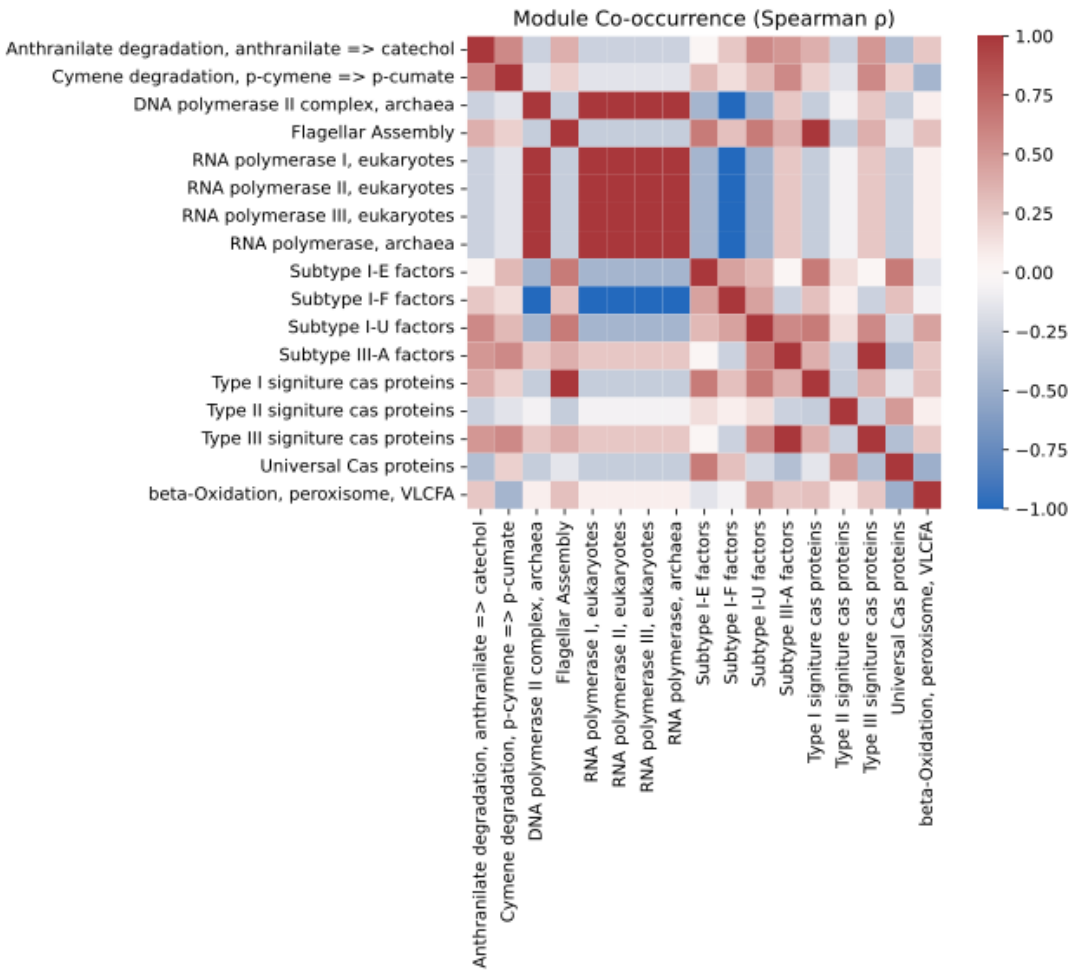

Figure 4.40. Module co-occurrence (Spearman).

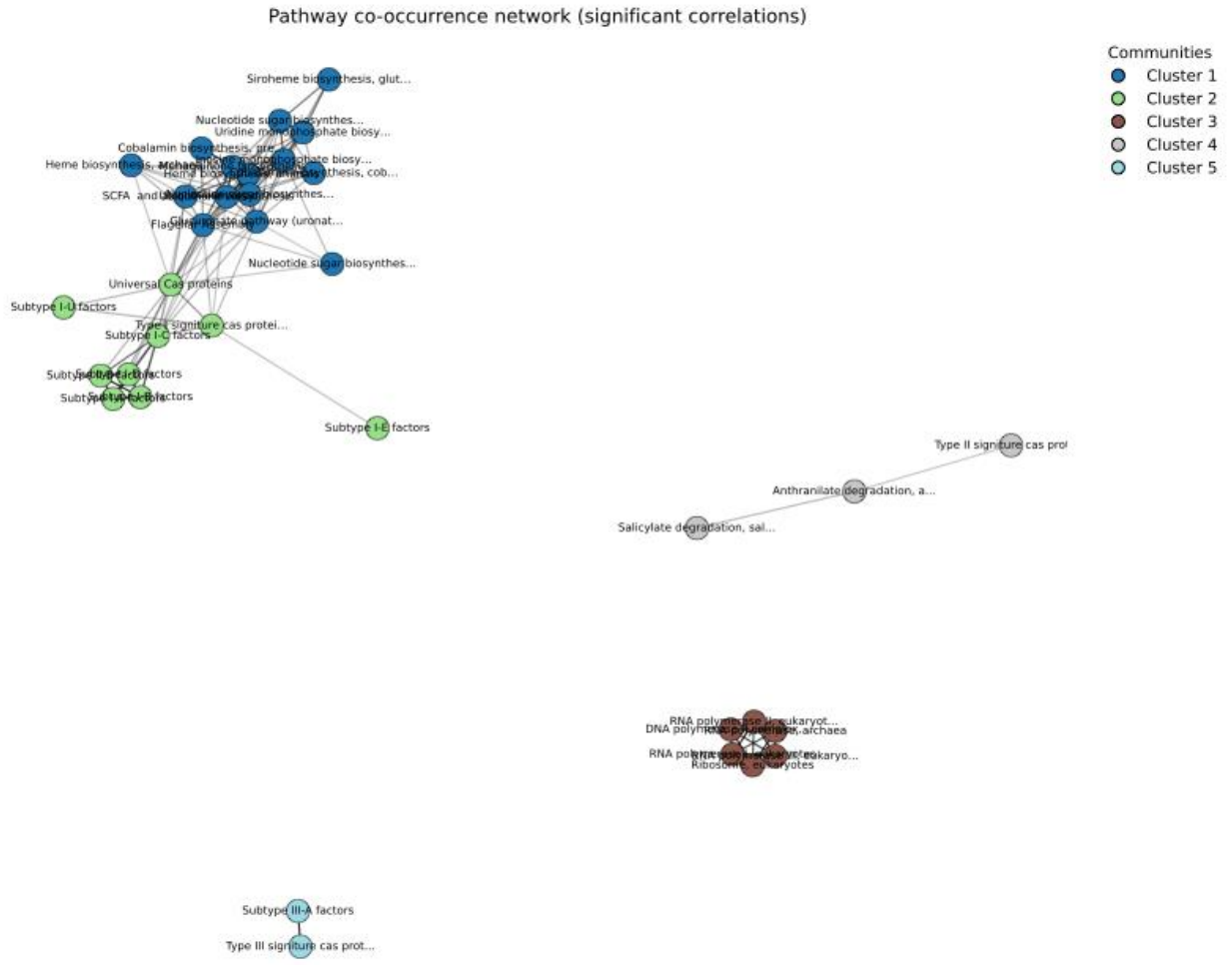

Figure 4.41. Pathway co-occurrence network.

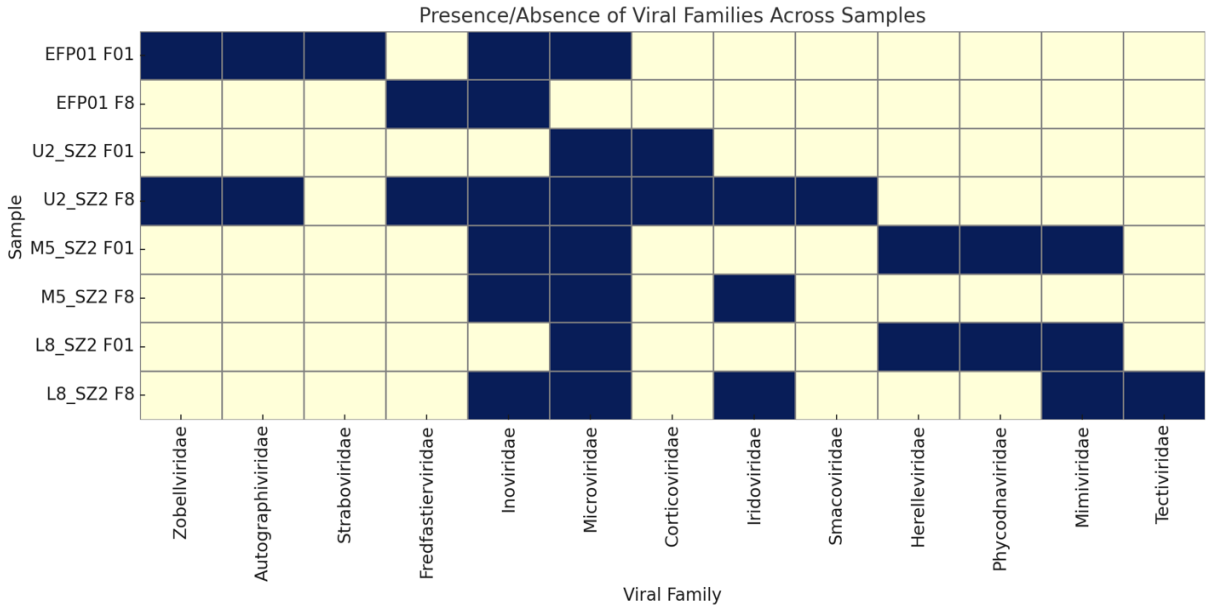

A

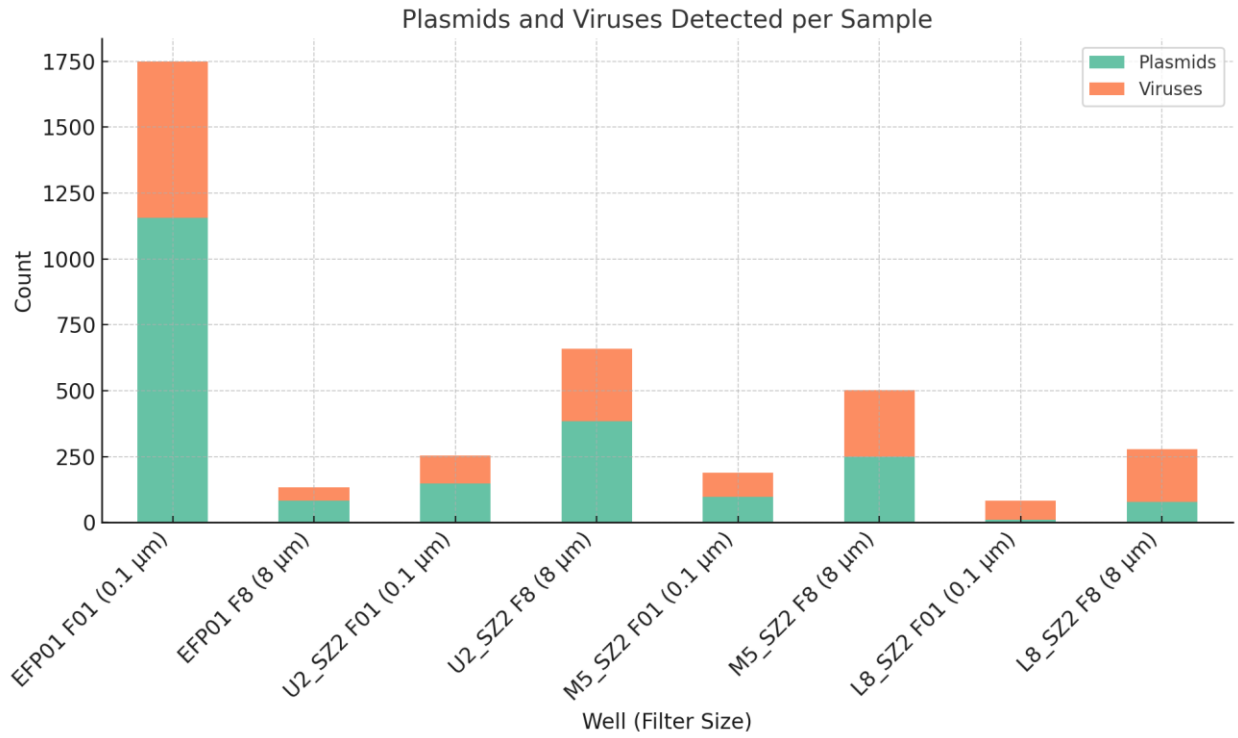

B

Figure 4.42. A. Presence and absence of viral families across samples. B Plasmids and viruses detected per sample.

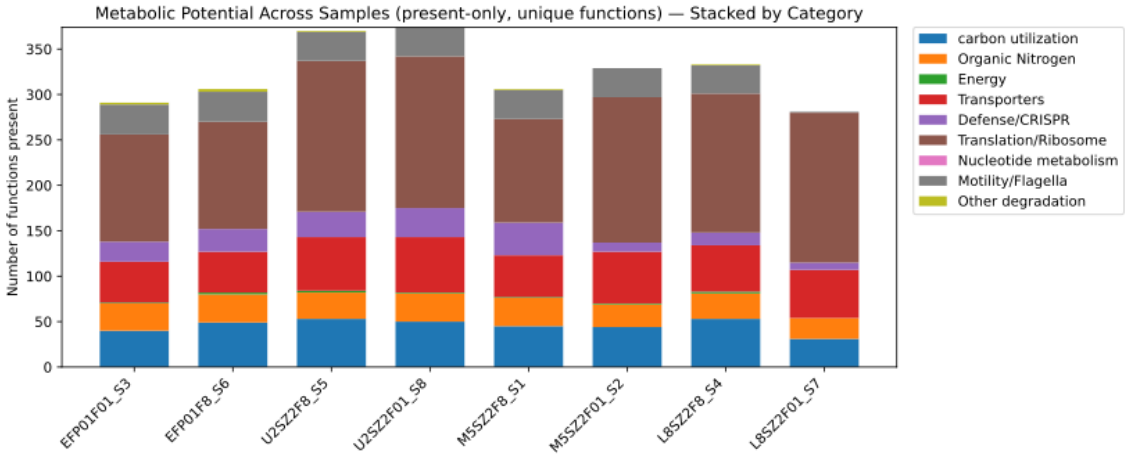

A

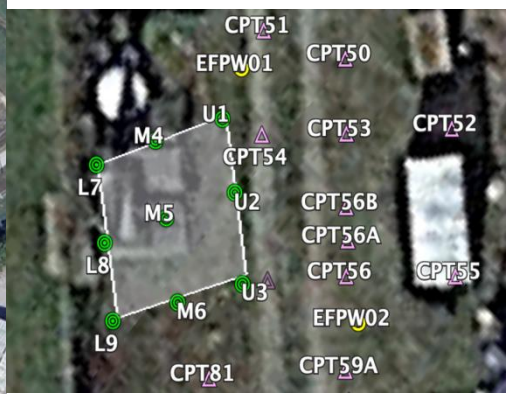

B C

Figure 4.42. A. Metabolic potential across samples (DRAM summary). We can see that EFP01 shows higher transporter diversity than SSO wells. B. The studied wells location next to the source of contamination (under the parking lot). C. Zoomed in wells location.

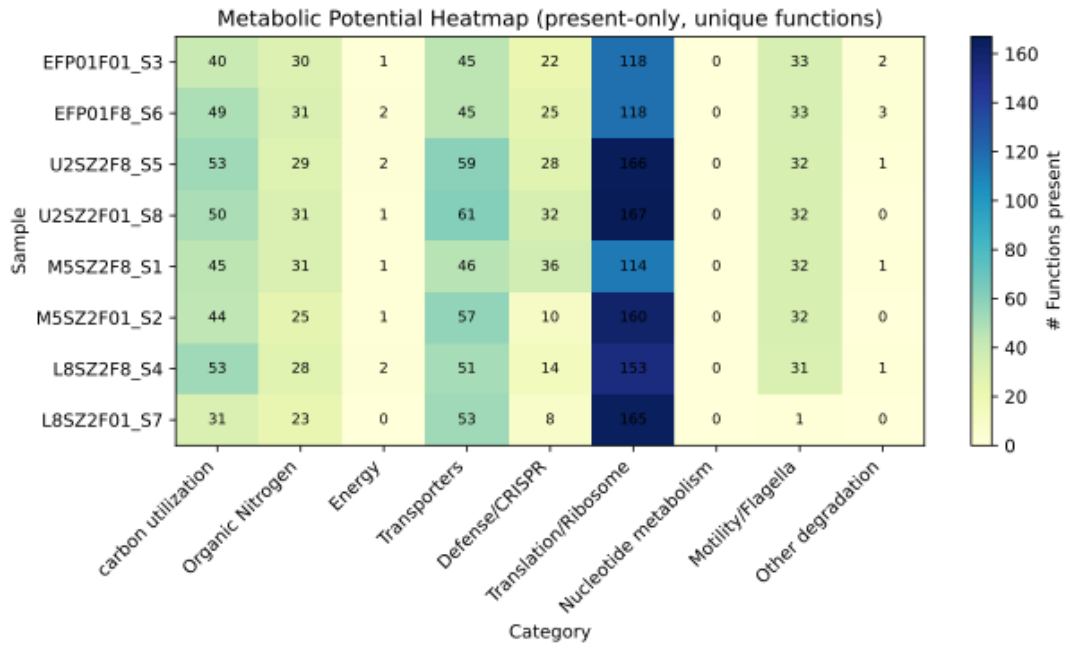

A

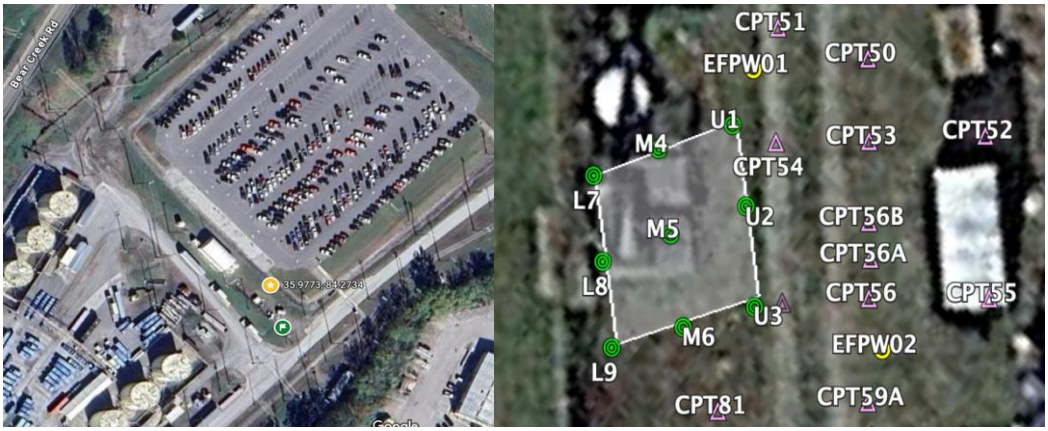

B C

Figure 4.41. A. Heatmap of Metabolic Potential across Samples. wells. B. The studied wells location next to the source of contamination (under the parking lot). C. Zoomed in wells location.

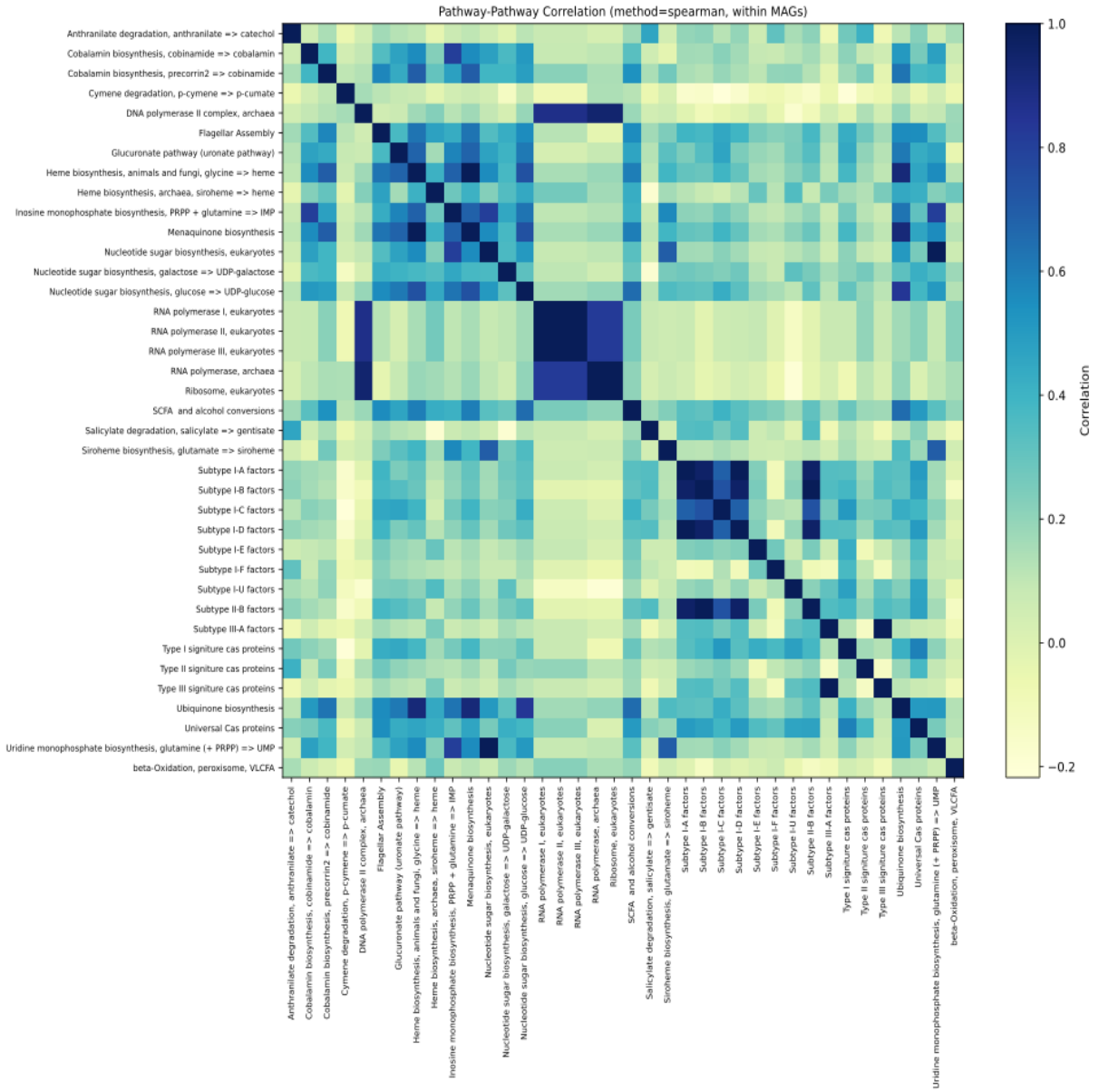

Figure 4.42. Pathway-Pathway Correlation (method=Spearman, within MAGS).

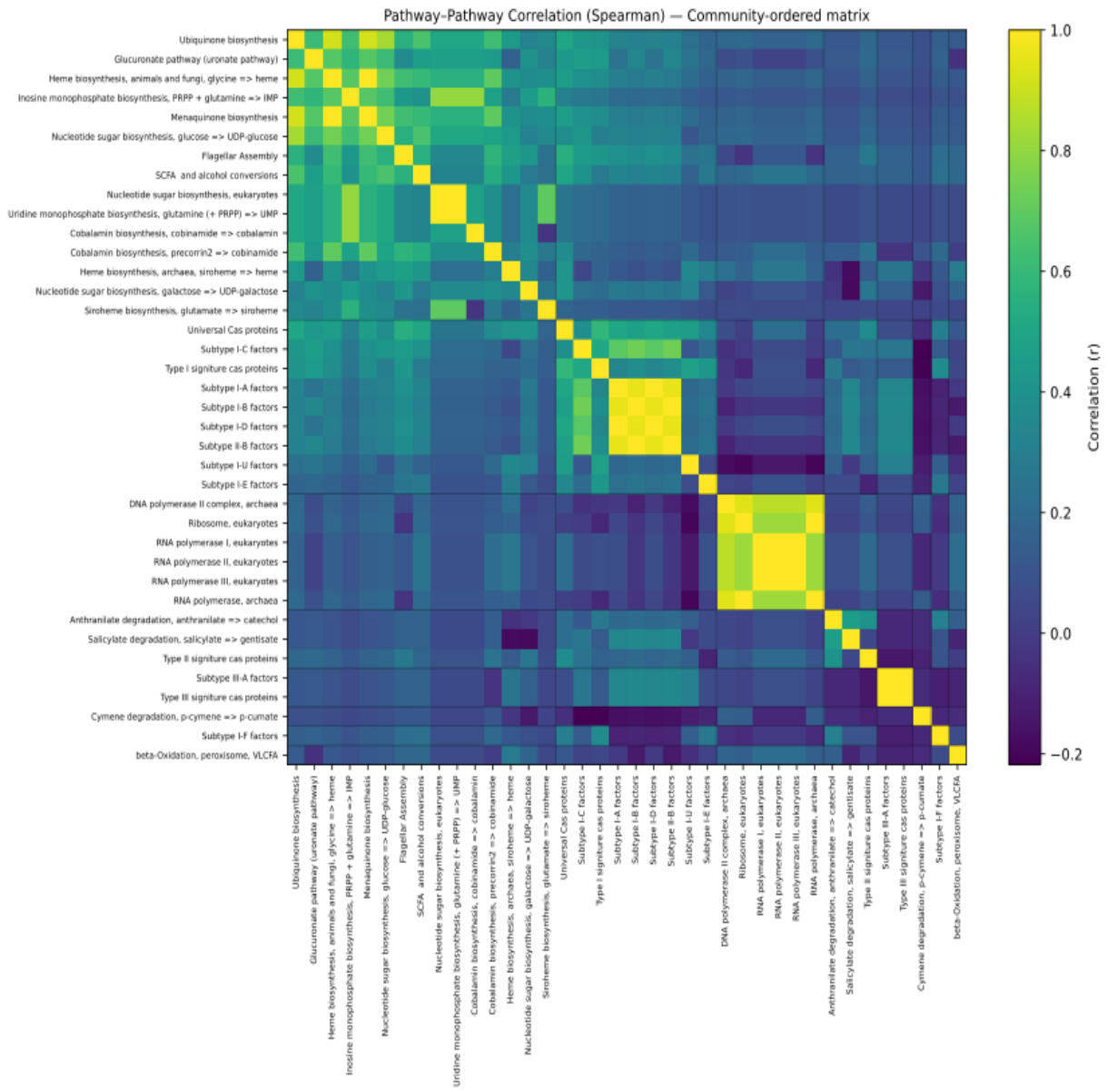

Figure 4.43. Pathway-Pathway Correlation (Spearman, within MAGS)-Community-ordered matrix.

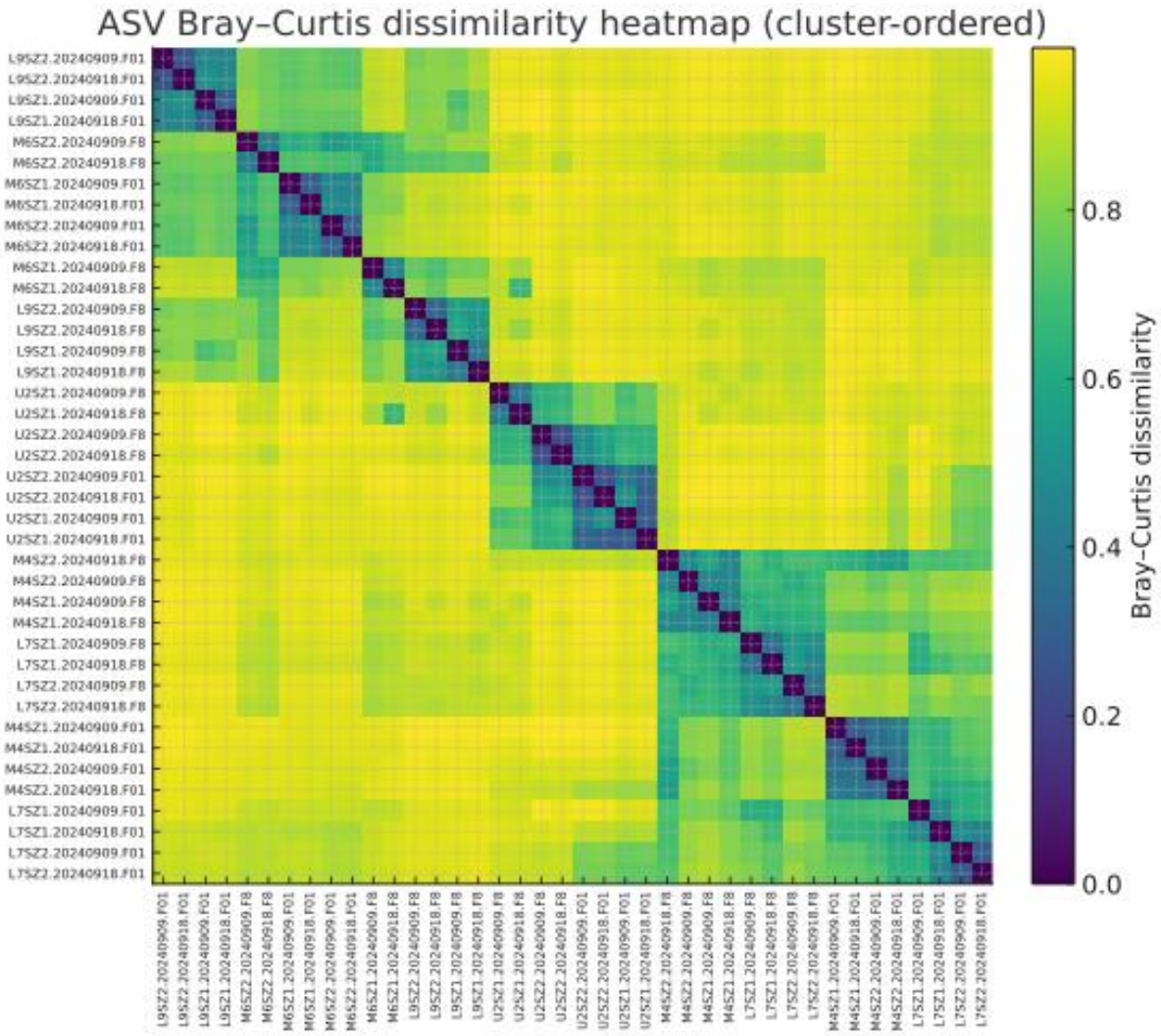

Figure 4.44. ASV Bray-Curtis dissimilarity heatmap (cluster-ordered).

Pilot studies.

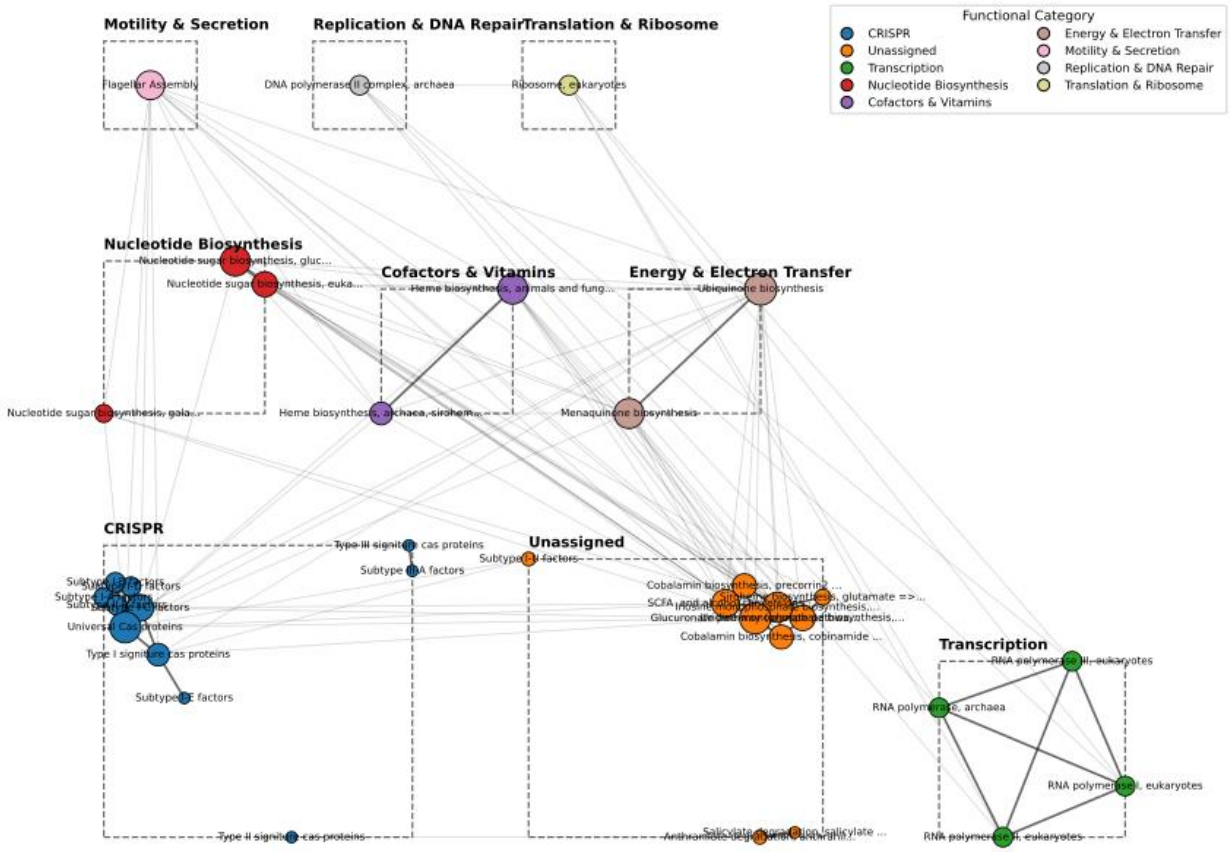

Figure 4.45. Functional Category Block Network of annotated genes and pathways.

Nodes represent annotated functional genes or modules, grouped into blocks according to major metabolic and defense categories. Node size is proportional to degree (connectivity), with intra-category edges drawn in darker lines and inter-category edges in lighter, semi-transparent lines. Blocks are arranged using a grid layout, and labels are shortened for readability. The network demonstrates both within-category clustering and cross-category linkages, illustrating the modular but interconnected organization of functional capacities in the dataset.

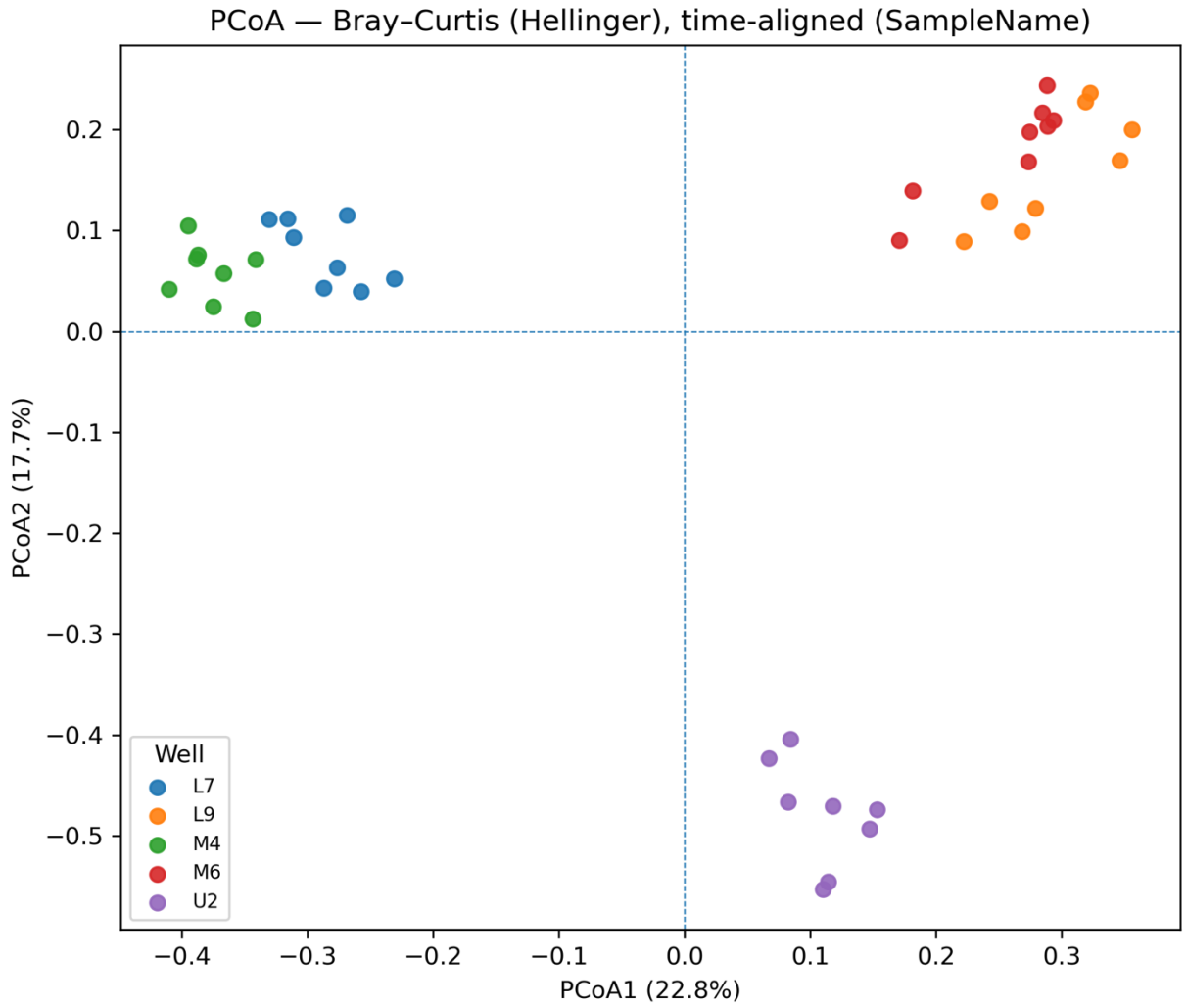

Figure 4.46. A Principal Coordinates Analysis (PCoA) plot by well.

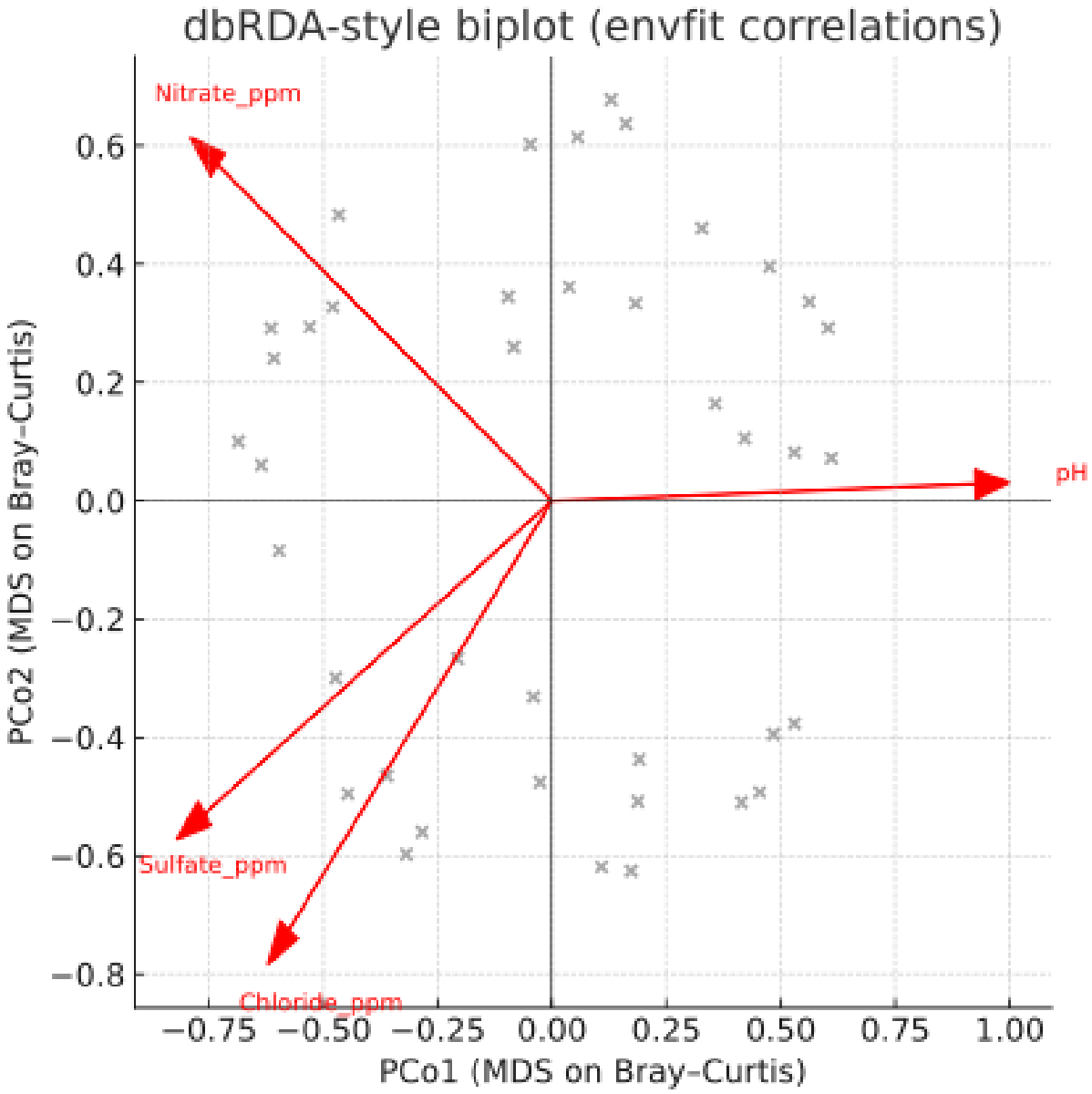

Figure 4.47. dbRDA-style biplot showing environmental variable correlations with microbial community structure (Bray-Curtis dissimilarities).

Gray crosses represent microbial communities across all samples. Red vectors indicate the direction and strength of significant correlations between environmental variables and ordination axes. pH strongly aligned with the primary axis (PCo1), indicating it was the dominant driver of community structure. Nitrate concentrations were positively associated with the secondary axis (PCo2), while sulfate and chloride co-varied along the negative PCo1 and PCo2 quadrant, exerting a weaker influence.

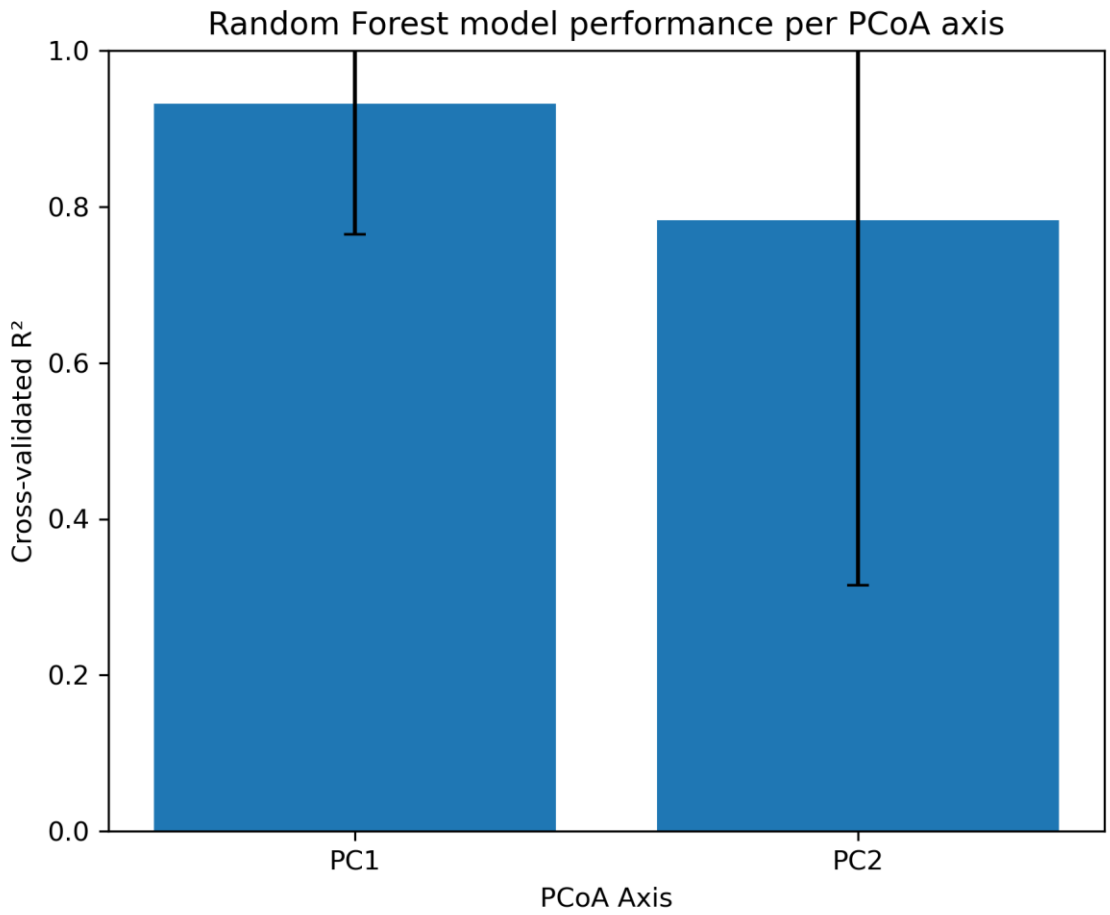

Figure 4.49. Random Forest model performance per PCoA axis.

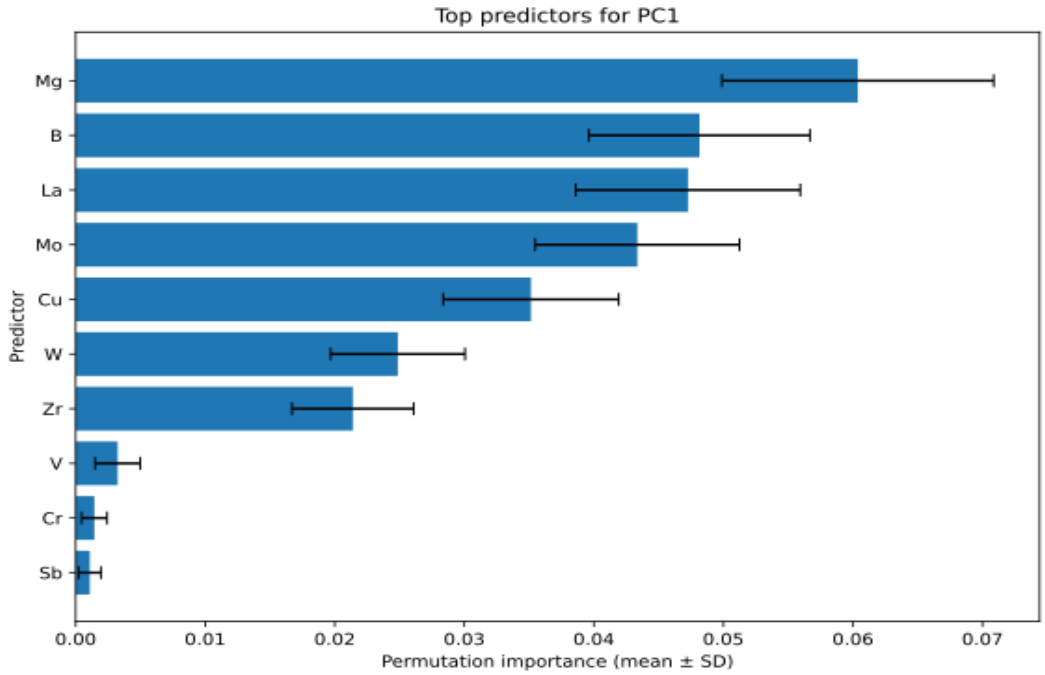

A

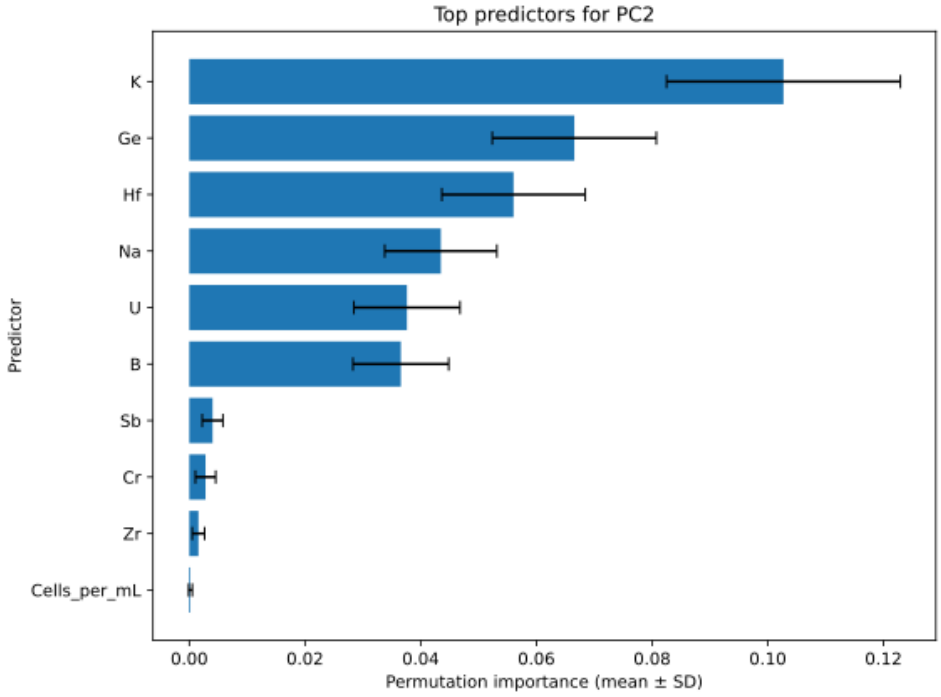

B

Figure 4.50. A. Metal Top predictors for PC1. B. Metal Top predictors for PC2.

Appendix 4: Tables

Table 4.1. DNA concentration and quality (DNA volume: 50 µL).

Sample ID in metadata sheet	Sample ID in output file	Qubit	Nanodrop		
		DNA con. (ng and µL)	DNA con. (ng and µL)	A260 and A280	A260 and A230
20240529-M5-SZ2-F8	M5SZ2.20240529.F8	3.67	6.1	1.88	0.35
20240529-M5-SZ2-F01	M5SZ2.20240529.F01	69.8	71.4	1.87	2.06
20240529-EFP01-F8	EFP01.20240529.F8	4.69	6.8	1.76	0.26
20240529-EFP01-F01	EFP01.20240529.F01	18.7	25.2	1.84	1.47
20240529-L8-SZ2-F8	L8SZ2.20240529.F8	0.713	1.4	1.4	0.11
20240529-L8-SZ2-F01	L8SZ2.20240529.F01	15.9	22.9	1.85	1.81
20240529-U2-SZ2-F8	U2SZ2.20240529.F8	2.52	3.6	1.87	0.17
20240529-U2-SZ2-F01	U2SZ2.20240529.F01	47.2	51.1	1.86	0.93
N and A	Control	<0.5	0.7	1.01	0.03

Table 4.2. Initial characterization: Acridine Orange Direct Count (AODC).

Sample ID	Cells/ml
U1-VSZ	2.36E+05
U1-SZ1	3.43E+05
U1-SZ2	2.36E+05
U2-SZ1	2.29E+05
U2-SZ2	3.02E+05
U3-VSZ	1.18E+05
U3-SZ1	1.51E+05
U3-SZ2	1.82E+05
M4-VSZ	8.03E+04
M4-SZ1	6.85E+04
M4-SZ2	1.16E+05
M5-VSZ	1.09E+05
M5-SZ1	3.36E+05
M5-SZ2	1.37E+05
M5-SZ3	1.04E+05
M6-VSZ	4.73E+05
M6-SZ1	1.75E+05
M6-SZ2	2.67E+05
L7-VSZ	1.04E+05
L7-SZ1	9.22E+04
L7-SZ2 Clumping	1.06E+05
L8-VSZ	1.23E+05
L8-SZ1	2.17E+05
L8-SZ2	1.61E+05
L9-VSZ	1.37E+05
L9-SZ1	1.16E+05
L9-SZ2	8.51E+04

Table 4.3. PERMANOVA results.

test	note	stat	p	n	k_groups	permutations
PERMANOVA	by Well	9.74043028	0.001	40	5	999
Mantel	community ~ geochem	0.51072906	0.001	40		
Mantel	community ~ colloids	0.06364745	0.137	40		
Partial Mantel	community ~ geochem | colloids	0.55821816	0.001	40		
Partial Mantel	community ~ colloids | geochem	0.05653024	0.344	40		

Table 4.4. Random Forrest Top 10 (PC1) permutation importance.

predictor	perm_importance_mean	perm_importance_std	mi
Mg	0.060375125	0.010488353	1.137158659
B	0.048150585	0.008529503	1.11691562
La	0.047267426	0.00866641	1.185956565
Mo	0.043359612	0.007885432	1.107871835
Cu	0.035144503	0.006774815	1.116049976
W	0.024869266	0.00518685	1.129137834
Zr	0.021395265	0.004697482	1.178717448
V	0.003239341	0.001741513	1.132482155
Cr	0.001440522	0.000982932	1.273126789
Sb	0.001087432	0.000865745	1.163648558
Th	0.001015312	0.00080747	1.136740446
K	0.000725674	0.00073532	1.113658271

Table 4.5. Random Forrest Top 10 (PC2) permutation importance.

predictor	perm_importance_mean	perm_importance_std	mi
K	0.102708991	0.020204047	1.045144856
Ge	0.066555317	0.014180504	1.03609429
Hf	0.056051523	0.012390085	1.016831424
Na	0.043478528	0.009691119	1.175646748
U	0.037627897	0.009170303	1.003679368
B	0.036568741	0.008275313	1.161531794
Sb	0.004024032	0.001791234	0.99902796
Cr	0.002811942	0.001752542	1.1085318
Zr	0.001581506	0.001065721	1.016701022
Cells_per_mL	0.000198746	0.000320831	1.004294624
mean_count	0.000130655	0.000124366	0.974167373
Al	1.32921E-06	0.000303186	1.056909956

Chapter V Conclusion

This dissertation presents a multidisciplinary investigation of colloid transport and microbial community structure in the highly contaminated groundwater of the ENIGMA Field Research Center (eFRC) at Y-12. By combining directional hydrology, conservative tracers, ion and metal chemistry, colloid statistics, transmission electron microscopy (TEM), and genome-resolved metagenomics and viromics, we reveal how geochemical gradients and colloids jointly shape subsurface ecology and contaminant mobility.

Our results bridge gene-level mechanisms and ecosystem dynamics within the FICSME framework (Lui et al., 2021). We complement FICSME model by showing that stress-adapted microbes at the eFRC stabilize nutrient assimilation and defense pathways while maintaining flexible energy metabolism. Our data is currently being used to map the ENIGMA isolate genomes to the SSO metagenomes. Our data will assist in determining which strains Adam Arkin ENIGMA's team will phenotype.

The introductory chapters of this dissertation give background information and survey core models of colloid transport (colloid filtration theory, DLVO interactions, and pore- to continuum-scale approaches). We showed that most models are developed for idealized systems (lab conditions) and remain undertested in nitrate-rich environments (in-situ) where geochemical and biological colloids behave differently. Addressing this gap, later chapters examine colloid-facilitated movement of contaminants, minerals, and biological colloids in heterogeneous, nitrate-intensive systems that can be used as foundation for future models for similar conditions.

Chapter III shows that colloid transport at Y-12 is structured by both hydrologic variability and strong geochemical gradients. Ion chemistry revealed nitrate and sulfate enrichment in upper wells and extreme anomalies in lower wells. Colloid distributions reflected these regimes. L8 emerged as a chemically forced, high-mobility hotspot. L7 showed intermediate behavior. Upper and middle wells clustered into more stable transport modes. Transmission electron microscopy images distinguished 3 groups: abiotic, biotic, and mixed colloids with well-specific signatures (highest biological diversity at L8; EPS-entangled cells and necromass at L7; predominantly abiotic material at U2 and EFP01). Viral states differed significantly among wells (χ^2= 14.26, df = 3, p = 0.0026). L7 was dominated by attached viruses, whereas L8 was dominated by free viruses. Pairwise Fisher's tests confirmed elevated attachment in L7 relative to L8 and M5. These observations document direct mineral-microbe-virus associations along the same gradients that structure colloid mobility.

Geochemistry shaped microbial community differences, and colloid abundance correlated with metals, ions, pH, and cell counts. Colloids thus emerge as a mechanistic bridge between contaminant chemistry and microbial ecology, validating the overarching hypothesis and providing strong support for both H1 and H2. Across the SSO wells, noticeable vertical and lateral heterogeneity was observed. Weak, diffuse flow orientations characterized shallow intervals. Watson-Williams tests confirmed strong vertical structure (26 and 28 significant unweighted contrasts; 21 and 28 significant with flux weighting, $p < 0.05$) and even sharper lateral divergence within SZ2 (35 and 36 significant pairwise differences, $p < 0.05$). Watson-Williams tests indicated distinct dominant transport pathways across the field site. Laboratory tests showed no measurable bromide sorption over 200 h, supporting its use as a non-reactive tracer at EFP01. Field ion data revealed extreme nitrate enrichment in upper wells and structured covariation among sulfate, chloride, and nitrate (ρCl-SO4 = 0.89; ρSO4-NO3 = 0.52). That trend is consistent with redox-sensitive stratification and mixed contamination sources. Deep zones paired chemical extremes with limited flow detection, suggesting accumulation domains intermittently connected to high-flux pathways.

Colloid behavior responded sensitively to this context. Pairwise Kolmogorov-Smirnov tests showed a strongly structured distribution of colloid counts. L8 had the largest dissimilarities ($D \approx 0.27$-0.46, all $p < 0.001$). L7 was intermediate; middle and upper wells formed a cohesive, low-variance cluster ($D \approx 0.04$-0.20). This trend aligns with the chemical gradient (with L8 as the uranium maximum spot) and indicates that solution chemistry modulates field-scale colloid attachment and mobility. A non-significant OLS relationship between mean flux and conductivity in a small-n depth profile shows that flux variability is multicausal and better captured by distribution-level (KS) contrasts than by a single linear predictor.

Chapter IV provides a genome-resolved view of how geochemistry structures microbiomes and their mobile gene pools. Integrating 16S rRNA profiles, MAGs, viromes, colloid measurements, and detailed chemistry (pilot SSO wells plus EFP01). With the combined data, we find strong support for H1: communities differ among wells (PERMANOVA pseudo-F = 9.74, $p = 0.001$) and track chemistry across the plume (Mantel $r = 0.628$, $p = 0.001$). Machine-learning models captured these structures with high accuracy (PC1 $cvR^2 = 0.93$), repeatedly elevating tungsten, zirconium, boron, cadmium, magnesium, manganese, and uranium as top predictors. Ecologically, U2-SZ2 represents an upper-plume, nitrate-rich niche; M5-SZ2 is a

redox-active transition; L8-SZ2 is a uranium hotspot with comparatively oligotrophic signatures. Alpha-diversity and functional breadth followed these settings: broader carbon and nitrogen capacities at U2 and M5; tighter, metal-adapted repertoires at L8.

H2 receives qualified support. Colloids alone did not dominate landscape-scale community structure, but they contributed beyond chemistry. For example, a partial Mantel test controlling for geochemistry showed a significant independent association between colloids and community dissimilarities ($r \approx 0.143$, $p = 0.005$). Viromes were dominated by *Caudoviricetes*, and mobile genetic elements were abundant. All that provided mechanisms for rapid horizontal gene transfer where colloid abundance and connectivity coincide. Functional groups co-occurred in predictable pairings. For instance, transporters grouped with CRISPR defenses, energy metabolism with nucleotide and cofactor biosynthesis-suggesting genomes are organized into integrated strategies favored under metal and anion stress, viral pressure, and episodic dispersal.

The case studies strengths this picture. *Rhodanobacter denitrificans* are most abundant where nitrate is high and pH are low, consistent with enriched denitrification modules but frequent truncation (such as absent nosZ). That implies potential nitrous oxide accumulation under stress. Patescibacteria are recovered primarily from fine fractions, consistent with episymbiotic lifestyles and streamlined genomes that persist in energy-limited settings. Jointly with the strong enrichment of transporter systems and CRISPR defenses in upper and transitional wells, these results support two adaptive axes repeated across the dataset: metal and anion management at the cell envelope and layered antiviral immunity.

Viruses in the eFRC Y-12 groundwater, especially in newly installed SSO wells, have not been systematically studied. Earlier eFRC work recovered limited viral sequences from non-SSO wells via plasmidome and mobilome approaches, but no comprehensive virome studies existed. Here we establish the first viromic baseline for SSO SZ2 wells, link vMAGs to hosts and functions, and identify auxiliary metabolic genes potentially supporting adaptation in contaminated aquifers, filling a major knowledge gap.

These findings have practical implications. Microbial communities act as biosensors of contamination class and well identity, suggesting 16S and MAG-derived metrics can augment routine monitoring. The recurrence of W, Zr, B, Cd, Mg, Mn, and U among top predictors argues for including these metals alongside anions to anticipate biological responses. Given dense mobile genetic elements and phages in colloid fractions, targeted surveillance of plasmid and

viral markers could provide early warning for the emergence or spread of resistance and stress-response traits.

This study addresses key knowledge gaps in contaminant hydrology and microbial ecology at legacy sites by grounding each claim in field-based evidence. First, colloids in extreme environments were poorly understood-borescope measurements revealed high particle fluxes (up to 1200 μm/s x particle counts) in acidic, nitrate-rich zones demonstrating that colloids are actively mobilized under conditions where dissolved-solute models predict limited transport; transmission electron microscopy images of colloids at eFRC were not studied before. Second, linkages between microbial communities and geochemical gradients were unexplored: 16S time series (n = 40) and genome-resolved metagenomes (n = 8) showed clear depth-structured microbial assemblages, with U2-SZ2 dominated by nitrate-tolerant specialists *(Rhodanobacter denitrificans* spp.) at $NO_3^- \approx 290$ ppm. At the same time, M5-SZ2 and L8 communities reflected Mn- and U-rich chemistries. These trends were quantitatively supported by PERMANOVA and dbRDA analyses linking nitrate, Mn, and pH gradients to community structure. Third, the connection between colloids, metals, and microbes was unclear: metals data revealed U, Mn, and Fe enrichment coinciding with colloid mobilization, while AODC cell counts and plasmid and virus inventories showed abundant biological material on particles. Mantel tests and Random Forest regressions demonstrated strong correlations between colloid distributions and microbial and viral diversity, indicating coupled transport. Finally, integrated frameworks were lacking: by merging hydrological flux indices, geochemical profiles, and multi-omics data, this work developed a unified, field-grounded framework linking colloid-mediated transport with both abiotic and biotic controls.

Limitations and next steps include broader spatial coverage (all zones for MAGs and viromes), temporal replication across hydrologic cycles to clarify mechanisms. Even with these limitations, our multi-omics profile (n = 40 for ASVs; n = 8 for MAGs and viromes) establishes essential baselines.

Overall, geochemical gradients impose the dominant ecological filter, while colloids provide an independent, field-scale signal by physically carrying cells and viruses along advective pathways. We also identified a predictive metals panel and plasmid and viral markers for monitoring.

Our findings contribute to predictive risk assessment frameworks and inform the design of monitoring programs in nuclear legacy sites. Ultimately, this work advances our ability to understand and forecast contaminant mobility under extreme geochemical conditions, strengthening efforts to protect groundwater resources, as well as human and ecosystem health.

References

Abdel-Salam, A., Chrysikopoulos, C.V., 1995. Analysis of a model for contaminant transport in fractured media in the presence of colloids. Journal of Hydrology 165(1-4), 261-281.

Allen, B., Bresnahan, J., Childers, L., Foster, I., Kandaswamy, G., Kettimuthu, R., Kordas, J., Link, M., Martin, S., Pickett, K., 2012. Software as a service for data scientists. Communications of the ACM 55(2), 81-88.

Alneberg, J., Bjarnason, B.S., De Bruijn, I., Schirmer, M., Quick, J., Ijaz, U.Z., Lahti, L., Loman, N.J., Andersson, A.F., Quince, C., 2014. Binning metagenomic contigs by coverage and composition. Nature methods 11(11), 1144-1146.

Anantharaman, K., Brown, C.T., Burstein, D., Castelle, C.J., Probst, A.J., Thomas, B.C., Williams, K.H., Banfield, J.F., 2016a. Analysis of five complete genome sequences for members of the class Peribacteria in the recently recognized Peregrinibacteria bacterial phylum. PeerJ 4, e1607.

Anantharaman, K., Brown, C.T., Hug, L.A., Sharon, I., Castelle, C.J., Probst, A.J., Thomas, B.C., Singh, A., Wilkins, M.J., Karaoz, U., 2016b. Thousands of microbial genomes shed light on interconnected biogeochemical processes in an aquifer system. Nature communications 7(1), 13219.

Babakhani, P., 2019. The impact of nanoparticle aggregation on their size exclusion during transport in porous media: One-and three-dimensional modelling investigations. Scientific reports 9(1), 14071.

Babakhani, P., Bridge, J., Doong, R.-a., Phenrat, T., 2017. Continuum-based models and concepts for the transport of nanoparticles in saturated porous media: A state-of-the-science review. Advances in colloid and interface science 246, 75-104.

Baca, C.F., Yu, Y., Rostøl, J.T., Majumder, P., Patel, D.J., Marraffini, L.A., 2024. The CRISPR effector Cam1 mediates membrane depolarization for phage defence. Nature 625(7996), 797-804.

Bales, R.C., Gerba, C.P., Grondin, G.H., Jensen, S.L., 1989. Bacteriophage transport in sandy soil and fractured tuff. Applied and Environmental Microbiology 55(8), 2061-2067.

Bales, R.C., Hinkle, S.R., Kroeger, T.W., Stocking, K., Gerba, C.P., 1991. Bacteriophage adsorption during transport through porous media: Chemical perturbations and reversibility. Environmental Science & Technology 25(12), 2088-2095.

Baumann, T., Toops, L., Niessner, R., 2010. Colloid dispersion on the pore scale. water research 44(4), 1246-1254.

Bedrikovetsky, P., Siqueira, F.D., Furtado, C.A., Souza, A.L.S., 2011. Modified particle detachment model for colloidal transport in porous media. Transport in porous media 86, 353-383.

Bekhit, H.M., Hassan, A.E., 2007. Subsurface contaminant transport in the presence of colloids: Effect of nonlinear and nonequilibrium interactions. Water resources research 43(8).

Berks, B.C., Page, M.D., Richardson, D.J., Reilly, A., Cavill, A., Outen, F., Ferguson, S.J., 1995. Sequence analysis of subunits of the membrane-bound nitrate reductase from a denitrifying bacterium: the integral membrane subunit provides a prototype for the dihaem electron-carrying arm of a redox loop. Molecular microbiology 15(2), 319-331.

Boguslavsky, A., Gaskova, O., Naymushina, O., Popova, N., Safonov, A., 2020. Environmental monitoring of low-level radioactive waste disposal in electrochemical plant facilities in Zelenogorsk, Russia. Applied geochemistry 119, 104598.

Bolger, A.M., Lohse, M., Usadel, B., 2014. Trimmomatic: a flexible trimmer for Illumina sequence data. Bioinformatics 30(15), 2114-2120.

Bolyen, E., Rideout, J.R., Dillon, M.R., Bokulich, N.A., Abnet, C.C., Al-Ghalith, G.A., Alexander, H., Alm, E.J., Arumugam, M., Asnicar, F., 2019. Reproducible, interactive, scalable and extensible microbiome data science using QIIME 2. Nature biotechnology 37(8), 852-857.

Borgman, O., Be'Er, A., Weisbrod, N., 2022. Direct visualization of colloid transport over natural heterogeneous and artificial smooth rock surfaces. Journal of Contaminant Hydrology 251, 104067.

Bradford, S.A., Bettahar, M., Simunek, J., Van Genuchten, M.T., 2004. Straining and attachment of colloids in physically heterogeneous porous media. Vadose Zone Journal 3(2), 384-394.

Bradford, S.A., Kim, H.N., Haznedaroglu, B.Z., Torkzaban, S., Walker, S.L., 2009. Coupled factors influencing concentration-dependent colloid transport and retention in saturated porous media. Environmental science & technology 43(18), 6996-7002.

Bradford, S.A., Simunek, J., Bettahar, M., Van Genuchten, M.T., Yates, S., 2006. Significance of straining in colloid deposition: Evidence and implications. Water Resources Research 42(12).

Bradford, S.A., Torkzaban, S., 2008. Colloid transport and retention in unsaturated porous media: A review of interface-, collector-, and pore-scale processes and models. Vadose Zone Journal 7(2), 667-681.

Bradford, S.A., Torkzaban, S., Simunek, J., 2011. Modeling colloid transport and retention in saturated porous media under unfavorable attachment conditions. Water Resources Research 47(10).

Braga, L.P.P., Pereira, R.V., Martins, L.F., Moura, L.M.S., Sanchez, F.B., Patané, J.S.L., Da Silva, A.M., Setubal, J.C., 2021. Genome-resolved metagenome and metatranscriptome analyses of thermophilic composting reveal key bacterial players and their metabolic interactions. BMC genomics 22(1), 652.

Brooks, S., Jardine, P., Taylor, D., 1998. Thermodynamics of bromide exchange on ferrihydrite: Implications for bromide transport. Soil Science Society of America Journal 62(5), 1275-1279.

Buddemeier, R.W., Hunt, J.R., 1988. Transport of colloidal contaminants in groundwater: radionuclide migration at the Nevada Test Site. Applied geochemistry 3(5), 535-548.

Callahan, B.J., McMurdie, P.J., Rosen, M.J., Han, A.W., Johnson, A.J.A., Holmes, S.P., 2016. DADA2: High-resolution sample inference from Illumina amplicon data. Nature methods 13(7), 581-583.

Camargo, A.P., Roux, S., Schulz, F., Babinski, M., Xu, Y., Hu, B., Chain, P.S., Nayfach, S., Kyrpides, N.C., 2024. Identification of mobile genetic elements with geNomad. Nature Biotechnology 42(8), 1303-1312.

Campbell, W.H., 1996. Nitrate reductase biochemistry comes of age. Plant Physiology 111(2), 355.

Caporaso, J.G., Lauber, C.L., Walters, W.A., Berg-Lyons, D., Huntley, J., Fierer, N., Owens, S.M., Betley, J., Fraser, L., Bauer, M., 2012. Ultra-high-throughput microbial community analysis on the Illumina HiSeq and MiSeq platforms. The ISME journal 6(8), 1621-1624.

Cardenas, E., Wu, W.-M., Leigh, M.B., Carley, J., Carroll, S., Gentry, T., Luo, J., Watson, D., Gu, B., Ginder-Vogel, M., 2010. Significant association between sulfate-reducing bacteria and uranium-reducing microbial communities as revealed by a combined massively

parallel sequencing-indicator species approach. Applied and Environmental Microbiology 76(20), 6778-6786.

Carlson, H.K., Price, M.N., Callaghan, M., Aaring, A., Chakraborty, R., Liu, H., Arkin, A.P., Deutschbauer, A.M., 2018. Defining the toxicity limits on microbial range in a metal-contaminated aquifer Running Title: Inorganic ion toxicity limits on microbial range. bioRxiv, 388306.

Chakraborty, R., Pettenato, A., Lancaster, A., Thorgersen, M.P., Poole, F., Vaccaro, B.A., Deutschbauer, A.M., Ray, J., Kazakov, A., Novichkov, P., 2014. Physiology of Nitrate-reducing Strains Cultivated from Contaminated Groundwater at the Oak-ridge Field Research Center, AGU Fall Meeting Abstracts. pp. B23D-0232.

Chaudhari, N.M., Pérez-Carrascal, O.M., Overholt, W.A., Totsche, K.U., Küsel, K., 2024. Genome streamlining in Parcubacteria transitioning from soil to groundwater. Environmental Microbiome 19(1), 41.

Chivian, D., Jungbluth, S.P., Dehal, P.S., Wood-Charlson, E.M., Canon, R.S., Allen, B.H., Clark, M.M., Gu, T., Land, M.L., Price, G.A., 2023. Metagenome-assembled genome extraction and analysis from microbiomes using KBase. Nature Protocols 18(1), 208-238.

Chrysikopoulos, C.V., Abdel-Salam, A., 1997. Modeling colloid transport and deposition in saturated fractures. Colloids and Surfaces A: Physicochemical and Engineering Aspects 121(2-3), 189-202.

Contardi, J., Turner, D., Ahn, T., 2001. Modeling colloid transport for performance assessment. Journal of contaminant hydrology 47(2-4), 323-333.

Corapcioglu, M.Y., Jiang, S., 1993. Colloid-facilitated groundwater contaminant transport. Water Resources Research 29(7), 2215-2226.

Cullen, E., O'Carroll, D.M., Yanful, E.K., Sleep, B., 2010. Simulation of the subsurface mobility of carbon nanoparticles at the field scale. Advances in water resources 33(4), 361-371.

Dai, M., Buesseler, K.O., Pike, S.M., 2005. Plutonium in groundwater at the 100K-Area of the US DOE Hanford Site. Journal of Contaminant Hydrology 76(3-4), 167-189.

Dai, M., Kelley, J.M., Buesseler, K.O., 2002. Sources and migration of plutonium in groundwater at the Savannah River Site. Environmental science & technology 36(17), 3690-3699.

Davis, S.N., Thompson, G.M., Bentley, H.W., Stiles, G., 1980. Ground-water tracers—A short review. Groundwater 18(1), 14-23.

de Jonge, L.W., Kjærgaard, C., Moldrup, P., 2004. Colloids and colloid-facilitated transport of contaminants in soils: An introduction. Vadose Zone Journal 3(2), 321-325.

Deb, D., Chakma, S., 2023. Colloid and colloid-facilitated contaminant transport in subsurface ecosystem—a concise review. International Journal of Environmental Science and Technology 20(6), 6955-6988.

Deutschbauer, A.M., Fields, M.W., Hazen, T.C., Northen, T.R., Adams, M.W., Alm, E.J., Chandonia, J.-M., Mukhopadhyay, A., Siuzdak, G.E., Stahl10, D.A., DOE BSSD Metrics Progress Report Q1: 01/12/2022 SFA Laboratory Research Manager: Paul D. Adams1, PDAdams@ lbl. gov SFA Technical Co-Manager: Adam P. Arkin1, APArkin@ lbl. gov 1Lawrence Berkeley National Laboratory, Berkeley CA 94720.

Elimelech, M., O'Melia, C.R., 1990. Kinetics of deposition of colloidal particles in porous media. Environmental science & technology 24(10), 1528-1536.

Fan, Y., Wang, D., Yang, J.X., Ning, D., He, Z., Zhang, P., Rocha, A.M., Xiao, N., Michael, J.P., Walker, K.F., 2025. Modest functional diversity decline and pronounced composition shifts of microbial communities in a mixed waste-contaminated aquifer. Microbiome 13(1), 1-13.

Fetter, C.W., Boving, T., Kreamer, D., 2017. Contaminant hydrogeology. Waveland Press.

Fetter Jr, C., 2001. Applied Hydrogeology Fetter Fourth Edition.

Flury, M., Aramrak, S., 2017. Role of air-water interfaces in colloid transport in porous media: A review. Water resources research 53(7), 5247-5275.

Flury, M., Qiu, H., 2008. Modeling colloid-facilitated contaminant transport in the vadose zone. Vadose Zone Journal 7(2), 682-697.

Foster, I., 2011. Globus Online: Accelerating and democratizing science through cloud-based services. IEEE Internet Computing 15(3), 70-73.

Freitas, T.A.K., Li, P.-E., Scholz, M.B., Chain, P.S., 2015. Accurate read-based metagenome characterization using a hierarchical suite of unique signatures. Nucleic acids research 43(10), e69-e69.

Frimmel, F.H., Von der Kammer, F., Flemming, H.-C., 2007. Colloidal transport in porous media. Springer.

Geesey, G., Jang, L., Jolley, J., Hankins, M., Iwaoka, T., Griffiths, P., 1988. Binding of metal ions by extracellular polymers of biofilm bacteria. Water Science and Technology 20(11-12), 161-165.

Goff, J.L., Szink, E.G., Thorgersen, M.P., Putt, A.D., Fan, Y., Lui, L.M., Nielsen, T.N., Hunt, K.A., Michael, J.P., Wang, Y., 2022. Ecophysiological and genomic analyses of a representative isolate of highly abundant Bacillus cereus strains in contaminated subsurface sediments. Environmental Microbiology 24(11), 5546-5560.

Green, S.J., Prakash, O., Gihring, T.M., Akob, D.M., Jasrotia, P., Jardine, P.M., Watson, D.B., Brown, S.D., Palumbo, A.V., Kostka, J.E., 2010. Denitrifying bacteria isolated from terrestrial subsurface sediments exposed to mixed-waste contamination. Applied and environmental microbiology 76(10), 3244-3254.

Green, S.J., Prakash, O., Jasrotia, P., Overholt, W.A., Cardenas, E., Hubbard, D., Tiedje, J.M., Watson, D.B., Schadt, C.W., Brooks, S.C., 2012. Denitrifying bacteria from the genus Rhodanobacter dominate bacterial communities in the highly contaminated subsurface of a nuclear legacy waste site. Applied and environmental microbiology 78(4), 1039-1047.

Griebler, C., Lueders, T., 2009. Microbial biodiversity in groundwater ecosystems. Freshwater biology 54(4), 649-677.

Grolimund, D., Borkovec, M., 2005. Colloid-facilitated transport of strongly sorbing contaminants in natural porous media: Mathematical modeling and laboratory column experiments. Environmental science & technology 39(17), 6378-6386.

Haliena, B., Zheng, H., Melson, N., Kaplan, D.I., Barnett, M.O., 2016. Decreased salinity and actinide mobility: colloid-facilitated transport or pH change? Environmental Science & Technology 50(2), 625-632.

Harris, C.R., Millman, K.J., Van Der Walt, S.J., Gommers, R., Virtanen, P., Cournapeau, D., Wieser, E., Taylor, J., Berg, S., Smith, N.J., 2020. Array programming with NumPy. nature 585(7825), 357-362.

Hatcher Jr, R.D., Lemiszki, P., Foreman, J., Dreier, R., Ketelle, R., Lee, R., Lee, S.Y., Lietzke, D., McMaster, W., 1992. Status report on the geology of the Oak Ridge Reservation. Oak Ridge National Lab., TN (United States).

Hazen, T.C., Jiménez, L., López de Victoria, G., Fliermans, C.B., 1991. Comparison of bacteria from deep subsurface sediment and adjacent groundwater. Microbial Ecology 22(1), 293-304.

He, Q., He, Z., Joyner, D.C., Joachimiak, M., Price, M.N., Yang, Z.K., Yen, H.-C.B., Hemme, C.L., Chen, W., Fields, M.M., 2010. Impact of elevated nitrate on sulfate-reducing bacteria: a comparative study of Desulfovibrio vulgaris. The ISME Journal 4(11), 1386-1397.

Hemme, C.L., Deng, Y., Gentry, T.J., Fields, M.W., Wu, L., Barua, S., Barry, K., Tringe, S.G., Watson, D.B., He, Z., 2010. Metagenomic insights into evolution of a heavy metal-contaminated groundwater microbial community. The ISME journal 4(5), 660-672.

Hemme, C.L., Green, S.J., Rishishwar, L., Prakash, O., Pettenato, A., Chakraborty, R., Deutschbauer, A.M., Van Nostrand, J.D., Wu, L., He, Z., 2016. Lateral gene transfer in a heavy metal-contaminated-groundwater microbial community. MBio 7(2), e02234-02215.

Hemme, C.L., Tu, Q., Shi, Z., Qin, Y., Gao, W., Deng, Y., Nostrand, J.D.V., Wu, L., He, Z., Chain, P.S., 2015. Comparative metagenomics reveals impact of contaminants on groundwater microbiomes. Frontiers in microbiology 6, 1205.

Hochella, M.F., Aruguete, D., Kim, B., Madden, A.S., 2012. Naturally occurring inorganic nanoparticles: general assessment and a global budget for one of earth's last unexplored major geochemical components. Nature's nanostructures, 1-31.

Im, J., Dwivedi, D., Putt, A., Walker, K.F., Marquis, J., Lui, L.M., Carr, A., Fan, Y., Goff, J., Hunt, K., 2023. Reactive Transport Modeling of N cycling for Prediction of N2O emitted from the Subsurface Observatory at Area 3 under Rainfall Events, AGU Fall Meeting Abstracts. pp. B13H-2002.

Jain, C., Rodriguez-R, L.M., Phillippy, A.M., Konstantinidis, K.T., Aluru, S., 2018. High throughput ANI analysis of 90K prokaryotic genomes reveals clear species boundaries. Nature communications 9(1), 5114.

Joudeh, N., Linke, D., 2022. Nanoparticle classification, physicochemical properties, characterization, and applications: a comprehensive review for biologists. Journal of nanobiotechnology 20(1), 262.

Kang, D.D., Froula, J., Egan, R., Wang, Z., 2015. MetaBAT, an efficient tool for accurately reconstructing single genomes from complex microbial communities. PeerJ 3, e1165.

Katoh, K., Misawa, K., Kuma, K.i., Miyata, T., 2002. MAFFT: a novel method for rapid multiple sequence alignment based on fast Fourier transform. Nucleic acids research 30(14), 3059-3066.

Katzourakis, V.E., Chrysikopoulos, C.V., 2014. Mathematical modeling of colloid and virus cotransport in porous media: Application to experimental data. Advances in water resources 68, 62-73.

Kersting, A., Efurd, D., Finnegan, D., Rokop, D., Smith, D., Thompson, J., 1999. Migration of plutonium in ground water at the Nevada Test Site. Nature 397(6714), 56-59.

Kheirabadi, M., Niksokhan, M.H., Omidvar, B., 2017. Colloid-associated groundwater contaminant transport in homogeneous saturated porous media: mathematical and numerical modeling. Environmental Modeling & Assessment 22, 79-90.

Khurana, S., Heße, F., Hildebrandt, A., Thullner, M., 2024. Microbial mediated carbon and nitrogen cycling in the spatially heterogeneous vadose zone: A modeling study. Vadose Zone Journal 23(2), e20315.

Kluyver, T., Ragan-Kelley, B., Pérez, F., Granger, B., Bussonnier, M., Frederic, J., Kelley, K., Hamrick, J., Grout, J., Corlay, S., 2016. Jupyter Notebooks–a publishing format for reproducible computational workflows, Positioning and power in academic publishing: Players, agents and agendas. IOS press, pp. 87-90.

Koh, H.-W., Hong, H., Min, U.-G., Kang, M.-S., Kim, S.-G., Na, J.-G., Rhee, S.-K., Park, S.-J., 2015. Rhodanobacter aciditrophus sp. nov., an acidophilic bacterium isolated from mine wastewater. International Journal of Systematic and Evolutionary Microbiology 65(Pt_12), 4574-4579.

Kothari, A., Roux, S., Zhang, H., Prieto, A., Soneja, D., Chandonia, J.-M., Spencer, S., Wu, X., Altenburg, S., Fields, M.W., 2021. Ecogenomics of groundwater phages suggests niche differentiation linked to specific environmental tolerance. Msystems 6(3), 10.1128/msystems. 00537-00521.

Kothari, A., Soneja, D., Tang, A., Carlson, H.K., Deutschbauer, A.M., Mukhopadhyay, A., 2019a. Native plasmid-encoded mercury resistance genes are functional and demonstrate natural transformation in environmental bacterial isolates. Msystems 4(6), 10.1128/msystems. 00588-00519.

Kothari, A., Wu, Y.-W., Chandonia, J.-M., Charrier, M., Rajeev, L., Rocha, A.M., Joyner, D.C., Hazen, T.C., Singer, S.W., Mukhopadhyay, A., 2019b. Large circular plasmids from groundwater plasmidomes span multiple incompatibility groups and are enriched in multimetal resistance genes. MBio 10(1), 10.1128/mbio. 02899-02818.

Kuzyakov, Y., Blagodatskaya, E., 2015. Microbial hotspots and hot moments in soil: concept & review. Soil Biology and Biochemistry 83, 184-199.

Lee, J., Choi, S.-U., Cho, W., 1999. A comparative study of dual-porosity model and discrete fracture network model. KSCE Journal of Civil Engineering 3(2), 171-180.

Leij, F.J., Bradford, S.A., 2013. Colloid transport in dual-permeability media. Journal of contaminant hydrology 150, 65-76.

Lin, X., Kennedy, D., Fredrickson, J., Bjornstad, B., Konopka, A., 2012. Vertical stratification of subsurface microbial community composition across geological formations at the Hanford Site. Environmental Microbiology 14(2), 414-425.

Ludwig, W., Viver, T., Westram, R., Gago, J.F., Bustos-Caparros, E., Knittel, K., Amann, R., Rossello-Mora, R., 2021. Release LTP_12_2020, featuring a new ARB alignment and improved 16S rRNA tree for prokaryotic type strains. Systematic and Applied Microbiology 44(4), 126218.

Lui, L.M., Nielsen, T.N., 2023. Decomposing a San Francisco Estuary microbiome using long read metagenomics reveals species and species-and strain-level dominance from picoeukaryotes to viruses. bioRxiv, 2023.2006. 2030.547288.

Lui, L.M., Nielsen, T.N., Smith, H.J., Chandonia, J.-M., Kuehl, J., Song, F., Sczesnak, A., Hendrickson, A., Hazen, T., Fields, M., 2024. Sediment and Groundwater Metagenomes from Subsurface Microbial Communities from the Oak Ridge National Laboratory Field Research Center, Oak Ridge, TN, USA.

Lui, L.M., Nielsen, T.N., Smith, H.J., Chandonia, J.-M., Kuehl, J.V., Song, F., Sczesnak, A., Hendrickson, A., Hazen, T.C., Fields, M.W., 2025. Sediment and groundwater metagenomes from subsurface microbial communities from the Oak Ridge National Laboratory Oak Ridge Reservation, Oak Ridge, Tennessee, USA. Microbiology Resource Announcements, e00014-00025.

Lukashenko, S., Kabdyrakova, A., Lind, O., Gorlachev, I., Kunduzbayeva, A., Kvochkina, T., Janssens, K., De Nolf, W., Yakovenko, Y., Salbu, B., 2020. Radioactive particles

released from different sources in the Semipalatinsk Test Site. Journal of Environmental Radioactivity 216, 106160.

Lycus, P., Lovise Bøthun, K., Bergaust, L., Peele Shapleigh, J., Reier Bakken, L., Frostegård, Å., 2017. Phenotypic and genotypic richness of denitrifiers revealed by a novel isolation strategy. The ISME journal 11(10), 2219-2232.

Maheshwari, A.J., Sunol, A.M., Gonzalez, E., Endy, D., Zia, R.N., 2023. Colloidal physics modeling reveals how per-ribosome productivity increases with growth rate in Escherichia coli. Mbio 14(1), e02865-02822.

Malkovsky, V., Pek, A., 2009. Effect of colloids on transfer of radionuclides by subsurface water. Geology of Ore Deposits 51(2), 79-92.

Malkovsky, V.I., Pek, A.A., 2009. Effect of elevated velocity of particles in groundwater flow and its role in colloid-facilitated transport of radionuclides in underground medium. Transport in porous media 78(2), 277-294.

McCarter, C., Rezanezhad, F., Quinton, W., Gharedaghloo, B., Lennartz, B., Price, J., Connon, R., Van Cappellen, P., 2020. Pore-scale controls on hydrological and geochemical processes in peat: Implications on interacting processes. Earth-Science Reviews 207, 103227.

McCarthy, J., Zachara, J., 1989. ES&T Features: Subsurface transport of contaminants. Environmental science & technology 23(5), 496-502.

McCarthy, J.F., McKay, L.D., 2004. Colloid transport in the subsurface: Past, present, and future challenges. Vadose Zone Journal 3(2), 326-337.

McKay, L., Sanford, W., Strong, J., 2000. Field-scale migration of colloidal tracers in a fractured shale saprolite. Groundwater 38(1), 139-147.

McKinney, W., 2010. Data structures for statistical computing in Python. scipy 445(1), 51-56.

Menzel, P., Ng, K.L., Krogh, A., 2016. Fast and sensitive taxonomic classification for metagenomics with Kaiju. Nature communications 7(1), 11257.

Michael, J.P., Putt, A.D., Yang, Y., Adams, B.G., McBride, K.R., Fan, Y., Lowe, K.A., Ning, D., Jagadamma, S., Moon, J.W., 2024. Reproducible responses of geochemical and microbial successional patterns in the subsurface to carbon source amendment. Water Research 255, 121460.

Molnar, I.L., Johnson, W.P., Gerhard, J.I., Willson, C.S., O'carroll, D.M., 2015. Predicting colloid transport through saturated porous media: A critical review. Water Resources Research 51(9), 6804-6845.

Molnar, I.L., Pensini, E., Asad, M.A., Mitchell, C.A., Nitsche, L.C., Pyrak-Nolte, L.J., Miño, G.L., Krol, M.M., 2019. Colloid transport in porous media: a review of classical mechanisms and emerging topics. Transport in Porous Media 130, 129-156.

Moon, J.-W., Paradis, C.J., Joyner, D.C., von Netzer, F., Majumder, E.L., Dixon, E.R., Podar, M., Ge, X., Walian, P.J., Smith, H.J., 2020. Characterization of subsurface media from locations up-and down-gradient of a uranium-contaminated aquifer. Chemosphere 255, 126951.

Morales, C.F.L., Strathmann, M., Flemming, H.-C., 2007. Influence of biofilms on the movement of colloids in porous media. Implications for colloid facilitated transport in subsurface environments. Water Research 41(10), 2059-2068.

Nair, V.V., Thampi, S.G., 2010. Numerical modelling of colloid transport in sets of parallel fractures with fracture skin. Colloids and Surfaces A: Physicochemical and Engineering Aspects 364(1-3), 109-115.

Nalin, R., Simonet, P., Vogel, T.M., Normand, P., 1999. Rhodanobacter lindaniclasticus gen. nov., sp. nov., a lindane-degrading bacterium. International Journal of Systematic and Evolutionary Microbiology 49(1), 19-23.

Natarajan, N., Kumar, G.S., 2010. Radionuclide and colloid co-transport in a coupled fracture-skin-matrix system. Colloids and Surfaces A: Physicochemical and Engineering Aspects 370(1-3), 49-57.

Nelson, K.E., Ginn, T.R., 2005. Colloid filtration theory and the Happel sphere-in-cell model revisited with direct numerical simulation of colloids. Langmuir 21(6), 2173-2184.

Ning, D., Wang, Y., Fan, Y., Wang, J., Van Nostrand, J.D., Wu, L., Zhang, P., Curtis, D.J., Tian, R., Lui, L., 2024. Environmental stress mediates groundwater microbial community assembly. Nature Microbiology 9(2), 490-501.

Nurk, S., Meleshko, D., Korobeynikov, A., Pevzner, P.A., 2017. metaSPAdes: a new versatile metagenomic assembler. Genome research 27(5), 824-834.

Oudega, T.J., Lindner, G., Derx, J., Farnleitner, A.H., Sommer, R., Blaschke, A.P., Stevenson, M.E., 2021. Upscaling transport of bacillus subtilis endospores and coliphage

phiX174 in heterogeneous porous media from the column to the field scale. Environmental Science & Technology 55(16), 11060-11069.

Pan, W., Tartakovsky, A., 2013. Dissipative particle dynamics model for colloid transport in porous media. Advances in water resources 58, 41-48.

Paradis, C.J., Miller, J.I., Moon, J.W., Spencer, S.J., Lui, L.M., Van Nostrand, J.D., Ning, D., Steen, A.D., McKay, L.D., Arkin, A.P., 2022. Sustained ability of a natural microbial community to remove nitrate from groundwater. Groundwater 60(1), 99-111.

Parks, D.H., Imelfort, M., Skennerton, C.T., Hugenholtz, P., Tyson, G.W., 2015. CheckM: assessing the quality of microbial genomes recovered from isolates, single cells, and metagenomes. Genome research 25(7), 1043-1055.

Peng, M., Wang, D., Lui, L.M., Nielsen, T., Tian, R., Kempher, M.L., Tao, X., Pan, C., Chakraborty, R., Deutschbauer, A.M., 2022. Genomic Features and Pervasive Negative Selection in Rhodanobacter Strains Isolated from Nitrate and Heavy Metal Contaminated Aquifer. Microbiology spectrum 10(1), e02591-02521.

Pettenato, A.S., M.; Ray, J., Deutschbauer; A., Hazen, T.; Arkin, A.; Chakraborty, R. , 2014. Nitrate-Contaminated Groundwater at Oakridge FRC. , American Society for Microbiology Annual Meeting. Boston, MA USA.

Prakash, O., Green, S.J., Singh, P., Jasrotia, P., Kostka, J.E., 2021. Stress-related ecophysiology of members of the genus Rhodanobacter isolated from a mixed waste contaminated subsurface. Frontiers of Environmental Science & Engineering 15(2), 1-9.

Price, M.N., Dehal, P.S., Arkin, A.P., 2009. FastTree: computing large minimum evolution trees with profiles instead of a distance matrix. Molecular biology and evolution 26(7), 1641-1650.

Price, M.N., Dehal, P.S., Arkin, A.P., 2010. FastTree 2–approximately maximum-likelihood trees for large alignments. PloS one 5(3), e9490.

Putt, A.D., 2022. The effects of physical and geochemical perturbation on small bacterial communities at a contaminated site with a focus on the model phylum Patescibacteria. University of Tennessee.

Putt, A.D., Kelly, E.R., Lowe, K.A., Rodriguez Jr, M., Hazen, T.C., 2022. Effects of cone penetrometer testing on shallow hydrogeology at a contaminated site. Frontiers in Environmental Science 9, 729.

Quast, C., Pruesse, E., Yilmaz, P., Gerken, J., Schweer, T., Yarza, P., Peplies, J., Glöckner, F.O., 2012. The SILVA ribosomal RNA gene database project: improved data processing and web-based tools. Nucleic acids research 41(D1), D590-D596.

Revil, A., Skold, M., Hubbard, S.S., Wu, Y., Watson, D.B., Karaoulis, M., 2013. Petrophysical properties of saprolites from the Oak Ridge integrated field research challenge site, Tennessee. Geophysics 78(1), D21-D40.

Revil, A., Skold, M., Karaoulis, M., Schmutz, M., Hubbard, S.S., Mehlhorn, T.L., Watson, D.B., 2013. Hydrogeophysical investigations of the former S-3 ponds contaminant plumes, Oak Ridge Integrated Field Research Challenge site, Tennessee. Geophysics 78(4), EN29-EN41.

Rivett, M.O., Buss, S.R., Morgan, P., Smith, J.W., Bemment, C.D., 2008. Nitrate attenuation in groundwater: a review of biogeochemical controlling processes. Water research 42(16), 4215-4232.

Rodríguez-Beltrán, J., DelaFuente, J., Leon-Sampedro, R., MacLean, R.C., San Millan, A., 2021. Beyond horizontal gene transfer: the role of plasmids in bacterial evolution. Nature Reviews Microbiology 19(6), 347-359.

Roux, S., Páez-Espino, D., Chen, I.-M.A., Palaniappan, K., Ratner, A., Chu, K., Reddy, T., Nayfach, S., Schulz, F., Call, L., 2021. IMG/VR v3: an integrated ecological and evolutionary framework for interrogating genomes of uncultivated viruses. Nucleic acids research 49(D1), D764-D775.

Russell, T., Bedrikovetsky, P., 2023. Colloidal transport in anisotropic porous media: Kinetic equation and its upscaling. Journal of Computational and Applied Mathematics 422, 114896.

Ryan, J.N., Elimelech, M., 1996. Colloid mobilization and transport in groundwater. Colloids and surfaces A: Physicochemical and engineering aspects 107, 1-56.

Sˇimunek, J., He, C., Pang, L., Bradford, S., 2006. Colloid-facilitated solute transport in variably saturated porous media: Numerical model and experimental verification. Vadose Zone Journal 5(3), 1035-1047.

Safonov, A., Lavrinovich, E., Emel'yanov, A., Boldyrev, K., Kuryakov, V., Rodygina, N., Zakharova, E., Novikov, A., 2022. Risk of colloidal and pseudo-colloidal transport of

actinides in nitrate contaminated groundwater near a radioactive waste repository after bioremediation. Scientific Reports 12(1), 4557.

Saiers, J.E., Hornberger, G.M., 1996. The role of colloidal kaolinite in the transport of cesium through laboratory sand columns. Water Resources Research 32(1), 33-41.

Saiers, J.E., Lenhart, J.J., 2003. Ionic-strength effects on colloid transport and interfacial reactions in partially saturated porous media. Water Resources Research 39(9).

Saiers, J.E., Ryan, J.N., 2006. Introduction to special section on colloid transport in subsurface environments. Water resources research 42(12).

Scanlon, B.R., Cook, P.G., 2002. Theme issue on groundwater recharge.

Seabold, S., Perktold, J., 2010. Statsmodels: econometric and statistical modeling with python. SciPy 7(1), 92-96.

Secchi, E., Savorana, G., Vitale, A., Eberl, L., Stocker, R., Rusconi, R., 2022. The structural role of bacterial eDNA in the formation of biofilm streamers. Proceedings of the National Academy of Sciences 119(12), e2113723119.

Sen, T.K., Shanbhag, S., Khilar, K.C., 2004. Subsurface colloids in groundwater contamination: a mathematical model. Colloids and Surfaces A: Physicochemical and Engineering Aspects 232(1), 29-38.

Şengör, S.S., Ünlü, K., 2023. Colloidal transport of heavy metals in low-advective-velocity environmental systems: Reactive transport model on biogeochemical and hydrodynamic impacts. Vadose Zone Journal 22(1), e20233.

Shen, C., Huang, Y., Li, B., Jin, Y., 2008. Effects of solution chemistry on straining of colloids in porous media under unfavorable conditions. Water resources research 44(5).

Sieber, C.M., Probst, A.J., Sharrar, A., Thomas, B.C., Hess, M., Tringe, S.G., Banfield, J.F., 2018. Recovery of genomes from metagenomes via a dereplication, aggregation and scoring strategy. Nature microbiology 3(7), 836-843.

Simon Andrews, F., Segonds-Pichon, A., Biggins, L., Krueger, C., Wingett, S., 2010. FastQC: a quality control tool for high throughput sequence data.

Šimůnek, J., Van Genuchten, M.T., Šejna, M., 2006. The HYDRUS software package for simulating two-and three-dimensional movement of water, heat, and multiple solutes in variably-saturated media. Technical manual, version 1, 241.

Smith, M.B., Rocha, A.M., Smillie, C.S., Olesen, S.W., Paradis, C., Wu, L., Campbell, J.H., Fortney, J.L., Mehlhorn, T.L., Lowe, K.A., 2015. Natural bacterial communities serve as quantitative geochemical biosensors. MBio 6(3), 10.1128/mbio. 00326-00315.

Spielman-Sun, E., Boye, K., Dwivedi, D., Engel, M., Thompson, A., Kumar, N., Noël, V., 2024. A critical look at colloid generation, stability, and transport in redox-dynamic Environments: Challenges and perspectives. ACS Earth and Space Chemistry 8(4), 630-653.

Stegen, J.C., Fredrickson, J.K., Wilkins, M.J., Konopka, A.E., Nelson, W.C., Arntzen, E.V., Chrisler, W.B., Chu, R.K., Danczak, R.E., Fansler, S.J., 2016. Groundwater–surface water mixing shifts ecological assembly processes and stimulates organic carbon turnover. Nature communications 7(1), 11237.

Stumm, W., Morgan, J.J., 1996. Aquatic chemistry: chemical equilibria and rates in natural waters. Environmental science and technology.

Sun, N., Elimelech, M., Sun, N.-Z., Ryan, J.N., 2001a. A novel two-dimensional model for colloid transport in physically and geochemically heterogeneous porous media. Journal of contaminant hydrology 49(3-4), 173-199.

Sun, N., Sun, N.Z., Elimelech, M., Ryan, J.N., 2001b. Sensitivity analysis and parameter identifiability for colloid transport in geochemically heterogeneous porous media. Water Resources Research 37(2), 209-222.

Thorgersen, M.P., Ge, X., Poole, F.L., Price, M.N., Arkin, A.P., Adams, M.W., 2019. Nitrate-utilizing microorganisms resistant to multiple metals from the heavily contaminated Oak Ridge Reservation. Applied and environmental microbiology 85(17), e00896-00819.

Thorgersen, M.P., Lancaster, W.A., Vaccaro, B.J., Poole, F.L., Rocha, A.M., Mehlhorn, T., Pettenato, A., Ray, J., Waters, R.J., Melnyk, R.A., 2015. Molybdenum availability is key to nitrate removal in contaminated groundwater environments. Applied and environmental microbiology 81(15), 4976-4983.

Tian, R., Ning, D., He, Z., Zhang, P., Spencer, S.J., Gao, S., Shi, W., Wu, L., Zhang, Y., Yang, Y., 2020. Small and mighty: adaptation of superphylum Patescibacteria to groundwater environment drives their genome simplicity. Microbiome 8(1), 51.

Torkzaban, S., Bradford, S.A., Vanderzalm, J.L., Patterson, B.M., Harris, B., Prommer, H., 2015. Colloid release and clogging in porous media: Effects of solution ionic strength and flow velocity. Journal of contaminant hydrology 181, 161-171.

Toropov, A., 2020. Migration forms of anthropogenic radionuclides in tunnel waters at the Degelen Mountains, Semipalatinsk Test Site. Geochemistry International 58(3), 342-351.

U.S.DOE, 2022. Integrated Microbial Genomes & Microbiomes (IMG/M) system. https://img.jgi.doe.gov/cgi-bin/m/main.cgi. 2022).

Urwin, L., Savva, O., Corrigan, R.M., 2024. Microbial Primer: what is the stringent response and how does it allow bacteria to survive stress? Microbiology 170(7), 001483.

Van der Hoven, S.J., Solomon, D.K., Moline, G.R., 2003. Modeling unsaturated flow and transport in the saprolite of fractured sedimentary rocks: Effects of periodic wetting and drying. Water Resources Research 39(7).

VanderWal, A.R., Park, J.-U., Polevoda, B., Nicosia, J.K., Molina Vargas, A.M., Kellogg, E.H., O'Connell, M.R., 2023. Csx28 is a membrane pore that enhances CRISPR-Cas13b–dependent antiphage defense. Science 380(6643), 410-415.

Vintró, L.L., Mitchell, P., Omarova, A., Burkitbayev, M., Nápoles, H.J., Priest, N., 2009. Americium, plutonium and uranium contamination and speciation in well waters, streams and atomic lakes in the Sarzhal region of the Semipalatinsk Nuclear Test Site, Kazakhstan. Journal of environmental radioactivity 100(4), 308-314.

Waldron, P.J., Wu, L., Nostrand, J.D.V., Schadt, C.W., He, Z., Watson, D.B., Jardine, P.M., Palumbo, A.V., Hazen, T.C., Zhou, J., 2009. Functional gene array-based analysis of microbial community structure in groundwaters with a gradient of contaminant levels. Environmental Science & Technology 43(10), 3529-3534.

Walker, K.F., 2024. Spatiotemporal dynamics of microbial communities in contaminated subsurface University of Tennessee.

Wang, C., Wang, R., Huo, Z., Xie, E., Dahlke, H.E., 2020. Colloid transport through soil and other porous media under transient flow conditions—A review. Wiley Interdisciplinary Reviews: Water 7(4), e1439.

Wang, C., Yu, Q.-Y., Ji, N.-N., Zheng, Y., Taylor, J.W., Guo, L.-D., Gao, C., 2023. Bacterial genome size and gene functional diversity negatively correlate with taxonomic diversity along a pH gradient. Nature Communications 14(1), 7437.

Wang, D., Wu, J., Wang, Y., Ji, Y., 2020. Finding high-quality groundwater resources to reduce the hydatidosis incidence in the Shiqu County of Sichuan Province, China: analysis, assessment, and management. Exposure and Health 12(2), 307-322.

Wang, Q., Garrity, G.M., Tiedje, J.M., Cole, J.R., 2007. Naive Bayesian classifier for rapid assignment of rRNA sequences into the new bacterial taxonomy. Applied and environmental microbiology 73(16), 5261-5267.

Wang, S., Zhu, D., Ge, T., Wang, Y., Zhang, Y., Liang, C., Liao, H., Liang, X., 2024. Unveiling the top-down control of soil viruses over microbial communities and soil organic carbon cycling: a review. Climate Smart Agriculture, 100022.

Wiesner, M.R., Lowry, G.V., Alvarez, P., Dionysiou, D., Biswas, P., 2006. Assessing the risks of manufactured nanomaterials. ACS Publications.

Wu, L., Wen, C., Qin, Y., Yin, H., Tu, Q., Van Nostrand, J.D., Yuan, T., Yuan, M., Deng, Y., Zhou, J., 2015. Phasing amplicon sequencing on Illumina Miseq for robust environmental microbial community analysis. BMC microbiology 15, 1-12.

Wu, Y.-W., Simmons, B.A., Singer, S.W., 2016. MaxBin 2.0: an automated binning algorithm to recover genomes from multiple metagenomic datasets. Bioinformatics 32(4), 605-607.

Wu, Y.-W., Tang, Y.-H., Tringe, S.G., Simmons, B.A., Singer, S.W., 2014. MaxBin: an automated binning method to recover individual genomes from metagenomes using an expectation-maximization algorithm. Microbiome 2, 1-18.

Wu, Z., Liu, T., Chen, Q., Chen, T., Hu, J., Sun, L., Wang, B., Li, W., Ni, J., 2024. Unveiling the unknown viral world in groundwater. Nature Communications 15(1), 6788.

Xing, Y., Ellis, A., Magnuson, M., Harper Jr, W.F., 2020. Adsorption of bacteriophage MS2 to colloids: Kinetics and particle interactions. Colloids and Surfaces A: Physicochemical and Engineering Aspects 585, 124099.

Yao, K.-M., Habibian, M.T., O'Melia, C.R., 1971. Water and waste water filtration. Concepts and applications. Environmental science & technology 5(11), 1105-1112.

Zachara, J.M., Chen, X., Murray, C., Hammond, G., 2016. River stage influences on uranium transport in a hydrologically dynamic groundwater-surface water transition zone. Water Resources Research 52(3), 1568-1590.

Zachara, J.M., Serne, J., Freshley, M., Mann, F., Anderson, F., Wood, M., Jones, T., Myers, D., 2007. Geochemical processes controlling migration of tank wastes in Hanford's vadose zone. Vadose Zone Journal 6(4), 985-1003.

Zhang, L., Li, L., Chen, K., Zhang, Q., Shao, J., Cui, Y., Zhu, J., Zhang, A., Yang, S., 2024. Adsorption-desorption of 241Am (III) on montmorillonite colloids and quartz sand: Effects of pH, ionic strength, colloid concentration and grain size. Journal of Environmental Radioactivity 275, 107430.

Zhang, W., Tang, X.-Y., Weisbrod, N., Zhao, P., Reid, B.J., 2015. A coupled field study of subsurface fracture flow and colloid transport. Journal of Hydrology 524, 476-488.

Zvikelsky, O., Weisbrod, N., 2006. Impact of particle size on colloid transport in discrete fractures. Water Resources Research 42(12).

Vita

Diliya Utegenovna Murtazina was born in the Kazakh SSR (part of the USSR) on May 7, 1991, which seven months later became the independent Republic of Kazakhstan. She was raised in Pereleski village, Denisov District, in the Kostanay region of Kazakhstan, in a Kazakh and Tatar family. This region, located in Central Asia, is characterized by an extreme continental and cold steppe climate, bordering the southern part of Siberia. She lived there and attended the local school until she was 16 years old. She graduated from Ozat Boarding School for Gifted Children in Kostanay city in 2009. She received a State Education Grant from the Republic of Kazakhstan, which covered tuition and provided a stipend, from 2009 to 2014, to study at Lomonosov Moscow State University in the Russian Federation. She earned a Bachelor of Ecology and Environmental Management with honors from the Department of Landscape Ecology at Lomonosov Moscow State University in 2014. During her undergraduate studies, she worked as an auditor intern in the Ecology Department of Kostanay Region, part of the Control and State Inspection in the Oil and Gas Complex of the Ministry of Energy, a government agency in Kostanay, Kazakhstan, during the summers of 2011 and 2012. After graduating, she worked as an Environmental Protection Engineer at Aray Holding in Kazakhstan for eight months in 2015. After completing six months of intensive self-study in academic English and passing the IELTS exam, she applied to graduate school in the U.S. She completed a Master of Engineering in Energy Systems at the University of Illinois at Urbana-Champaign in the Department of Nuclear, Plasma, and Radiological Engineering in 2017. She held a sustainability intern position at the Institute for Sustainability, Energy, and Environment (iSEE) in Urbana, Illinois, where she also worked part-time for ten months. Following her master's degree, she received a fellowship to pursue a PhD in Energy Science and Engineering at the Bredesen Center (Oak Ridge Innovation Institute) at the University of Tennessee, Knoxville. She joined the Hazen lab at the University of Tennessee in November 2021.